

Organic neuromorphic computing

Citation for published version (APA):

van Doremaele, E. R. W. (2023). *Organic neuromorphic computing: at the interface with bioelectronics*. [Phd Thesis 1 (Research TU/e / Graduation TU/e), Mechanical Engineering]. Eindhoven University of Technology.

Document status and date:

Published: 25/05/2023

Document Version:

Publisher's PDF, also known as Version of Record (includes final page, issue and volume numbers)

Please check the document version of this publication:

- A submitted manuscript is the version of the article upon submission and before peer-review. There can be important differences between the submitted version and the official published version of record. People interested in the research are advised to contact the author for the final version of the publication, or visit the DOI to the publisher's website.
- The final author version and the galley proof are versions of the publication after peer review.
- The final published version features the final layout of the paper including the volume, issue and page numbers.

[Link to publication](#)

General rights

Copyright and moral rights for the publications made accessible in the public portal are retained by the authors and/or other copyright owners and it is a condition of accessing publications that users recognise and abide by the legal requirements associated with these rights.

- Users may download and print one copy of any publication from the public portal for the purpose of private study or research.
- You may not further distribute the material or use it for any profit-making activity or commercial gain
- You may freely distribute the URL identifying the publication in the public portal.

If the publication is distributed under the terms of Article 25fa of the Dutch Copyright Act, indicated by the "Taverne" license above, please follow below link for the End User Agreement:

www.tue.nl/taverne

Take down policy

If you believe that this document breaches copyright please contact us at:

openaccess@tue.nl

providing details and we will investigate your claim.

Organic neuromorphic computing

at the interface with bioelectronics

Organic neuromorphic computing at the interface with bioelectronics

Copyright © 2023 Eveline van Doremaele

A catalogue record is available from the Eindhoven University of Technology Library.

ISBN: 978-90-386-5734-9

All rights reserved. No part of this book may be reproduced, stored in a database or retrieval system, or published, in any form or in any way, electronically, mechanically, by print, photo print, microfilm or any other means without prior permission by the author.

Printing: Ridderprint

Cover design: Eveline van Doremaele

This thesis was financially supported by The European Union's Horizon 2020 Research and Innovation Programme (grant agreement no. 802615)

Organic neuromorphic computing

at the interface with bioelectronics

PROEFSCHRIFT

ter verkrijging van de graad van doctor aan de Technische Universiteit Eindhoven,
op gezag van de rector magnificus prof.dr. S.K. Lenaerts voor een commissie
aangewezen door het College voor Promoties, in het openbaar te verdedigen op
donderdag 25 mei 2023 om 16:00 uur.

door

Eveline Rosa Wilhelmina van Doremaele

geboren te Sittard

Dit proefschrift is goedgekeurd door de promotoren en de samenstelling van de promotiecommissie is als volgt:

Voorzitter	prof.dr.ir. L.E. Govaert	
1 ^e promotor	dr.ir. Y.B. van de Burgt	
2 ^e promotor	prof.dr.ir. J.M.J. den Toonder	
Leden:	prof.dr. E.W. Meijer	
	prof.dr. G.G. Malliaras	(University of Cambridge)
	dr. S. Fabiano	(Linköping University)
	prof.dr. J. Rivnay	(Northwestern University)
	prof.dr. F. Santoro	(RWTH Aachen)

Het onderzoek of ontwerp dat in dit proefschrift wordt beschreven is uitgevoerd in overeenstemming met de TU/e Gedragscode Wetenschapsbeoefening.

Summary

Traditional computers are optimized for high precision calculations, tasks which are difficult for humans. However, there is a shift towards applications that operate more like humans: processing unstructured and noisy data in real time, while adapting to change. Nowadays we see many of these applications, such as self-driving cars, problem solving tasks and facial and language recognition. This can be realized by Artificial Intelligence (AI), supported by large artificial neural networks and while powerful, these software-based learning algorithms are energy-inefficient. Our brain on the other hand is extremely efficient in similar tasks. Unlike traditional computers it allows for highly parallel computation, it is dynamic, reconfigurable and can learn from experience. Neuromorphic computing aims to mimic several crucial concepts of the brain to efficiently emulate AI tasks and apply learning at the hardware level. While many technologies and materials are being currently investigated for applications in neuromorphic computing, this thesis particularly focuses on organic materials that have significant advantages for applications at the interface with biology. At the same time, the field of bioelectronics is also rapidly increasing and has made enormous progress towards the development of devices capable of sensing, monitoring, and controlling a biological environment. Nevertheless, fully autonomous bioelectronic applications do not only demand the acquisition of biological signals, but also require local low power operation, data processing and storage. In this thesis we use organic materials as the building blocks for neuromorphic systems to advance future intelligent bioelectronic applications.

Many hardware applications rely on training algorithms executed in software. Here we demonstrate a smart biosensing platform that can be trained completely on-chip to classify a model disease. It is based on organic neuromorphic devices as the synaptic weights of a hardware neural network, its associated output classification hardware, and sensors. The versatility of the neuromorphic system is highlighted via on-chip retraining, by switching sensor input signals and by the formation of logic gates on the same chip. This training algorithm represents the hardware analogue of the software perceptron algorithm (that allows classification of linear separable binary data). While it is the first demonstration of training fully in hardware, efforts have been made to design hardware algorithms that allow for more complex classification problems using a multilayer neural network that requires training with a backpropagation algorithm. In this thesis we propose a novel updating sequence that enables

backpropagation in hardware without the need to store the values of weights and gradients throughout the learning phase which has been considered one of the greatest challenges. In order to integrate these neuromorphic circuitries with true biological systems we aim to bridge the gap by replicating the biological neuronal pathway. The fundamental communication mechanism within the human body relies on the spiking frequency of action potentials which can be modulated by neurotransmitters. In this thesis we present a novel adaptive spiking circuit that replicates the key biological functions of neurons and its synapses and their interdependent chemical synaptic connection. We combine these functionalities to establish an artificial retinal pathway and show the signal transduction from light stimulus to spiking frequency and to dopamine-mediated plasticity. The chemically adaptive neuromorphic spiking circuit constitutes a fundamental building block for programmable neural pathways that can locally transduce and process both physical as well as physiological environmental information, an essential step towards realizing processors at the biohybrid interface. Advanced concepts enabling computing systems that can interact with the biological environment clearly need stable materials that can operate at biological interfaces. We consider various organic materials. We designed an n-type copolymer and systematically alter the length of its side chains in order to understand the structure-performance relationship to allow for design of high-performance materials. One remarkable high-performance material is highlighted due to its versatility. We show a tunable sensing circuit constructed from this single material, based on a complementary logic inverter combined with a neuromorphic memory element, and which can locally modulate biologically relevant signals. The ability to preprocess signals locally is important as (hardware) neural network applications require processed signals such as input normalization.

Publiekssamenvatting

De traditionele computersystemen zijn geoptimaliseerd in het heel precies uitvoeren van berekeningen. Echter, we zien steeds meer toepassingen die acties van de mens uitvoeren, zoals het leren en aanpassen aan een veranderende omgeving, zelfs in real-time, en omgaan met ongestructureerde en imperfecte data. Dit zijn taken die een stuk lastiger zijn voor de klassieke computers. Deze toepassingen zien we bijvoorbeeld terug in zelf-rijdende auto's, en gezichts- en taalherkenning, en zijn gebaseerd op kunstmatige intelligentie (oftewel artificial intelligence). Kunstmatige intelligentie bestaat uit grote neurale netwerken die erg succesvol zijn maar middels de huidige computersystemen ook erg inefficiënt in het energieverbruik. Onze hersenen, daarentegen, zijn juist heel efficiënt in het uitvoeren van dit soort complexe taken. In tegenstelling tot de traditionele computersystemen, kan ons brein processen en berekeningen tegelijkertijd uitvoeren en leren aan de hand van eerdere ervaringen.

Het vakgebied van *Neuromorphic computing* streeft er naar om de hersenen na te bootsen met als doel deze toepassingen efficiënt uit te kunnen voeren, slimme toepassingen te realiseren die lokaal kunnen leren en zelfs een interactie tussen machine en mens te creëren. Er zijn verschillende technologieën en materialen die worden onderzocht, echter in deze thesis wordt er vooral gefocust op organische materialen, welke grote voordelen hebben voor slimme toepassingen die een raakvlak met de biologie hebben. Het betreft geleidende organische polymeren, lange moleculen die een elektrische stroom kunnen doorlaten. Ze kunnen hun weerstand aanpassen aan de hand van negatief (elektronen) of positief (ionen) geladen deeltjes die het materiaal binnenkomen of verlaten. Het materiaal onthoudt die aangepaste weerstand en kan gezien worden als een geheugen functie. Veel communicatie in ons lichaam en in onze hersenen verloopt ook via ionen. Dat maakt deze materialen dus zo geschikt, niet alleen om de werking van cellen in ons brein te imiteren, maar ook om direct met de cellen te communiceren. We onderzoeken verschillende organische materialen die dienen als de bouwstenen voor neuromorfische systemen. Met deze materialen maken we elektronische circuits die aspecten van het brein kunnen imiteren zoals het communiceren tussen cellen, het leren en het verwerken van informatie. Zo willen we toepassingen realiseren die autonoom en adaptief in een biologische omgeving zoals het menselijk lichaam kunnen functioneren.

Table of contents

Summary	i
Publiekssamenvatting	iii
Table of contents	x
1 Introduction to neuromorphic computing	1
1.1 From analog to digital computers	2
1.2 Neuromorphic computing: Best of both worlds	3
1.3 Thesis outline	4
Bibliography	7
2 Towards organic neuromorphic devices for adaptive sensing and novel computing paradigms in bioelectronics	9
2.1 Introduction	10
Bibliography	20
3 Retractable neuromorphic biosensor for on-chip learning and classification	21
3.1 Introduction	22
3.2 Generating input signals from ion sensors	23
3.3 Training in hardware for on-chip classification	24
3.4 Update behaviour of the neuromorphic circuit	25

3.5	On-chip retraining	27
3.6	Conclusion	28
3.7	Methods	28
3.7.1	EC-RAM fabrication	28
3.7.2	Ion selective OECT fabrication	29
3.7.3	Sweat samples	29
3.7.4	Data acquisition	30
3.8	Supporting Information	30
3.8.1	Ion selective electrodes (ISE) and organic electrochemical transistors (IS-OECT)	30
3.8.2	EC-RAM modulation and state retention	34
3.8.3	Backpropagation in the neuromorphic circuit	37
3.8.4	Effect of different input values	37
3.8.5	Hardware neural network circuit	40
	Bibliography	46
4	Novel implementation of the backpropagation algorithm for <i>in situ</i> training of multi-layer hardware neural networks using progressive gradient descent	47
4.1	Introduction	48
4.2	Hardware implementation gradient descent	49
4.3	Results	50
4.3.1	Classification performance of parallel versus progressive update	50
4.3.2	<i>In situ</i> hardware classification performance	52
4.4	Conclusion	55

4.5	Methods	55
4.5.1	EC-RAM fabrication	55
4.6	Supporting Information	56
4.6.1	Transistor multiplication	56
4.6.2	Weight modulation EC-RAM	56
4.6.3	Hardware neural network simulation	57
4.6.4	Hardware neural network testing	58
4.6.5	Impact weight initialization	60
4.6.6	Discussion hardware classification performance	61
	Bibliography	65
5	Organic neuromorphic spiking circuit for retina-inspired sensory coding and neurotransmitter-mediated neural pathways	67
5.1	Introduction	68
5.2	Methods	74
5.2.1	p(C4-T2-C0-EG) devices fabrication	74
5.2.2	P-3O devices fabrication	74
5.2.3	Biohybrid synapse and capacitor fabrication	74
5.2.4	Neurotransmitters solutions preparation	74
5.2.5	Spiking circuit connections	75
5.2.6	Electrical measurements	75
5.3	Supporting Information	76
5.3.1	Spiking circuit	76
5.3.2	Sensory coding with pressure sensor	78

5.3.3	Bio-hybrid synapse and its synaptic modulation	80
5.3.4	Sensory coding with neurotransmitters dopamine and serotonin	81
5.3.5	Voltage divider and switch circuit to connect the two bio-hybrid synapses	84
5.3.6	Sensory coding with light	87
	Bibliography	91
6	Adaptive biosensing and neuromorphic classification based on an ambipolar organic mixed ionic–electronic conductor	93
6.1	Introduction	94
6.2	Results & Discussion	95
6.3	Conclusion	103
6.4	Experimental Section	103
6.4.1	Materials	103
6.4.2	Device Fabrication and Characterization	103
6.5	Supporting Information	104
6.5.1	Material characterization	104
6.5.2	OECTs	106
6.5.3	Dopamine sensing	107
6.5.4	EC-RAM	108
6.5.5	Ambipolar inverter	109
6.5.6	Neuromorphic inverter simulation for EMG signal processing	111
6.5.7	EC-RAM based neural network simulation	111
	Bibliography	117

7	High-performance organic electrochemical transistors and neuromorphic devices comprising naphthalenediimide-dialkoxybithiazole copolymers bearing glycol ether pendant groups	119
7.1	Introduction	120
7.2	Results and discussion	122
7.2.1	Molecular Design and Characterization	122
7.2.2	Aqueous Electrolyte Gated OECTs	124
7.2.3	Ion Gel Gated Electrochemical Transistors and Resistive Random-Access Memory Devices (EC-RAMs)	129
7.3	Conclusion	131
7.4	Experimental Section	131
7.4.1	Materials	131
7.4.2	Device Fabrication and Characterizations	132
7.4.3	Cyclic Voltammetry (CV) and Electrochemical Impedance Spectroscopy (EIS)	132
7.4.4	UV-vis-NIR Electrochemical Spectroscopy	132
7.4.5	GIWAXS	132
7.5	Supporting Information	133
7.5.1	Water contact angle	133
7.5.2	UV-vis-NIR Absorption Spectroscopy	133
7.5.3	Cyclic voltametry	134
7.5.4	Organic Field-Effect Transistor (OFET) Fabrication and Performance of Polymers. OFET fabrication and characterization	135
7.5.5	Atomic force microscopy	136
7.5.6	UV-vis-NIR Electrochemical Spectroscopy	136

7.5.7	Grazing Incidence Wide Angle X-Ray Scattering (GIWAXS)	138
7.5.8	Organic Electrochemical Transistors (OECTs)	139
7.5.9	Ion gel electrolyte side-gated OECTs	146
	Bibliography	154
8	Conclusion	155
8.1	Conclusions	156
8.2	Outlook	158
	Scientific Output	161
	Curriculum Vitae	163
	Acknowledgements	165

Chapter 1

Introduction to neuromorphic computing

Computers have become essential to all aspects of modern life and are everywhere all over the globe. The history of computing has been marked by constant innovation and transformation, with new paradigms emerging as researchers seek to overcome the limitations of existing technologies. Up until the 1960s the most powerful computers were analog. Digital computers exploded to the scenes with the advent of transistors and now, almost everything is digital. While digital computing has been the dominant computing paradigm for several decades, it is now facing new challenges that are driving the need for a new type of computing. Neuromorphic, or brain-inspired, computing uses both analog and digital computing to mimic the efficient information processing of the brain. Combined with bioelectronics it has the potential to realize smart and adaptive systems at the interface with biology.

1.1 From analog to digital computers

The history of computing machines can be traced back to the earliest human civilizations, who developed mechanical devices such as the abacus for performing basic calculations. Over time, more sophisticated devices were developed, including slide rules, logarithmic tables, and other tools that made it easier to perform complex mathematical operations. However, it was not until the development of electronic computers in the 20th century that computing truly became a technology that had a profound and far-reaching impact. The first computers were analog machines that used physical components such as gears, levers, and springs to perform calculations. These machines were used primarily for scientific and engineering applications, such as calculating the trajectory of artillery shells and predicting the weather.[1]

One of the most famous early analog computers was the Antikythera mechanism, an ancient Greek device having gears that represent the motion of celestial objects that was used to calculate astronomical positions and eclipses.[2] During World War II analog computers were used extensively, particularly in the development of radar and other military technologies. However, these were limited in their capabilities such as speed and accuracy and were eventually superseded by digital computers. The problem with analog computers is that the physical device is a model for the real world. Therefore, any inaccuracy in the components translates into inaccuracy of the computation. The important discovery made by Claude Shannon in 1936 opened the door to the digital revolution. He showed that any numerical operation can be carried out using the basic building blocks of Boolean algebra: two values true or false (one or zero), and three operations, AND, OR, and NOT. This makes digital computers the ideal versatile machines.[1, 3]

The first digital computers were developed in the 1940s and 1950s, and were based on the binary number system, using only two digits (0 and 1) to represent all numbers and operations. The first digital computer was the Electronic Numerical Integrator and Computer (ENIAC), which used vacuum tubes to perform calculations and could perform up to 5,000 additions per second.[4] Vacuum tubes were widely used in electronic devices until the invention of the transistor in the 1950s, a fundamental building block in modern electronic systems. Its invention revolutionized the field of electronics. It was smaller, cheaper, and more reliable than the existing vacuum tubes. It was only after the transistor and the subsequent development of the integrated circuit in the 1960s that it became possible to build smaller and more powerful computers. These were based on the so called von Neumann architecture which enabled to build general-purpose devices, unlike analog computers which were an analog for only one type of problem.[1] Furthermore, since they operate on symbols (ones and zeros)

digital computers provide exact answers, and their operations are repeatable and far more resilient to noise.[5] Moreover, almost any computation can be executed using only a few components which allows those components to be fully miniaturized and optimized. As a result, digital computing has been the dominant computing paradigm for several decades. However, it is facing new challenges that are driving the need for a new type of computing.

1.2 Neuromorphic computing: Best of both worlds

Digital computing has been highly effective in processing large amounts of data, but it has its shortcomings. Moore's Law, a prediction made by Gordon Moore which states that the number of transistors on a chip doubles every two years, is reaching its limit because transistors have now nearly the same size as atoms. Simultaneously, data-intensive applications have placed a high demand on hardware performance as advancements in machine learning are straining the capabilities of digital computers. One of the biggest challenges faced by digital computing today is the growing demand for more efficient and powerful computing systems. The computing systems based on the von Neumann architecture have a physical separation between processing and memory units and are therefore largely inefficient due to the relatively slow and energy demanding data movement between these two units.[1, 6]

As a solution to these challenges, a new generation of computing has emerged that takes its inspiration from the human brain: *Neuromorphic computing* (see Fig. 1.1). Unlike conventional von Neumann computers the brain is extremely efficient in dealing with complex, unstructured and noisy data and it can adapt in real-time. The term "neuromorphic" was first used in the early 1990s by Carver Mead, to describe a new approach to computing that was inspired by the information processing of the

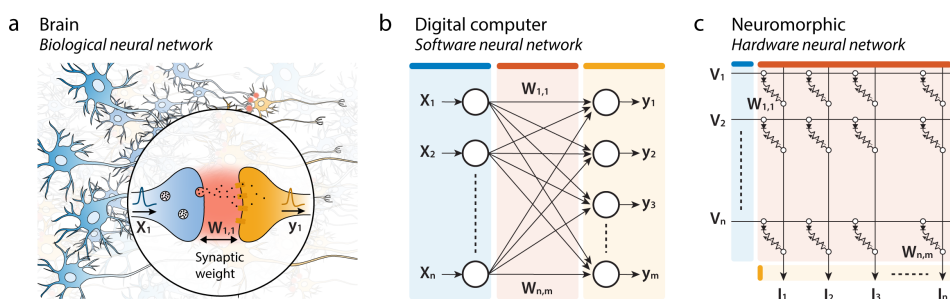


Figure 1.1: Neural network architectures. Schematic representation of a) a biological neural network as in the brain, b) an artificial software neural network used in digital computers and, c) an artificial hardware neural network used in neuromorphic (brain-inspired) computing.

brain.[7] One important aspect is that the computational and organizing principles of the nervous system differ significantly from modern computers. In contrast to Boolean logic and precise digital representations, nervous systems carry out robust and reliable computation using hybrid analog/digital unreliable processing elements.[5, 8] The term neuromorphic computing is somewhat flexible. It describes electronic processing systems that emulate the bio-physics of real neurons and synapses, ranging from reproducing neurophysiological principles with detailed synaptic chemical dynamics to a more high-level brain-inspired representation such as the vector-matrix multiplication.[6]

The goal of neuromorphic computing is to develop more efficient and powerful computing systems that can perform complex tasks with greater speed and accuracy than is possible with traditional digital computing. While promising, neuromorphic computing is still in the early stages of development. Ongoing research focuses on exploring neuromorphic algorithms and circuitry and developing new devices and materials. Simultaneously, the field of applications for neuromorphic computing is still growing. In this work we focus on applications that combine neuromorphic computing with bioelectronics, with the potential to realize smart and autonomous systems at the interface with biology. To achieve this, suitable materials that can operate at biological interfaces are clearly needed. The success of many organic bioelectronic applications results from reduced interface impedance and extraordinarily high electrochemical transconductance (ion-to-electron transduction) in organic mixed ionic–electronic conductors (OMIECs). These and other unique properties such as biocompatibility, low voltage operation, simple fabrication processing, and stretchability and flexibility of materials have opened a wide variety of possible bioelectronic applications. Recently, these materials have also emerged in tunable neuromorphic devices and biohybrid systems due to their dynamic range, the ability to electrochemically dope these polymers and their interaction with neurotransmitters.

1.3 Thesis outline

In this thesis we discuss various aspects of organic neuromorphic computing that are central for realizing smart and adaptive bioapplications. The thesis starts with a perspective in chapter 2. Chapter 3 and 4 are dedicated to executing the conventional software algorithms on hardware, while chapter 5 aims to mimic essential biological functions as building blocks of artificial neuronal pathways. Chapters 6 and 7 continue on neuromorphic materials and lastly chapter 8 concludes this thesis.

In **chapter 2**, we highlight the recent* trends in organic neuromorphic devices and organic bioelectronic sensing platforms. We discuss opportunities in merging these two fields to further close the loop between sensing and stimulation/actuation for smart bioelectronic applications. Materials and devices that exhibit memory and have the potential to operate at the interface with biology can pave the way for novel data classification paradigms with bio-inspired features in information processing. We envision smart multi-modal sensor platforms and local neuromorphic processing to enable fully autonomous applications in the future.

Chapter 3 demonstrates a programmable biosensor as a showcase for advanced adaptive bioelectronic systems. We show the classification of the genetic disease cystic fibrosis from artificial sweat using ion selective sensors. We highlight the versatility of the organic neuromorphic chip by demonstrating multiple retraining processes for various sets of input signals.

In **chapter 4** we propose an alternative to the traditional backpropagation algorithm, which can be executed fully in hardware to bypass the power-hungry alternative in software. Importantly, this approach updates its layers progressively by propagating the information back through the network which allows for expanding to multilayer neural networks and does not require the storage of weight information. First, we show with a neuromorphic circuit simulation that the layer-by-layer error backpropagation approach yield similar accuracy compared to the software alternative. We further demonstrate the working principle of the *in situ* error calculation and the proposed progressive backpropagation method using a single and double layer hardware neural network for binary and XOR classification.

In **chapter 5** we present a novel adaptive spiking circuit that is able to replicate various functionalities of neurons and their synapses. We emulate the afferent neurons sensory coding from external physical stimuli and the neuromodulatory activity of interneurons. We further demonstrate an interdependent chemical synaptic connection by associating the spiking circuit with biohybrid synapses. The circuit constitutes a fundamental building block for programmable neural pathways that can locally transduce and process both physical as well as physiological environmental information. Finally, we combine both functionalities to establish a full neuronal pathway replicating the retina as a biological system model and show the signal transduction from light stimulus to spiking frequency and to dopamine-mediated plasticity.

Chapter 6 demonstrates a novel high-performance material, P-3O, which allows for the fabrication of a monolithically integrated adaptive sensor. We show the

*Research after June 2019 is not included in this chapter.

remarkable characteristics of this semiconducting polymer, including symmetric p- and n-type transfer curves, high performance, and ambient stability. We fabricated a tunable sensing circuit based on a complementary logic inverter combined with a neuromorphic memory element constructed from this single material, and show that it can modulate biologically relevant signals like electromyograms (EMGs) and electrocardiograms (ECGs) locally. Finally, we demonstrate that a small neuromorphic array based on this material yields high classification accuracy in heartbeat anomaly detection.

Chapter 7 focuses on three non-fused, NDI-2Tz copolymers decorated with and without hydrophilic TEG side chains. We demonstrate the transistor performance of the materials in aqueous environment and relate this to the hydrophilicity and electron affinity. We also show the transistor as well as their neuromorphic performance while operating with a solid state electrolyte. This chapter contributes to the understanding of the structure-performance relationship of these n-type materials and demonstrates that non-fused donor-acceptor conjugated polymers can achieve high electron mobility and ion penetration capability simultaneously.

1. O'Regan, G. *A Brief History of Computing*. en. ISBN: 978-3-030-66598-2 (Springer International Publishing, Cham, 2021).
2. Freeth, T. *et al.* [Decoding the ancient Greek astronomical calculator known as the Antikythera Mechanism](#). en. *Nature* **444**, 587–591. ISSN: 0028-0836, 1476-4687 (Nov. 2006).
3. Shannon, C. E. [A symbolic analysis of relay and switching circuits](#). en. *Electrical Engineering* **57**, 713–723. ISSN: 0095-9197 (Dec. 1938).
4. Haigh, T., Priestley, M. & Rope, C. *ENIAC in Action: Making and Remaking the Modern Computer*. EN. ISBN: 0-262-53517-3 (The MIT Press, Jan. 2019).
5. Douglas, R., Mahowald, M. & Mead, C. Neuromorphic Analogue VLSI. en (1995).
6. Christensen, D. V. *et al.* [2022 roadmap on neuromorphic computing and engineering](#). en. *Neuromorphic Computing and Engineering* **2**. Publisher: IOP Publishing, 022501. ISSN: 2634-4386 (May 2022).
7. Mead, C. Neuromorphic Electronic Systems. en. *PROCEEDINGS OF THE IEEE* **78** (1990).
8. Chicca, E., Stefanini, F., Bartolozzi, C. & Indiveri, G. [Neuromorphic electronic circuits for building autonomous cognitive systems](#). en. *Proceedings of the IEEE* **102**. arXiv:1403.6428 [cs, q-bio], 1367–1388. ISSN: 0018-9219, 1558-2256 (Sept. 2014).

Chapter 2

Towards organic neuromorphic devices for adaptive sensing and novel computing paradigms in bioelectronics

Bioelectronics has made enormous progress towards the development of concepts, materials and devices that are capable of sensing, monitoring and controlling a biological environment, by incorporating concepts such as local drug delivery and electrical, chemical or mechanical stimulation. Nevertheless, fully autonomous bioelectronic applications demand not only the acquisition of biological signals, but also local low power data processing, storage and the extraction of specific features of merit. Here, we present an overview of the latest studies on organic neuromorphic and sensing devices. We also speculate on the need for smart and adaptive sensing and highlight the potential of these concepts to enhance the interaction efficiency between electronics and biological substances.

This chapter is based on *Towards organic neuromorphic devices for adaptive sensing and novel computing paradigms in bioelectronics*, **Eveline R. W. van Doremale**, Paschalis Gkoupidenis, Yoei van de Burgt, *Journal of Materials Chemistry C*, **7**, (41), 2019.

2.1 Introduction

Traditional computing systems are unable to capture the capability of the brain in real world information processing as evidenced by the anticipated end to Moore's law. Organic (electrochemical) materials have recently emerged as building blocks of neural processing[1] and possess basic forms of neuroplasticity that are able to emulate brain-like functionality at the device level [2] (see Fig. 2.1). Compared to inorganic materials, the excellent characteristics of organic electronic materials, such as low energy operation and tunability, allow these materials to be used as a first step towards efficient neuromorphic computing systems.[7] In fact, devices based on organic-mixed conductors demonstrate good electrical stability (10^5 sec retention time)[8] as well as excellent endurance ($> 10^9$ switching cycles)[6] and allow for direct control of material characteristics. A recently demonstrated ionic floating gate concept based on organic devices shows efficient parallel updating of a small array.[6] Small-scale perceptron-based artificial neural networks have also been demonstrated.[9] Another concept was recently presented based on an evolvable organic electrochemical transistor, where long-

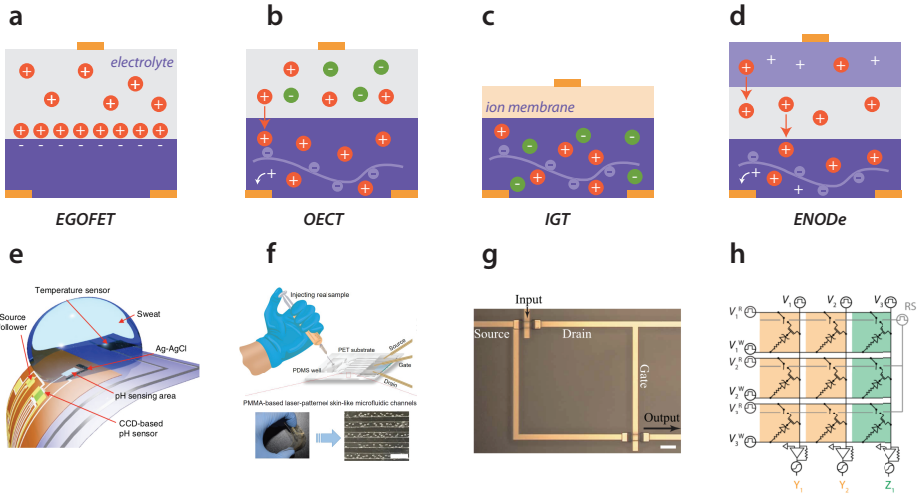


Figure 2.1: Recent examples of organic transistors in neuromorphic and sensing applications. (a) Electrolyte-gate organic field effect transistor. A gate pulse forms a double layer between the electrolyte and organic semiconductor, which turns the channel on. (b) Organic electrochemical transistor (OECT). The electrolyte and ions penetrate the complete volume of the (semi)-conducting polymer, thereby switching the channel on or off. (c) Internal ion-gated organic electrochemical transistor (IGT). Here, contained mobile ions within the conducting polymer channel are responsible for the conductance switching, which enables both volumetric capacitance and short ionic transit time. (d) Electrochemical non-volatile organic device (ENODE). This device combines an OECT with a polymeric gate material, to allow for non-volatile switching of the channel.[1] (e) pH sensor based on a charge-coupled device.[3] (f) Wearable cortisol sensor based on an OECT channel.[4] (g) Example of a simple circuit based on IGT devices.[5] (h) Simple neuromorphic array based on ENODE devices, that allows for parallel updating by employing memristors as access devices.[6]

term changes rely on the electro-polymerization of a conductive polymer between the device terminals.[10] Apart from organic mixed conductors, ferroelectric organic neuromorphic transistors have also been demonstrated recently.[11] These examples showcase the initial efforts towards building blocks for the realization of small organic-based neural networks and applications in local computation and feature extraction.

Due to their ability to operate in global or shared electrolytes, organic neuromorphic devices have shown multi-terminal operations [12], global connectivity control[13] as well as phase-dependent synchrony through global electrical oscillations.[14] The introduction of global phenomena in organic neuromorphic devices demonstrates the effectiveness in mimicking brain-like functionality in a more bio-plausible way. Indeed, in the brain, apart from local neuronal development through synaptic potentiation and depression, the global electrochemical environment of biological neural networks is essential for the network functionality. Moreover, neuromorphic sensing implies a common electrochemical environment in which the neuromorphic circuitry might be immersed. Therefore, besides local device training, global electrochemical regulation of the circuitry can offer additional degrees of freedom that are necessary for feature extraction. However, a challenge remains to develop organic devices and architectures capable of reproducing neuro-inspired information processing functions with the potential to actually operate at the interface with biology. Such architectures will have significant impact in applications that span from brain–computer-interfaces and neuroscience to bioinformatics and the definition of novel computational paradigms at the interface with biology. Initial reports in this direction include time-dependent classification, by leveraging the inherent global phenomena of organic electrochemical transistors in the framework of reservoir computing.[15] However, the field is at an early stage and in need for novel materials, devices and circuit concepts. Nevertheless, the rapid rise of sensing platforms based on organic electrochemical transistors,[16] as well as novel concepts as building blocks for bioelectronic circuits and devices[5], greatly enhance the validity of this field for smart or even neuromorphic bio-signal processing.

To effectively enhance the operational ability of bioelectronics beyond sensing or stimulation, a bi-directional coupling is essential. On the one hand, a biological process transfers a signal to an organic electronic device where for instance an enzymatic reaction, changes the current flow through the polymer transistor, see Fig. 2.2a. In the opposite direction, an organic electronic device can trigger a biochemical reaction or biological process, for instance by the application of electrical stimuli on a conducting polymer electrode, and the activity of biological neural networks can be modulated.[17] This modulation can also be achieved chemically by local drug delivery.[18] By merging both directions of coupling, a closed-loop system can be implemented. Closed-loop systems can be found in for instance glucose sensing for diabetes patients (see Fig. 2.2b), where temporal evolution of glucose release is a multi-variable function that also depends on the activity history of the patient. Closed-loop systems can also be found in less conventional but long-term applications, such as in control and training of neurorobotic systems using neuronal cultures on multi-electrode arrays.[19] In the future, to further advance the sustainability of bioelectronic platforms in a biological environment, this bi-directional coupling should be smart, dynamic and adaptable, and rely

on multiple input variables to improve the accuracy of the neuromorphic system, similar to the working principles of neural networks (see Fig. 2.2c).

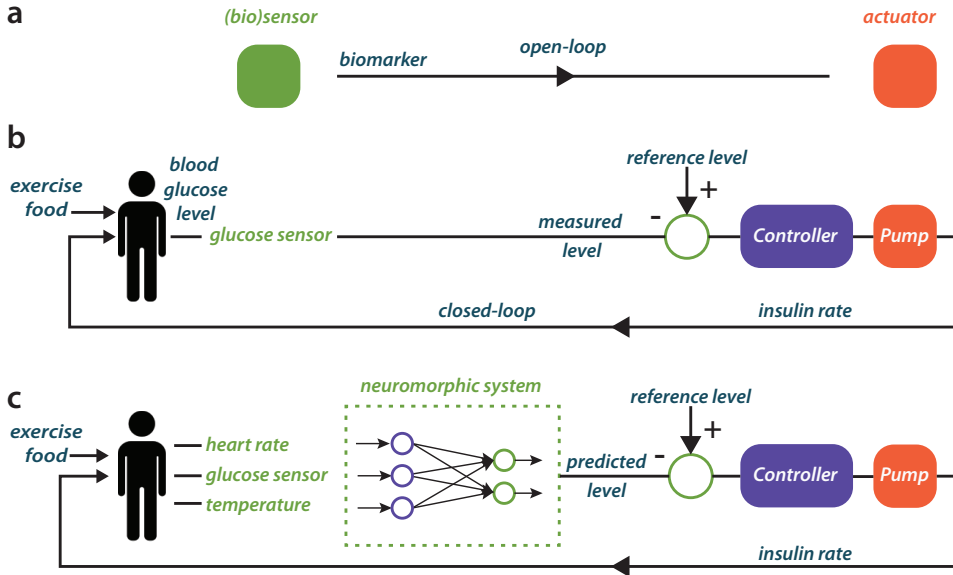


Figure 2.2: Open-loop and closed-loop systems. (a) Schematic of an open-loop system that includes a (bio)sensor and an actuator or stimulation. (b) A glucose sensor measures the blood glucose level, which is compared with a reference level. The controller acts on the difference between the two levels and operates the insulin pump. However, disturbances like sugar intake or exercise influence this. (c) By combining multiple sensors with a neuromorphic system, the network can predict a blood glucose level, which can improve the efficiency of the controller.

Traditional (organic) field effect transistors have been extensively implemented as biosensors,[20] and can be operated in a liquid electrolyte, see Fig. 2.1a. Yet, in recent years, organic electrochemical transistors (OECTs), have been increasingly reported to transduce biological (ion- or chemical-based) signals into electronic signals.[16] To a large extent, this trend results from the additional degrees of freedom that these electrochemical devices offer, compared with passive (capacitive) sensors. An OECT consists of a semiconductor polymer channel, a common example is poly(ethylenedioxythiophene):poly(styrene-sulfonate) (PEDOT:PSS), that can be gated through a solid or aqueous electrolyte, see Fig. 2.1b. By applying a gate potential, anions or cations (depending on the polarity of the gate) in the electrolyte are introduced into the organic semiconductor channel and dope/de-dope the entire volume, changing its conductivity.[21] Typically, the electrolyte of OECT-based biosensors is aqueous as they target biomarkers/ionic species in a biological solution (e.g. sweat or in-vivo). Compared to standard potentiometric sensors, OECTs have the advantage of a significant signal amplification with the potential to yield biosensors with a low detection limit and high sensitivity, even in an interfering environment.[22] The high sensitivity is based on the high transconductance, which results from the fact that the whole volume of the organic materials

partakes in the channel switching (see Fig. 2.1b).[16] Smart designs of the electronic circuit, such as the Wheatstone bridge layout, can even further improve the sensor sensitivity. This layout also yields an inherent background subtraction, eliminating interference arising from other factors.[23, 24] Using these concepts, a wide variety of sensors have been developed, ranging from in vitro to in vivo or wearables. The latter is useful for non-invasive monitoring of biomarkers such as long-term and continuous glucose monitoring[25] or pH sensing.[3] Towards this direction, cheap and disposable devices were recently shown, such as a fully inkjet-printed glucose sensor.[26] Apart from sensing in humans, glucose sensing with organic devices is also used for real-time monitoring of biological processes in plants.[27]

Although originally OECTs transduce (biological) ion-based signals into electrical signals, targeting of specific molecules can also be done using antibodies or enzymes as specific recognition elements.[28, 29] These biosensors are label-free and require the immobilization of the bioreceptor at one of the relevant device interfaces. Since these biosensors are often vulnerable to interference from other ions present in the sample solutions, the use of a molecularly imprinted polymer can be beneficial. By positioning this molecular selective membrane in between the gate electrode and the channel, the ion flow is manipulated (blocked in case of high target concentration) resulting in a change in the difference of the source-drain current (ΔI_{SD}) which depends on the concentration of the target.[4, 30] This method also allows for targets without electronic charge to be detected. An extended gate FET concept can be used which has the advantage of separating the wet and dry environment. The sensing part extends off chip and can be immersed into the solution without the transducer part.[20] A similar concept was also reported for an organic electrochemical transistor-based sensor system employing a floating gate[31] and was used to detect gluten.[32] Another concept that has no direct contact between the active material and the electrolyte or analyte, is the internal ion-gated transistor (IGT), see Fig. 2.1c. Compared to a regular OECT, where the speed is limited by the travel time of ions between the electrolyte and the conducting polymer channel, this device has a significantly faster time response.[5] The ionic transit time was shortened by using contained mobile ions within the conducting polymer channel. In this way, the time that these ions have to travel to participate in the (de)doping process is reduced. The authors further demonstrate that these devices are of great potential for logic circuits, as the preloaded ions do not require an external source of ions, see Fig. 2.1g. The above mentioned building blocks and other simple circuits (for example differential measurements with Wheatstone bridges[23]), are used as an essential first step towards smart processing.

Recent examples for (biological) stimulation or delivery of biological components, were achieved by using an organic electronic ion pump (OEIP). An OEIP is an electrophoretic delivery device that transduces electronic signals into ionic fluxes. The polymer delivery channel is a material with high ionic but low electronic conductivity that allows for the selective transport of anions or cations. An advantage of this mechanism is that the electrophoretic transport does not require liquid flow and only the charged particles are delivered to the target region. Not only atomic ions can be transported but also larger molecules as demonstrated by the delivery of an aromatic compound to a living plant model by using a dendrolyte-based OEIP.[33] Charged compounds can also be released independently from several delivery points within tens of milliseconds by adding control electrodes under each delivery point, resulting in

vertical potential gradients through the device's thin films. A bipolar membrane allows for the control of the delivery as the resistance can be increased or decreased under reversed or forward bias, respectively.[34] The main limitation of the OEIP for in vivo use is that often high voltages are required for its operation. To overcome this limitation, a microfluidic ion pump was designed to bring the drug molecules close to the delivery point, where they can be pumped outward to the target (by electrophoresis), offering low-voltage operation.[18] Combining this microfluidic ion pump with a conformable electrocorticography device with recording sites embedded next to the drug delivery outlets, makes it possible to deliver drugs and record local neural activity simultaneously on the surface of the brain.[35, 36]

The next step includes not only simultaneous sensing and actuation or stimulation, but also local processing of data. This concept has been demonstrated in recent biomimetic application examples, where artificial organs that sense relevant signals such as light, pressure or sound, are used as the input.[37] An organic artificial afferent nerve was developed that can detect the movement of objects[38] (see Fig. 2.3b). Another sensory device was reported to demonstrate tactile learning.[40] Using light as the input to a photonic synapse can be used for artificial retinas[41] as well as an input to organic optoelectronic sensorimotor synapses.[42] This latter uses an organic optoelectronic synapse and a neuromuscular system based on a stretch-

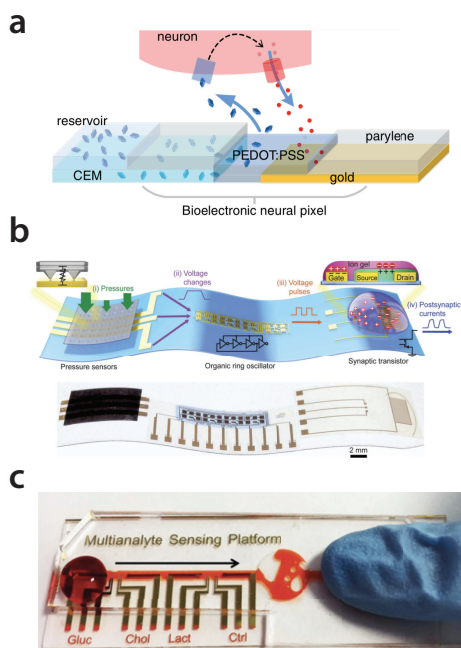


Figure 2.3: Examples of transducing, sensing and actuation microsystems. (a) Bioelectronic neural pixel with chemical stimulation and electrical sensing at the same site.[35] (b) Bioinspired flexible organic artificial afferent nerve.[38] (c) Organic-transistor array-based multi-analyte sensing platform for saliva testing.[39]

able organic nanowire synaptic transistor (s-ONWST). The voltage pulses of a self-powered photodetector triggered by optical signals drive the s-ONWST. The resulting informative synaptic outputs can be used not only for optical wireless communication of human-machine interfaces but also for light-interactive actuation of an artificial muscle actuator mimicking the contraction of a biological muscle fiber.[42]

Ideally, complete systems and devices will include all three components locally: sensing, processing and actuation, and operate in a closed-loop fashion. For that, the devices need to be stable in an aqueous solution and operate with low-power consumption. Even with current technologies, control parameters can already be tuned for optimization, but novel systems can also be envisioned where a neuromorphic core is responsible for the prediction and classification of relevant behavior and signals. These autonomous applications demand operation in a real biological environment, where organic materials have an advantage, but also require long term operation. In fact, many applications for the classification of signals and relevant behaviour will require analysis in real time. These systems should be able to not only classify anomalies in the time domain but also predict long-living (i.e. low frequency) patterns.

Potentially the inter-correlation of multi-variables that influence the biological environment can be adopted to increase the effectiveness. An example of a multi-analyte sensing platform was demonstrated on saliva,[39] as shown in Fig. 2.3c. By combining such multi-sensor information with local neuromorphic processing as well as stimulation, a dynamic smart and adaptable device can be envisioned. By measuring and processing information locally with an organic neuromorphic sensing platform relevant signals and information can be extracted. The platform can thus be trained for classification applications, and as such does not require extremely high-bandwidth signals (to be analyzed remotely), nor risks losing the essence of the information at the source (when high-bandwidth is not possible).

A hypothetical application is shown in Fig. 2.4, based on the bioelectronic neural pixel,[35] where a device can both sense neuronal activity as well as release a drug (to reduce epileptic seizures). However, in this previously demonstrated example the decision to release the drug is done manually and at a remote location. Ideally, this should be done locally and in situ. By combining multi-modal sensors at various locations, the neuromorphic core can be trained to improve the analysis and classification of the signals and behavior of the biological environment autonomously in a closed loop fashion. In this particular case, the platform could start the drug release to counteract the seizures.

In summary, we have highlighted the recent trends in organic neuromorphic devices and organic bioelectronic sensing platforms. We see opportunities in merging these two fields to further close the loop between sensing and stimulation/actuation for smart bioelectronics applications. Materials and devices that exhibit memory and have the potential to operate at the interface with biology can pave the way for novel data classification paradigms with bio-inspired features in information processing. These materials might thus offer promising solutions for the manipulation and the processing of biological signals, spanning from novel brain-computer-interfaces and adaptive prosthetics to bioinformatics and the definition of novel computational paradigms at the interface with biology. For such applications, we

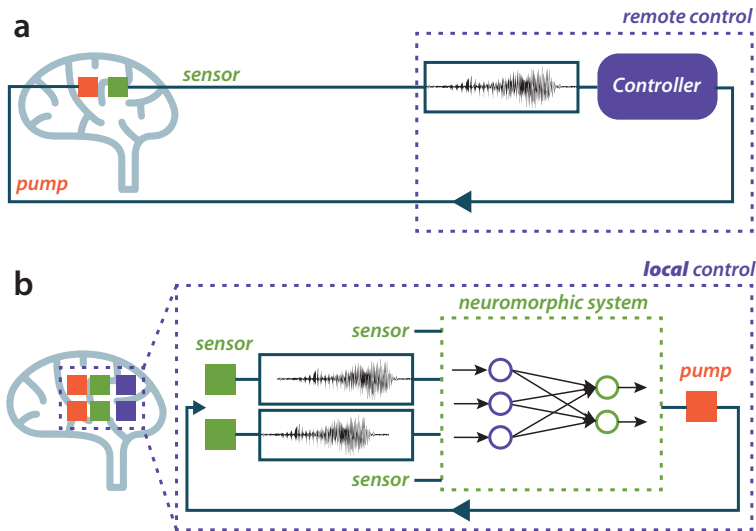


Figure 2.4: Remote versus local and adaptive control for the detection of seizures. (a) A traditional sensor acquires the electrical signal behavior of the brain which is analyzed and processed remotely. The drug release is subsequently started manually. (b) A smart and adaptable system includes multiple sensors that collectively form the input to a local neuromorphic unit that classifies the signals and starts the drug release locally and autonomously.

envision smart multi-modal sensor platforms and local neuromorphic processing. Sensing and processing will be tightly bound in a closed loop manner in order to reduce local data volume and thus allow fully autonomous applications in the future.

Bibliography

1. Van de Burgt, Y. *et al.* [A non-volatile organic electrochemical device as a low-voltage artificial synapse for neuromorphic computing](#). en. *Nature Materials* **16**, 414–418. ISSN: 1476-1122, 1476-4660 (Apr. 2017).
2. Gkoupidenis, P., Schaefer, N., Garlan, B. & Malliaras, G. G. [Neuromorphic Functions in PEDOT:PSS Organic Electrochemical Transistors](#). *Advanced Materials* **27**, 7176–7180. ISSN: 1521-4095 (2015).
3. Nakata, S. *et al.* [A wearable pH sensor with high sensitivity based on a flexible charge-coupled device](#). en. *Nature Electronics* **1**, 596–603. ISSN: 2520-1131 (Nov. 2018).
4. Parlak, O., Keene, S. T., Marais, A., Curto, V. F. & Salleo, A. [Molecularly selective nanoporous membrane-based wearable organic electrochemical device for noninvasive cortisol sensing](#). en. *Science Advances* **4**, eaar2904. ISSN: 2375-2548 (July 2018).
5. Spyropoulos, G. D., Gelinas, J. N. & Khodagholy, D. [Internal ion-gated organic electrochemical transistor: A building block for integrated bioelectronics](#). en. *Science Advances* **5**, eaau7378. ISSN: 2375-2548 (Feb. 2019).
6. Fuller, E. J. *et al.* [Parallel programming of an ionic floating-gate memory array for scalable neuromorphic computing](#). en. *Science*, eaaw5581. ISSN: 0036-8075, 1095-9203 (Apr. 2019).
7. Van de Burgt, Y., Melianas, A., Keene, S. T., Malliaras, G. & Salleo, A. [Organic electronics for neuromorphic computing](#). en. *Nature Electronics* **1**, 386–397. ISSN: 2520-1131 (July 2018).
8. Keene, S. T., Melianas, A., van de Burgt, Y. & Salleo, A. [Mechanisms for Enhanced State Retention and Stability in Redox-Gated Organic Neuromorphic Devices](#). *Advanced Electronic Materials* **5**, 1800686. ISSN: 2199-160X (Feb. 2019).
9. Battistoni, S., Erokhin, V. & Iannotta, S. [Organic memristive devices for perceptron applications](#). en. *Journal of Physics D: Applied Physics* **51**, 284002. ISSN: 0022-3727, 1361-6463 (July 2018).
10. Gerasimov, J. Y. *et al.* [An Evolvable Organic Electrochemical Transistor for Neuromorphic Applications](#). en. *Advanced Science* **6**, 1801339. ISSN: 2198-3844, 2198-3844 (Apr. 2019).

11. Jang, S. *et al.* Ultrathin Conformable Organic Artificial Synapse for Wearable Intelligent Device Applications. *ACS Applied Materials & Interfaces* **11**, 1071–1080. ISSN: 1944-8244 (Jan. 2019).
12. Gkoupidenis, P., Koutsouras, D. A., Lonjaret, T., Fairfield, J. A. & Malliaras, G. G. Orientation selectivity in a multi-gated organic electrochemical transistor. *eng. Scientific Reports* **6**, 27007. ISSN: 2045-2322 (June 2016).
13. Gkoupidenis, P., Koutsouras, D. A. & Malliaras, G. G. Neuromorphic device architectures with global connectivity through electrolyte gating. *en. Nature Communications* **8**, 15448 (May 2017).
14. Koutsouras, D. A., Prodromakis, T., Malliaras, G. G., Blom, P. W. M. & Gkoupidenis, P. Functional Connectivity of Organic Neuromorphic Devices by Global Voltage Oscillations. *en. Advanced Intelligent Systems* **1**. _eprint: <https://onlinelibrary.wiley.com/doi/pdf/10.1002/aisy.201900013>, 1900013. ISSN: 2640-4567 (2019).
15. Pecqueur, S. *et al.* Neuromorphic Time-Dependent Pattern Classification with Organic Electrochemical Transistor Arrays. *en. Advanced Electronic Materials* **4**. _eprint: <https://onlinelibrary.wiley.com/doi/pdf/10.1002/aelm.201800166>, 1800166. ISSN: 2199-160X (2018).
16. Rivnay, J. *et al.* Organic electrochemical transistors. *en. Nature Reviews Materials* **3**, 17086. ISSN: 2058-8437 (Feb. 2018).
17. Owens, R. M. & Malliaras, G. G. Organic Electronics at the Interface with Biology. *en. MRS Bulletin* **35**, 449–456. ISSN: 1938-1425, 0883-7694 (June 2010).
18. Uguz, I. *et al.* A Microfluidic Ion Pump for In Vivo Drug Delivery. *en. Advanced Materials* **29**, 1701217. ISSN: 09359648 (July 2017).
19. *In vitro neuronal networks: from culturing methods to neuro-technological applications* (eds Chiappalone, M., Pasquale, V. & Frega, M.) *Advances in neuro-biology* **volume 22**. OCLC: 1101786249. ISBN: 978-3-030-11135-9 (Springer, Cham, Switzerland, 2019).
20. Kaisti, M. Detection principles of biological and chemical FET sensors. *Biosensors and Bioelectronics* **98**, 437–448. ISSN: 0956-5663 (Dec. 2017).
21. Berggren, M. & Malliaras, G. G. How conducting polymer electrodes operate. *en. Science* **364**, 233–234. ISSN: 0036-8075, 1095-9203 (Apr. 2019).
22. Giordani, M. *et al.* Specific Dopamine Sensing Based on Short-Term Plasticity Behavior of a Whole Organic Artificial Synapse. *en. ACS Sensors* **2**, 1756–1760. ISSN: 2379-3694, 2379-3694 (Dec. 2017).

23. Braendlein, M. *et al.* [Lactate Detection in Tumor Cell Cultures Using Organic Transistor Circuits](#). en. *Advanced Materials* **29**, 1605744. ISSN: 09359648 (Apr. 2017).
24. Scheiblin, G., Coppard, R., Owens, R. M., Mailley, P. & Malliaras, G. G. [Referenceless pH Sensor using Organic Electrochemical Transistors](#). en. *Advanced Materials Technologies* **2**, 1600141. ISSN: 2365709X (Feb. 2017).
25. Mano, T. *et al.* [Printed Organic Transistor-Based Enzyme Sensor for Continuous Glucose Monitoring in Wearable Healthcare Applications](#). en. *ChemElectroChem* **5**, 3881–3886. ISSN: 2196-0216, 2196-0216 (Dec. 2018).
26. Bihar, E. *et al.* [A fully inkjet-printed disposable glucose sensor on paper](#). en. *npj Flexible Electronics* **2**, 30. ISSN: 2397-4621 (Dec. 2018).
27. Diacci, C. *et al.* [Real-Time Monitoring of Glucose Export from Isolated Chloroplasts Using an Organic Electrochemical Transistor](#). en. *Advanced Materials Technologies* **0**, 1900262. ISSN: 2365-709X.
28. Diacci, C. *et al.* [Label-free detection of interleukin-6 using electrolyte gated organic field effect transistors](#). en. *Biointerphases* **12**, 05F401. ISSN: 1934-8630, 1559-4106 (Dec. 2017).
29. Berto, M. *et al.* [Label free detection of plant viruses with organic transistor biosensors](#). en. *Sensors and Actuators B: Chemical* **281**, 150–156. ISSN: 09254005 (Feb. 2019).
30. Zhang, L. *et al.* [Selective recognition of Histidine enantiomers using novel molecularly imprinted organic transistor sensor](#). en. *Organic Electronics* **61**, 254–260. ISSN: 15661199 (Oct. 2018).
31. White, S. P., Dorfman, K. D. & Frisbie, C. D. [Operating and Sensing Mechanism of Electrolyte-Gated Transistors with Floating Gates: Building a Platform for Amplified Biodetection](#). *The Journal of Physical Chemistry C* **120**, 108–117. ISSN: 1932-7447 (Jan. 2016).
32. White, S. P., Frisbie, C. D. & Dorfman, K. D. [Detection and Sourcing of Gluten in Grain with Multiple Floating-Gate Transistor Biosensors](#). *ACS Sensors* **3**, 395–402 (Feb. 2018).
33. Poxson, D. J. *et al.* [Regulating plant physiology with organic electronics](#). en. *Proceedings of the National Academy of Sciences* **114**, 4597–4602. ISSN: 0027-8424, 1091-6490 (May 2017).
34. Jonsson, A., Sjöström, T. A., Tybrandt, K., Berggren, M. & Simon, D. T. [Chemical delivery array with millisecond neurotransmitter release](#). en. *Science Advances* **2**, e1601340. ISSN: 2375-2548 (Nov. 2016).

35. Jonsson, A. *et al.* Bioelectronic neural pixel: Chemical stimulation and electrical sensing at the same site. en. *Proceedings of the National Academy of Sciences* **113**, 9440–9445. ISSN: 0027-8424, 1091-6490 (Aug. 2016).
36. Proctor, C. M. *et al.* An Electrocorticography Device with an Integrated Microfluidic Ion Pump for Simultaneous Neural Recording and Electrophoretic Drug Delivery In Vivo. en. *Advanced Biosystems* **3**, 1800270. ISSN: 23667478 (Feb. 2019).
37. Lee, Y. & Lee, T.-W. Organic Synapses for Neuromorphic Electronics: From Brain-Inspired Computing to Sensorimotor Nerve. en. *Accounts of Chemical Research*. ISSN: 0001-4842, 1520-4898 (Mar. 2019).
38. Kim, Y. *et al.* A bioinspired flexible organic artificial afferent nerve. *Science* **360**. Publisher: American Association for the Advancement of Science, 998–1003 (June 2018).
39. Pappa, A.-M. *et al.* Organic Transistor Arrays Integrated with Finger-Powered Microfluidics for Multianalyte Saliva Testing. en. *Advanced Healthcare Materials* **5**. _eprint: <https://onlinelibrary.wiley.com/doi/pdf/10.1002/adhm.201600494>, 2295–2302. ISSN: 2192-2659 (2016).
40. Wan, C. *et al.* An Artificial Sensory Neuron with Tactile Perceptual Learning. en. *Advanced Materials* **30**. _eprint: <https://onlinelibrary.wiley.com/doi/pdf/10.1002/adma.201801291>, 1801291. ISSN: 1521-4095 (2018).
41. Wang, Y. *et al.* Photonic Synapses Based on Inorganic Perovskite Quantum Dots for Neuromorphic Computing. en. *Advanced Materials* **30**. _eprint: <https://onlinelibrary.wiley.com/doi/pdf/10.1002/adma.201802883>, 1802883. ISSN: 1521-4095 (2018).
42. Lee, Y. *et al.* Stretchable organic optoelectronic sensorimotor synapse. en. *Science Advances* **4**, eaat7387. ISSN: 2375-2548 (Nov. 2018).

Chapter 3

Retrainable neuromorphic biosensor for on-chip learning and classification

3

Neuromorphic computing aims to mimic the brain in complex classification tasks directly in hardware and has great potential for local edge computing in applications such as smart wearable, implantable, and point-of-care devices. Successful implementation requires straightforward training, low power operation, and facile sensor integration. Despite the emergence of organic materials as building blocks for neuromorphic systems due to their low voltage operation and excellent tunability, these systems still rely on external training in software. Here we demonstrate a smart biosensing platform, based on an integrated array of organic neuromorphic devices as the synaptic weights of a hardware neural network, its associated output classification hardware, and sensors, completely trained on-chip to classify a model disease. The versatility of the neuromorphic system is highlighted via on-chip retraining, by switching sensor input signals and the formation of logic gates on the same chip. These results pave the way for advanced adaptive bioelectronic systems.

This chapter is based on *Retrainable neuromorphic biosensor for on-chip learning and classification*, **Eveline R. W. van Doremaele**, Xudong Ji, Jonathan Rivnay, Yoeri van de Burgt. *Under review*.

3.1 Introduction

Organic electronic materials have recently emerged as building blocks for brain-inspired processing[1–3], as they possess favourable characteristics with respect to neuroplasticity and memory tuning that are instrumental to low-power neuromorphic circuits [4, 5]. Besides low-energy, linear and symmetric tuning [6], relatively high stability [7], and a large range of accessible analogue conductance states, organic materials can take on unique form factors and show potential for biocompatibility[8]. These characteristics allow for operation at the interface with biological systems and dynamic biohybrid connections that interact with the physiological environment[9] and biological systems[10]. Because of the volumetric doping mechanism, this particular class of organic electronic materials – organic mixed ionic-electronic conductors – allow for large transconductance [11] and high sensitivity [12] and have been utilized in a wide variety of organic electrochemical transistor and sensor applications [13–17]. Despite these notable examples, these applications often still require some form of external monitoring, processing or control [18] to successfully operate, while ideally smart point-of-care devices operate locally and autonomously [19, 20]. At the same time, the requirements for point-of-care devices often differ considerably from person to person while personalized healthcare demands that these devices can adapt to the patients’ needs. Neural networks can be used to overcome issues related to those variabilities but the software algorithms that support them operate on external computers or on energy inefficient and privacy-sensitive data centres in the cloud and cannot be trained autonomously and locally. In contrast, the smart biosensor we present here, is a modular chip enabling standalone, local operation, consisting of a sensor input layer, a network of organic neuromorphic devices forming the hardware neural network and an output classification layer, see Fig. 3.1.

Though training of small neuromorphic arrays was recently demonstrated [4, 21, 22], some form of external computing and control was still necessary, notably the crucial step in determining the level of weight update – generally done via an error backpropagation software algorithm [23]. In our standalone smart biosensor this weight update step is done in hardware too, thus highlighting the versatility of low power organic neuromorphic arrays by demonstrating on-chip training without the help of an external computer. We demonstrate a specific use case by classifying the genetic disease cystic fibrosis from (modified) donor sweat using ion selective sensors, followed by retraining after swapping sensor inputs into the hardware neural network module. In this work, the application of cystic fibrosis is a proof of concept; the sensor module can, in principle, be swapped out to retrain the network for other applications in diagnostics or environmental monitoring.

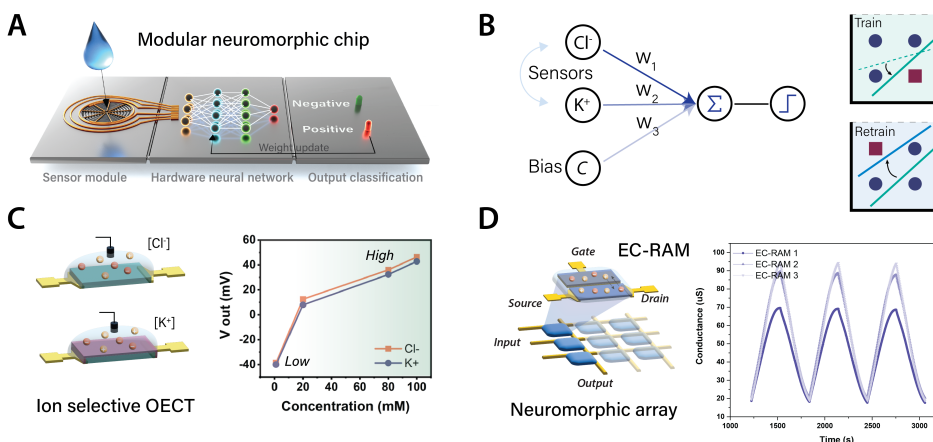


Figure 3.1: Modular neuromorphic biosensor chip. a, Illustration of the modular biosensor with the distinct functions. b, Single layer neural network (perceptron) with sensor inputs and linear classification for trained and retrained input values. c, Depiction of the ion selective OECT sensors manipulated with and without ion selective membrane for measuring the K^+ and Cl^- concentration. Sensor output vs ion concentration after the current-to-voltage and offset circuit module. d, EC-RAM as part of a small neuromorphic array and the conductance values for the 3 EC-RAM devices used as synaptic weights.

3.2 Generating input signals from ion sensors

Cystic fibrosis is a hereditary disease that affects the lungs and digestive system and can be detected through a sweat test. A high level of chloride anions in sweat (>60 mmol/L) indicates that cystic fibrosis is likely to be diagnosed.[24–27] In the context of this work, it provides a simplified proof-of-concept as diagnosis via available and existing analyte recognition elements is well studied and requires a minimal set of sensors. We note that this proof of concept is not tested for diagnostics of cystic fibrosis with real patient data. We measure the concentration of chloride and to account for external biases in the system (including higher concentrations due to evaporation) the concentration of potassium serves as a control. We use both commercially available ion selective electrodes (ISEs) and ion selective organic electrochemical transistors (IS-OECTs)[12, 28, 29] that can detect physiological levels of potassium and chloride and will serve as the input signals to the hardware-implemented neural network on the biosensor chip (see Supporting Information 3.8.1). Whereas the commercially available ISEs enable an easy-to-use rapid test platform, the IS-OECTs allow us to demonstrate the potential of a fully standalone biosensor chip. The use of multiple sensor types further emphasizes the ability to readily implement various modalities of sensors. The organic electrochemical transistor (OECT) is a three-terminal device comprising an organic semiconducting polymer as the channel (with two metal contacts to establish an electric current) that is in contact with an electrolyte in which a gate electrode is immersed[30]. Via a gate potential, ions can be injected in the channel which changes the doping state of the film and subsequently its conductivity. This mixed ionic-electronic conducting property within the

whole volume of the material results in efficient sensing[31]. Additionally, to target specific ions or biomarkers ion selective membranes can be added [32].

3.3 Training in hardware for on-chip classification

Classification is done according to the perceptron algorithm used for supervised learning of binary data, where we define a set of “high” and “low” concentrations for chloride and potassium to represent the labelled sweat samples (see Methods 3.7.3). It makes a classification decision based on the value of a linear combination of the input with the set of weights w_i [33]. Since this algorithm requires only a single layer, it allows us to understand and visualize the working principle. The adjustable weight is represented by the conductance of an organic neuromorphic device (EC-RAM). Its conductance – or synaptic weight – is non-volatile and can be adjusted (modulated to higher and lower values in an analogue matter) by applying a gate voltage pulse (see Supporting Information 3.8.2 and Figs. 3.S9 and 3.S10) as previously reported[6]. To account for negative weight values an inverted voltage signal is fed through a reference resistor parallel to the neuromorphic device. According to this, the weight can be described as the conductance difference between the neuromorphic device and the reference resistor, resulting in a current output given by[34]:

$$I_j^l = \sum_{i=1}^n V_i^{l-1} (G_{ij \text{ ECRAM}} - G_{ij \text{ ref}})$$

where V_i represents the input voltage for layer l , and directly depends on the ionic concentration of chloride and potassium in labelled (with and without the disease) sample sweat. The feed-forward phase (inference-mode) directly computes the output signal in hardware using Ohm’s law and Kirchhoff’s law [35] followed by a threshold activation function in order to power light emitting diodes (LED). The threshold activation function converts any current output greater than 0 to a positive voltage which lights up a green coloured LED classifying the output as “healthy” i.e., a negative diagnosis. Any current output smaller than 0 is converted to a negative voltage such that a red coloured LED lights up to classify the output as “diseased” i.e., a positive diagnosis (see Supporting Fig. 3.S15 for a picture of the hardware neural network). In the learning phase, supervised training is done by correcting for incorrect output decisions. In the case of an incorrect classification, an error feedback signal is transmitted back by means of a pushbutton that results in a voltage applied at the gate of each neuromorphic device, causing a weight update (see Fig. 3.2 and Supporting Information 3.8.3). The gate voltage, update value, depends on the error ($Y_{exp} - Y_{out}$) multiplied by the input and the duration, similar to the learning rate in software neural networks. Note that this is the update value corresponding with the single layer perceptron algorithm. Since the classification output is binary, the error is either positive ($Y_{exp} > Y_{out}$) or negative ($Y_{exp} < Y_{out}$) and by multiplying it with the input voltage, individual weight update values can be realized. This supervised training cycle with labelled inputs is repeated until the circuit has been fully trained and correctly classifies each sample.

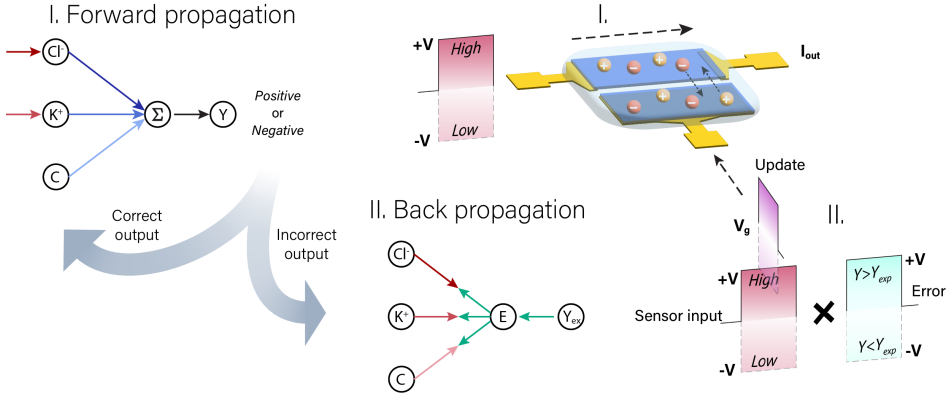


Figure 3.2: Hardware neural network principle. Schematic illustration showing the forward (I) and back propagation (II) together with its hardware representation. In case of a correct classification output from the forward propagation this step is repeated (with a different set of inputs). After an incorrect classification output, the forward propagation is followed by a back propagation step.

3.4 Update behaviour of the neuromorphic circuit

To demonstrate the working principle of training the hardware-based neural network, the weights, inputs, and output are monitored with a data acquisition device (DAQ, see Methods 3.7.4) during the training process (Fig. 3.3a-c and Supporting Fig 3.S3 for training using the ISEs without offset circuit). The output of the chloride and potassium sensors (in this case the ISEs) serve as inputs 1 and 2 for the hardware neural network, respectively. The sensor output for high and low ion concentrations are extracted from sweat samples and are -15mV for chloride and -90mV for potassium corresponding to a low concentration and -45mV for chloride and -60mV for potassium for a high concentration (see Supporting Fig. 3.S1). With an additional circuit the sensor output is offset and scaled such that the input voltage is approximately ± 30 mV (see Supporting Fig. 3.S2). For further details see Supporting Information 3.8.1 and 3.8.4. The bias represents input 3 and is set at a constant voltage of 60 mV. The weights, that ultimately determine whether a given set of inputs is classified as a “positive” or “negative” diagnosis are randomly initialized, and in this case two weights start at a positive value and one weight at a negative value (see Fig. 3.3a). Weight 1 and 2 represent the weights corresponding to the chloride and potassium sensor (input 1 and 2) whereas the third weight is connected to the bias.

The case of high chloride (-0.035V) and low potassium (-0.035V) concentration is labelled as “positive” and should result in a negative output voltage, $V < 0$, lighting up the red LED after training (see Fig. 3.3d). For each measurement a randomized combination of high/low input voltages – resembling labelled samples of a “positive” or “negative” diagnosis – is applied to the neural network followed by an output decision. If the combination of inputs is correctly classified (green LED for a “negative” and red LED for a “positive” sample), no update is

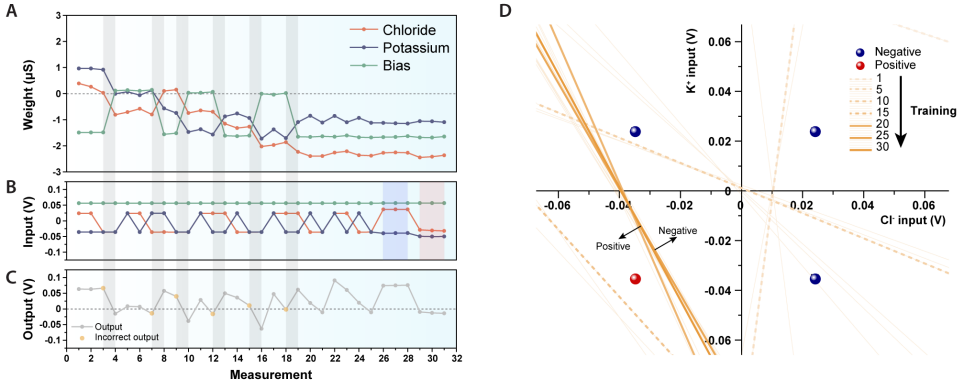


Figure 3.3: Visualization of the synaptic weight update and corresponding classification line during training. a, Values of the weights corresponding to b, the inputs representing the voltage output for a high or low ion concentration measured with the ISEs. Measurements 26-28 show the input of a negative sweat sample (indicted in blue) and measurements 29-31 show the input of a positive sweat sample (indicated in red). c, The output for each measurement cycle, measured before the threshold activation function triggering the LEDs. A negative voltage output corresponds to a positive diagnosis and vice versa. d, 2-D graphical representation of the classification problem of cystic fibrosis where the dashed lines show the decision boundary on every 5th measurement. The solid lines correspond to measurements (> 19) with lines showing a correct classification.

needed, and the neural network is presented with a new combination of inputs to start a new measurement. In the case that the output gave an incorrect classification, the pushbutton is pressed in order to update the weights. This is repeated in the next measurements until the output is correct and new inputs can be selected. When all (four different) input combinations give correct classification outputs, the network is considered fully trained (measurement > 19). We test the neural network by measuring sample sweat from healthy donors (negative sample) and modified sample sweat to represent cystic fibrosis (positive sample, see Methods 3.7.3). Measurements 26-28 show the input of a negative sweat sample (indicted in blue) and measurements 29-31 show the input of a positive sweat sample (indicated in red) both with correct output classification (see Fig. 3.3b,c). See Supporting Fig. 3.S7 for the details of each measurement corresponding to the training and Supporting Fig. 3.S8 for the link to a recording of the training process as described here.

The solution to a single layer perceptron classification can be represented graphically by a hyperplane depending on the number of inputs to the neural network. Figure 3.3d represents the 1-dimensional solution of the perceptron neural network given by the weights at the first and every 5th measurement (dashed lines in Fig. 3.3d). This solution line can be written as:

$$y = -\frac{w_1}{w_2}x - \frac{0.06 \cdot w_3}{w_2}$$

where y represents input 2 from the K^+ sensor and x input 1 from the Cl^- sensor. Looking at the last training measurements from 19 to 31, only the input combination of high Cl^- and low K^+ concentrations, representing cystic fibrosis (measurement 21, 25, and 29-31), is classified “positive” (output voltage $Y_{out} < 0V$), whereas the other inputs are correctly classified as a “negative” diagnosis (output voltage $Y_{out} > 0V$). The solid lines constructed from the weights at measurements 20, 25, and 30 show a correct classification (Fig. 3.3d), where all input combinations above the line give a healthy, negative diagnosis ($Y_{out} > 0V$) and below the line is a diseased, positive diagnosis ($Y_{out} < 0V$), showing that the hardware based neural network is fully trained.

3.5 On-chip retraining

To further demonstrate the versatility of the hardware neural network circuit and its potential as a modular neuromorphic biosensor, a fully trained system is retrained on-chip after reorganizing the different inputs. The weights are re-tuned in order to solve the new problem (see Fig. 3.4). To decrease the number of updates necessary to train the problem, the input

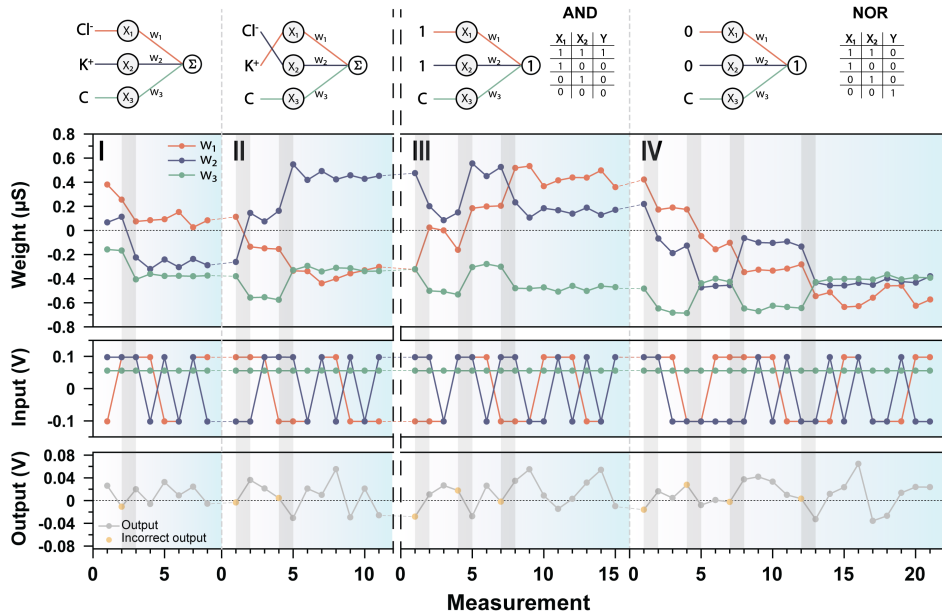


Figure 3.4: Display of various consecutive training cycles. Classifying: I. cystic fibrosis, II. cystic fibrosis after switching the sensor inputs, III. AND logic gate and, IV. NOR logic gate. The panels show the corresponding weights, input and output voltages, respectively, where updates are indicated in grey.

signals are scaled such that 0.1V represents a high and -0.1V represents a low input (see Supporting Information 3.8.4). (The bias remains at the constant voltage of 60mV). During the first training cycle (I) the chloride and potassium sensors represent inputs X_1 and X_2 , respectively, (similar to the previous example in Fig. 3.3). When the neuromorphic circuit is

fully trained to correctly classify cystic fibrosis the neuromorphic devices have a conductance such that the weights correctly separate the distinct cases. Directly after, during the second training cycle (II) the sensors are connected to a different input of the neuromorphic circuit, such that the potassium sensor represents input X1 and the chloride sensor to input X2. In this case the system produces incorrect outputs again. The circuit should thus be further trained by remodulating the weights until the disease can be correctly classified again and produces no incorrect outputs for all input samples. This example demonstrates the versatility of on-chip learning using any type of sensor (and in any order) in combination with labelled data and can be further extended into classification of signals where separation of data is not obvious. Similarly, the same neuromorphic circuit can be used to form arbitrary logic gates (such as AND and NOR) based on their representative truth tables. In Fig. 3.4 we continue to train the programming of several logic operators in sequence, meaning they are programmed to display AND gate behaviour (cycle III) and subsequently reprogrammed to display the behaviour of a NOR gate (cycle IV). Importantly, all training cycles are done without a computer or software program and completely take place on the chip itself, highlighting the versatility of locally programmable neuromorphic devices for classification tasks as well as dynamic logic circuits.

3.6 Conclusion

Neuromorphic circuits have shown excellent capabilities in classification tasks beyond traditional applications such as image recognition. The programmable biosensor we have presented here showcases a first demonstration of possibilities for locally trained and optimized neural network applications in hardware operating autonomously. The training was done on-chip using error signal feedback to modulate the conductance of organic neuromorphic devices to correctly classify a model disease. We have shown the versatility of the organic neuromorphic chip with multiple retraining processes for various sets of input signals highlighting the ability to retrain any arbitrary set of inputs for classifying linearly separable problems. The neuromorphic circuit demonstrated the use of a single layer perceptron algorithm, though expanding the neural network to multiple layers allows for classification beyond linearly separable problems. Introducing additional inputs is straightforward and will further expand the capabilities of hardware neuromorphic chips into more sophisticated biosensors and classification circuits. Next to demonstrating the highly versatile nature of low-power and easy-to-tune organic neuromorphic devices in true hardware arrays and circuits, this work opens up a wide variety of opportunities in smart and reprogrammable applications capable of local and continuous learning, optimizable edge-computing devices and adaptive biosensors.

3.7 Methods

3.7.1 EC-RAM fabrication

EC-RAMs were fabricated on patterned ITO slides (20 ohm/sq) purchased from Xinyan Technology LTD. The slides were cleaned with soap, acetone, isopropanol and deionized water followed by UV-ozone treatment before spin-coating the polymer layer. The commercial PEDOT:PSS (Hereaus, Clevios PH 1000) aqueous solution was modified by adding

15 vol% of the molecular de-dopant N-methyl-2,2'-diaminodiethylamine (DEMTA, Sigma Aldrich), 6 vol% ethylene glycol (EG, Sigma Aldrich) to enhance the morphology, 1 vol% (3-glycidyloxypropyl)trimethoxysilane (GOPTS, Sigma Aldrich) as a crosslinking agent to improve mechanical stability. The de-doped PEDOT:PSS solution was filtered through a 0.45 μm polytetrafluoroethylene filter and spun on the patterned ITO substrate at 1500 RPM for 1 minute and baked at 120 °C for 30 minutes. Thereafter the substrate was gently rinsed in deionized water to eliminate residual contents and subsequently dried at 120 °C for 10 minutes. For the aqueous electrolyte gated EC-RAMs, a polymer was removed from the substrate to define the 5 \times 5 mm channel. A polydimethylsiloxane well was fixed to the substrate to contain the aqueous electrolyte solution (100 mM NaCl) whereas for the solid electrolyte gated EC-RAMs ion gel solution was drop casted on the channel and gate. The ion gel solution was prepared by dissolving ionic liquid (EMIM:TFSI) and poly(vinylidene fluoride-co-hexafluoropropylene) (4:1w/w) in acetone with the following proportions: 17.6 wt% ionic liquid, 4.4 wt% polymer, and 78 wt% solvent. The resulting ion gel solution was stirred at 40 °C for at least 30 min.

3.7.2 Ion selective OECT fabrication

Cr (5nm) / Au (100 nm) electrodes were patterned on cleaned glass substrates by photolithography and the subsequent lift-off process of the negative photoresist (AZ nLOF 2035). After a surface treatment with the adhesion promoter Silane A-174, a 2 μm -thick parylene C was deposited on the substrate to electrically isolate the electrodes. A diluted Micro-90 (2% v/v in DI water) was spin-coated as an anti-adhesive layer, and subsequently, a sacrificial second parylene C layer of 2 μm was deposited. The OECT channels, with a width of 100 μm and length of 10 μm , and contact pads were opened through successive photolithography (AZ P4620 photoresist) and reactive ion etching steps (Samco RIE-10NR). After surface activation by UV ozone for 5 minutes, the PEDOT:PSS blend consisting of 5 vol% ethylene glycol (EG), 1 vol% (3-glycidyloxypropyl)trimethoxysilane (GOPS), and 0.5 vol% dodecylbenzene sulfonic acid (DBSA), filtered through a 0.45 μm polytetrafluoroethylene filter was spin-coated on the sample at 2000 rpm. After brief thermal annealing at 90 °C for 2 minutes, the sacrificial parylene layer was removed to pattern the OECT channels, followed by thermal crosslinking at 140 °C for 60 min. The OECT device was then rinsed by DI water to remove any excess compounds. The PSS:Na mixture was spin-coated on the PEDOT:PSS channels at 1000 rpm, and then the polyelectrolyte film with GOPS was crosslinked by baking at 130 °C for 60 min and subsequently immersed in a 0.1 M NaCl solution overnight to keep Na ions in the film. Finally, the solution of K⁺ ion selective membrane (ISM) was spin-coated (1000 rpm, twice) on PSS:Na film and dried at room temperature to make the K⁺ ISM film. All materials were purchase from Sigma Aldrich unless otherwise indicated.

3.7.3 Sweat samples

Donor sweat (1 mL) from 3 healthy donors was purchased from Medix Biochemica. The sweat of 2 donors was mixed to obtain the negative sweat sample and a 1mL solution (containing 1M NaCl and 1mM KCl) was added to the other donor sweat representing the positive sweat sample with the same [K⁺] and a higher [Cl⁻] concentration than the negative sweat sample.

Stock solutions for artificial sweat were prepared by dissolving 584.4 mg NaCl and, 745.5 mg KCl in 100 mL deionized water (Milli-Q). 100×10^{-3} M NaCl and KCl solutions were diluted to achieve the concentrations of interest (1, 20, 80, and 100 mM [NaCl] and [KCl]).

3.7.4 Data acquisition

An NI USB 6009 data acquisition device (DAQ) is used to monitor the inputs, output, and weights during the training process using MATLAB. The input voltage of the hardware neural network is multiplied by 10 using an operational amplifier (OPA4196) to increase the sensitivity of the DAQ. Due to Kirchhoff's and Ohms law the output of the hardware neural network is represented by a current that drives either one of two LEDs. In order to monitor the output, the current is converted to a voltage (1:1) to make it compatible with the DAQ. To track the value of the weights each weight is paired with a small ($1\text{k}\Omega$) resistor in series. The voltage difference across the EC-RAM and the resistor in series (from which the current can be determined) is measured. Using Ohms law, the conductance of the EC-RAM and thus the weight can be calculated. (See Supporting Fig. 3.S16 for the electronic circuit design).

3.8 Supporting Information

3.8.1 Ion selective electrodes (ISE) and organic electrochemical transistors (IS-OECT)

ISE

Commercially available ion selective electrodes (ISE, Mettler Toledo) were used for the detection of $[\text{K}^+]$ and $[\text{Cl}^-]$ and calibrated using stock solutions 1, 10, 100 and 1000 mM KCl (see Supporting Fig. 3.S1a). The training visualized in Fig. 3.3 is done using input values extracted from the ISE sensor output when measuring sample sweat (Supporting Fig. 3.S1b). These values are offset and scaled using an offset circuit (see Supporting Fig. 3.S2) such that both sensors operate in the same range, and such that the high and low concentrations are represented by positive and negative output values, to make the training more efficient (see Supporting Information 3.8.4). A training cycle using ISE values that are not offset is visualized in Supporting Fig. 3.S3 showing that training is possible but generally requires more updates.

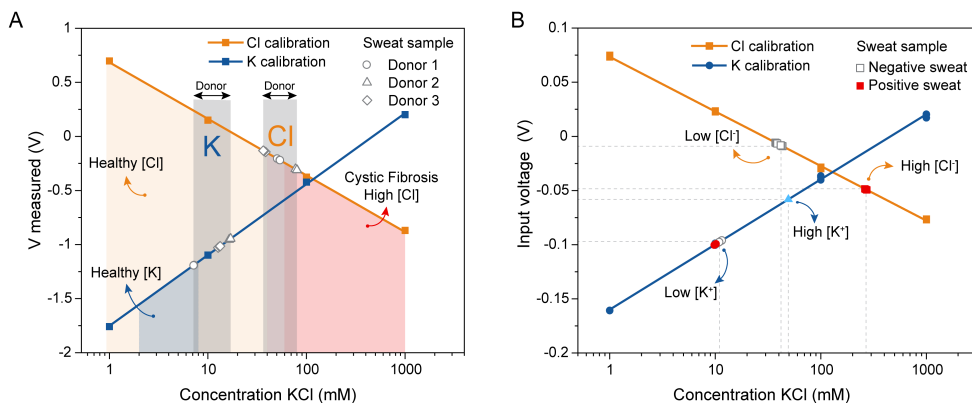


Figure 3.S1: Voltage output as a function of the ion concentration in KCl including donor sweat. a, Commercially available ion selective electrodes (ISE, Mettler Toledo) were used for the detection of $[K^+]$ and $[Cl^-]$ and voltage output calibration, measured after an 11x amplification, with stock solutions. Sweat samples from 3 donors were also measured and are indicated in the graph. b, Input voltage (calculated before amplification) to define the values for high/low ion concentration used for training. The negative sweat sample is obtained from the sweat of 2 healthy donors and the positive sweat sample is based on the sweat of 1 healthy donor with additional NaCl. A low concentration corresponds to -0.015V for chloride and -0.090V for potassium and a high concentration corresponds to -0.045V for chloride and -0.060V for potassium.

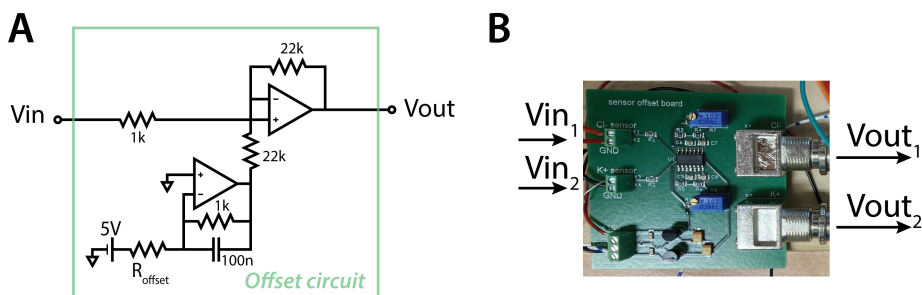


Figure 3.S2: Offset circuit. a, Schematic of the offset circuit for a single sensor input and output. The offset resistor is a potentiometer that can be increased or decreased to define the desired offset. b, Photo of the offset circuit PCB for two inputs and outputs that can each be offset independently.

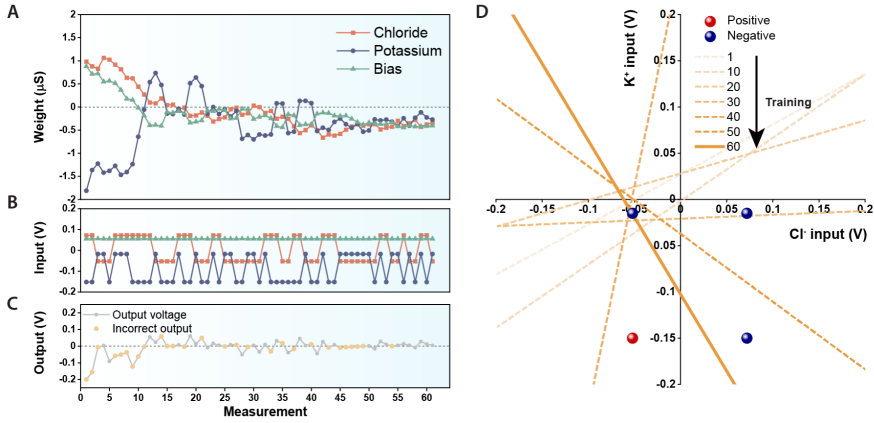


Figure 3.S3: Visualization of the weight update during a training cycle using ion selective electrodes without offset. a, Values of the weights corresponding to b, the inputs representing the voltage output for a high (100 mM) or low (1 mM) ion concentration measured with the commercially available ISEs (Supporting Fig. 3.S1). A low concentration (1mM) corresponds to 0.075V for chloride and -0.150V for potassium and a high concentration corresponds to -0.050V for chloride and -0.015V for potassium. c, The output for each measurement cycle, measured before the threshold activation function triggering the LEDs. d, 2-D graphical representation of the classification problem of cystic fibrosis where the dashed lines show the decision boundary on the first and every 10th iteration. The solid line corresponds to the last (60th) measurement and shows a correct classification.

IS-OECT

IS-OECTs have the potential to be fabricated on-chip rather than the large ISEs. The conductance depends on the ion concentration (see Supporting Fig. 3.S4). To serve as the input of the hardware neural network module the IS-OECT is implemented in a voltage divider circuit to produce a voltage output dependent on the ion concentration (see Supporting Fig. 3.S5). In this circuit a reference resistor R_{ref} is paired in series with the OECT channel. The output voltage depends on the value of the resistance according to:

$$V_{out} = V_{drain} \cdot \frac{R_{IS-OECT}}{R_{ref} + R_{IS-OECT}}$$

With the additional electronic offset circuit, an offset and multiplication are introduced, realizing a sensor output between ± 45 mV for both sensor modules (Supporting Fig. 3.S5c). Training of the hardware neural network using the IS-OECT is visualized in Supporting Fig. 3.S6.

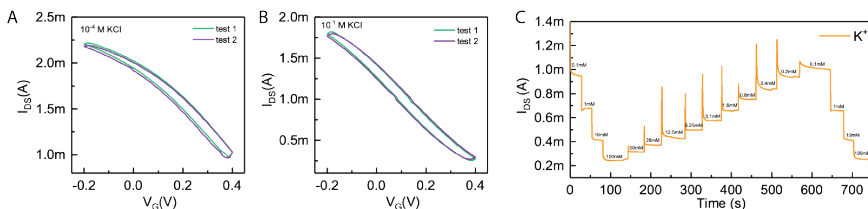


Figure 3.S4: Characteristics of the potassium IS-OECT. a, b, Two transfer curves of the potassium IS-OECT in 10^{-4} M KCl and 10^{-1} M KCl ($V_{DS} = -0.1$ V). c, Steady-state current response against KCl with different concentration ($V_G = 0.4$ V, $V_{DS} = -0.1$ V).

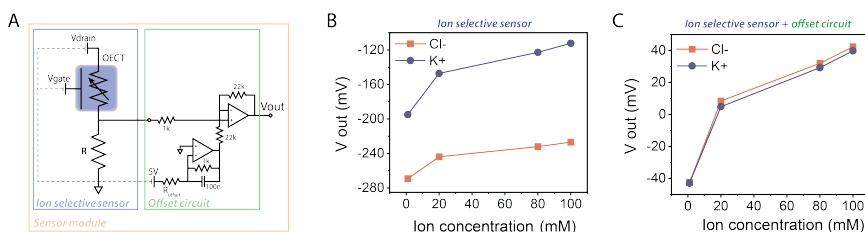


Figure 3.S5: Sensor module for scaling sensor output. a, Circuit diagram of the IS-OECT in a voltage divider configuration together with the offset circuit. In the voltage divider configuration $V_{drain} = -0.4$ V and for the potassium selective sensor $V_{gate} = 0.2$ V and $R = 300 \Omega$ and for the chloride selective sensor gate is grounded and $R = 91 \Omega$. The resistor in the offset circuit for the chloride sensor module is $R_{offset} = 10k\Omega$ and for the potassium sensor module is $R_{offset} = 24k\Omega$. b, Shows the resulting voltage output for both sensor modules without the offset circuit and c, with the offset circuit.

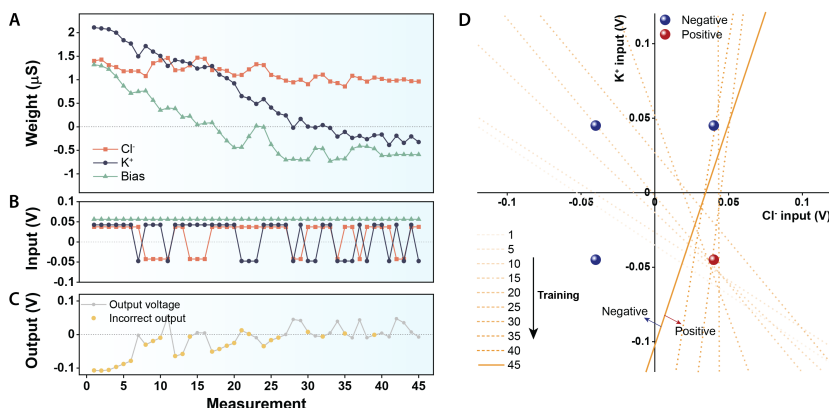


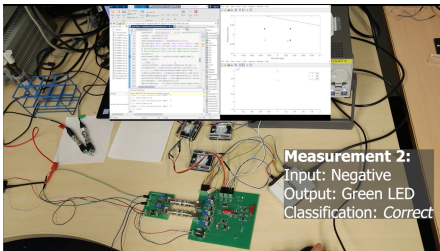
Figure 3.S6: Visualization of the synaptic weight update and corresponding classification line during training with IS-OECTs. a, Values of the weights corresponding to b, the inputs representing the voltage output for a high (100 mM) or low (1 mM) ion concentration measured with the IS-OECTs. c, The output for each measurement cycle, measured before the threshold activation function triggering the LEDs. d, 2-D graphical representation of the classification problem of cystic fibrosis where the dashed lines show the decision boundary on every 5th iteration. The solid line corresponds to the last (45th) measurement and shows a correct classification.

#	Cl	K	Target	Output
1	LO	LO	Negative	Correct
2	LO	LO	Negative	Correct
3	HI	LO	Positive	Incorrect
4	HI	LO	Positive	Correct
5	LO	HI	Negative	Correct
6	LO	LO	Negative	Correct
7	HI	HI	Negative	Incorrect
8	HI	HI	Negative	Correct
9	HI	LO	Positive	Incorrect
10	HI	LO	Positive	Correct
11	LO	HI	Negative	Correct
12	LO	LO	Negative	Incorrect
13	LO	LO	Negative	Correct

#	Cl	K	Target	Output
14	HI	HI	Negative	Correct
15	HI	LO	Positive	Incorrect
16	HI	LO	Positive	Correct
17	LO	HI	Negative	Correct
18	LO	LO	Negative	Incorrect
Trained				
19	LO	LO	Negative	Correct
20	HI	HI	Negative	Correct
21	HI	LO	Positive	Correct
22	LO	HI	Negative	Correct
23	LO	LO	Negative	Correct
24	HI	HI	Negative	Correct
25	HI	LO	Positive	Correct

#	Cl	K	Target	Output
Test using sweat samples				
26	LO	LO	Negative	Correct
27	LO	LO	Negative	Correct
28	LO	LO	Negative	Correct
29	HI	LO	Positive	Correct
30	HI	LO	Positive	Correct
31	HI	LO	Positive	Correct

Figure 3.S7: List with measurement details corresponding to the training cycle in Fig. 3.3. The list shows the details during the training process visualized in Fig. 3.3 for each measurement step (1-31). During each step the input corresponds to a solution with a high (HI) or low (LO) ion concentration (Cl or K). All four different combinations are color-coded to better visualize the order. The next column (Target) shows the classification target (Positive or Negative) corresponding to the input combination with the validation of the output (Correct or Incorrect) in the last column (Output).



<https://youtu.be/VwNFiUc9Yd4>

Figure 3.S8: Video of the training process of the hardware neural network. A snap shot of the video that shows the hardware neural network training process with the QR code on the right containing the link to the video.

3.8.2 EC-RAM modulation and state retention

The EC-RAMs adopt a similar configuration as the OECT but have an $8M\Omega$ resistor in series with the gate to limit the gate current and work both with an aqueous electrolyte as well as with a solid electrolyte (ion gel). In the neuromorphic circuit their gates are connected to a switch in order to increase the state retention by preventing back flow of the current. The active gate and channel material is a PEDOT:PSS blend dedoped with N-methyl-2,2'-diaminodiethylamine (DEMTA). Keene et al. showed that by adding a small molecular weight amines the threshold voltage shifts to negative values and lowers the channel current at $V_{gate} = 0V$. [7] Introducing the DEMTA PEDOT:PSS mixtures into EC-RAMs allows for a more linear conductance modulation, higher state retention and stability. The conductance of the EC-RAMs was measured under a constant bias at the drain ($V_{drain} = -0.1V$) while grounding the source. Alternating positive and negative gate pulses with amplitude 5V and duration 1s,

modulate the channel conductance to respectively lower or higher values (see Supporting Fig. 3.S9 and 3.S10).

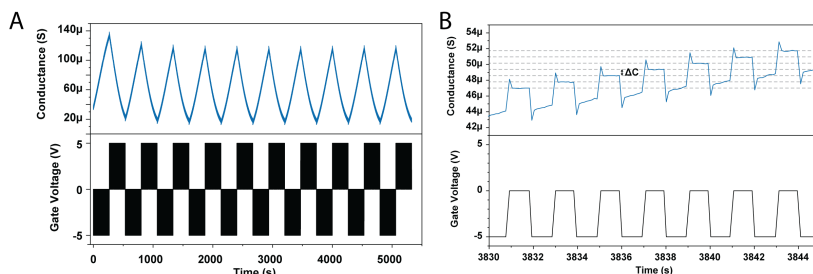


Figure 3.S9: a, EC-RAM conductance modulation operated with aqueous electrolyte by applying alternating positive (128x) and negative (128x) gate pulses with amplitude 5V and duration 1s ($V_d = -0.1V$). b, An enlarged graph showing the individual conductance states.

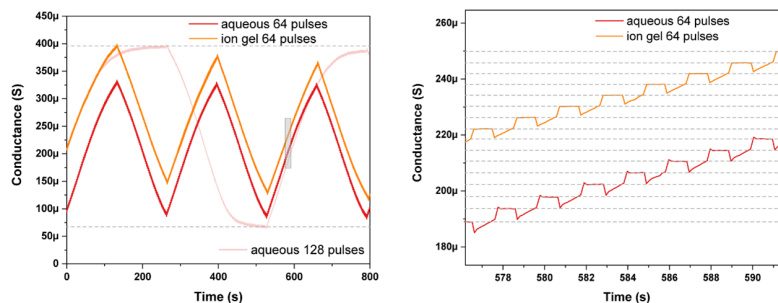


Figure 3.S10: EC-RAM conductance modulation by applying alternating positive (64x) and negative (64x) gate pulses with amplitude 5V and duration 1s ($V_d = -0.1V$) on the same device, once with an aqueous and once with a solid electrolyte. When applying 128 pulses the maximum conductance range is shown.

To account for negative weight values, every EC-RAM is paired with a complementary resistor with a resistance value within its conductance range. The change in conductance, ΔG , scales with the product of the gate voltage and pulse duration in the linear conductance regime. A correct classification depends on the ratio between the weights and therefore the state retention of the conductance (weights) determines the data retention of a trained system (i.e. the time that a previously trained system is able to correctly classify data before it requires another update due to drifting weight values). Supporting Fig. 3.S11 shows the state retention of multiple conductance values and Supporting Fig. 3.S12 shows the data retention of a trained system. Similar to Fig. 3.3, all weights have a negative conductance and are able to correctly classify negative (blue) and positive (red) sweat samples (measurements 1-8). After 30 min (measurement 9) and 60 min (measurements 10-22) the weights are still able to

correctly classify the sample sweat, demonstrating a classification retention of more than 1h. For facile device integration EC-RAMs using a solid state electrolyte are also investigated. Their behaviour show similar performance to the aqueous operated EC-RAMs and can be interchanged in hardware neural network application (see Supporting Fig. 3.S10 and 3.S11).

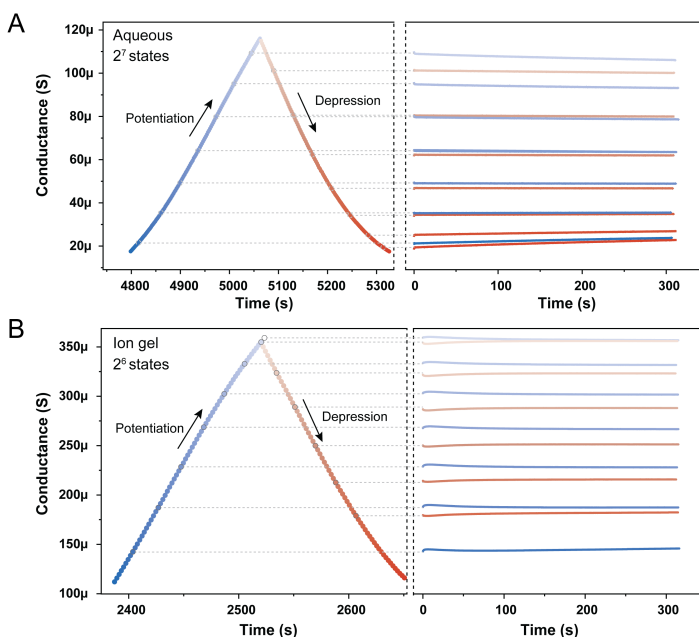


Figure 3.S11: a, EC-RAM state retention of multiple states in a potentiation and depression cycle measured for 5 minutes of an aqueous electrolyte gated device and b, a solid electrolyte gated device.

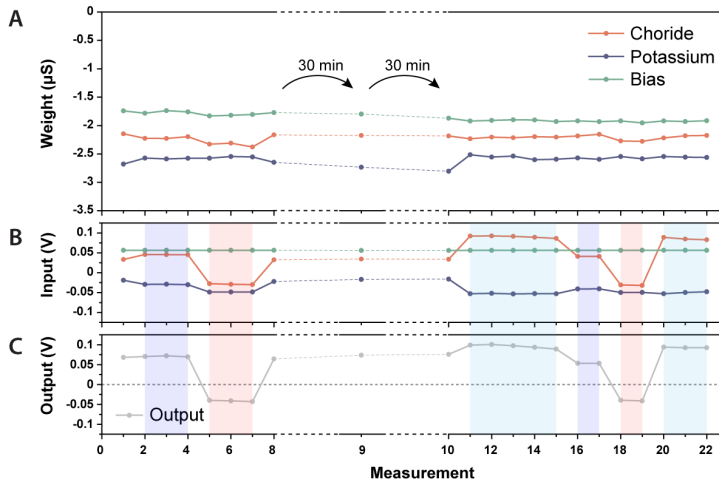


Figure 3.S12: a, Values of the weights corresponding to b, the inputs for negative (blue) and positive (red) sample sweat. c, The output for each measurement cycle, measured before the threshold activation function triggering the LEDs. A positive output voltage corresponds to a negative classification and vice versa. The weights are pretrained showing a correct classification for the sample sweat (1-8). Measurement 9 shows the weights after 30 minutes and measurements 10-22 show the classification output 1 hour after training. The dark and light blue areas correspond to negative sweat samples and the red to positive sweat sample.

3.8.3 Backpropagation in the neuromorphic circuit

When the classification is incorrect, manual feedback opens a switch to disconnect the input from the feedforward circuit so that the sensor output can be used for backpropagation. By means of a multiplier each input is multiplied with the error (equal to the binary output), resulting in the update signal. The same action closes the circuit to the gate of the EC-RAMs in series with a current limiting resistor ($8\text{M}\Omega$). The error is the same for all weights, so the difference in the update is caused by different input values (update = input \times error \times learning rate). The update is analogous to the gate current, able to change the conductance of the EC-RAMs. The learning rate therefore depends on the gate voltage and the duration of the update. Besides the product of input and error, the scaling factor in the circuit determines the update value. This scaling factor is fixed and depends on the EC-RAM properties. The update time can either be fixed or a variable by simply changing the time of pressing the button. When expanding to larger neural networks, these multipliers can be exchanged by another crossbar array for more efficient updating.

3.8.4 Effect of different input values

In software neural networks it is standard to normalize input values, whereas in hardware neural networks this is less straightforward. The input values have a strong impact on the update mechanism of this algorithm and therefore choosing on how to normalize these can

directly impact the training of the neural network. The perceptron algorithm computes its update value according to the product of the error and input. Since the output is a binary value there are three options for the error value: $-a$, $+a$ or 0, with a equal to $|Y_{exp} - Y_{out}|$. Therefore, the value that the error computes in case an update is needed is always the same except the direction and thus the sign depending on the output. Hence the value of the update strongly depends on the input voltage and is the most effective when the difference between high and low input is large (see Supporting Fig. 3.S13). Ideally, a positive and negative voltage input voltage should be used for the high and low input (Supporting Fig. 3.S13a), although voltages of the same sign can also be considered (Supporting Fig. 3.S13b). This often requires more update steps for the hardware neural network to be trained as the sign of the updates depends only on the error which is equal for all weights. To independently update the individual weights multiple updates steps are needed that exploit the difference in high and low to influence the effective update direction. On the other hand, the input voltage is also limited. Because the input voltage is directly connected to the drain of the neuromorphic devices it can alter the conductance state of the device as this is determined by the ions in the channel. A change in potential disturbs the equilibrium. In order to minimize this effect, inherent to the electrochemical property of the neuromorphic device, the input voltage should be as constant as possible. As a result, a trade-off should be found between the update efficacy and the allowed fluctuation of the conductance and thus the variability of the weight value.

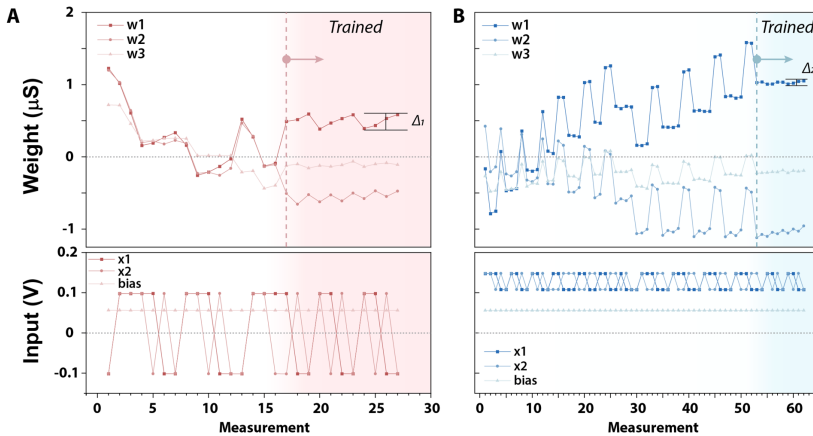


Figure 3.S13: Effect of the input voltage on the weight update during a training cycle. a, Training cycle with high positive and negative input values of 0.1V and -0.1V for high and low ion concentrations, showing training in 17 measurement steps and a weight value variation ($\Delta 1$) caused by the different input values. b, Training cycle where the input values are scaled to the positive range resulting in 0.15V and 0.10V for high and low ion concentration, respectively. Compared to (a) this requires more measurement steps (53) to get fully trained but shows less variation in the weight value ($\Delta 2 < \Delta 1$) caused by the input voltage

Another consideration regarding the input values of hardware neural networks is noise. Unlike in software executing the algorithm directly in hardware can give rise to variations in the input values due to noise. While a lot of noise is intrinsically unwanted it does not always

lead to problems. In Supporting Fig. 3.S14 the classification problem similar to Fig. 3.3 is schematically shown with the addition of noise clouds. Although the training of the hardware neural network remains the same in some cases the same input of sweat can lead to different classification outputs due to noise on the input values, depending on the classification boundary (see solid line in Supporting Fig. 3.S14). In this illustrative example, input II will most of the time be correctly classified as ‘negative’ however in two cases an incorrect ‘positive’ classification occurs. By further training of incorrect classification outputs, the classification boundary will update accordingly (dashed line) and is able to correctly distinguish the two classes including input variations. When dealing with noise or other variations on the input, declaring a neural network trained after one correct output for each input combination should be done with care. In this case it is better to cycle multiple times through every input combination to prevent that a trained classification boundary lies within a noise cloud. On the other hand, training with input variations results in classification boundaries that lie further from the true input, and consequently wrong classification outputs due to variations in the weights (state retention) happen less frequently (see Supporting Information 3.8.2). When considering the electrochemical property of the neuromorphic device and choosing input combinations with a small difference, the effect of noise becomes critical. In case that the noise clouds of the two input classes overlap, classification becomes impossible.

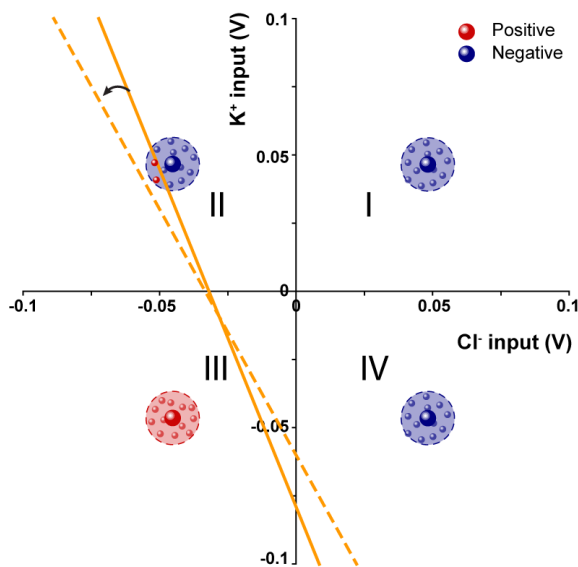


Figure 3.S14: Effect of noise of the input voltage on classification. 2-D graphical representation of a classification problem example with noise clouds around the input values. The input combinations I, II, and IV represent the negative class and the III the positive class. The solid line shows the classification boundary that does not always classify input II correct. The dashed line corresponds to another classification boundary that allows for a correct classification even with noise present on the input.

3.8.5 Hardware neural network circuit

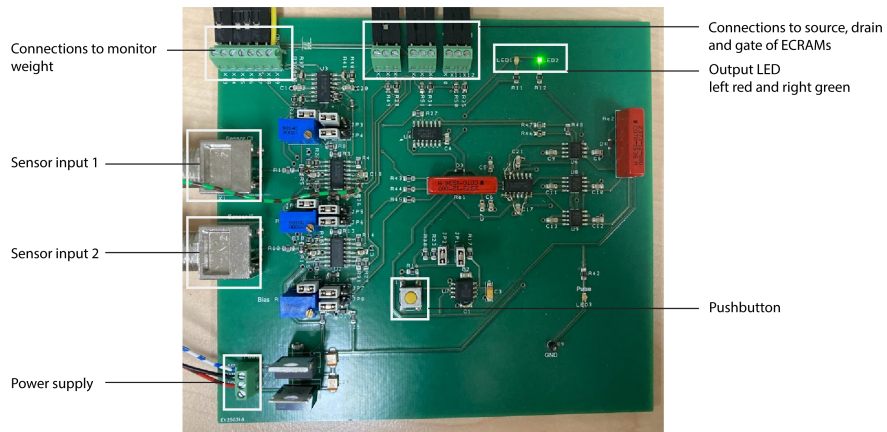


Figure 3.S15: Hardware neural network. Photo of the hardware neural network PCB with relevant components indicated.

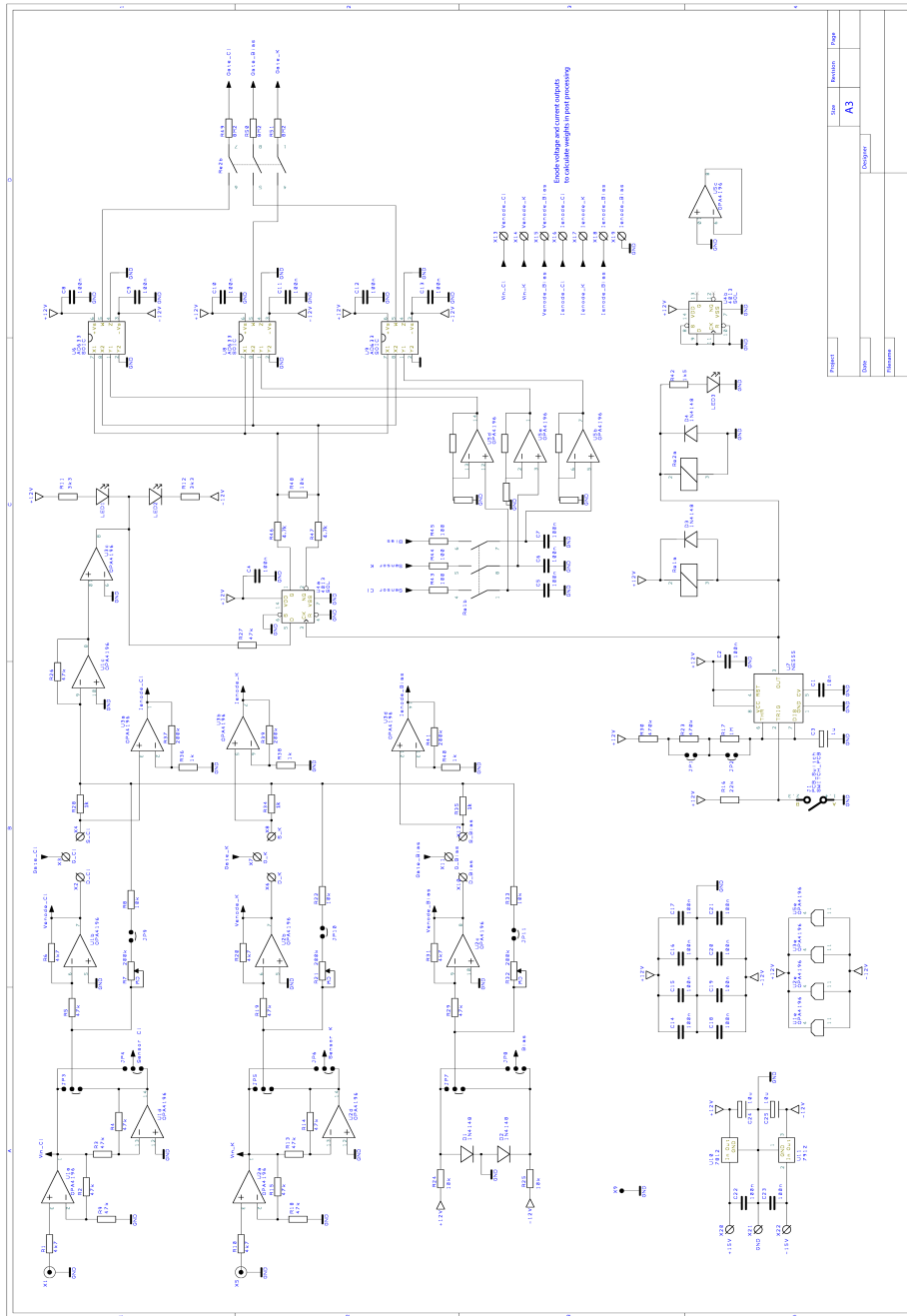


Figure 3.S16: Electronic circuit. Schematic of the electronic circuit design of the hardware neural network PCB module as in Supporting Fig. 3.S15

Author contributions

YvdB and JR. conceived the idea. **Eveline van Doremaele** performed and analyzed the experiments. XJ fabricated the ion selective OECTs. **Eveline van Doremaele** and YvdB wrote the manuscript. All authors reviewed and approved the final manuscript.

Bibliography

1. Van de Burgt, Y., Melianas, A., Keene, S. T., Malliaras, G. & Salleo, A. **Organic electronics for neuromorphic computing**. en. *Nature Electronics* **1**, 386–397. ISSN: 2520-1131 (July 2018).
2. Gkoupidenis, P., Schaefer, N., Garlan, B. & Malliaras, G. G. **Neuromorphic Functions in PEDOT:PSS Organic Electrochemical Transistors**. *Advanced Materials* **27**, 7176–7180. ISSN: 1521-4095 (2015).
3. Van de Burgt, Y. & Gkoupidenis, P. **Organic materials and devices for brain-inspired computing: From artificial implementation to biophysical realism**. en. *MRS Bulletin* **45**, 631–640. ISSN: 1938-1425 (Aug. 2020).
4. Fuller, E. J. *et al.* **Parallel programming of an ionic floating-gate memory array for scalable neuromorphic computing**. en. *Science*, eaaw5581. ISSN: 0036-8075, 1095-9203 (Apr. 2019).
5. Xia, Q. & Yang, J. J. **Memristive crossbar arrays for brain-inspired computing**. en. *Nature Materials* **18**, 309–323. ISSN: 1476-1122, 1476-4660 (Apr. 2019).
6. Van de Burgt, Y. *et al.* **A non-volatile organic electrochemical device as a low-voltage artificial synapse for neuromorphic computing**. en. *Nature Materials* **16**, 414–418. ISSN: 1476-1122, 1476-4660 (Apr. 2017).
7. Keene, S. T., Melianas, A., van de Burgt, Y. & Salleo, A. **Mechanisms for Enhanced State Retention and Stability in Redox-Gated Organic Neuromorphic Devices**. *Advanced Electronic Materials* **5**, 1800686. ISSN: 2199-160X (Feb. 2019).
8. Kim, K.-N., Sung, M.-J., Park, H.-L. & Lee, T.-W. **Organic Synaptic Transistors for Bio-Hybrid Neuromorphic Electronics**. en. *Advanced Electronic Materials* **8**. _eprint: <https://onlinelibrary.wiley.com/doi/pdf/10.1002/aelm.202100935>, 2100935. ISSN: 2199-160X (2022).
9. Keene, S. T. *et al.* **A biohybrid synapse with neurotransmitter-mediated plasticity**. en. *Nature Materials*. ISSN: 1476-1122, 1476-4660 (June 2020).
10. Harikesh, P. C. *et al.* **Organic electrochemical neurons and synapses with ion mediated spiking**. en. *Nature Communications* **13**. Number: 1 Publisher: Nature Publishing Group, 901. ISSN: 2041-1723 (Feb. 2022).

11. Rivnay, J. *et al.* High-performance transistors for bioelectronics through tuning of channel thickness. en. *Science Advances* **1**, e1400251. ISSN: 2375-2548 (May 2015).
12. Sessolo, M., Rivnay, J., Bandiello, E., Malliaras, G. G. & Bolink, H. J. Ion-Selective Organic Electrochemical Transistors. *Advanced Materials* **26**, 4803–4807. ISSN: 1521-4095 (2014).
13. Ohayon, D. *et al.* Biofuel powered glucose detection in bodily fluids with an n-type conjugated polymer. en. *Nature Materials*. ISSN: 1476-1122, 1476-4660 (Dec. 2019).
14. Bai, L. *et al.* Biological Applications of Organic Electrochemical Transistors: Electrochemical Biosensors and Electrophysiology Recording. English. *Frontiers in Chemistry* **0**. Publisher: Frontiers. ISSN: 2296-2646 (2019).
15. Pitsalidis, C. *et al.* Organic Bioelectronics for In Vitro Systems. *Chemical Reviews*. Publisher: American Chemical Society. ISSN: 0009-2665 (Dec. 2021).
16. Strakosas, X., Bongo, M. & Owens, R. M. The organic electrochemical transistor for biological applications. en. *Journal of Applied Polymer Science* **132**. _eprint: <https://onlinelibrary.wiley.com/doi/pdf/10.1002/app.41735>. ISSN: 1097-4628 (2015).
17. Rashid, R. B. *et al.* Ambipolar inverters based on cofacial vertical organic electrochemical transistor pairs for biosignal amplification -supp. en. *Science Advances* **7**, eabh1055. ISSN: 2375-2548 (Sept. 2021).
18. Ji, X. *et al.* Mimicking associative learning using an ion-trapping non-volatile synaptic organic electrochemical transistor. en. *Nature Communications* **12**. Bandiera_abtest: a Cc_license_type: cc_by Cg_type: Nature Research Journals Number: 1 Primary_atype: Research Publisher: Nature Publishing Group Subject_term: Electrical and electronic engineering;Electronic devices Subject_term_id: electrical-and-electronic-engineering;electronic-devices, 2480. ISSN: 2041-1723 (Apr. 2021).
19. Zhou, F. & Chai, Y. Near-sensor and in-sensor computing. en. *Nature Electronics* **3**. Number: 11 Publisher: Nature Publishing Group, 664–671. ISSN: 2520-1131 (Nov. 2020).
20. Christodouleas, D. C., Kaur, B. & Chorti, P. From Point-of-Care Testing to eHealth Diagnostic Devices (eDiagnostics). en. *ACS Central Science* **4**, 1600–1616. ISSN: 2374-7943, 2374-7951 (Dec. 2018).
21. Lim, S. *et al.* Adaptive learning rule for hardware-based deep neural networks using electronic synapse devices. en. *Neural Computing and Applications*. ISSN: 0941-0643, 1433-3058 (July 2018).

22. Krauhausen, I. *et al.* Organic neuromorphic electronics for sensorimotor integration and learning in robotics. EN. *Science Advances*. Publisher: American Association for the Advancement of Science (Dec. 2021).
23. Wright, L. G. *et al.* Deep physical neural networks trained with backpropagation. en. *Nature* **601**. Number: 7894 Publisher: Nature Publishing Group, 549–555. ISSN: 1476-4687 (Jan. 2022).
24. LeGrys, V. A. Sweat testing for the diagnosis of cystic fibrosis: Practical considerations. en. *The Journal of Pediatrics* **129**, 892–897. ISSN: 0022-3476 (Dec. 1996).
25. Gonzalo-Ruiz, J. *et al.* Early determination of cystic fibrosis by electrochemical chloride quantification in sweat. en. *Biosensors and Bioelectronics* **24**, 1788–1791. ISSN: 0956-5663 (Feb. 2009).
26. Bandodkar, A. J. *et al.* Sweat-activated biocompatible batteries for epidermal electronic and microfluidic systems. en. *Nature Electronics*. ISSN: 2520-1131 (July 2020).
27. Kwon, K. *et al.* An on-skin platform for wireless monitoring of flow rate, cumulative loss and temperature of sweat in real time. en. *Nature Electronics* **4**. Number: 4 Publisher: Nature Publishing Group, 302–312. ISSN: 2520-1131 (Apr. 2021).
28. Han, S., Yamamoto, S., Polyravas, A. G. & Malliaras, G. G. Microfabricated Ion-Selective Transistors with Fast and Super-Nernstian Response. en. *Advanced Materials* **n/a**. _eprint: <https://onlinelibrary.wiley.com/doi/pdf/10.1002/adma.202004790>, 2004790. ISSN: 1521-4095 (2020).
29. Pierre, A., Doris, S. E., Lujan, R. & Street, R. A. Monolithic Integration of Ion-Selective Organic Electrochemical Transistors with Thin Film Transistors on Flexible Substrates. en. *Advanced Materials Technologies* **4**, 1800577. ISSN: 2365-709X (2019).
30. Rivnay, J. *et al.* Organic electrochemical transistors. en. *Nature Reviews Materials* **3**, 17086. ISSN: 2058-8437 (Feb. 2018).
31. Paulsen, B. D., Tybrandt, K., Stavrinidou, E. & Rivnay, J. Organic mixed ionic–electronic conductors. en. *Nature Materials* **19**, 13–26. ISSN: 1476-4660 (2020).
32. Li, Y. *et al.* Ion-Selective Organic Electrochemical Transistors: Recent Progress and Challenges. en. *Small*. _eprint: <https://onlinelibrary.wiley.com/doi/pdf/10.1002/sml.202107413>, 2107413. ISSN: 1613-6829 (2022).

33. Battistoni, S., Erokhin, V. & Iannotta, S. [Organic memristive devices for perceptron applications](#). en. *Journal of Physics D: Applied Physics* **51**, 284002. ISSN: 0022-3727, 1361-6463 (July 2018).
34. Prezioso, M. *et al.* [Training and operation of an integrated neuromorphic network based on metal-oxide memristors](#). en. *Nature* **521**, 61–64. ISSN: 1476-4687 (May 2015).
35. Chen, J., Li, J., Li, Y. & Miao, X. [Multiply accumulate operations in memristor crossbar arrays for analog computing](#). en. *Journal of Semiconductors* **42**, 013104. ISSN: 1674-4926, 2058-6140 (Jan. 2021).

Chapter 4

Novel implementation of the backpropagation algorithm for *in situ* training of multi-layer hardware neural networks using progressive gradient descent

4

The process of neural network training can be slow and energy-intensive due to the transfer of weight data between digital memory and processor chips. Neuromorphic computing can accelerate neural networks by performing multiply-accumulate operations in parallel using non-volatile analogue memory. However, the training algorithm (backpropagation) in multi-layer neural networks requires information - and therefore storage - on the partial derivatives of the weight values, which is undesired in hardware neural networks. Here we propose a novel strategy of the backpropagation algorithm that progressively updates each layer using *in situ* gradient descent avoiding the storage requirement. We experimentally demonstrate the working principle of the *in situ* error calculation and the proposed progressive backpropagation method using a single and double layer hardware neural network. We show with simulations that the progressive backpropagation method achieves the same classification accuracy compared to conventional backpropagation in software. These results show that the novel backpropagation strategy has the potential to enable fast and efficient training in hardware neural networks without sacrificing accuracy.

This chapter is based on the manuscript titled *Novel implementation of the backpropagation algorithm for in situ training of multi-layer hardware neural networks using progressive gradient descent*, Eveline R. W. van Doremaele, Tim Stevens, Stijn Ringeling, Marco Fattori, Yoeri van de Burgt. *Manuscript in preparation*.

4.1 Introduction

Neural networks have become increasingly popular due to their ability to solve complex problems and process and structure large amounts of data. However, their growing size and complexity have resulted in an exponential increase in the computational power (and energy) required to process the information. This has led to the limitations of traditional computing architecture, where the processing and memory units are separated. To address these limitations, neuromorphic computing has emerged as a promising alternative. This brain-inspired architecture allows for efficient vector-matrix multiplications, and has been successful in accelerating neural networks[1–3] using in-memory computing. The weights of the neural networks are represented by the conductance of neuromorphic devices, which have been demonstrated in a wide variety of materials and systems, ranging from PCM[4], RRAM[5, 6], EC-RAMs[7–9], etc. Commonly, the neural network is trained in software (*ex situ*) and subsequently the weights are transferred directly to the neuromorphic devices by mapping conductance values. Importantly, to achieve an accuracy comparable to software neural networks the weights need to be precisely programmed with the correct conductance values. Various research has been reported on improved programming schemes to increase the programming efficiency and accuracy [4, 5, 10–12].

However, hardware imperfections, such as defective devices and parasitic wire resistance and capacitance are inevitable, and are the main cause of inferior hardware neural network performance. *In situ* training on the other hand adapts the weights and compensates for these imperfections automatically.[13, 14] Hybrid training methods can be used to adapt to device imperfections and improve the overall system performance. After the *ex situ* trained weights are transferred to the neuromorphic devices, the weights of one (or more) layers are reprogrammed using the backpropagated gradients calculated from hardware-measured outputs.[15] Another hybrid method uses the hardware measured outputs for training in software to progressively program the weights layer-by-layer.[16]

While these strategies are efficient in mitigating accuracy loss due to hardware imperfections, they still require computationally expensive training *ex situ* by calculating the weight update and programming the update using software. In an effort to mimic the efficient learning process of the brain, *in situ* learning methods such as the forward-forward algorithm, have been developed.[17] While this algorithm has several advantages that allow for a simpler hardware implementation, its performance is insufficient to replace the established backpropagation algorithm. Methods to perform *in situ* backpropagation have been investigated and simulated but are limited to a single layer[18, 19], require a binary update step[20, 21] or binary weights[22, 23], or storage of weight values[24]. Backpropagation using (stochastic) gradient descent allows to differentiate between the weights and update them in proportion to their relative contribution to the error, ensuring maximum error reduction. Compared to update mechanisms with the same magnitude, gradient descent allows for more efficient weight updates and overall better neural network accuracy, but is more complex to execute in hardware due to the required calculation of partial derivatives (for multi-layer neural networks). Here we propose a novel approach to integrate backpropagation directly on the chip using hardware-based stochastic gradient descent suitable for multi-layer neural networks. We introduce a method to calculate the partial derivatives of the weights

locally, which allows for efficient weight updates during the training (backpropagation) phase.

4.2 Hardware implementation gradient descent

The proposed mechanism works by calculating the weight change layer-by-layer and implement this directly in hardware. During feed forward (inference), the output z of layer L is calculated through a vector-matrix multiplication of the input times the weights ($w^{(L)}$) and an activation function $a^{(L)} = \sigma(z^{(L)})$, with the input equal to $a^{(L-1)}$. The weight update for each weight is relative to its contribution to the error E and calculated according to

$$\Delta w_{ij}^L = -\eta \frac{\partial E}{\partial w_{ij}^L} E \quad (4.1)$$

where η is the learning rate, a hyperparameter used for scaling the update step and the error equals the output ($a^{(L)}$) minus target (y). For a single-layer neural network (e.g. perceptron) this is relatively straightforward since the update only depends on the input and output that are directly available in hardware and only the derivative of the activation function needs to be calculated which is 1 or 0 (in the case of a ReLU) see $\frac{\partial E}{\partial w_1}$ in Fig.4.1a.

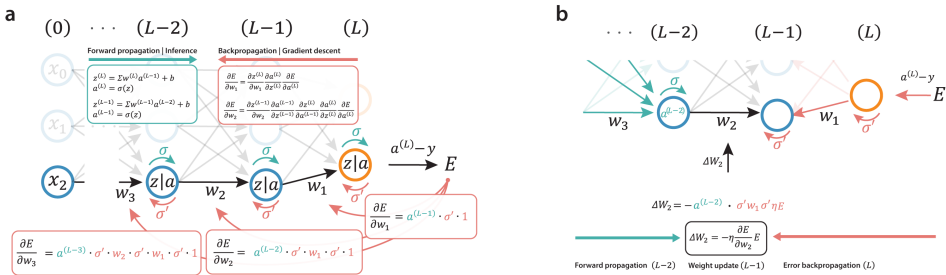


Figure 4.1: Backpropagation algorithm | a) Schematic illustration of the partial derivatives required for backpropagation including the corresponding formulas b) Mechanism to update weight 2 in layer $L-1$ that depends of the forward signal of layer $L-2$ and the backpropagated error through layer L .

However, in a multi-layer neural network the weight update is influenced by the surrounding layers and depends on the activation of the previous neurons ($a^{(L-2)}$) and the weights in posterior layers (w^L) for weights in layer $L-1$. As a result, the gradient descent algorithm typically requires storing the values of the neuron activation (intermediate output) as well as the weight values, which is undesirable for hardware neural networks. The implementation method we propose here allows to circumvent this restriction by progressively updating a single layer. We calculate the weight update by applying the feedforward and the backpropagation signal at the same time (see Fig.4.1b). The feedforward signal travels downstream through the network (representing $a^{(L-2)}$) until the layer $(L-1)$ that requires updating. The error propagates backward (upstream) through the network until the layer $L-1$ and is therefore multiplied by the weights (w^L). To facilitate the multiplication for the updates we use a transistor of

which the drain current is linearly proportional to the gate voltage (feed forward) and the drain voltage (back flowing error), (see Supporting Information 4.6.1). The transistor at every weight allows for efficient vector-vector multiplications and enable parallel weight updates for each layer.

4.3 Results

4.3.1 Classification performance of parallel versus progressive update

While the progressive layer-by-layer update approach completely avoids the storage requirements and allows for efficient multiplication operations during backpropagation, the update values deviate slightly from the perfect update values as calculated by traditional gradient descent. After the error calculation, the last layer will get the ideal update step according to the gradient descent algorithm. However, the layers before the last one will get a slightly different backflowing error signal as the weights through which the error signal propagates are already updated. Although this deviation is unfavorable, generally neural networks thrive when using large datasets while doing very small update steps. The weight update (Δw_{ij}^L) after evaluating a single data point is small enough, that we assume that the value of the weight before and after the update is (almost) equal ($w_{ij}^L \approx w_{ij}^L + \Delta w_{ij}^L$). We thus expect that the impact of the imperfect backflowing error signal is minimal and does not significantly contribute to any accuracy loss. We verify this by simulating the performance of the proposed layer-by-layer backpropagation approach compared to the traditional parallel update method in software.

We used Python to model the behavior of the software and hardware neural network with the parallel and progressive gradient decent respectively. We chose a (2x7x1) neural network structure with two layers to classify a binary data set. In principle, classification of the problem can be done with only two neurons in the hidden layer. However, due to the inherent stochastic behaviour of neural networks, the training could get stuck in local minima depending on random weight initialization values. For robustness, we chose seven neurons in the hidden layer to counteract the probability of ending up in a local minimum. The dataset consist of data clusters, generated by sampling 100 individual data points from a Gaussian distribution, $X \sim N(\mu, \sigma^2)$, with a given mean (μ) and standard deviation (σ). Because this dataset can be easily visualized (two input features can be represented on a 2D plane) it allows for better comparison and analysis on a qualitative level. We use a ReLU and a Linear Sigmoid activation function for the hidden and output layers, respectively, which can also be implemented directly in hardware [21]. The model for the software and hardware neural network are the same except for two important differences: First, the software model updates all layers in parallel (i.e. storing partial derivatives with respect to the weights in memory), while the hardware model updates layers progressively allowing slight deviations in error signals and consequently in the update steps. Second, the weight values in software can be programmed completely linear and exact, while the weights in the hardware model are retrieved from measurement data which includes non-linearity and noise (see Supporting Information 4.6.3). All other parameters and processes such as learning rate, number of epochs, weight initialization, data pre-processing, network structure, activation functions, error function, and dataset are kept the same. To demonstrate the effect of the transistor multiplication, the hardware model allows

us to perform the update multiplication either in software or with the data of the transistor multiplication. Figure 4.2 shows the training accuracy after every epoch for the software neural network model and both hardware neural network models (with and without transistor multiplication) for 100 cycles. The performance strongly depends on the (randomized) initial weight values and varies cycle-to-cycle however both software and hardware models show similar performance, by converging to 100% accuracy within 10 epochs (except for a few cycles that were stuck in local minima).

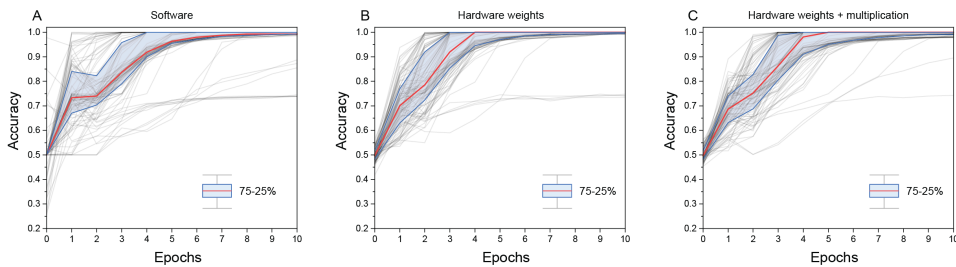


Figure 4.2: Accuracy comparison for software vs hardware model. Training accuracy after every epoch for the a) software model, b) hardware model without and c) hardware model with transistor multiplication, showing 100 training cycles (with randomized initial weight values). The blue area indicates the 25-75% boundaries and the red line the median.

Figure 4.3 shows the discrimination boundaries and corresponding weight convergence which demonstrates similar learning characteristics between the hardware model, using the progressive gradient descent approach and transistor multiplication, and the software model. When comparing the discrimination boundaries (Fig.4.3 a and b), the added noise in the hardware model is clearly visible - while the software model shows perfectly straight lines - however does not impact the accuracy since the noise level is much smaller than the input features. Furthermore, when inspecting the convergence of the weights (Fig.4.3 c and d) we see that the behavior of the weights in the software and hardware model are identical on a qualitative level and again show potential of the progressive gradient descent approach for hardware neural networks. The stochastic nature of the backpropagation algorithm in combination with the random weight initialization results in different learning cycles.

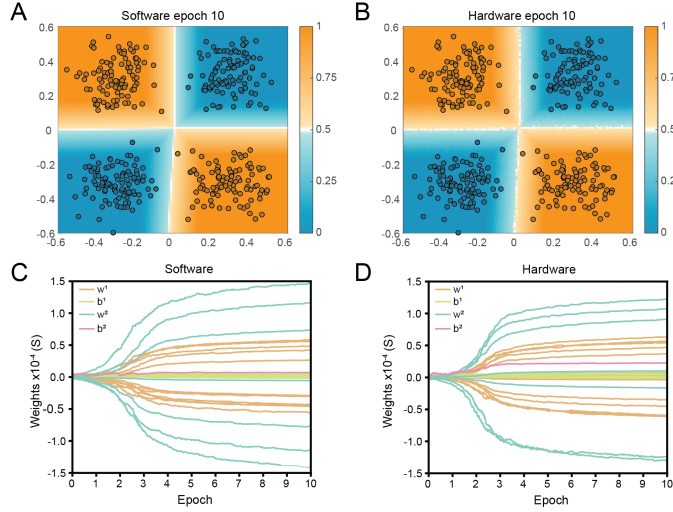


Figure 4.3: Decision boundaries and weight convergence comparison for binary data. a) Discrimination boundary for software model. b) Discrimination boundary for hardware model including the transistor multiplication. c) Corresponding weight convergence for the software and d) hardware model. Weights and biases corresponding to neurons of the same layer are indicated with the same color.

4.3.2 *In situ* hardware classification performance

To demonstrate the *in situ* hardware classification we fabricated the peripheral circuit of the hardware neural network on a PCB using EC-RAMs as the weights (see Fig.4.4 and Methods 4.5.1), such that every PCB represents 1 layer (including the activation function) that can be cascaded to construct multi-layer hardware neural networks. Figure 4.5 shows the PCB designed to operate as a single crossbar (network layer) of size 2x2.

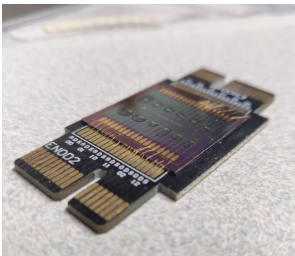


Figure 4.4: Photo of substrate with EC-RAMs

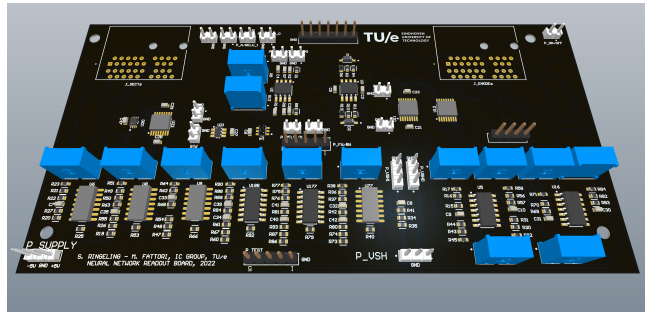


Figure 4.5: Design of the PCB. Equivalent to one network layer including the activation function (ReLU) and necessary control operations for the inference task and backpropagation algorithm.

This architecture requires 6 EC-RAMs, 4 that represent the weight values (w_{ij}^L) connected to the inputs and 2 that represent the bias (b_j^L). The gates of EC-RAMs are each connected to a transistor in order to perform the multiplication for the update (see Supporting Information 4.6.1), and both are being offset by a reference resistor which allows for negative conductance values. The crossbar can operate in two directions, forward and backward. In feedforward mode the output ($I_j^L = \sum_{i=1}^n V_i^{L-1} w_{ji}^L + b_j$, with $w_{ji}^L = (G_{ji,ECRAM} - G_{ji,ref})$) is converted to a voltage signal and passed through the ReLU activation function (ϕ). The ReLU activation function is implemented in hardware using a diode such that only positive output values go through:

$$\phi(x) = \max(0, x) = \begin{cases} x & x \geq 0 \\ 0 & x < 0 \end{cases} \quad \phi'(x) = \begin{cases} 1 & x \geq 0 \\ 0 & x < 0 \end{cases} \quad (4.2)$$

During forward operation a latch is controlled to store the gradient of the ReLU ($\phi' = 0$ or 1). In the backward mode the backflowing error ($I_i^{(L-1)} = \sum_{j=1}^m V_j^L w_{ji}^L$) travels in opposite direction and is converted to a voltage multiplied by the derivative of the ReLU activation function (ϕ'). The third mode of operation is the update mode and allows the board to use both the feedforward and feedback signal from the adjacent layers in order to change the weight values accordingly (as discussed in section 4.2). Similar to the model as described in section 4.3.1, the activation function of the output layer is a Linear Sigmoid, calculated in software, since it only affects the last layer.

First we demonstrate the behavior of a single crossbar using the transistor multiplication to update the weights, by replicating a single-layer (2x1) neural network using only 1 output column of a single crossbar with 3 weights. The dataset ($X \sim N(\mu, 0)$) consist of two clusters with 2 data points with $\mu_1 = (-0.3, 0.3)$ and $\mu_2 = (0.3, -0.3)$, for class 1 (orange) and 0 (blue), respectively. Figure 4.6 shows the decision boundaries for Epoch 0, 1 and 10.

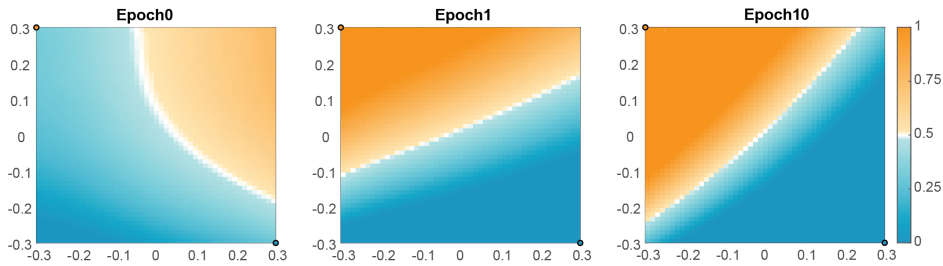


Figure 4.6: Decision boundaries after weight initialization (Epoch 0) and after training Epoch 1 and Epoch 10. For the evaluation of the decision boundaries the output values are recorded while sweeping over the input values from -0.3V to 0.3V in a grid of 50x50. $\mu_1 = (-0.3, 0.3)$ represents class 1 (orange) and $\mu_2 = (0.3, -0.3)$ class 0 (blue).

Epoch 0 represents the classification output when the weights are randomly initialized and the network is not trained. We can clearly see that the values of the weights are close to zero, as

the decision boundary of epoch 0 is curved. Note that a single-layer neural network (with 2 weights and a bias) only allows for a linear separation between classes. The curved decision boundary is the effect of noise on the weights. Every epoch the network runs through all data points and updates the weights accordingly. From the decision boundaries we can clearly see the update mechanism works well since the accuracy of epoch 1 and 10 is 100% for this data set. We also see that the contribution of noise is reduced after only 1 epoch. After 10 epochs the networks shows an almost perfect classification boundary. The classification using 1 layer shows that the update method using the transistor multiplication works as expected. However, it only allows us to demonstrate the forward and update mode of the crossbar (and not the backflowing error). To demonstrate the progressive update approach in hardware we cascade two crossbars to classify an XOR dataset with a $2 \times 2 \times 1$ neural network. The last layer (2×1) is the same as the single-layer neural network described before but its input comes directly from the output of the ReLU activation of the first crossbar (2×2 layer). We randomly initialize all weights close to zero by discharging the gate of the EC-RAMs. Figure 4.7 shows the decision boundaries for various epochs between 0 and 10. Epoch 0 shows that all the weights are close to zero before training. One epoch means one cycle through the feedforward and progressively update both layers from back to front for all data points (4 clusters with $\mu_1 = ([-0.2, 0.2], [0.2, -0.2])$ for class 1 indicated in orange and $\mu_2 = ([-0.2, -0.2], [0.2, 0.2])$ for class 0 indicated in blue and $\sigma = 0.0015$ with 20 data points per cluster).

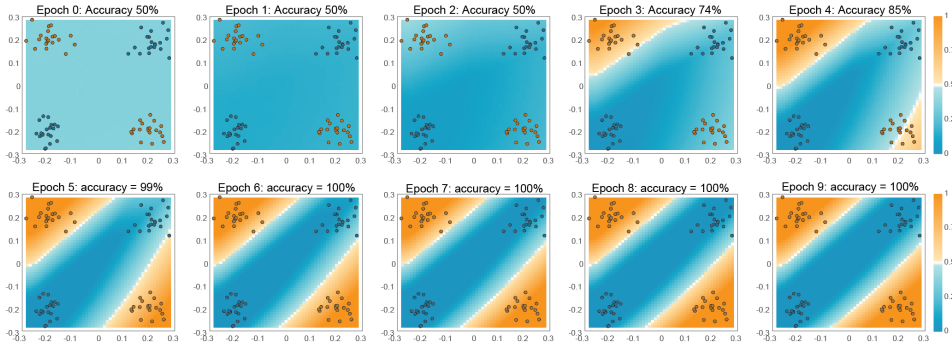


Figure 4.7: Decision boundaries for a 2-layer classification after weight initialization (Epoch 0) and after 9 consecutive epochs. For the evaluation of the decision boundaries the output values are recorded while sweeping over the input values from -0.3V to 0.3V in a grid of 50×50 . Blue and orange data points represent class 0 and 1.

After the first two update cycles (epoch 1 and 2) all the weights have a value such that the output class is 0 in all cases (accuracy = 50%). After a few more epochs the weights are further updated and reach an accuracy of 100% at epoch 6. The weights continue to update leading to sharper decision boundaries but quickly saturate as the error, and thus the update, becomes zero. Due to the neural network structure, specifically the 2 neurons in the hidden layers, not all weight initializations lead to a global minimum and result in a 100% output accuracy. In Supporting Fig. 4.S9 we show another training process of the same neural network where the weights have different initialization values which leads to a local minimum obtaining 75%

accuracy. To reduce the probability of the neural network arriving in a local minimum, the number of hidden neurons can be increased (as demonstrated with the hardware and software simulations in Fig. 4.2). Still, the weight initialization step remains important and should be random, free from any biases caused by device imperfections or offsets, non-linearity and imperfections in the electronic circuit and components. Especially in the beginning of the training when weight values are close to zero these imperfections become significant and can skew the results. Although those imperfections cannot be completely avoided, the hardware neural network can be further optimized by tuning amplification factors and offsets to reduce its impact (see Supporting Information 4.6.6). Even in software neural networks, fine tuning of the hyperparameters can have a large impact on the outcome. However, in software many tools are available, such as normalization and regularization, whereas in hardware this still requires manual optimization.

4.4 Conclusion

We introduced a novel strategy for the backpropagation algorithm that progressively updates the neural network layers directly in hardware. This method allows to calculate the partial derivative of the error with respect to the weight *in situ* to bypass the need to store information of the weights. We showed using a simulation that the trade-off of the error signal propagating through an already updated layer, has no impact on the classification accuracy for a 2-layer neural network. We further demonstrated the classification of a single-layer hardware neural network by efficient vector-vector multiplication of the update signal using a transistor at the gate of the EC-RAMs. Finally, we executed training of a multi-layer neural network using progressive gradient descent in hardware and obtained a classification accuracy of 100%. These results show that the progressive backpropagation approach creates opportunities for training large neural networks more efficient and enables further advancements in intelligent computing systems.

4.5 Methods

4.5.1 EC-RAM fabrication

Cr (5nm) / Au (50 nm) electrodes were patterned on a SiO_x substrate using photolithography and the subsequent lift-off process of the negative photoresist (AZ nLOF 2035). After a surface treatment with the adhesion promoter Silane A-174, parylene C was deposited (~1.7 μ m) on the substrate to electrically isolate the electrodes. A diluted Micro-90 (2% v/v in DI water) was spin-coated as an anti-adhesive layer, and subsequently, a sacrificial second parylene C layer (~2 μ m) was deposited. The EC-RAM channels, with a width of 200 μ m and length of 500 μ m, and contact pads were opened through successive photolithography (AZ10XT photoresist) and reactive ion etching steps (Nordson March RIE 1701). A PE-DOT:PSS (Hereaus, Clevios PH 1000) solution containing 6 vol% ethylene glycol (EG, Sigma Aldrich) to enhance the morphology, 1 vol% (3-glycidyloxypropyl)trimethoxysilane (GOPTS, Sigma Aldrich) as a crosslinking agent to improve mechanical stability, was filtered through a 0.45 μ m polytetrafluoroethylene filter and spin-coated on the patterned substrates (1500 RPM

for 1 minute) and baked at 120 °C for 10 minutes. Thereafter the substrate was gently rinsed in deionized water to eliminate residual contents and subsequently dried at 120 °C for 60 minutes after which the sacrificial parylene-C layer was removed. The ion gel solution was prepared by dissolving ionic liquid (EMIM:TFSI) and poly(vinylidene fluoride-co-hexafluoropropylene) (4:1 w/w) in acetone (17.6 wt% ionic liquid, 4.4 wt% polymer, and 78 wt% solvent) and stirred at 40 °C for at least 30 min, after which it was drop casted on the EC-RAM substrate to define the solid electrolyte.

4.6 Supporting Information

4.6.1 Transistor multiplication

For the multiplication of the feedforward and backflowing error (Supporting Fig.4.S1 we use a normally semi-open JFET transistor operating in the linear region where the output current I_D is proportional to:

$$I_D \propto V_G V_D \Leftrightarrow |V_G| \gg |V_D| \quad (4.3)$$

We pair the transistor with a 100 Ω resistor to correct for the offset such that its conductance is zero when $V_G = 0V$. Supporting Fig.4.S2 shows the output current as a result of the voltage multiplication. The linearity of this multiplication directly impacts the weight update and thus the network performance.

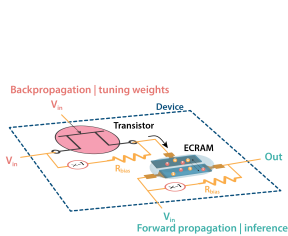


Figure 4.S1: Update EC-RAM by multiplying feedforward with backflowing error using a transistor

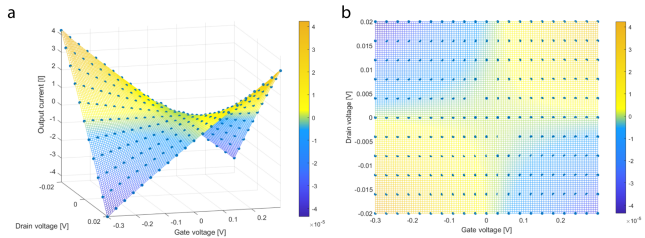


Figure 4.S2: Transistor multiplication measurement. Side view a) and top view b) of the transistor measurement for different drain and gate voltages, using a reference resistor of 100 Ω for offsetting the conductance. The colorbar represents the output current.

4.6.2 Weight modulation EC-RAM

We implemented a current source (Supporting Fig.4.S3a) in front of the EC-RAM gate to scale the output current from the transistor (the result from the forward and backward multiplication) to the desired update steps. The use of the current source allows for linear update steps and facilitates to set the maximum and minimum conductance values by balancing the resistors to

prevent device damage. Supporting Fig.4.S3b shows the conductance modulation by applying alternating pulse trains of positive and negative voltage to the input of the current source. When increasing the number of pulses we can see that the maximum and minimum values set by the current source are reached (Supporting Fig.4.S3c).

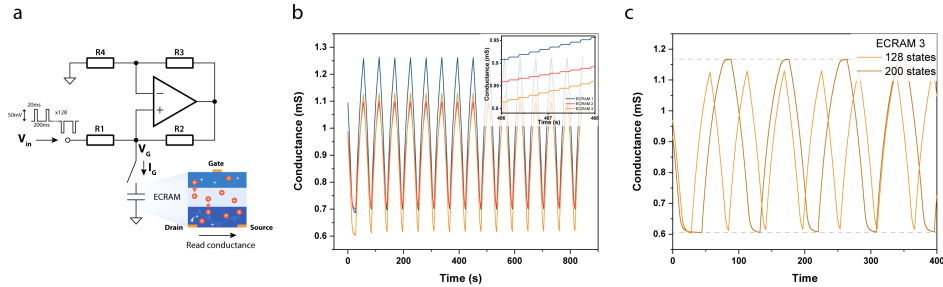


Figure 4.S3: Weight modulation. a) Schematic of the current source used to tune the conductance values of the EC-RAM. b) Conductance modulation of 3 EC-RAMS by applying 128 potentiation and depression pulses with amplitude $\pm 50\text{mV}$ and duration 20ms and delay 200ms. c) Conductance modulation of EC-RAM 3 with 128 and 200 pulses demonstrating the capping behavior of the current source.

4.6.3 Hardware neural network simulation

The simulation of the hardware neural network is done in Python where the neural network is constructed from crossbars each containing EC-RAMs of which the experimental data is provided (see Supporting Fig. 4.S4). The EC-RAM data of the conductance modulation (Supporting Fig.4.S3b,c) is divided in a reset (potentiation) and set (depression) file containing each 128 (or 200) states for all cycles (see Supporting Fig.4.S5).

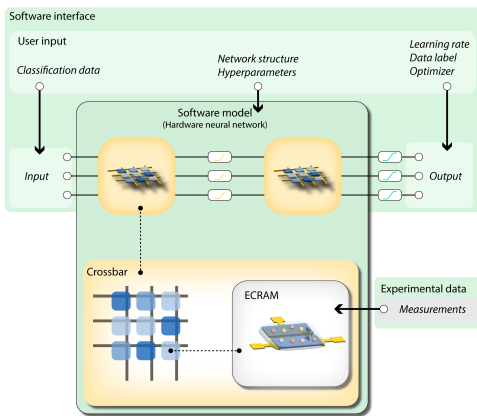


Figure 4.S4: Hardware neural network model simulated with Python.

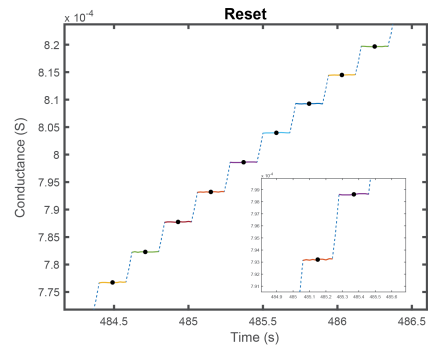


Figure 4.S5: Zoom in on the conductance states of the reset pulse (-50mV , 20ms).

The average conductance per state is defined as the average conductance of 10 data points per state and the read noise is equal to the standard deviation ($\sigma_{rn} = 8.3 \cdot 10^{-8}$) of those points. The average gradient for potentiation and depression per conductance state is calculated and interpolated for conductance values in between. Since the update (change in conductance) is proportional to the time and the voltage amplitude, the average gradient is divided by the pulse duration (20ms) and gate voltage ($\pm 50\text{mV}$). The write noise is determined by the standard deviation between cycles ($\sigma_{wn} = 2.6 \cdot 10^{-5}$). Supporting Fig.4.S6 shows the cumulative distribution function (cdf) of the mean conductance gradient versus conductance for potentiation and depression of the conductance values.

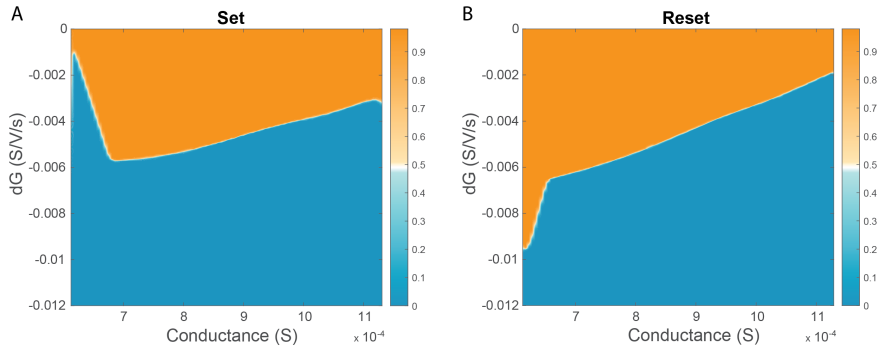


Figure 4.S6: CDF plot of conductance modulation of a) depression (set) and b) potentiation (reset).

It shows that the updates are symmetric but slightly non-linear in the conductance range $C = 7 \cdot 10^{-4}$ S to $C = 11 \cdot 10^{-4}$ S. This is caused by the drain voltage ($V_D=0.1\text{V}$) during the measurement. Below conductance values of $C = 7 \cdot 10^{-4}$ S we see the capping effect of the current source indicating conductance values close to its boundary preventing further updates towards low conductance values. The offset value (to realize negative weight values) is determined by the intersection of the increasing and decreasing gradient, preventing biases introduced by different update values for increasing and decreasing states.

4.6.4 Hardware neural network testing

The PCB is able to execute all computations (except for the generation of input data and the error calculation) depending on the mode of operation (MOO) and is controlled by an NI multifunction I/O device (DAQ) using MATLAB software (see Supporting Fig.4.S7 and Table 4.S1).

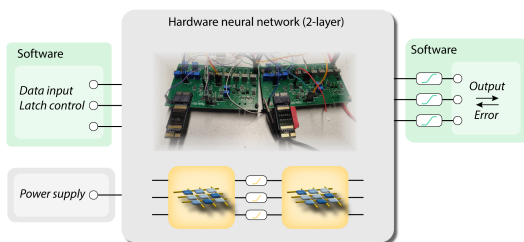


Figure 4.S7: Hardware neural network testing

Table 4.S1: I/O channels: PCB to National instrument

Channel	PCB pins	NI I/O
1	Input crossbar (1)	AO
2	Input crossbar (2)	AO
3	Bias crossbar	AO
4	Backflowing error (1)	AO
5	Backflowing error (2)	AO
6	Mode of operation: Feedforward	DO
7	Mode of operation: Feedbackward	DO
8	Mode of operation: Update	DO
9	Store ReLU gradient	DO
10	Apply learning	DO
11	Output crossbar (1)	AI
12	Output crossbar (2)	AI

From the perspective of the NI board, the first 5 channels are analogue outputs (AO), responsible for input features and backflowing errors in the crossbar. Channel 6 through 8 are connected to digital outputs (DO) to control the mode of operation (feedforward, feedbackward or update), referring the progressive backpropagation (Fig.4.1b). Channel 9 and 10 are also digital outputs (DO), which are used to store the gradient of the activation function (0 or 1) during feedforward and to apply the update on the gate of the EC-RAMs, respectively. The last two channels are analogue inputs (AI) used to measure the output of the crossbar. Note that each additional crossbar comes with the same channel configuration where the crossbar output can be connected directly to the input channels of the next crossbar in order to create a multi-layer neural network. To classify an XOR dataset, 2 crossbars have to be connected in series, representing a 2x2x1 hardware neural network, and progressively need to change their mode of operation. Supporting Fig.4.S8 shows the control sequence of the 2-layer hardware neural network.

	Time		
Channels	Feed forward Inference	Feed backward Update CB 2	Feed backward Update CB 1
MOO CB1	Forward	Forward	Update
MOO CB2	Forward	Update	Backward
Input 1 (CB1)			
Input 2 (CB1)			
Bias (All CBs)			
Error input (CB2)			
Store Δ ReLU (All CBs)			
Update CB 1			
Update CB 2			

Figure 4.S8: Signal sequence generated by software to evaluate one data point and update the hardware layers accordingly.

During the first part of the signal sequence, both crossbars are set to the forward mode in order to apply the input signals which will result in a network prediction, where after the gradient

values for the ReLU activation functions are stored. The second and third part of the signal sequence are responsible for updating crossbar 2 (CB2) and crossbar 1 (CB1), respectively. The error, calculated in the first sequence, is propagated backwards through the crossbars by applying the correct mode of operation. The update channels can then be used to apply the update to each crossbar, using the signal duration as learning rate.

4.6.5 Impact weight initialization

Due to the stochastic behavior of the backpropagation algorithm the neural network is not always able to find the global minimum and depends on the weight initialization. Supporting Fig. 4.S9 shows the decision boundaries for various epochs between 0 and 10. Epoch 0 shows that all the weights are close to zero before training. After the first update cycle (epoch 1) all the weights have a value such that the output is always negative (accuracy = 50%) classifying class 0. After a few more epochs the weights are updated and reach an accuracy of 75% at epoch 5. The weights continue to update but after 10 epochs the output accuracy remains 75% and the network is unable to correctly classify the data points at $(-0.3, 0.3)$ as class 1. This inaccuracy is the results of the network being stuck in a local minimum. As discussed in section 4.3.1, when dealing with a small number of neurons the probability that the network encounters a local minimum is significant and the success of the neural network training strongly depends on the weight initialization. In the simulation we decreased this probability by increasing the amount of neurons in the hidden layer to 7 such that the network is able to select the useful weights. Since we are limited by the dimensions of the designed crossbar we can only use 2 neurons for this demonstration. Restarting the training process and re-initializing of the weights can lead to different results such as in Fig. 4.7.

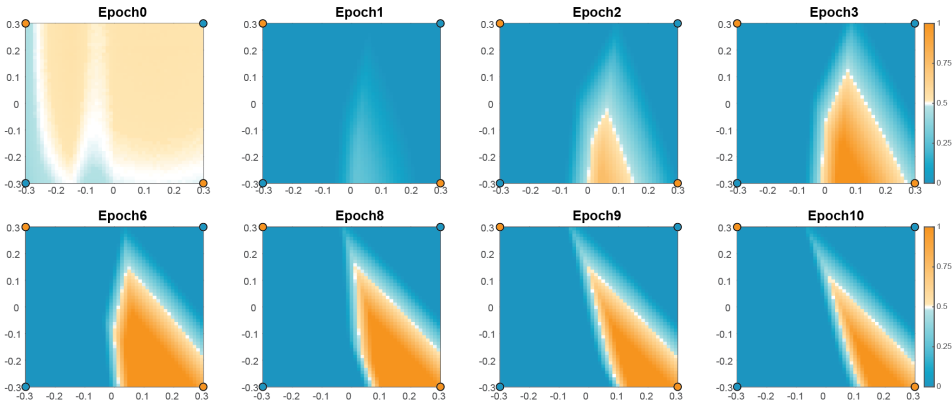


Figure 4.S9: Decision boundaries for a 2-layer classification after weight initialization (Epoch 0) and after various epochs. For the evaluation of the decision boundaries the output values are recorded while sweeping over the input values from -0.3V to 0.3V in a grid of 50×50 . Blue and orange data points represent class 0 and 1 ($\sigma = 0$).

4.6.6 Discussion hardware classification performance

Successful operation of neural networks both hardware as well as software require fine tuning of the hyperparameters. The first consideration is signal strength throughout multiple layers (in software referred to as vanishing signals). While the input to the first layer is normalized (in software) the output of the first layer is orders of magnitude lower due to the multiplication of the weight value (~ 0.1 mS range). In software the output signal in between layers can be normalized, while in hardware we implemented an amplification factor that requires careful tuning. If the amplification factor is too small the signals throughout the layers will vanish and only noise will have an impact on the system. On the other hand, if the amplification factor is too large the devices will break down. Furthermore, since the output value is an accumulation of all the currents in the column the amplification depends on the amount of neurons and on the conductance range of each EC-RAM. The same is true for the backflowing error, which vanishes throughout the multi-layer neural network if the amplification between layers is too small. The output of the backflowing error is accumulated over all currents in a row, and its optimum amplification can thus be different from the forward signal amplification. Another parameter that requires optimization is the activation function, in particular the one of the output layer. We have implemented a linear sigmoid that scales the output values to a prediction with a certain probability, and allows to differentiate between different error strengths. We can define its boundaries such that the error of correct predictions contributes more or less to the total error by increasing or decreasing the boundaries of the sigmoid, respectively. For example by decreasing the boundaries the slope of the sigmoid increases which means that small variations in the output results in a large impact on the error while an output voltage (larger than defined boundary), results in a maximum output and if this prediction is correct, does not contribute to the error. If the boundary is set too small (set to zero it becomes a Heaviside step function), the error is unable to differentiate between the output since after the activation function all outputs will be binary, resulting in either a maximum error or no error value.

Author contributions

Eveline van Doremaele and TS initiated the idea. TS performed the experiments with active involvement as well as experimental contribution of **Eveline van Doremaele**. **Eveline van Doremaele** fabricated the devices. SR and MF designed the electronic circuit. TS performed the simulations. YvdB supervised the project.

Bibliography

1. Agarwal, S. *et al.* Resistive memory device requirements for a neural algorithm accelerator. in *2016 International Joint Conference on Neural Networks (IJCNN)* ISSN: 2161-4407 (July 2016), 929–938.
2. Agarwal, S. *et al.* Energy Scaling Advantages of Resistive Memory Crossbar Based Computation and Its Application to Sparse Coding. *Frontiers in Neuroscience* **9**. ISSN: 1662-453X (2016).
3. Hu, M. *et al.* Memristor-Based Analog Computation and Neural Network Classification with a Dot Product Engine. en. *Advanced Materials* **30**. _eprint: <https://onlinelibrary.wiley.com/doi/pdf/10.1002/adma.201705914>, 1705914. ISSN: 1521-4095 (2018).
4. Ambrogio, S. *et al.* Equivalent-accuracy accelerated neural-network training using analogue memory. en. *Nature* **558**, 60–67. ISSN: 1476-4687 (June 2018).
5. Kadetotad, D. *et al.* Parallel Architecture With Resistive Crosspoint Array for Dictionary Learning Acceleration. *IEEE Journal on Emerging and Selected Topics in Circuits and Systems* **5**. Conference Name: IEEE Journal on Emerging and Selected Topics in Circuits and Systems, 194–204. ISSN: 2156-3365 (June 2015).
6. Yao, P. *et al.* Face classification using electronic synapses. en. *Nature Communications* **8**. Number: 1 Publisher: Nature Publishing Group, 15199. ISSN: 2041-1723 (May 2017).
7. Keene, S. T. *et al.* Optimized pulsed write schemes improve linearity and write speed for low-power organic neuromorphic devices. en. *Journal of Physics D: Applied Physics* **51**. Publisher: IOP Publishing, 224002. ISSN: 0022-3727 (May 2018).
8. Melianas, A. *et al.* Temperature-resilient solid-state organic artificial synapses for neuromorphic computing. en. *Science Advances* **6**, eabb2958. ISSN: 2375-2548 (July 2020).
9. Felder, D. *et al.* Coupled Ionic–Electronic Charge Transport in Organic Neuromorphic Devices. en. *Advanced Theory and Simulations* **n/a**. _eprint: <https://onlinelibrary.wiley.com/doi/pdf/10.1002/adts.202100492>, 2100492. ISSN: 2513-0390 (2022).

10. Gao, L. *et al.* [Fully parallel write/read in resistive synaptic array for accelerating on-chip learning](#). en. *Nanotechnology* **26**. Publisher: IOP Publishing, 455204. ISSN: 0957-4484 (Oct. 2015).
11. Mackin, C. *et al.* [Optimised weight programming for analogue memory-based deep neural networks](#). en. *Nature Communications* **13**. Number: 1 Publisher: Nature Publishing Group, 3765. ISSN: 2041-1723 (June 2022).
12. Fuller, E. J. *et al.* [Parallel programming of an ionic floating-gate memory array for scalable neuromorphic computing](#). en. *Science*, eaaw5581. ISSN: 0036-8075, 1095-9203 (Apr. 2019).
13. Li, C. *et al.* [Efficient and self-adaptive in-situ learning in multilayer memristor neural networks](#). en. *Nature Communications* **9**. Number: 1 Publisher: Nature Publishing Group, 2385. ISSN: 2041-1723 (June 2018).
14. Wright, L. G. *et al.* [Deep physical neural networks trained with backpropagation](#). en. *Nature* **601**. Number: 7894 Publisher: Nature Publishing Group, 549–555. ISSN: 1476-4687 (Jan. 2022).
15. Yao, P. *et al.* [Fully hardware-implemented memristor convolutional neural network](#). en. *Nature* **577**. Number: 7792 Publisher: Nature Publishing Group, 641–646. ISSN: 1476-4687 (Jan. 2020).
16. Wan, W. *et al.* [A compute-in-memory chip based on resistive random-access memory](#). en. *Nature* **608**. Number: 7923 Publisher: Nature Publishing Group, 504–512. ISSN: 1476-4687 (Aug. 2022).
17. Hinton, G. *The Forward-Forward Algorithm: Some Preliminary Investigations* en. arXiv:2212.13345 [cs]. Dec. 2022.
18. Alibart, F., Zamanidoost, E. & Strukov, D. B. [Pattern classification by memristive crossbar circuits using ex situ and in situ training](#). en. *Nature Communications* **4**. Number: 1 Publisher: Nature Publishing Group, 2072. ISSN: 2041-1723 (June 2013).
19. Prezioso, M. *et al.* [Training and operation of an integrated neuromorphic network based on metal-oxide memristors](#). en. *Nature* **521**, 61–64. ISSN: 1476-4687 (May 2015).
20. Hasan, R. & Taha, T. M. *Enabling back propagation training of memristor crossbar neuromorphic processors*. in *2014 International Joint Conference on Neural Networks (IJCNN)* ISSN: 2161-4407 (July 2014), 21–28.
21. Lim, S. *et al.* [Adaptive learning rule for hardware-based deep neural networks using electronic synapse devices](#). en. *Neural Computing and Applications*. ISSN: 0941-0643, 1433-3058 (July 2018).

22. Karakiewicz, R., Genov, R. & Cauwenberghs, G. 1.1 TMACS/mW Fine-Grained Stochastic Resonant Charge-Recycling Array Processor. en. *IEEE Sensors Journal* **12**, 785–792. ISSN: 1530-437X, 1558-1748, 2379-9153 (Apr. 2012).
23. Cheng, Z., Soudry, D., Mao, Z. & Lan, Z. *Training Binary Multilayer Neural Networks for Image Classification using Expectation Backpropagation* en. arXiv:1503.03562 [cs]. Mar. 2015.
24. Soudry, D., Castro, D. D., Gal, A., Kolodny, A. & Kvatinsky, S. Memristor-Based Multilayer Neural Networks With Online Gradient Descent Training. *IEEE Transactions on Neural Networks and Learning Systems* **26**. Conference Name: IEEE Transactions on Neural Networks and Learning Systems, 2408–2421. ISSN: 2162-2388 (Oct. 2015).

Chapter 5

Organic neuromorphic spiking circuit for retina-inspired sensory coding and neurotransmitter-mediated neural pathways

The fundamental mechanisms of signal communication within the human body rely on the spiking frequency of action potentials.[1, 2] Through biological receptors and afferent neuronal cells, stimuli from the external world are encoded into a spiking pattern and transmitted to the central nervous systems where they are processed via interneurons. Replicating the interdependent functions of receptors, afferent neurons and interneurons with spiking circuits [1], sensors[3] and biohybrid synapses[4] is an essential first step towards merging neuromorphic circuits and biological systems, crucial for computing at the biological interface. We present a novel adaptive spiking circuit that replicates afferent neurons sensory coding from external physical stimuli. We emulate the neuromodulatory activity of interneurons by associating the spiking circuit with biohybrid synapses demonstrating an interdependent chemical synaptic connection. To establish a full neuronal pathway, we combine these key biological functions, showing the signal transduction from light stimulus to spiking frequency and to dopamine-mediated plasticity: a retinal pathway primitive.

This chapter is based on *Organic neuromorphic spiking circuit for retina-inspired sensory coding and neurotransmitter-mediated neural pathways*, Giovanni Maria Matrone*, **Eveline R. W. van Doremaele***, Sophie Griggs, Gang Ye, Iain McCulloch, Francesca Santoro, Yoeri van de Burgt, *In submission*

5.1 Introduction

Neuromorphic electronics is currently experiencing a huge increase in research activity. Inspired by neuroscience, it aims to mimic the architecture of the human brain to enable parallel computing with high energy efficiency[1, 2] and local processing[3], which advances edge-computing[4], smart robotics[5, 6] and intelligent systems interfacing with the human body[7, 8]. However, establishing an active interaction with biological tissues, especially with the central nervous system, requires adaptive computing systems that are not only able to receive biologically encoded inputs but also to process and communicate these. The complex sensory systems in the human body share a coding mechanism based on the frequency modulation of action potentials[1]. The physical perception starts with millions of highly specific sensory receptor cells which respond to definite stimuli at distinct locations on the body. The intensity over time of an external stimulation is first converted into a receptor potential and then encoded in the firing frequency of (afferent) neurons. The direct dependence of spikes frequency on the magnitude of the stimulus is generally referred to as sensory coding. The sensory information is then transmitted to the central nervous system where it is processed through a complex network of inhibitory/excitatory interneurons that work as computing units by modulating the spiking frequency in parallel. The circuitual design of current spiking circuits is predominantly based on inorganic materials, particularly on silicon-based devices[9]. However, neuromorphic applications operating at the biointerface clearly favour organic materials[2]. Next to their soft and flexible properties, high tunability and low operational voltage, organic mixed ion-electron conductors conduct both electrons and ions[10]. This mixed conduction allows organic materials to closely match the operating timescales of their biological counterparts[11] and mimic ion-based biological functions such as neuronal ion-flux communication and neurotransmitter-receptor binding[2], which are required to interact with biological tissues and to design adaptive bio-interfaces[12]. Recently, organic materials have been employed to build electronic circuits that mimic the spiking behaviour of neurons[13, 14]. Despite processing complex sensorial input[15], these systems still lack mechanisms to modulate the encoded signal[16]. Organic materials can be used to recreate a neuronal network that in nature relies on the cooperation of spiking elements (afferent neurons and interneurons) and non-spiking elements such as mechano-chemical sensors (receptors), as well as neuromodulator junctions (chemical synapses). We prove this concept by fabricating a neuromorphic spiking circuit which comprises different bioelectronics devices to emulate the interwoven biological functions of retinal sensory coding. The adaptable organic neuromorphic spiking circuit (see Fig. 5.1a) is able to replicate the spiking activity of both afferent neurons (sensory coding) as well as interneurons (neuromodulation). The circuit (see Fig. 5.1b) consists of an organic capacitor (PEDOT:PSS[17]), a resetting electrochemical transistor (P-3O[18]) and a pair of ambipolar inverters (p(C4-T2-C0-EG)[19]), comprising four organic electrochemical transistors (OECTs). This system works both as an afferent neuron receiving external stimuli such as light or pressure, as well as an interneuron by receiving input from a biohybrid synapse[20]. This input potential activates the neuromorphic spiking circuit by charging the capacitor. When the capacitor output reaches the transition voltage of the inverter pair, the voltage inversion triggers the resetting OECT which allows the capacitor to discharge and start the next cycle. The circuit and individual device characteristics can be found in Supporting Information 5.S1.

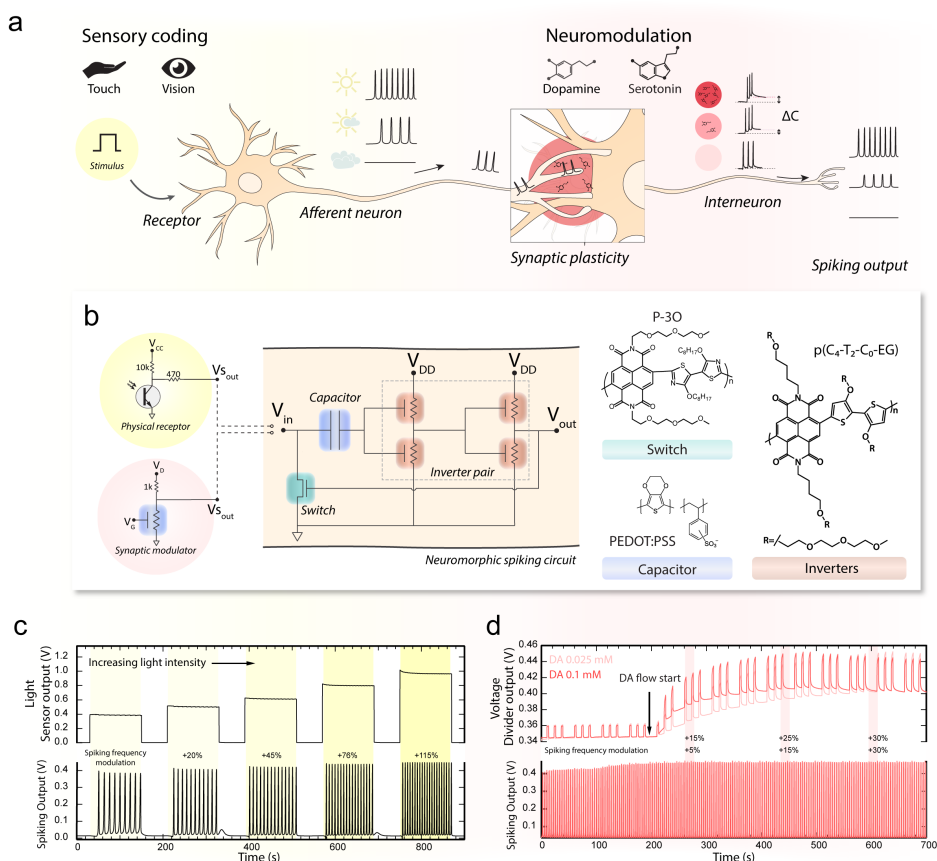


Figure 5.1: Neuromorphic spiking circuit emulating sensory coding and neuromodulation. a) Illustration representing sensory coding of visual (and tactile) senses by the afferent neuron and neuromodulation using dopamine (and serotonin) by the interneuron. b) Schematic of the neuromorphic spiking circuit consisting of a capacitor, inverter pair and switch with its corresponding active materials. For sensory coding a physical receptor is connected and for neuromodulation a synaptic modulator circuit is employed. c) Sensory coding of light using an ambient light sensor as physical receptor showing an increasing spiking frequency output with increasing sensor output. Frequency output is with respect to the first spiking frequency (0.08 Hz). d) Neuromodulation with dopamine using the synaptic modulator circuit showing the modulation of spiking frequency depending on the dopamine concentration. The frequency modulation is in percentage (top, high DA concentration and bottom, low DA concentration) with respect to the spiking frequency of PBS (0.22 Hz)

Figure 5.1c demonstrates the sensory coding of light stimuli (see Supporting Information 5.3.2 for sensory coding of pressure stimuli). We connect a commercial light sensor that replicates the function of the cones in the retina, transducing different light intensities to specific receptor potentials that are used as the input to the neuromorphic circuit, thus emulating afferent neurons. Each input generates a train of voltage spikes with a characteristic

frequency ranging from 0.08 Hz to 0.18 Hz (Supporting Information 5.3.6) leading to a maximum 115% modulation. Although afferent neurons are fundamental for sensory coding they represent only a small proportion of human neurons, while interneurons represent the 99% of the total[21]. Besides being responsible for transmitting the signal between different areas of the brain, their crucial task is to locally modulate the spiking pattern through different neuromodulators at chemical synapses. Our neuromorphic spiking circuit is also able to mimic neuromodulation by an interneuron using dopamine. Dopamine (DA) is a well-known neuromodulator essential for motor control functions, rewards, and addiction[22]. In addition, recent studies have addressed its involvement in information processing, neurogenesis and diurnal patterns showing how this neurotransmitter influences sensory coding systems[23]. We replicate the interneuron connection to a neighbouring neuron by introducing an organic neuromorphic device within a voltage divider circuit as a synaptic modulator (see Fig. 5.1a). This neuromorphic device adopts an OECT-like configuration, as previously reported (see Supporting Information 5.3.3), and its conductance can be modulated in a volatile way upon ion injection by a train of gate voltage pulses. When an electro-active neurotransmitter, such as dopamine or serotonin (5-HT), is present in the electrolyte, the oxidation of these species leads to a non-volatile conductance modulation. To mimic dopamine mediated plasticity, the synaptic modulator is connected to the neuromorphic spiking circuit. A voltage pulse greater than the oxidation potential of dopamine ($V_{ox_{DA}} > 0.3V$) is applied to the gate of the OECT, a non-volatile change in conductance induced, resulting in a modulation of the synaptic modulator output voltage. The spiking circuit receives this variable output voltage and alters the spiking frequency accordingly. Figure 5.1d shows the modulation of the spiking frequency over time for two different concentrations of dopamine, 0.025mM (light red) and 0.1mM (dark red), respectively. After 200s, dopamine is introduced in the system so that the output of the synaptic modulator gradually increases from 0.35V to 0.40V, and as a result, the spiking frequency shows a 36% increase at $t=600s$ with a different temporal evolution for the two concentrations. In contrast to the previous afferent neuron where a light stimulus directly generates a spiking pattern, here the presence of dopamine regulates the frequency of interneuronal spikes arriving from a previous neuron in the circuit. Furthermore, the temporal modulation depends on the dopamine concentration similar to the biological mechanism of synaptic plasticity[15]. Thus, this circuit is able to replicate the functions of a single neuron and its chemical synapse. However, biological processors require a collective set of computing elements (neurons) to operate. In the human brain, every single neuron computes the spikes received from many interneuron connections and fires a spiking output if the sum of the input stimuli has reached a specific threshold[21]. Neural pathways, the connections formed by an axon and its synapse, link neurons from different locations and enable the transmission of signals from one region of the nervous system to another[24]. We attempt to replicate a neural pathway by coupling two interneuron synapses. The first synapse is located on the “sending neuron” and receives an external signal that needs to be computed and transmitted to the second synapse which is connected to the “receiving neuron” (see Fig. 5.2a). The input signal consists of periodic voltage pulses and represents the spikes generated by the neuromorphic spiking circuit (neuron) that activate the neuromodulation. We selected the neurotransmitters dopamine and serotonin due to their well-known involvement in cognitive and behavioural functions, including mood and reward. Moreover, dopaminergic and serotonergic neurons are often interwoven through interneuron connections even if located in different brain areas[25].

Here we prove that the connected synapses are able to replicate the dependency of dopamine expression on the activity of serotonergic neurons[26]. The serotonin and dopamine mediated synapses are connected through an electronic circuit, which adopts the same voltage divider-configuration as the synaptic modulator (Fig. 5.1a) with the addition of an organic electronic switch (see Supporting Information 5.3.4 and 5.3.5). The switch in this circuit is a p(C4-T2-C0-EG)-based OECT. The sending neuron (serotonin) receives the pre-synaptic input voltage, and its output triggers the switch which regulates the signal transmission to the receiving neuron (dopamine). Figure 5.2b visualizes the activity of the neural pathway by monitoring the output of the sending neuron (Fig. 5.2bi), and the input voltage and the conductance of the receiving neuron (Fig. 5.2b ii and iii).

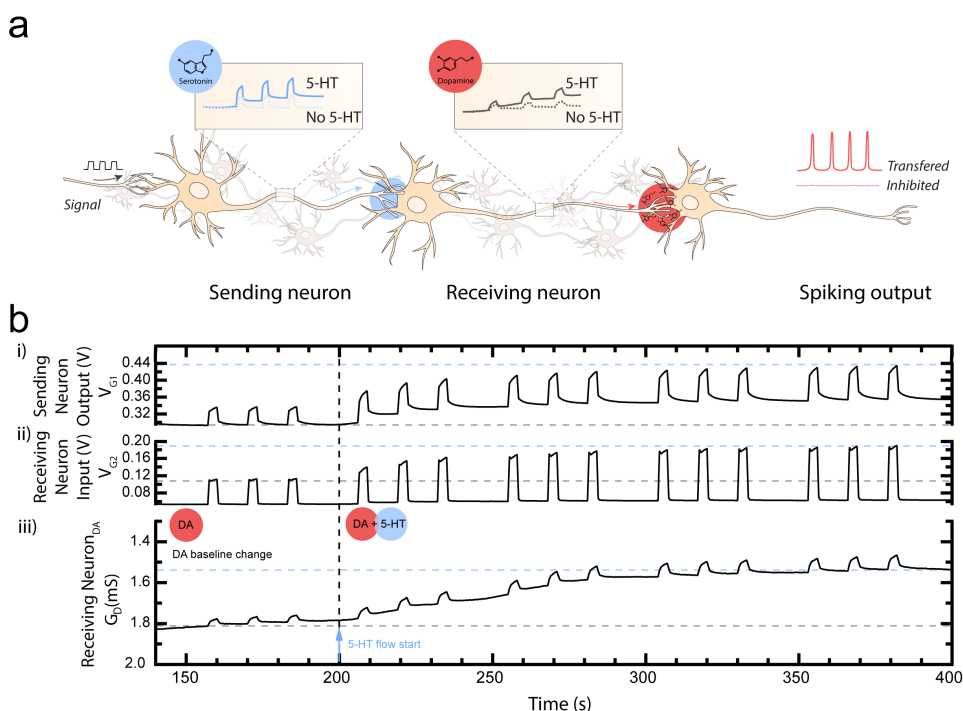


Figure 5.2: Neural pathway of two coupled synapses. a) Illustration of the neural pathway between the sending serotonergic neuron and receiving dopaminergic neuron. b) i. Output voltage of the sending neuron, ii. Input voltage of the receiving neuron, iii. Conductance modulation of the receiving neuron

During the measurement (see Supporting Information 5.3.5 for data before $t=140s$) the receiving neuron is placed in a dopamine-rich environment (0.025 mM) while the serotonin concentration affecting the sending neuron is variable. In the first time-window (140-200s) the serotonergic neuron is active (i.e., a voltage pulse train is applied to the gate of this device to replicate neural spikes), but the neurotransmitter is absent in the microfluidic module. In this initial condition, the output (0.3 – 0.32 V, Fig. 5.2bi) from the voltage divider (post-synaptic pulses of the sending neuron) is below the turn-on voltage of the switch. As a result,

the input signal received by dopaminergic synapse and its neuron is low (0.1 V, Fig. 5.2b ii) and emulates the biological scenario where a serotonin neuron inhibits the modulation of the dopamine synapse. At $t=200$ s, a 0.05mM serotonin solution is introduced in the microfluidic module of the first synapse. This activates the neural pathway excitatory functions as the oxidation of serotonin causes a decrease in the conductance of the OEET which allows the voltage divider output to increase (up to 0.44V, Fig. 5.2bi) and to turn on the switch. Now, the periodic voltage pulses of 0.2 V (Fig. 5.2bii) trigger the partial oxidation of dopamine on the receiving neuron and modulate the conductance of the synapse. After 300s, the conductance modulation saturates, limited by the dynamic range of the OEET (Fig. 5.2biii). This shows that the conductance modulation of the second synapse, mediated by dopamine, is strictly controlled by the modulation of the serotonin mediated synapse as activated by the sending neuron. The periodic voltage pulses (external input signal of sending neuron) can be replaced with the voltage spikes from the neuromorphic spiking circuit, establishing a full, direct connection that replicates the function of an interneuron or an afferent neuron. To demonstrate the latter, we aim to combine both neuronal functionalities (sensory coding and neuromodulation) in the organic neuromorphic circuit adopting the retina as a biological system model. As shown in Fig. 5.1c the light intensity can be encoded in the spiking frequency so it can be sent to higher order computing units (e.g., through the optic nerve to the central nervous system). The power of the retina resides in its “in-sensor” functions, performed by the close-interaction of bipolar cells and amacrine cells. This allows the signal reaching the inner retina to be highly pre-processed, reducing the power consumption and increasing computing performance[27]. Some crucial steps in the pre-processing of visual information such as shape recognition and light adjustment mechanisms, only occur through the local action of neuromodulators, including dopamine[21]. The synthesis and activity of this neurotransmitter in dopaminergic amacrine cells (acting as interneurons), spike in response to light onset[28]. To mimic this in our artificial retina prototype, the light-induced spiking pattern modulates the synaptic plasticity of a chemical synapse that is mediated by dopamine (Fig. 5.3a).

In Fig. 5.3bi the light sensor is exposed to two light conditions (low and high intensity) that correspond to two levels of receptor potential which have been employed to trigger spike trains of increasing frequencies (see Supporting Information 5.3.6). These spike patterns induce a permanent plasticity modulation of the synapse through the mechanisms described in Supporting Information 5.3.3 and 5.3.6, depending on the concentration of dopamine present in the electrolyte (0.025 mM and 0.1 mM). To de-couple the role of dopamine concentration on the spiking frequency, for each light condition, an input length triggering three spikes have been selected. Both the concentration of dopamine and the intensity of light (spiking frequency) affect the synaptic plasticity (Fig. 5.3b ii). In the low light condition the lowest dopamine concentration (0.025 mM) leads to a 0.10 mS synaptic modulation, while the highest dopamine concentration (0.1 mM) results in a 0.20 mS modulation (Fig. 5.3b ii). Increasing the ambient light intensity, the synaptic modulations shift to 0.12 mS and 0.23 mS modulation for the lowest and highest dopamine concentrations, respectively. The same set of light conditions is repeated, proving that a similar synaptic modulation is achieved, even though the baseline of the synaptic conductance has shifted due to the previous modulations. The neuromorphic system enables the transduction of the ambient light intensities to a voltage

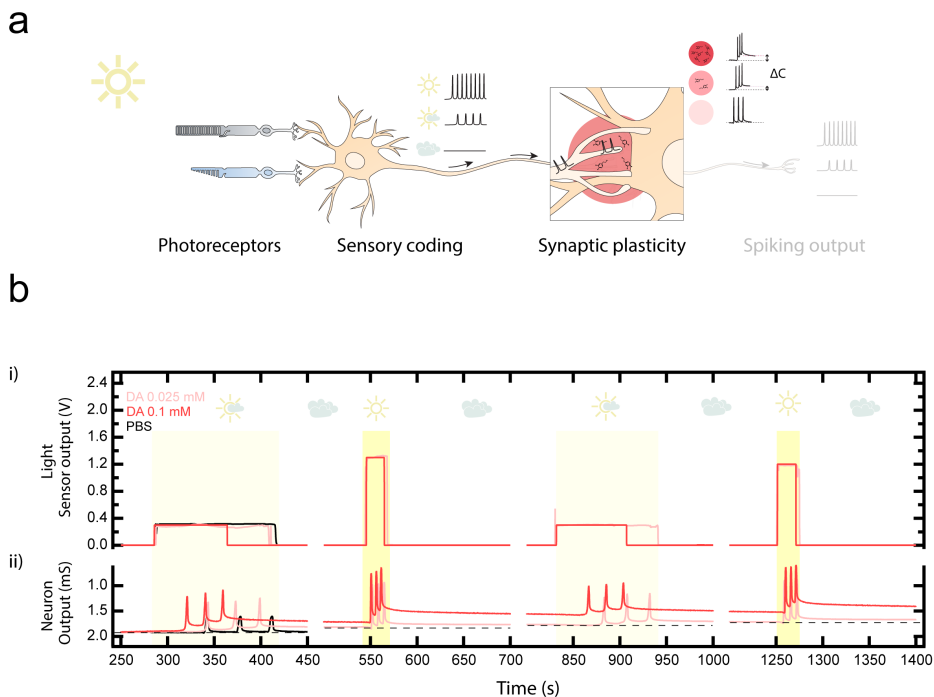


Figure 5.3: Combining sensory coding and neuromodulation in a neuromorphic artificial retina. a) Illustration of the neural pathway of the retina starting with photoreceptors transducing light intensity to spiking frequency (sensory coding) followed by the frequency modulation (neuromodulation) at the synapse mediated by dopamine. b) Voltage output of the light sensor (i) for different light conditions and corresponding neuron output (ii) comparing 2 concentrations of dopamine (0.025mM light and 0.1mM dark red).

potential and subsequently to a precise spike pattern which translates to specific synaptic modulations. As such, this biohybrid synapse can retain the information it has received and is able to adjust it based on the spiking pattern: a key to replicate the biological photic regulation mediated by retinal dopamine.

The chemically-adaptive neuromorphic spiking circuit presented in this work constitutes a fundamental building block for programmable neural pathways that can locally transduce and process both physical as well as physiological environmental information, an essential step towards realizing processors at the biohybrid interface. We envision integrating novel algorithms to perform organ-specific computing functions realising adaptive biohybrid bridges between (damaged) pre- and high order processing biological units.

5.2 Methods

5.2.1 p(C4-T2-C0-EG) devices fabrication

The p(C4-T2-C0-EG) was synthesized by McCulloch group (see Supporting Information 5.3.1)[29]. The material solutions were prepared in chloroform at the concentration of 20 mg mL⁻¹. As substrates, interdigitated microelectrodes IDA-Au-6 (channel length L 5 μ m, individual channel width, w, 1.8 mm, number of pairs 30, number of channels, n, 59, total channels width, W = n \times w = 10.62 cm) were purchased from MicruX technologies. The interdigitated microelectrodes were pre-treated with UV ozone over 15 min. The polymer solutions were spin-coated at 500 rpm for 60 s to fabricate the OECT comprising the inverter of the spiking circuit. The polymer solutions were spin-coated at 200 rpm for 60 s (no post-processing treatment) to fabricate the OECT comprising the switch element of the spiking circuit.

5.2.2 P-3O devices fabrication

The P-3O was synthesized by Gang Ye and the material solutions were prepared in chloroform at the concentration of 5 mg mL⁻¹. As substrates, interdigitated microelectrodes IDA-Au-6 (channel length L 5 μ m, individual channel width, w, 1.8 mm, number of pairs 30, number of channels, n, 59, total channels width, W = n \times w = 10.62 cm) were purchased from MicruX technologies (SPAIN). The interdigitated microelectrodes were pre-treated with UV ozone over 15 min. The polymer solutions were spin-coated at 1000 rpm for 30 s.

5.2.3 Biohybrid synapse and capacitor fabrication

The neuromorphic devices (constituting the biohybrid synapse and capacitor elements) were fabricated on glass-ITO patterned substrates purchased from Xin Yan Technology Ltd. The size of the glass square substrates is 25mm with patterned squares of ITO (20ohm sq⁻¹) of 10 mm covering each corner. Substrates were cleaned through sonication in IPA (Sigma-Aldrich, USA) for 20 min. Employing Kapton tape and using a PMMA master mask, 2 stripes connecting opposed ITO squares (with fixed width 5mm) were traced for the deposition of the polymer mixture. PEDOT:PSS (Hereaus, Clevios PH 1000) aqueous solution was prepared by adding 6 vol.% ethylene glycol (Sigma-Aldrich, USA) to increase the PEDOT:PSS conductivity, 0.1 vol.% dodecylbenzene sulfonic acid (Sigma-Aldrich, USA) as a surfactant, and 1 vol.% (3-glycidyloxypropyl)trimethoxysilane (Sigma-Aldrich, USA) as a crosslinking agent to improve mechanical stability. PEDOT:PSS solution was spun on the selected areas of the substrate at 1000 rpm for 2 min and baked at 120 °C for 20 min. Before operation the devices were conditioned at least 20 min in PBS solution, in order to avoid swelling effects during electrical measurements.

5.2.4 Neurotransmitters solutions preparation

Neurotransmitter solutions were freshly prepared by dissolving dopamine hydrochloride (98%, Sigma-Aldrich, USA) and serotonin hydrochloride (98%, Sigma-Aldrich, USA) into

Dulbecco's Phosphate Buffered Saline (Modified, without calcium chloride and magnesium chloride, Sigma-Aldrich, USA) at multiple concentrations ranging from 0.01mM to 0.1 mM.

5.2.5 Spiking circuit connections

The individual devices composing the spiking circuit (see also Supporting Information 5.3.1) were connected using needle probes and the input/output voltage were coupled through direct BNC cable connections. For connection with the 5 MicruX substrates i.e. the ambipolar inverter pair (four p(C4-T2-C0-EG) OECTs) and the P-3O switch device, a commercial contact box was employed, fabricated by MicruX technologies (SPAIN), to establish a reliable contact to the source and drain. An Ag/AgCl pellet was used as the gate electrode.

5.2.6 Electrical measurements

The individual devices and the spiking circuit were characterized using ARKEO multichannel developed by Cicci Research (Italy). The system comprises a thermal controlled stage, two microfluidic pumps and eight-channel source meter units, respectively. Each device of the circuit was operated and monitored through one of the available channels of this system. Needle probes were used to access the ENODE's gate and drain electrodes.

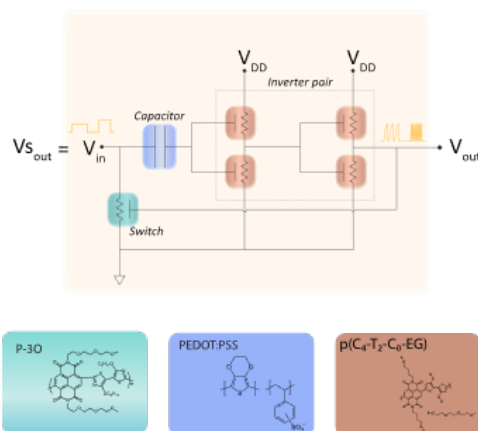


Figure 5.S1: Schematic illustrating the neuromorphic spiking circuits connections, highlighting the different materials used to fabricate the different electronic components. In green the P-3O-based OECT used as an electronic switch, in blue the PEDOT:PSS-based capacitor and in orange the p(C4-T2-C0-EG)-based OECTs composing the inverter pairs.

5.3 Supporting Information

5.3.1 Spiking circuit

In this section the devices and materials that compose the spiking circuits (Fig.5.1 and Supporting Fig.5.S1) are presented and the single device voltage and transfer characteristics are displayed (Supporting Figs. 5.S2 - 5.S5). The spiking circuit features a capacitor (PEDOT:PSS OECT) which receives the external input in forms of voltage potential charging from 0 to 0.26 V (see Supporting Fig.5.S5). A 330 kOhm resistor is used to connect the capacitor to the V_{in} . The capacitor is connected to the ground through a switch device (series connection through the channel terminal of this device). The switch (P-3O OECT) opens and closes the ground connection of the capacitor depending on its resistance (Supporting Fig.5.S4). The switch device is in ON/OFF state depending on the voltage applied to its gate terminal and allows the capacitor to charge and discharge (Supporting Fig.5.S5). The inverter pair of the neuromorphic circuits are constituted by four identical p(C4-T2-C0-EG) OECTs. p(C4-T2-C0-EG) is an ambipolar material so the inverter of these OECTs can behave both as n-type and p-type transistors (Supporting Fig.5.S2).

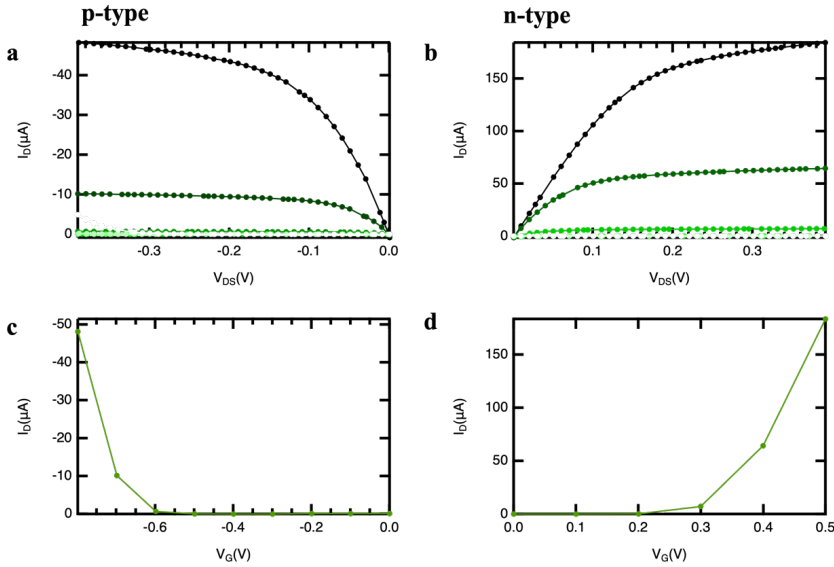


Figure 5.S2: p(C4-T2-C0-EG) transfer and output curves for both n-type and p-type behaviors. a) p-type output curve V_G from 0 to -0.8 V (step-size 0.1V). b) n-type output curve V_G from 0 to 0.4 V (step-size 0.1V). c) p-type transfer curve at $V_{DS} = -0.1$ V. d) n-type transfer curve at $V_{DS} = 0.1$ V.

To the first inverter a $VDD_1 = 0.5$ V is applied, while on the second inverter $VDD_2 = 0.8$ V is applied. The VDD unbalance was introduced to optimize the double-stage inverter realizing a sharper inversion point (increasing the gain and the inversion range of the second inverter)

which is key to replicate neural spikes. When the capacitor charge reaches the inverters threshold (0.3 V) the first inverter characteristic voltage, due to the low VDD_1 , moves from 0.3 to 0 V (Supporting Fig.5.S3, top panel). The second inverter, receiving as input voltage the output of the first inverter, displays a characteristic curve with an inversion point (0.26 V) with the voltage moving from 0 to 0.7 V (Supporting Fig.5.S3, bottom panel). The output terminal of the double stage inverter is connected to the gate terminal of the switch device so that the voltage inversion (0 to 0.7 V) of this system modulate the change of the state of the switch from OFF to ON (Supporting Fig.5.S4). When the switch is in the ON state the connection to the ground is closed and the capacitor discharges to 0V, allowing a new cycle to start.

Supporting Fig.5.S6 shows a frequency modulation experiment with relevant parameters reported in Table 5.S1. In this case the capacitor was directly connected to an external voltage supplier and the voltage input was increased from 0.3 to 0.6V (0.05 V step).

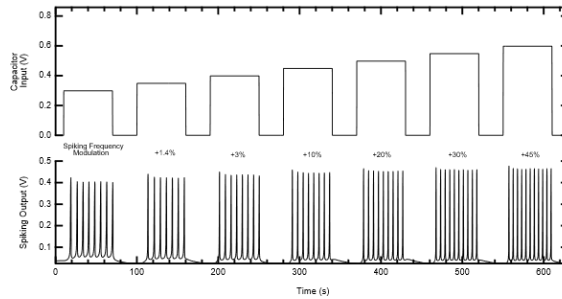


Figure 5.S6: The voltage spikes (bottom) generated by the neuromorphic circuit responding to different voltages applied (top), through an external voltage supplier), directly to the capacitor element. In between top and bottom panels, the spiking frequency change (in percentage) corresponding to each spike pattern-voltage pair is reported.

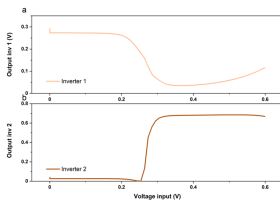


Figure 5.S3: Ambipolar inverter characteristics for both single and double stage inverters.

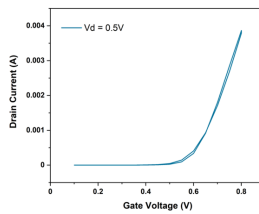


Figure 5.S4: P-3O transfer curve.

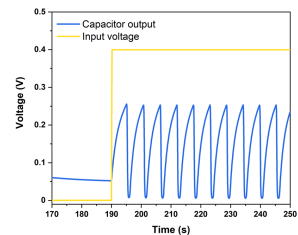


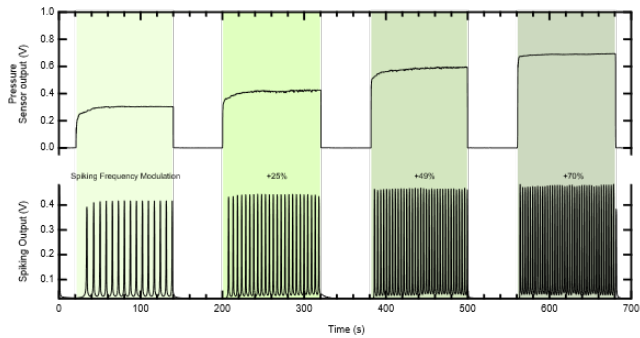
Figure 5.S5: Capacitor characteristic.

Table 5.S1: Spikes modulation data as extracted from the trace in Supporting Fig.5.S6.

Capacitor Input (V)	Spikes timing (s)	Frequency (Hz)	Change (%)
0.3	7	0.14	0.00
0.35	6.9	0.145	1.45
0.4	6.8	0.15	2.94
0.45	6.4	0.16	9.38
0.5	5.9	0.17	18.64
0.55	5.4	0.19	29.63
0.6	4.8	0.21	45.83

5.3.2 Sensory coding with pressure sensor

In this section we describe in detail the mechanisms of coupling of the commercially available force sensor (Grove-Round Force Sensor, FSR402, see Supporting Fig.5.S7) to the neuromorphic spiking circuit. The results of the spiking activity are presented in Supporting Fig.5.S8. The pressure sensor is a force sensitive module with at the end a round force sensitive resistor (R_{FSR}). This resistance depends on the pressure applied to this resistor: the greater the pressure, the smaller the resistance. Output voltage is equal to: $V_{out} = \frac{R_M \cdot V_{CC}}{R_M + R_{FSR}}$, where the measuring resistor $R_M = 30 \text{ k}\Omega$ and the supply voltage $V_{CC} = 1\text{V}$.

**Figure 5.S7:** Figure of the Grove-Round Force Sensor (FSR402).**Figure 5.S8:** Sensory coding of touch using the force sensor as physical receptor showing an increasing spiking frequency output with increasing sensor output voltage.

We connect the force sensor that replicates the behavior of biological skin receptors by transducing a set of pressure stimuli (i.e. the weight of four different objects) into voltage potentials that are used as the input to the neuromorphic circuit (afferent neuron). Each input generates a train of voltage spikes with a characteristic frequency as reported in Table 5.S2. The spiking frequency (ranging from 0.14Hz to 0.35Hz) shows a linear response to the pressure stimuli emulating the biological mechanism of conscious sensation on the skin of the

hand where receptors are programmed to respond to different pressures by featuring specific thresholds (Supporting Fig. 5.S9 and 5.S10).

Table 5.S2: Spikes modulation data as extracted from the trace in Supporting Fig. 5.S8.

Mass (g)	Pressure Sensor Output (V)	Spikes timing (s)	Frequency (Hz)	Change (%)
55	0.3	7	0.14	0.00
67	0.41	5.6	0.18	25.00
87	0.59	4.7	0.21	48.94
116	0.69	4.1	0.24	70.73

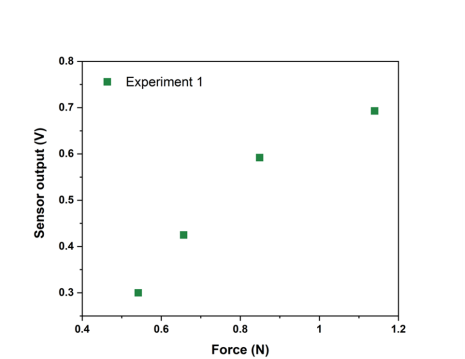


Figure 5.S9: Relationship of the sensor output voltage and the applied force after placing 4 ob-
jects with a weight varying from 55g to 116 g.

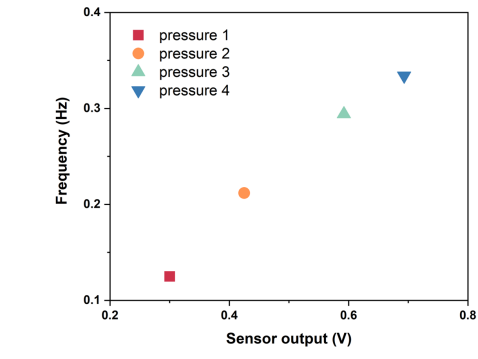


Figure 5.S10: Output spiking frequency of the
spiking neuron with depending on the pres-
sure sensor output voltage corresponding to the
weights ranging from 55g to 116 g.

5.3.3 Bio-hybrid synapse and its synaptic modulation

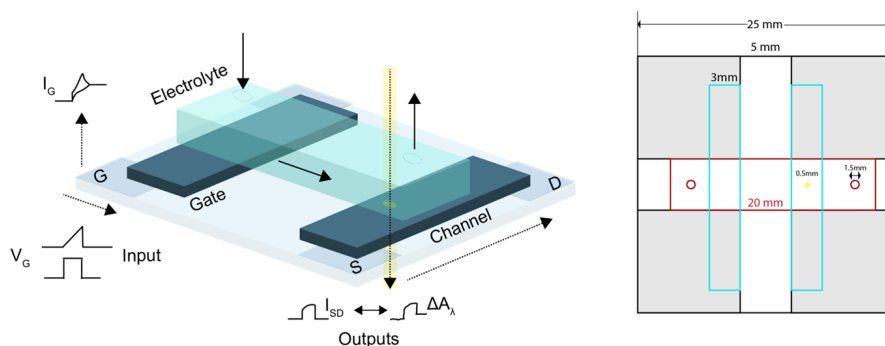


Figure 5.S11: Overall bio-hybrid synapse layout (left) and layout of the glass-ITO substrate.

In Supporting Fig. 5.S11 the overall bio-hybrid synapse layout is depicted on the left of the figure, showing the G (gate), S (source), D (drain) ITO electrodes, as reported in a previous work. On the right the transparent glass is depicted where the grey areas represent the ITO electrode, the blue rectangle are the PEDOT:PSS films used as gate and channel of the transistor, the blue area corresponds to the microfluidic module. In Supporting Fig. 5.S12 the bio-hybrid synapse conductance modulation is reported in case dopamine (left) and serotonin (right) is employed. In this experiment the input voltage applied to the bio-hybrid gate consist of three periodic voltage pulses of 300 mV (dopamine) and 400 mV (serotonin) with width 3s and delay of 10s. The conductance G_D depends on the concentration of neurotransmitter and on the number of voltage pulses applied (in these graphs only three). As more pulses are applied the dynamic range of the device saturates (Fig.5.2b) and the conductance modulation per pulse decreases.

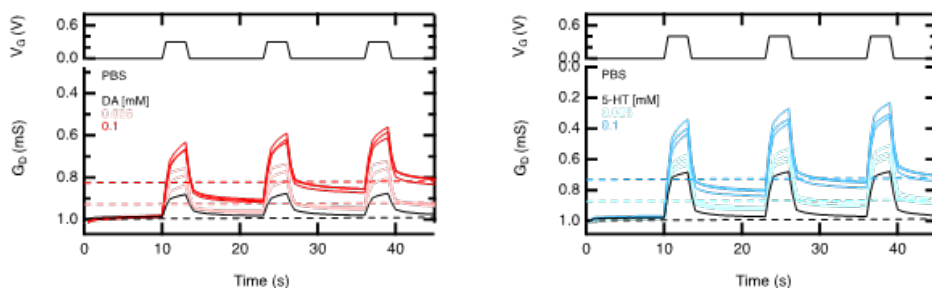


Figure 5.S12: Bio-hybrid synapse characteristic with and without DA and 5-HT neurotransmitters

5.3.4 Sensory coding with neurotransmitters dopamine and serotonin

In this section the strategy to employ the bio-hybrid synapse to modulate the spiking frequency of the circuit is presented. The bio-hybrid synapse is included in a voltage divider configuration (Supporting Fig. 5.S13) connected in series with a 1k Ω resistor.

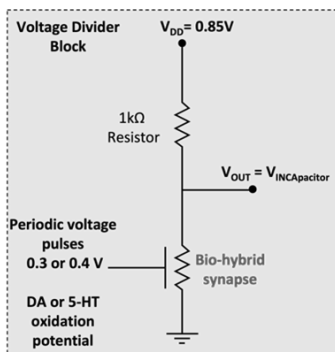


Figure 5.S13: Voltage divider configuration for exploiting the bio-hybrid synapse as a chemical receptor

The V_{out} of this voltage divider depends on the ratio of the resistance of the two elements comprising the circuit according to:

$$V_{out} = \frac{R_{OS}}{R_{OS} + R_{1k\Omega}} \quad (5.1)$$

In the above equation we assume the bio-hybrid synapse to be a tunable resistor. The resistance of the PEDOT:PSS-based synapse can be tuned by applying a gate potential $>0V$, i.e. switching off the OECT. During the course of the experiments (Fig. 5.1d and Supporting Fig. 5.S12) periodic voltage pulses are applied to the gate of the bio-hybrid synapse, matching the oxidation potential of DA or 5-HT. In case of PBS (no neurotransmitter in solution) the voltage applied to the gate biohybrid synapse enables a reversible modulation of its resistance, so that the V_{out} of the voltage divider does not change. When DA or 5-HT are introduced in solution the oxidation of these molecules leads to an increase of the resistance of the bio-hybrid synapse that depends on the number of pulses applied and on the concentration of the neurotransmitters. This leads to an increase of the voltage divider output and is used as input voltage to charge the capacitor of the spiking circuit. Hence, the spiking frequency is modulated (increased) depending on the type of neurotransmitter used and on the pulsing time. Supporting Fig. 5.S14 and 5.S15 report the spiking output trace at different time (Fig. 5.1d) that have been used to extract the temporal evolution of the frequency modulation (Tables 5.S3, 5.S4).

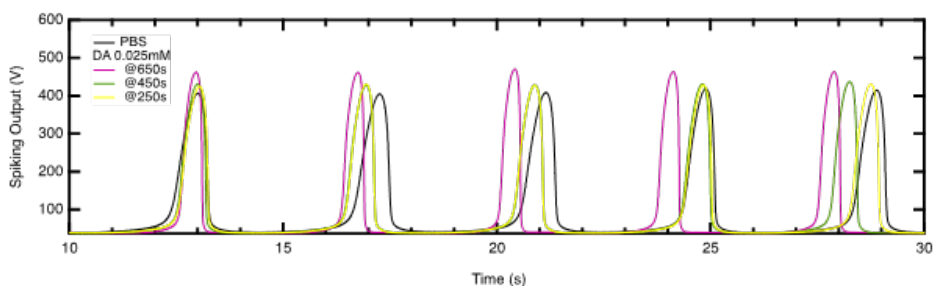


Figure 5.S14: Spiking output plot used to calculate the spiking frequency modulation as shown in Fig. 5.1 as a 0.025mM DA solution is set to flow in the microfluidic module of the biohybrid synapse. The flow of DA solution starts at time 200s. The spiking frequency is extracted at time 0 (PBS), time 250 s (yellow), time 450 s (green) and time 650 s (violet).

Table 5.S3: Spikes modulation data as extracted from the trace in Fig. 5.1d for DA 0.025 mM

Time (s)	Voltage Divider Output (V)	Spikes timing (s)	Frequency (Hz)	Change (%)
0	0.34	5.00	0.2	0
250	0.37	4.76	0.21	5.1
450	0.38	4.35	0.23	15.3
650	0.41	3.85	0.26	30.2

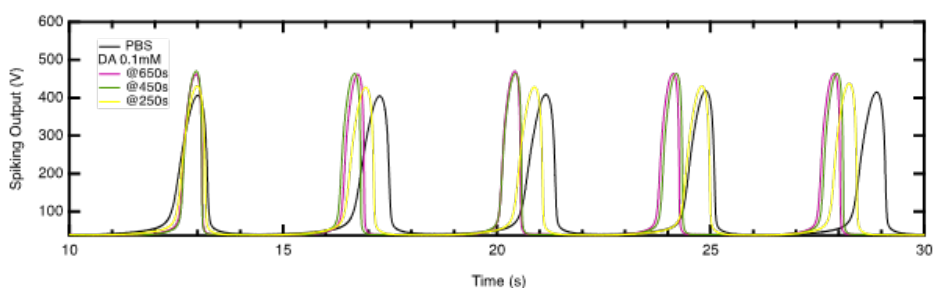


Figure 5.S15: Spiking output plot used to calculate the spiking frequency modulation as shown in Fig. 5.1 as a 0.1mM DA solution is set to flow in the microfluidic module of the biohybrid synapse. The flow of DA solution starts at time 200s. The spiking frequency is extracted at time 0 (PBS), time 250 s (yellow), time 450 s (green) and time 650 s (violet).

Table 5.S4: Spikes modulation data as extracted from the trace in Fig. 5.1d for DA 0.1 mM.

Time (s)	Voltage Divider Output (V)	Spikes timing (s)	Frequency (Hz)	Change (%)
0	0.34	5.00	0.2	0
250	0.39	4.35	0.23	5.05
450	0.40	4.00	0.25	15.25
650	0.41	3.83	0.26	30.3

As for DA in Fig. 5.1d, the same mechanism has been replicated with the use of two different concentrations of 5-HT (0.01mM and 0.05mM). Indeed, Supporting Fig. 5.S16 is the replica of Fig. 5.1d in case of 5-HT while Supporting Fig. 5.S17 shows the plots that have been used to extract the frequency modulation (Tables 5.S5, 5.S6). In 5-HT case, the evolution of the frequency modulation is faster and only the frequency at time >500s are reported.

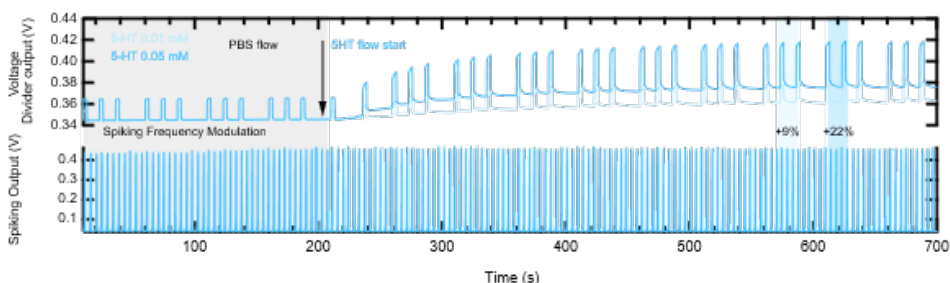


Figure 5.S16: The spikes generated by the neuromorphic circuit responding to different concentrations of the neurotransmitter serotonin (0.01mM pale blue, 0.05mM darker blue). On top, the voltage divider output is plotted.

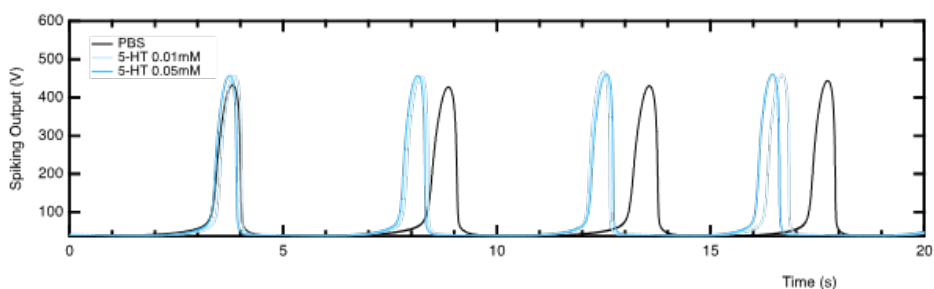


Figure 5.S17: Spiking output plot used to calculate the spiking frequency modulation as shown in Supporting Fig. 5.S16 as 0.01mM (pale blue) and 0.05mM (darker blue) 5-HT solution are used to modulate the resistance of the biohybrid synapse. The frequency values are extracted after 500s, when the voltage divider output modulation is finished.

Table 5.S5: Spikes modulation data as extracted from the trace in Supporting Fig. 5.S16 5-HT 0.01 mM.

Time (s)	Voltage Divider Output (V)	Spikes timing (s)	Frequency (Hz)	Change (%)
0	0.33	4.55	0.22	0.00
>500	0.37	4.17	0.24	9.09

Table 5.S6: Spikes modulation data as extracted from the trace in Supporting Fig. 5.S16 5-HT 0.05 mM.

Time (s)	Voltage Divider Output (V)	Spikes timing (s)	Frequency (Hz)	Change (%)
0	0.33	4.55	0.22	0.00
>500	0.39	3.70	0.27	22.73

5.3.5 Voltage divider and switch circuit to connect the two bio-hybrid synapses

The circuit presented in this section (referring to Fig. 5.2) has been designed to connect two organic synapses, O.S.1 and O.S.2 (Supporting Fig. 5.S18a), that operate with 5-HT and DA respectively without recurring to a neuromorphic spiking circuit. The combination of the voltage divider and the switch block constitutes the "sending neuron". The broad scope of the circuit is to provide a technological approach to transmit the signal of an O.S. (conductance modulation) to multiple devices.

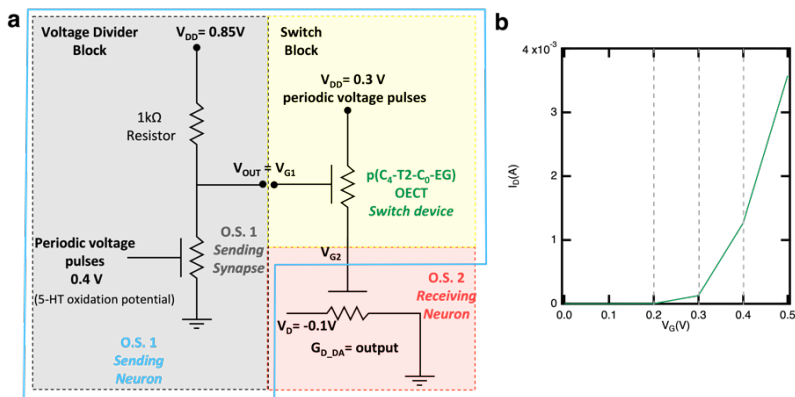


Figure 5.S18: Schematics of the circuit, comprising a voltage divider and a switch OECT, used to connect organic synapse O.S.1 (working with 5-HT) with O.S.2 (working with DA). The combination of the voltage divider and the switch block constitute the sending neuron. b) Transfer characteristic of the p(C4-T2-C0-EG) based OECT used as a switch device.

The operation of the switch device has been assessed before connecting this element to the voltage divider. To create a voltage-controlled switch device, the channel of a p(C4-T2-C0-EG)-based OECT has been connected in series with the gate of the O.S.2. Thus, the voltage V_{G2} applied on the O.S.2 depends on the state of the switch device (ON/OFF). The p(C4-T2-C0-EG)-based OECT displays a sharp turn on voltage around 0.3V (Supporting Fig. 5.S18b). However, the device enters a completely ON-state around 0.4V which is needed to sustain larger currents. Indeed, when V_{G1} is externally controlled by a voltage supplier (Supporting Fig. 5.S19a), applying 0.3V does not activate the switch device (black curve) and leads to values of V_{G2} below 0.1V (O.S.2 conductance reversible modulation is low). When the voltage supplier sets $V_{G1} = 0.5V$ (red curves), V_{G2} reaches 0.2V which trigger a visible modulation of the O.S.2 conductance.

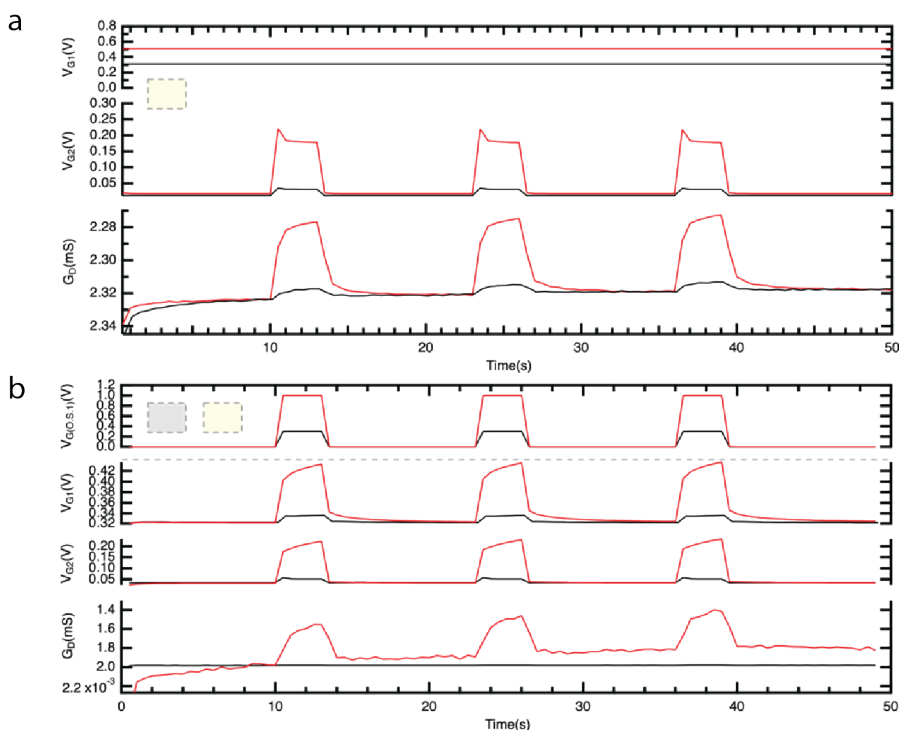


Figure 5.S19: a) Voltage and current characteristics of the switch element (in red) when V_{G2} is externally connected to a controlled voltage supplier. b) Voltage and current characteristics of the voltage divider (in black) connected to the switch element (red) under different input voltages.

For the voltage divider (Supporting Fig. 5.S18a in blue) a commercial resistor of 1k Ω has been connected in series with the O.S.1 (as described in section 5.3.4, with O.S.1 the tunable resistor in equation 5.1). Indeed, the resistance of the PEDOT:PSS-based O.S.1 can be tuned by applying a gate potential > 0 V, i.e. switching off the OECT. In Fig. 5.2 this has been achieved by using a 0.05mM 5-HT solution while pulsing the gate of the O.S.1 at 0.4 V. However, in the preliminary experiments performed to check the characteristic of the voltage

divider and presented in this section, a PBS solution has been used (Supporting Fig. 5.S19 black curves). In the starting condition (O.S. 1 is ON) the $V_{out=G_1}$ of this voltage divider is around 0.3 V. If a 0.3 V pulsing input is applied to the gate of the O.S. 1 the $V_{out=G_1}$ oscillates around 0.3 V (Supporting Fig. 5.S19b first two rows, black curves). To switch OFF (and simulate the condition achieved in the manuscript by using 5-HT) the O.S.1 and tune the V_{out} , the amplitude of the pulsing on the gate of O.S.1 is increased from 0.3 to 1 V. In this condition, the V_{out} (connected to the following element of the circuit and corresponds to V_{G_1} in the same graph) moves from 0.3V to values above 0.4V. In the experiment presented in the manuscript (Fig. 5.2), the resistance of O.S.1 is increased to the value that corresponds to a $V_{out=G_1} \approx 0.4V$ by pulsing the gate at 0.4 V while using a 0.05mM 5-HT solution. At this stage, the overall operation of the circuit (voltage divider + switch = sending neuron, Supporting Fig. 5.S19b and 5.S20) has been assessed before operating the circuit with the neurotransmitters DA and 5-HT. Again, the O.S.1 conductance modulation achievable with the 5-HT, has been simulated by the application of a large gate input (1V) on O.S.1. As from Supporting Fig. 5.S19b, a train of pulses of 0.3V on the gate of O.S.1 simulate the circuit situation before the 5-HT is infused in the microfluidic module. Indeed, the voltage divider output V_{OUT} is around 0.3V corresponding to a $V_{G_2} < 0.1V$. As such, O.S.2 conductance is poorly modulated. Increasing the amplitude of the train of pulses on the gate of O.S.1 to 1V moves the voltage divider V_{out} to values $>0.4V$. These values are enough to switch ON the switch device. Hence, the input of the "receiving neuron", V_{G_2} , reaches 0.2V which is enough to appreciate a reversible modulation of O.S.2 conductance. As in Fig. 5.2, in presence of DA in the microfluidic module of O.S.2, the increase of resistance of O.S.1 with 5-HT, by moving the V_{G_2} from $<0.1V$ to $\approx 0.2V$ trigger a partial oxidation of DA allowing to establish a connection between the conductance modulation of the two O.S. devices. Finally, Supporting Fig. 5.S20 represents the extended version of Fig. 5.2 including the time window (0-140s) where (due to the start of the DA flow on the receiving neuron) the biohybrid synapse conductance level experience a baseline change (conductance decrease).

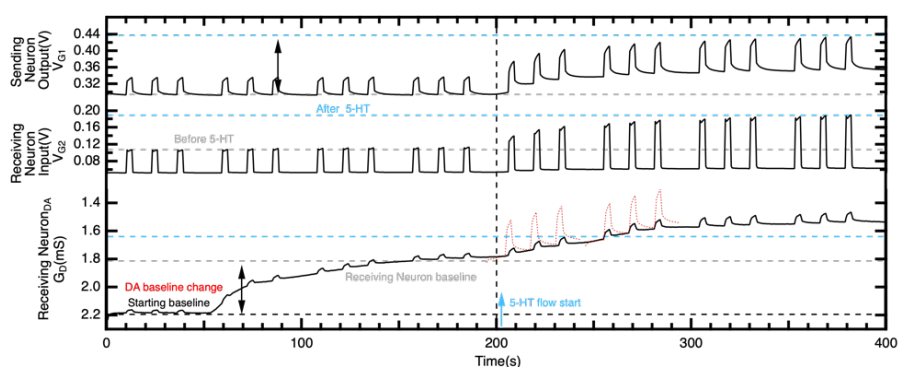


Figure 5.S20: Complete voltage and conductance monitoring of the key elements of the circuit, showing the initial (time 0-140s) baseline DA-dependent baseline change. (Extended version of Fig. 5.2).

This is caused by the occurrence of a new equilibrium condition established between the PEDOT:PSS OECT channel and electrolyte protons when passing from a PBS to a PBS+DA solution. However, before the activation of the 5-HT flow and so the start of the neural cascade, the conductance level of the receiving neuron has reached a stable baseline (140-200 s).

5.3.6 Sensory coding with light

As reported in Fig. 5.1c, different light conditions have been employed to test the light sensory coding capability of the neuromorphic circuit. Relevant parameters, extracted from the spiking pattern of Fig. 5.1c, are reported in Table 5.S7.

Table 5.S7: Spikes modulation data as extracted from the trace in Fig. 5.1c.

Light sensor output(V)	Spikes timing (s)	Frequency (Hz)	Change (%)
0.38	12	0.08	0.00
0.5	10	0.10	20.00
0.6	8.2	0.12	46.34
0.8	6.8	0.15	76.47
1	5.6	0.18	114.29

The light sensor we used is the DFRobot's Analog Ambient Light Sensor (DFR0026) with a voltage supply of 5V (Supporting Fig. 5.S21). The light sensor was shielded from the ambient light except for a small opening on top of the sensor. This opening was fully or partially covered to simulate various light conditions (low, high light intensity).



Figure 5.S21: Analog ambient light sensor (supply voltage 5V).

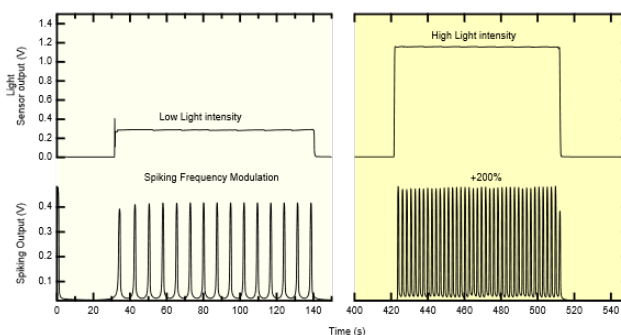


Figure 5.S22: The spikes generated by the neuromorphic circuit corresponding to the light conditions used in Fig. 5.3.

In Fig. 5.3 we used two different light conditions to replicate a retinal neural pathway. Calibration experiments are here reported (Supporting Fig. 5.S22) showing a modulation of the spiking frequency from 0.14 Hz to 0.45 Hz, as extracted in Table 5.S8, when moving from low light (0.3V light sensor output) to high light intensity (1.2 V sensor output).

Table 5.S8: Spikes modulation data as extracted from the trace in Fig. 5.S22, comprising the light sensor output, the time between each pair of spikes, the corresponding frequency and the percentage of frequency change.

Light sensor output(V)	Spikes timing (s)	Frequency (Hz)	Change (%)
0.3	7	0.14	0.00
1.2	2.22	0.45	221.75

Author contributions

GMM and YvdB conceptualized the research and established the theoretical approach. **Eve-line van Doremaele** and GMM designed and performed the experiments while they both also analysed the data and prepared the manuscript. IM, SG and GY synthesized the materials as reported in Methods.

Bibliography

1. Furber, S. [Large-scale neuromorphic computing systems](#). en. *Journal of Neural Engineering* **13**, 051001. ISSN: 1741-2560, 1741-2552 (Oct. 2016).
2. Gumyusenge, A., Melianas, A., Keene, S. T. & Salleo, A. [Materials Strategies for Organic Neuromorphic Devices](#). *Annual Review of Materials Research* **51**. _eprint: <https://doi.org/10.1146/annurev-matsci-080619-111402>, 47–71 (2021).
3. Liu, F. *et al.* [Neuro-inspired electronic skin for robots](#). *Science Robotics* **7**. Publisher: American Association for the Advancement of Science, eabl7344 (June 2022).
4. Covi, E. *et al.* [Adaptive Extreme Edge Computing for Wearable Devices](#). *Frontiers in Neuroscience* **15**, 429. ISSN: 1662-453X (2021).
5. Sandamirskaya, Y., Kaboli, M., Conradt, J. & Celikel, T. Neuromorphic computing hardware and neural architectures for robotics. eng. *Science Robotics* **7**, eabl8419. ISSN: 2470-9476 (June 2022).
6. Krauhausen, I. *et al.* [Organic neuromorphic electronics for sensorimotor integration and learning in robotics](#). EN. *Science Advances*. Publisher: American Association for the Advancement of Science (Dec. 2021).
7. Fu, T. *et al.* [Self-sustained green neuromorphic interfaces](#). en. *Nature Communications* **12**. Number: 1 Publisher: Nature Publishing Group, 3351. ISSN: 2041-1723 (June 2021).
8. Yoo, J. & Shoaran, M. [Neural interface systems with on-device computing: machine learning and neuromorphic architectures](#). en. *Current Opinion in Biotechnology. Tissue, Cell and Pathway Engineering* **72**, 95–101. ISSN: 0958-1669 (Dec. 2021).
9. Serb, A. *et al.* Memristive synapses connect brain and silicon spiking neurons. eng. *Scientific Reports* **10**, 2590. ISSN: 2045-2322 (Feb. 2020).
10. Paulsen, B. D., Tybrandt, K., Stavrinidou, E. & Rivnay, J. [Organic mixed ionic–electronic conductors](#). en. *Nature Materials* **19**, 13–26. ISSN: 1476-4660 (2020).
11. Simon, D. T., Gabrielsson, E. O., Tybrandt, K. & Berggren, M. [Organic Bioelectronics: Bridging the Signaling Gap between Biology and Technology](#). *Chemical Reviews* **116**, 13009–13041. ISSN: 0009-2665 (Nov. 2016).

12. Bettucci, O., Matrone, G. M. & Santoro, F. **Conductive Polymer-Based Bioelectronic Platforms toward Sustainable and Biointegrated Devices: A Journey from Skin to Brain across Human Body Interfaces.** en. *Advanced Materials Technologies* **7**. _eprint: <https://onlinelibrary.wiley.com/doi/pdf/10.1002/admt.202100293>, 2100293. ISSN: 2365-709X (2022).
13. Hosseini, M. J. M. *et al.* **Organic electronics Axon-Hillock neuromorphic circuit: towards biologically compatible, and physically flexible, integrate-and-fire spiking neural networks.** en. *Journal of Physics D: Applied Physics* **54**. Publisher: IOP Publishing, 104004. ISSN: 0022-3727 (Dec. 2020).
14. Harikesh, P. C. *et al.* **Organic electrochemical neurons and synapses with ion mediated spiking.** en. *Nature Communications* **13**. Number: 1 Publisher: Nature Publishing Group, 901. ISSN: 2041-1723 (Feb. 2022).
15. Thivierge, J.-P., Rivest, F. & Monchi, O. **Spiking neurons, dopamine, and plasticity: Timing is everything, but concentration also matters.** en. *Synapse* **61**. _eprint: <https://onlinelibrary.wiley.com/doi/pdf/10.1002/syn.20378>, 375–390. ISSN: 1098-2396 (2007).
16. Go, G.-T., Lee, Y., Seo, D.-G. & Lee, T.-W. **Organic Neuroelectronics: From Neural Interfaces to Neuroprosthetics.** en. *Advanced Materials* **34**. _eprint: <https://onlinelibrary.wiley.com/doi/pdf/10.1002/adma.202201864>, 2201864. ISSN: 1521-4095 (2022).
17. Janson, P., Gabrielsson, E. O., Lee, K. J., Berggren, M. & Simon, D. T. **An Ionic Capacitor for Integrated Iontronic Circuits.** en. *Advanced Materials Technologies* **4**, 1800494. ISSN: 2365-709X (2019).
18. Zhang, Y. *et al.* **Adaptive Biosensing and Neuromorphic Classification Based on an Ambipolar Organic Mixed Ionic–Electronic Conductor.** en. *Advanced Materials* **34**. _eprint: <https://onlinelibrary.wiley.com/doi/pdf/10.1002/adma.202200393>, 2200393. ISSN: 1521-4095 (2022).
19. Rashid, R. B. *et al.* **Ambipolar inverters based on cofacial vertical organic electrochemical transistor pairs for biosignal amplification -supp.** en. *Science Advances* **7**, eabh1055. ISSN: 2375-2548 (Sept. 2021).
20. Keene, S. T. *et al.* **A biohybrid synapse with neurotransmitter-mediated plasticity.** en. *Nature Materials*. ISSN: 1476-1122, 1476-4660 (June 2020).
21. Kandel, E. R., Schwartz, J., Jessell, T. M., Siegelbaum, S. A. & Hudspeth, A. J. *Principles of Neural Science Kandel 4th Ed* (McGraw-hill, New York, 2000).

22. Klein, M. O. *et al.* Dopamine: Functions, Signaling, and Association with Neurological Diseases. eng. *Cellular and Molecular Neurobiology* **39**, 31–59. ISSN: 1573-6830 (Jan. 2019).
23. Ott, T. & Nieder, A. Dopamine and Cognitive Control in Prefrontal Cortex. en. *Trends in Cognitive Sciences* **23**, 213–234. ISSN: 1364-6613 (Mar. 2019).
24. *The Synaptic Organization of the Brain* (ed Shepherd, G. M.) ISBN: 978-0-19-515956-1 (Oxford University Press, Jan. 2004).
25. Taber Pierce, E., Foote, W. E. & Hobson, J. A. The efferent connection of the nucleus raphe dorsalis. en. *Brain Research* **107**, 137–144. ISSN: 0006-8993 (Apr. 1976).
26. Hervé, D., Pickel, V. M., Joh, T. H. & Beaudet, A. Serotonin axon terminals in the ventral tegmental area of the rat: fine structure and synaptic input to dopaminergic neurons. eng. *Brain Research* **435**, 71–83. ISSN: 0006-8993 (Dec. 1987).
27. Euler, T., Haverkamp, S., Schubert, T. & Baden, T. Retinal bipolar cells: elementary building blocks of vision. eng. *Nature Reviews. Neuroscience* **15**, 507–519. ISSN: 1471-0048 (Aug. 2014).
28. Zhang, D.-Q. *et al.* Intraretinal signaling by ganglion cell photoreceptors to dopaminergic amacrine neurons. eng. *Proceedings of the National Academy of Sciences of the United States of America* **105**, 14181–14186. ISSN: 1091-6490 (Sept. 2008).
29. Ohayon, D. *et al.* Influence of Side Chains on the n-Type Organic Electrochemical Transistor Performance. en. *ACS Applied Materials & Interfaces* **13**, 4253–4266. ISSN: 1944-8244, 1944-8252 (Jan. 2021).

Chapter 6

Adaptive biosensing and neuromorphic classification based on an ambipolar organic mixed ionic–electronic conductor

Organic mixed ionic–electronic conductors (OMIECs) are central to bioelectronic applications such as biosensors, health-monitoring devices, and neural interfaces, and have facilitated efficient next-generation brain-inspired computing and biohybrid systems. Despite these examples, smart and adaptive circuits that can locally process and optimize biosignals have not yet been realized. Here, a tunable sensing circuit is shown that can locally modulate biologically relevant signals like electromyograms (EMGs) and electrocardiograms (ECGs), that is based on a complementary logic inverter combined with a neuromorphic memory element, and that is constructed from a single polymer mixed conductor. It is demonstrated that a small neuromorphic array based on this material effects high classification accuracy in heartbeat anomaly detection. This high-performance material allows for straightforward monolithic integration, which reduces fabrication complexity while also achieving high on/off ratios with excellent ambient p- and n-type stability in transistor performance. This material opens a route toward simple and straightforward fabrication and integration of more sophisticated adaptive circuits for future smart bioelectronics.

This chapter is based on *Adaptive Biosensing and Neuromorphic Classification Based on an Ambipolar Organic Mixed Ionic–Electronic Conductor*, Yanxi Zhang*, **Eveline R. W. van Doremaele***, Gang Ye, Tim Stevens, Jun Song, Ryan C. Chiechi, Yoeri van de Burgt, *Advanced Materials*, **34**, (20), 2022.

6.1 Introduction

The success of many organic bioelectronic applications results from reduced interface impedance and extraordinarily high electrochemical transconductance (ion-to-electron transduction) in organic mixed ionic–electronic conductors (OMIECs).[1, 2] These and other unique properties such as biocompatibility, low voltage operation, simple fabrication processing, and stretchable and flexible materials have opened a wide variety of possible bioelectronic applications such as neural probes[1] and sensors for ions,[3] metabolites,[4] bacteria,[5] and viruses[6] that benefit from the extensive capabilities in tailoring molecular structures and functions via chemical synthesis. Furthermore, the dynamic range and ability to dope these polymers electrochemically have produced tunable analog neuromorphic devices[7, 8] with high stability,[9] resulting in proof-of-principle circuits[10, 11] as well as biohybrid systems directly modulated by locally secreted neurotransmitters.[12]

Current organic bioelectronic applications are commonly based on commercially available blends of poly(3,4-ethylene-dioxythiophene):polystyrene sulfonate (PEDOT:PSS), which is a p-type (hole) conductive polymer that operates in depletion-mode. This material is conductive as-prepared and can be turned off by applying a gate potential. Enhancement-mode p-type devices exist, by design,[13] or by the dedoping of PEDOT:PSS with small molecule amines.[14] However, a combination of p- and n-type materials is required to form logic gates and complementary circuits[15] and, to date, highly stable and high-performance n-type materials are rare.[16] As a result, there is a clear need for stable materials that can operate at biological interfaces and that are able to transduce ionic to electronic signals effectively. In fact, despite the vast amount of information available at the physiological level, thus far no smart and integrated bioelectronic circuits exist that can locally adapt to and process information. At the same time, neuromorphic systems have proven successful in typical classification tasks such as digital image recognition, but nevertheless (partly) rely on software and are still outperformed by traditional software neural networks.[17] However, for applications requiring the local, real-time processing of biological and physiological data, the use of software is undesirable and can be problematic. Consequently, bioelectronic circuits integrated with neuromorphic systems could provide the rapid on-site processing and classification of biosignals without the need for external computation and signal analysis to generate relevant optimized actions such as drug delivery or prosthetic movements.[18]

In this work, we show an adaptable circuit that can locally process and tailor biologically relevant signals, such as electromyograms (EMGs) and electrocardiograms (ECGs), that serve as inputs to a neuromorphic classification array and act directly as an in-sensor computing system[19] (see Figure 6.1). Our system is based on a monolithically integrated semiconducting polymer that forms both the ambipolar inverter for signal amplification and normalization, as well as the neuromorphic memory element to tune the gain properties locally by modulation of the conductance (or synaptic weight). The nonvolatile tuning of the neuromorphic elements also allows for hardware neural network integration and the local classification of signals. The use of a single polymer mixed conductor significantly reduces fabrication complexity, while its unrivaled performance and ambient stability highlight a route toward long-term smart sensing systems and chronic implants.

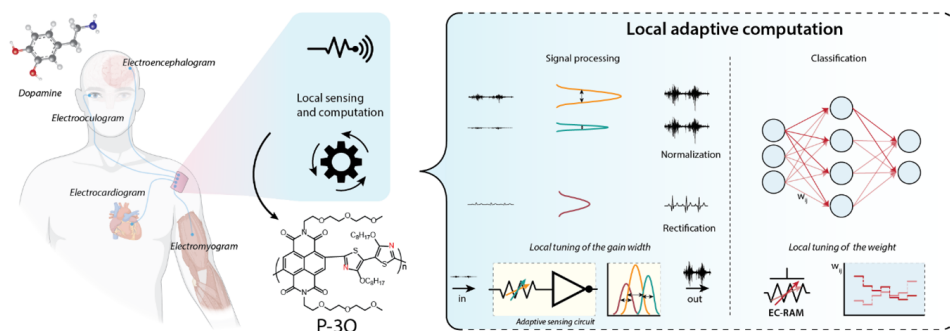


Figure 6.1: Schematic of an adaptive neuromorphic biosensor. The adaptive organic electronic circuit can locally process (for example, amplify, rectify, normalize, etc.) biosignals by tuning the gain peak of the inverter using a neuromorphic element. Simultaneously, a hardware-based neural network could classify input signals, for instance, to detect heartbeat anomalies. Both functionalities can be realized using a single OMIEC (P-30).

6.2 Results & Discussion

Electronic circuits operating at the interface with biology require both p-type and n-type OMIECs. To date, the number of n-type semiconductors as well as their performance is still inferior compared to their p-type counterparts. The key issues are that doped n-type materials are generally unstable when exposed to air and achieving high electron mobilities has proved more difficult than for their p-type counterparts. To reduce the fabrication complexity ambipolar materials are desirable as it decreases the number of lithography steps. At the same time, ambipolar materials impose the challenging constraint of being able to be doped by both cations and anions as well as conducting both holes and electrons. One strategy to design ambipolar polymer mixed conductors is copolymerizing an electron deficient moiety (acceptor), such as naphthalenediimide (NDI) or diketopyrrolopyrrole (DPP), with an electron rich moiety (donor) like thiophene to obtain a narrow bandgap.[20, 21] These donor–acceptor (D–A) polymers are modified with hydrophilic ethylene glycol (EG) type side chains for aqueous electrolyte gated organic electrochemical transistors (OECTs). The EG chains support highly efficient electrochemical doping within the whole volume and enables low voltage (<1 V) operation, which is essential when using an aqueous electrolyte. These OECTs exhibit p- and n-type characteristics, and are integrated into ambipolar inverters for logic circuits[21] and biosignal amplifiers.[22] In order to operate stable OMIEC devices properly in n-type mode in water, a lowest unoccupied molecular orbital (LUMO) level below -4 eV is required to avoid side reactions with water and oxygen.[23] High-performance OMIECs additionally require balancing ionic and electron/hole mobility, while maintaining unperturbed crystalline structures upon electrochemical doping.[24] It has been reported that embedding sp²-N into polymer backbones results in a more planar structure, enhancing the π – π stacking and increasing the electron mobility.[25, 26] Capitalizing on these properties, the material we present here is an NDI-bithiozale D–A copolymer (referred to as P-30, shown in Figure 6.1)

functionalized with EG side chains, which allows for a stable transistor operation both with a solid electrolyte as well as in aqueous environments.

Ideally, a multi-sensor approach for on-site classification and personalized actions based on biosignals requires a method for local signal processing. The ability to amplify low signal-to-noise ratio biosignals is also important, particularly for small signals like EEG.[27] However, any computational action such as a decision or classification is still made externally. In order to judge and process a plethora of signals, local amplification, and normalization is needed. At the same time, in-sensor computing requires the modulation of signals over a variety of inputs, while ensuring that signals are correctly tuned to the synaptic weights for use in (neuromorphic) classification algorithms.[19] Furthermore, relevant information could be lost if signals from one sensor (e.g., ECG) outweigh others (e.g., EMG). Our proposed adaptive neuromorphic circuit is schematically shown in Figure 6.1, where various electrophysiological signals can serve as an input for local adaptive processing (such as normalization or rectification). The circuit consists of an ambipolar inverter combined with an adaptive memory element and is based entirely on the ambipolar material P-3O.

The ambipolar inverter comprises two complementary transistors, one operating in n-type and one in p-type mode. An all-solid-state environment is desirable in applications associated with electronic circuitry, logic circuits, and neuromorphic computing, as the operation of circuits in aqueous environments can lead to interference with the surrounding electronics and neighboring devices. From a technological point of view, the use of liquid electrolytes limits the high-density integration of devices.[28] The solid electrolyte consists of an ionic liquid (1-ethyl-3-methylimidazolium bis(trifluorosulfonyl)imide, EMIM:TFSI) within a polymer matrix (poly(vinylidene fluoride-co-hexafluoropropylene), PVDF-HFP), [29] which has been demonstrated to be able to operate at kHz frequencies.[30] Figure 6.2A shows the architecture of the solid electrolyte gated device. The devices can be designed with a side gate, which simplifies the fabrication by avoiding a complex layer-by-layer process to construct a stacked structure. Figure 6.2B,C shows the output and transfer characteristic of the P-3O OECT exhibiting near-symmetric ambipolar electrical behavior when operated in the ambient environment with a solid gel-electrolyte. The polymer achieves an on/off ratio of 10^4 and stable operation for more than 20000 cycles for both p- and n-type in ambient conditions (Figure 6.2D,E).

Since both the p- and n-type transfer curves have near-identical behavior (shown in Figure 6.2C), the ambipolar inverter can be constructed. An inverter is a fundamental building block of electronic circuits and is used in both digital circuits such as logic gates, as well as in analog circuits such as voltage amplifiers. It inverts the applied input voltage (V_{in}) from a high to low voltage and vice versa (see Figure 6.2F,G). At the transition region, it shows a high gain which makes organic inverters relevant for a wide variety of applications in several fields, including printed electronics, imperceptible and wearable electronics, sensors and bioelectronics.[22, 31, 32] Figure 6.2F shows the performance of the solid-state ambipolar inverter with a gain of 12 at $V_{DD} = 0.8$ V, along with Figure 6.2G presenting the logic NOT gate operation where a high input results in a low output voltage.

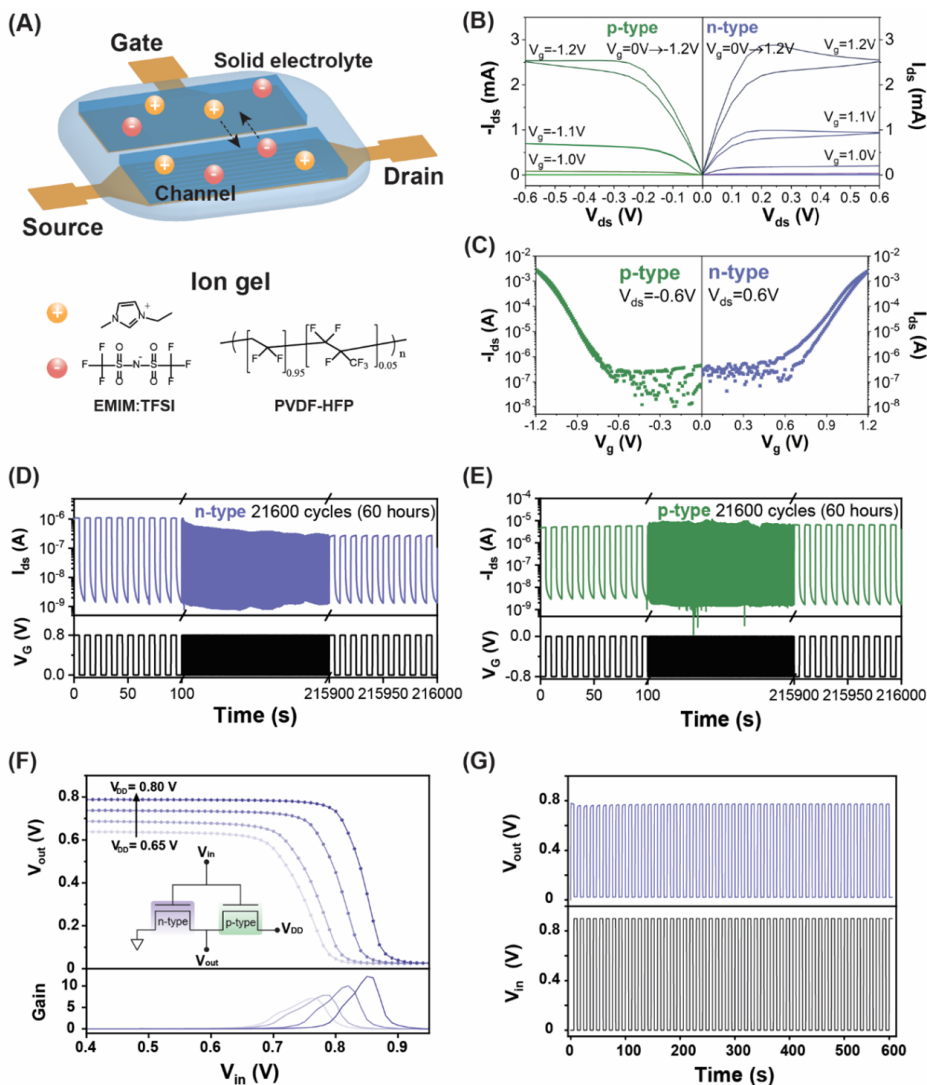


Figure 6.2: A) Schematic of the ion gel side-gated organic electrochemical transistor together with the chemical structure of the ion gel. B) Ambipolar output curve. C) Ambipolar semilog transfer curve carried out in ambient environment. D) n-type and E) p-type operational stability measurement of the ion gel gated transistor. The drain current (I_{ds}) is monitored when applying a 5 s gate voltage pulse ($|V_g| = 0.8$ V with an interval time of 5 s for 21600 pulse cycles ($|V_{ds}| = 0.1$ V). F) Ambipolar inverter behavior at different V_{DD} voltages with below the corresponding gain ($\partial V_{out}/\partial V_{in}$) and the inset representing the schematic inverter circuit. G) Complementary logic gate behavior of a NOT gate with $V_{DD} = 0.8$ V and the input V_{in} pulsing between 0 and 0.9 V for 6 s.

Pairing the P-3O ambipolar inverter with electrochemical random-access memory (ECRAM) at the inverter gate allows for the construction of a neuromorphic inverter that can locally tune the amplification of input signals (see Figure 6.3A). The P-3O EC-RAMs adopt a similar

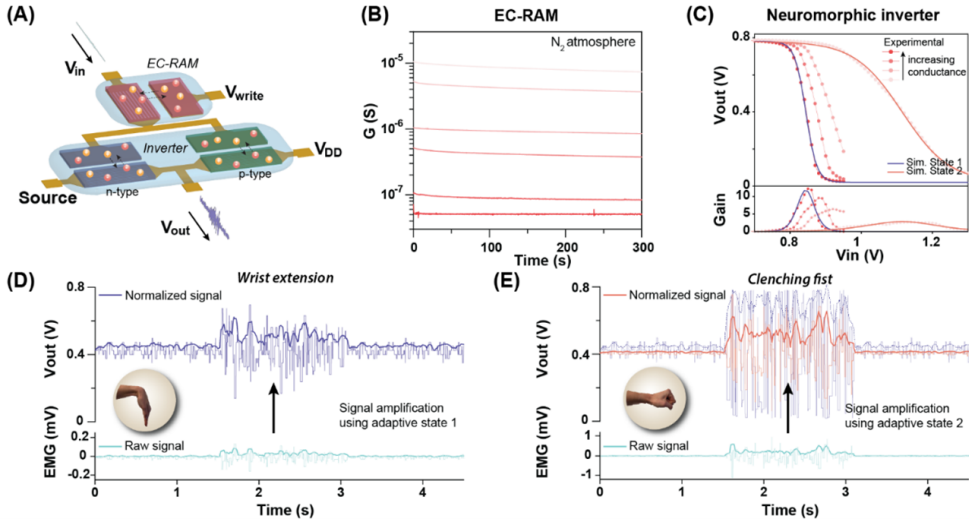


Figure 6.3: A) Schematic of an adaptable inverter including an EC-RAM in series with the gate of the ambipolar inverter. B) State retention of EC-RAM in a N_2 environment for 5 min at different conductance states over two orders of magnitude. C) The top panel shows the behavior of the neuromorphic inverter ($V_{DD} = 0.8$ V) when tuning the EC-RAM to different conductance states and bottom panel shows the corresponding gain. The dashed lines represent the experimental data, and the two solid lines represent the simulated inverter behavior of two different EC-RAM conductance states. State 1 resembles a neuromorphic inverter with a negligible EC-RAM resistance whereas State 2 represents one with a high EC-RAM resistance ($C = 167$ nS). D,E) The use of the neuromorphic inverter applied to locally amplify EMG signals from two different gestures, wrist extension and clenching of a fist, respectively. Each signal can be normalized between 0 and V_{DD} , depending on the state of the neuromorphic inverter.

configuration as the solid-state electrochemical transistor (Figure 6.2A) and maintain non-volatile memory by employing an open gate circuit in combination with a current limiting resistor. Figure 6.3B shows the excellent state retention of 6 representative memory states across two orders of magnitude for 5 min in a nitrogen environment. By tuning the neuromorphic memory device to different conductance values, we can directly and locally tune the gain of the adaptive inverter circuit (see Figure 6.3C), a characteristic feature used to extract, for example, electrophysiological signals.[33] Lowering the conductance results in a shift in the transition region to higher input voltages as well as a broadening of the transition region. The opposite is true for an increase in the conductance, which moves the transition region to lower input voltages and makes it narrower. As such, we can adjust the fully integrated adaptive neuromorphic sensing circuit to modulate and normalize biosignals of different amplitudes without increasing fabrication complexity, assuming signals with a sufficient signal-to-noise ratio. Figure 6.3D,E demonstrates the signal normalization of EMG signals for two different

gestures using the behavior of the neuromorphic inverter (see the Supporting Information 6.5.6). The signal envelope (an essential feature encompassing relevant information of the gesture) of the wrist extension (Figure 6.3D) is correctly preserved after normalization using adaptive state 1 whereas the signal envelope of a clenched fist is completely lost (Figure 6.3E, purple line). To correctly retrieve the signal envelope after amplification the signal of a clenched fist should be normalized using adaptive state 2 (Figure 6.3E, red line). While the two different gestures require a different amplification of the biosignals to correctly scale and retrieve the signal envelope, the adaptive nature of the neuromorphic inverter makes it generalizable to local processing applications such as smart autonomous robotics,[34] in-sensor classification and prosthetic motion control,[19] or for further processing and classification in hardware-based neural networks.[18]

In fact, when integrated into large crossbar arrays (Figure 6.4A), P-3O EC-RAMs can be used as the synaptic weights in an artificial neural network for local classification. In this array, each weight in the hardware neural network is represented by the conductance of an EC-RAM, which can be randomly accessed over a large range and in an analog fashion, enabling parallel computation[10] and increasing energy efficiency. Organic EC-RAMs are able to operate at low voltage and with high write speeds (20 ns pulse).[35] The P-3O EC-RAMs operate in n-type mode (positive read voltage, ± 5 V on the gate circuit with the current limiting 1 GOhm resistor, writing speed less than 300 ms) and can access over 25 conductance states, in linear fashion, and with high state retention (see Figure 6.4B). Operating in ambient conditions mandates encapsulation due to the presence of oxygen and water (see Figures 6.S9 and 6.S10 in the Supporting Information). The state retention can be further improved by optimizing the device geometry and purifying the ion gel. Furthermore, to avoid possible crosstalk in neuromorphic array operation, other device geometries like vertical gate architecture[36] or patterning ion gel[37] can be used. Our n-type P-3O-based EC-RAM exhibits comparable performance to p-type polymer based EC-RAMs such as PEDOT:PSS,[9] p(g2T-TT),[35] and P3HT.[36] Even though the P-3O polymer is ambipolar, in p-type mode (negative read voltage) EC-RAM decays fast, even in nitrogen atmosphere (see Figure 6.S11 in the Supporting Information), which might indicate that the energetic barrier for back diffusion of the anions (TFSI⁻) is low,[38] and the generated holes are unstable due to the low-lying HOMO (Table 6.S1, Supporting Information).[39] The linear and symmetric behavior of potentiation and depression of the conductance (Figure 6.4B) results in efficient training and inference of the neural network. To highlight this, we simulate the behavior of a neuromorphic array based on the P-3O EC-RAM, in its performance to recognize and classify heartbeat anomalies in ECG signals (see the Supporting Information 6.5.7). Figure 6.4C shows the five different ECG classes serving as the input for the neural network depicted in Figure 6.4D. ECG signals are generally very similar and known to be difficult to classify,[40] hindering real-time diagnoses. Local processing and computation using a hardware-based neural network could facilitate on-site real-time classification. Figure 6.4E shows that training an EC-RAM based neural network approaches ideal numerical accuracy (over 70% training accuracy after 20 epochs), which is the theoretical limit for this algorithm. The corresponding confusion matrix is presented in Figure 6.4F, demonstrating the successful classification of the five ECG classes based on the EC-RAM hardware array. Note that increasing the complexity of the neural network architecture can lead to higher accuracies. However, since in this work

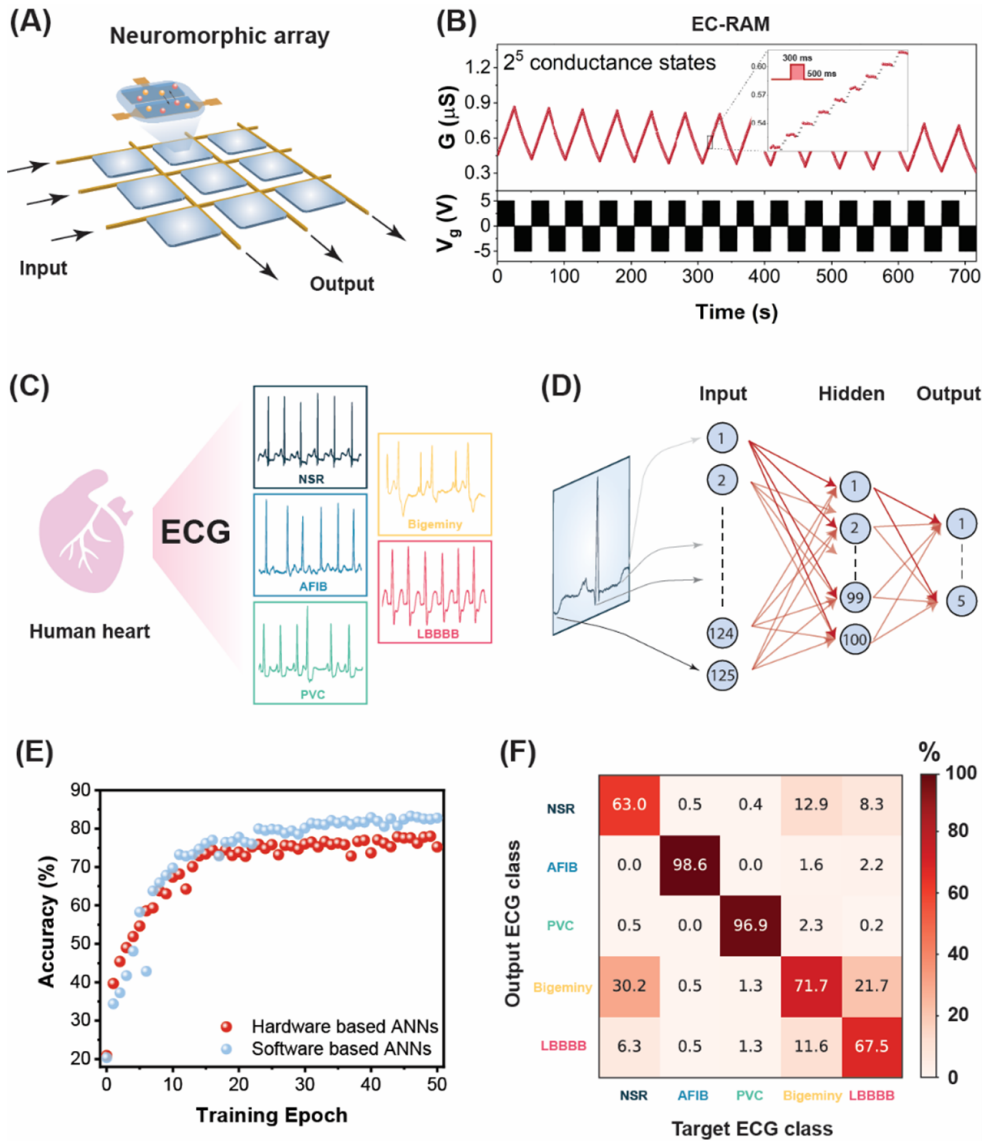


Figure 6.4: A) Schematic representation of a neuromorphic array based on P-3O EC-RAMs. B) 14 cycles of 32 conductance states showing linear potentiation and depression (pulse width 300 ms and delay 500 ms). C) 5 different ECG classes represent the normal sinus rhythm (NSR) and 4 heartbeat anomalies. D) Neural network architecture consisting of 125 input neurons, 1 hidden layer with 100 neurons and 5 neurons in the output layer. E) Classification accuracy as a function of the training epochs for both the hardware neural network based on P-3O (red) and the ideal software limit (blue). F) Confusion matrix for all 5 classes using the hardware-based network.

we focus on hardware neural networks and specifically the EC-RAM functioning within a neural network, we have chosen to restrict the neural network architecture to a single fully connected layer with one hidden layer. On the other hand, this network structure still faces a significant integration challenge which would benefit from down scaling the network structure and sacrificing accuracy or implementing more complex neural network architectures (e.g., convolutional and pooling layers, or a recurrent neural network) or additional preprocessing steps (e.g., Fourier transform).

Conventional complementary circuits based on a combination of a p- and n-type material commonly require multiple or complex fabrication steps. Using our ambipolar conductive polymer, we can significantly decrease this complexity by monolithic fabrication, including the added neuromorphic traits. This expands the capabilities of the complementary circuits in bioelectronics and sensors, in which OMIECs have already proven to be powerful due to their large volumetric ionic capacitance, which allows for significant amplification when transducing biological signals. In biological, aqueous environments, stable p-type OMIECs are common, whereas high-performance n-type materials, in terms of stability and electrical behavior, are not. However, for biosensors detecting anions or some metabolites like glucose, stable n-type materials are crucial.

We studied the behavior of a 100×10^{-3} M NaCl aqueous electrolyte gated OEET using P-3O as the active channel, and Ag/AgCl as the gate electrode (shown in Figure 6.5A). In this configuration P-3O also exhibits ambipolar behavior in transistor performance (see Figure 6.5B,C for the output and transfer curves), which indicates that the polymer could also be doped by both cations (Na^+) and anions (Cl^-). In n-type mode, the P-3O polymer works exceptionally well with a stable on/off ratio of approximately four orders of magnitude for more than 21600 cycles, shown in Figure 6.5D. After continuously operating for more than 60 h, the on-current only exhibits a slight decrease ($\approx 25\%$) but maintains the on/off ratio at similar orders of magnitude (see Figure 6.S3 in the Supporting Information). The remarkable stability is a result of the precise tailoring of the energy levels (LUMO -4.30 eV, see Figure 6.S1 and Table 6.S1 in the Supporting Information) with respect to oxygen and water.[23] Despite the extremely high stability of the p-type mode transistor using ion-gel, the material performance in liquid electrolytes in p-type mode is less (see Figure 6.S5 in the Supporting Information), showing a two order of magnitude on/off ratio for over two hours operation. The aqueous electrolyte operated ambipolar inverter and the tuning of it using the EC-RAM is demonstrated in Figures 6.S13 and 6.S15 in the Supporting Information. We further show the exceptional n-type performance of the P-3O polymer in an aqueous environment by demonstrating its behavior as a neurotransmitter sensor (see Figure 6.5E), which has potential in advanced biohybrid systems.[12] We adopted the Au side-gated device configuration in Figure 6.2A and monitored the drain current at a drain potential of $V_d = 0.1$ V, while oxidizing the dopamine at the gate electrode by applying a gate potential of $V_G = 0.6$ V. A faradaic gate current was observed when different concentrations of dopamine analyte were added (Figure 6.5E bottom panel), which lowers the potential drop at the Au gate and electrolyte interface, leading to more effective gating at the channel (see Figure 6.S6 in the Supporting Information). Meanwhile, the drain current increases in response to increased dopamine concentrations (Figure 6.5E top panel and Figures 6.S7 and 6.S8 in the Supporting Information). These results prove the

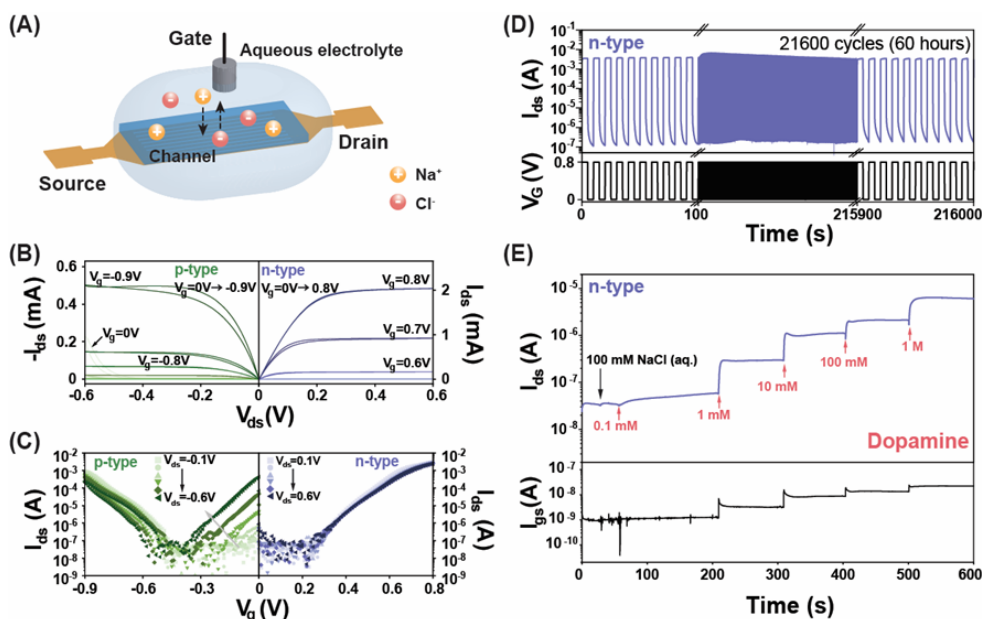


Figure 6.5: A) Schematic of aqueous electrolyte gated OECT. B) Ambipolar P-3O OECT output curve. C) Ambipolar P-3O OECT semilog transfer curve. D) N-type OECTs ($V_G = 0.8$ V, $V_{ds} = 0.5$ V) operation stability in 100 mM NaCl aqueous electrolyte for 21600 pulse cycles. A gate voltage pulse V_G was applied for 5 s with an interval time of 5 s. E) Au side-gated OECTs for dopamine sensing. The output drain current I_{ds} , gate current I_{gs} were monitored when adding different concentrations of dopamine into the 100 mM NaCl (aq.) electrolyte at $V_{ds} = 0.1$ V and $V_G = 0.6$ V. A glass well was glued to the device using poly(dimethylsiloxane) to retain the electrolyte. Starting with 40 μL 100 mM NaCl aqueous solution. 10 μL analyte solution was added into the well each time.

interaction of P-3O as an excellent electron conductor with neurotransmitters like dopamine, showing its potential in adaptive biohybrid applications.

6.3 Conclusion

Due to the intrinsic ionic–electronic coupling, organic mixed ionic–electronic conductors exhibit great potential not only in bridging electronics and biological systems, but also in operating as non-volatile memory devices in hardware neural networks. In this work, we have presented the capability to integrate individual devices into circuits for applications like adaptive biosensors and brain-inspired computing, utilizing the ambipolar NDI-bithiazole conjugated polymer P-3O. Though ambipolar materials do not always have better performance, the remarkable characteristics of this semiconducting polymer, including symmetric p- and n-type transfer curves, high performance, and ambient stability, allow for straightforward monolithic fabrication and integration of single devices, including transistors, logic gates, neuromorphic memory, and sensors. Though neural network simulations based on the experimentally obtained behavior of P-3O EC-RAMs demonstrate the capabilities of local classification of biosignals, full hardware integration remains a challenge. This is partly because of the EC-RAM encapsulation requirements, but mostly due to the complexity in hardware-based learning rules (e.g., gradient descent and activation function) and the hardware circuit design (e.g., the peripheral circuit and the coupling of multiple network layers). Consequently, smart local modulation and learning demonstrated by a monolithically integrated adaptive sensor clearly highlight a path toward next-generation adaptive and personalized bioelectronic applications.

6.4 Experimental Section

6.4.1 Materials

The P-3O synthesis details and characterization are described in the Supporting Information of the manuscript [41]. Chloroform, 1-ethyl-3-methylimidazolium bis(trifluorosulfonyl)imide, poly(vinylidene fluoride-co-hexafluoropropylene), and dopamine hydrochloride are purchased from Sigma-Aldrich and used as received. The ion gel solution was prepared following the reported method[29] without further baking the ionic liquid. Ionic liquid (EMIM:TFSI) and poly(vinylidene fluoride-co-hexafluoropropylene) (4:1 w/w) were dissolved in acetone with the following proportions: 17.6 wt% ionic liquid, 4.4 wt% polymer, and 78 wt% solvent. The resulting ion gel solution was stirred at 40 °C for at least 30 min. The interdigitated microelectrodes IDA-Au-6 (channel length L 5 μm , individual channel width, w , 1.8 μm , number of pairs 30, number of channels, n , 59, total channels width, $W = n \times w = 10.62 \mu\text{m}$) are purchased from MicruX technologies.

6.4.2 Device Fabrication and Characterization

The polymer solutions were prepared in chloroform at the concentration of 5 mg mL^{-1} . The interdigitated microelectrodes were treated with UV ozone over 15 min, following spin-coating the polymer solutions at 1000 rpm for 30 s. The samples were annealed on the hotplate at 100 °C for 30 min. For side gate devices, the gate and active channel were separated by excimer laser ablation. The ion gel solution was drop-casted on top of the active area

and dried in the fume hood. For EC-RAM measurements, the devices were stored in the nitrogen atmosphere glovebox. The electrical characterization of OECTs is recorded by a Keithley sourcemeter SMU 2602B, which is controlled by the software Arkeo developed by Cici research. The EC-RAMs are recorded by Keithley 2602B with Labview and the inverter data is acquired with a NI DAQ USB-6363 and with Keithley SMU 2636B controlled with Matlab software.

6.5 Supporting Information

6.5.1 Material characterization

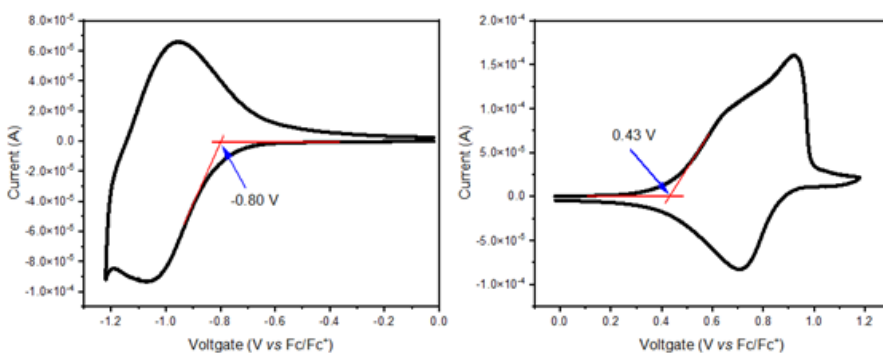


Figure 6.S1: Cyclic voltammograms of the conjugated polymer P-3O thin films deposited on the glass carbon working electrode in CHCN3 solution containing Bu4NPF6 electrolyte

Table 6.S1: Optical and electrochemical data for the polymer P-3O.

Polymer	λ_{max}^{film} (nm)	λ_{onset}^{film} (nm)	E_g^{opt*} (eV)	HOMO [†] (eV)	LUMO [‡] (eV)	E_{onset}^{ox} (V)	E_{onset}^{red} (V)	E_g^{ec} (eV)
P-3O	973	1225	1.01	-5.53	-4.30	0.43	-0.80	1.23

* $E_g^{opt} = 1240 / \lambda_{onset}^{film}$

† HOMO = $-(5.10 + E_{onset}^{ox})$ eV

‡ LUMO = $-(5.10 + E_{onset}^{red})$ eV

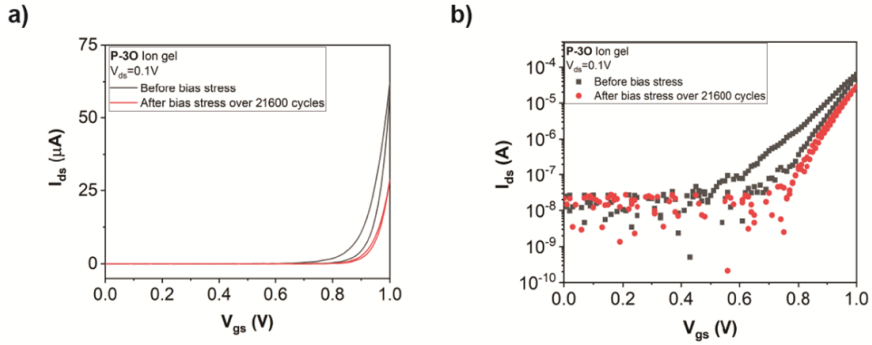


Figure 6.S2: Comparison of P-3O ion gel OECT n-type transfer curve ($V_{ds}=0.1V$) before and after bias stress stability over 21600 cycles (pulse 5s, interval 5s, over 60 hours). a) Linear plot, b) Semi-log plot.

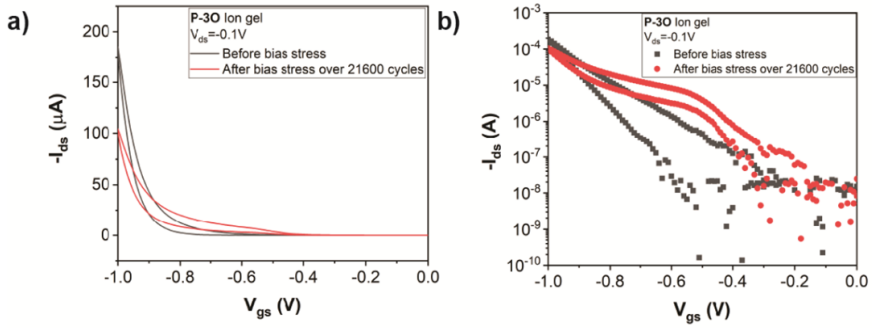


Figure 6.S3: Comparison of P-3O ion gel OECT p-type transfer curve ($V_{ds}=-0.1V$) before and after bias stress stability over 21600 cycles (pulse 5s, interval 5s, over 60 hours). a) Linear plot, b) Semi-log plot.

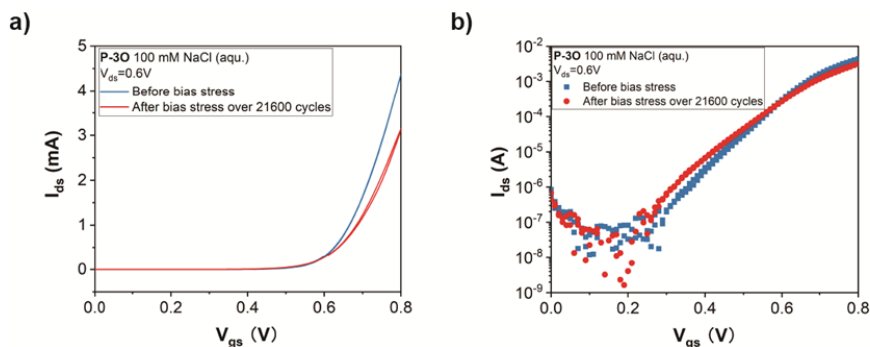


Figure 6.S4: Comparison of P-3O 100mM NaCl aqueous OECT transfer curve ($V_{ds}=0.6V$) before and after bias stress stability over 21600 cycles (pulse 5s, interval 5s, over 60 hours). a) Linear plot, b) Semi-log plot.

6.5.2 OECTs

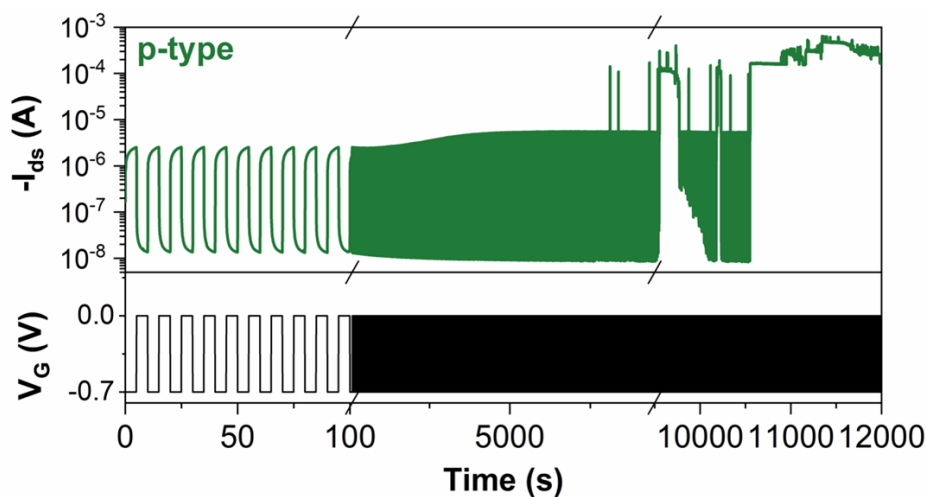


Figure 6.S5: P-type ($V_g=-0.7V$, $V_{ds}=-0.1V$) OECTs operation stability in 100mM NaCl aqueous electrolyte. A gate voltage pulse V_g was applied for 5 s with an interval time of 5 s. The device became unstable after 950 cycles and broke down eventually.

6.5.3 Dopamine sensing

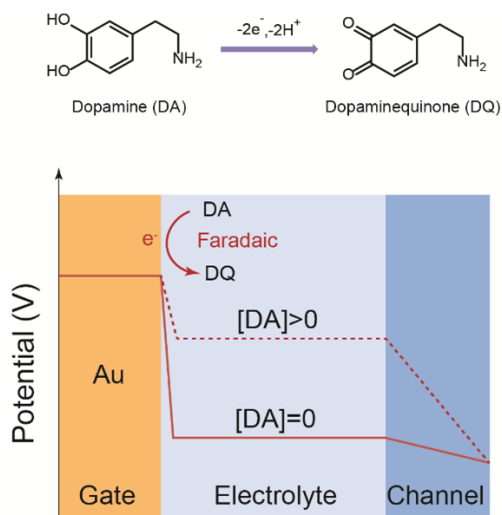


Figure 6.S6: Dopamine (DA) can be electrochemical oxidized to its quinone form (DQ). This schematic illustrates the potential drop across the Au gate OECTs system. When a gate potential (higher than the oxidation potential of DA) is applied, Dopamine is oxidized electrochemically at the Au gate electrode. The oxidation of DA generates Faradaic currents, which lower the potential drop across the Au/electrolyte interface, leading to more effective gating at the active channel.

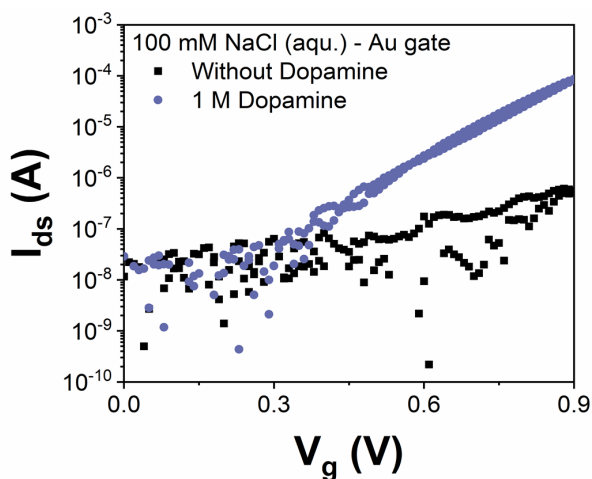


Figure 6.S7: Comparison of P-3O Au side-gated OECT transfer curve ($V_{ds}=0.1V$) with and without 1 M dopamine in 100mM NaCl aqueous electrolyte.

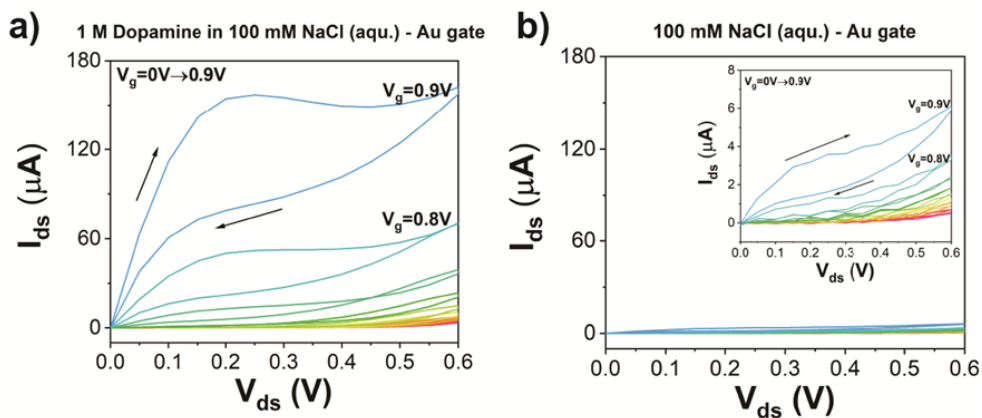


Figure 6.S8: Comparison of P-3O Au side-gated OEECT output curve a) with 1 M dopamine, b) without dopamine in 100mM NaCl aqueous electrolyte.

6.5.4 EC-RAM

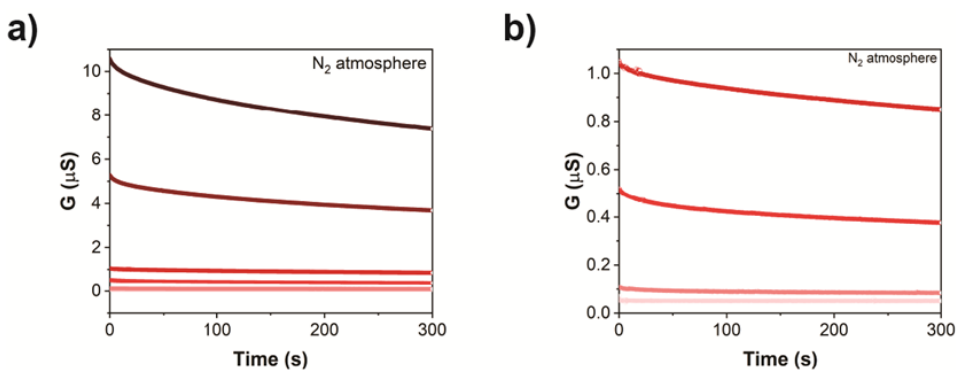


Figure 6.S9: Linear plot of P-3O EC-RAMs n-type conductance state retention over time (5 mins).

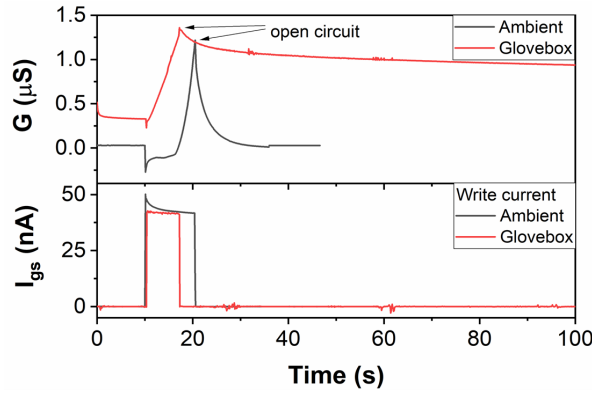


Figure 6.S10: The retention time comparison of P-3O EC-RAM devices n-type operation in ambient and N₂ atmosphere glovebox. The conductance state decays faster when oxygen and water present ($V_{ds}=0.1V$).

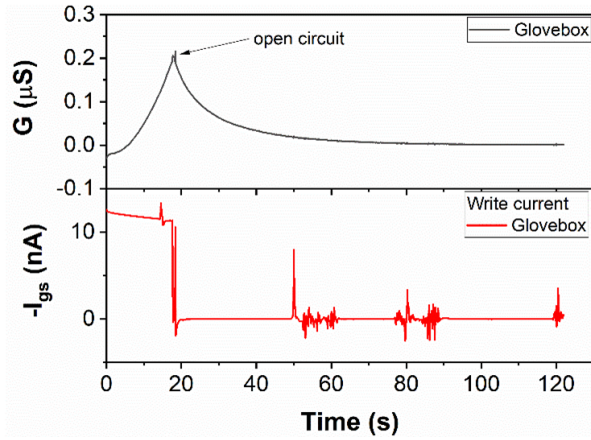


Figure 6.S11: The retention time of P-3O EC-RAM devices p-type operation in N₂ atmosphere glovebox. The conductance state decays very fast ($V_{ds}=-0.1V$).

6.5.5 Ambipolar inverter

The ambipolar inverter is realized by connecting two single ion-gated transistors with a shared ion gel or aqueous electrolyte. One of the two channels of the Keithley SMU 2636B is used to supply the input voltage (V_{in}) whereas the other channel is used for the potential at V_{DD} . Each of these voltages including the output voltage (V_{out}) is recorded with a DAQ NI USB-6353. The operation with either a solid ion gel or aqueous electrolyte shows the transition from a high to low output at a different input value. This correlates to the different values of the threshold voltage obtained from the transfer curve (Figure 6.S2 and 6.S4). The higher

gain for aqueous electrolyte gated inverters can be explained by the higher on/off ratio for the individual OEET devices. Due to the increased conductance at the gate-electrolyte interface the voltage drop across this interface is reduced and the gating at the channel is more effective compared to the ion-gel gated equivalent.

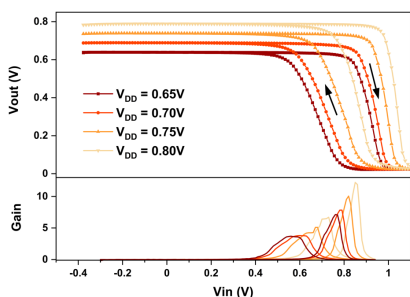


Figure 6.S12: Solid state ambipolar inverter behavior for increasing V_{DD} (0.65V to 0.80V). Input voltage V_{in} is scanned from -0.3V to 1.1V and back (0.01V/s).

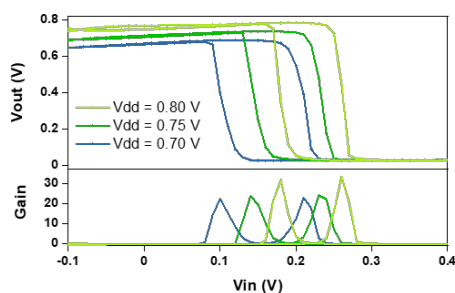


Figure 6.S13: Aqueous gated ambipolar inverter behavior for increasing V_{DD} (0.70V to 0.80V). Input voltage V_{in} is scanned from -0.2V to 0.5V and back (0.01V/s).

The neuromorphic ambipolar inverter is configured in a similar fashion as the regular ambipolar inverter, with the difference that the EC-RAM channel is in series with the gate (previously V_{in}) of the regular inverter. The conductance state of the EC-RAM is modified with Keithley SMU 2602B using LabView software.

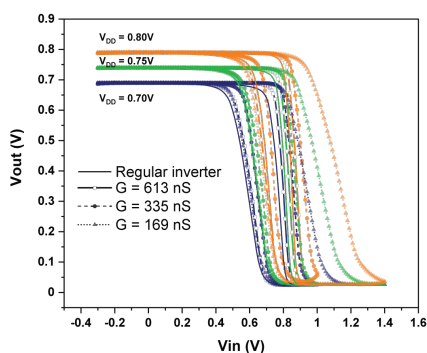


Figure 6.S14: Solid-state neuromorphic inverter behavior for $V_{DD} = 0.70V$, $V_{DD} = 0.75V$, and $V_{DD} = 0.80V$ with each scan a decreasing EC-RAM conductance. Input voltage V_{in} is scanned from -0.3V to 1.0V and back (0.01V/s). For the sweep at the lowest conductance value V_{in} is scanned to 1.4V in order to completely turn the inverter output off.

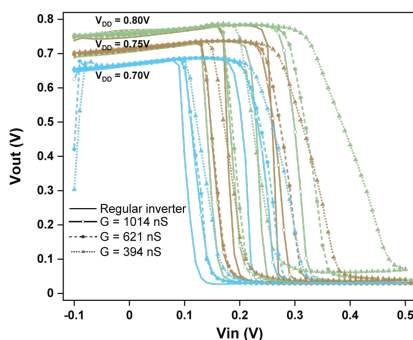


Figure 6.S15: Aqueous neuromorphic inverter behavior for $V_{DD} = 0.70V$, $V_{DD} = 0.75V$, and $V_{DD} = 0.80V$ with each scan a decreasing EC-RAM conductance. Input voltage V_{in} is scanned from -0.1V to 0.5V and back (0.01V/s).

6.5.6 Neuromorphic inverter simulation for EMG signal processing

The experimental results of the neuromorphic inverter, V_{out} as a function of the input voltage, are fitted by

$$V_{out}(V_{in}) = B / (1 + e^{(V_{in} - V_m)^A}) + C \quad (6.1)$$

where the constants B and C, 0.76 and 0.02 respectively, determine the range of V_{out} . V_m is the voltage at the maximum gain and A describes the slope at the transition region. For the neuromorphic inverter at state 1, $V_m = 0.844$ and $A = 64.8$, resembling an inverter with a negligible EC-RAM resistance at the gate. For state 2, $V_m = 1.115$ and $A = 15$, simulating the neuromorphic inverter with an EC-RAM conductance value of 169 nS. The EMG data is obtained from gestures data set [42] and the signals used are measured through channel 1 while person 1 makes two gestures, hand clenched into a fist and second wrist extension. The baseline is considered to be the signal while the hand is in rest position. The root-mean-square (RMS) envelope of the EMG signal is calculated using a moving window of 50 bins. The EMG signals from the database are multiplied by 200 and given an offset equal to V_m in order to compute the output from the neuromorphic inverter.

6.5.7 EC-RAM based neural network simulation

In order to verify the EC-RAM's ability to function as the weight in a hardware neural network, the classification performance of an array of these devices is examined. A model of a crossbar array is simulated using a customized Python script. The network architecture consists of 3 layers (125 x 100 x 5) and is used to classify 5 different heartbeat waveforms: normal sinus rhythm (NSR), atrial fibrillation (AFIB), premature ventricular contraction (PVC), ventricular bigeminy (Bigeminy), left bundle branch block beat (LBBBB) from the MIT-BIH Arrhythmia database [43]. The data is processed by down sampling to 125 Hz, cut at 1s intervals and normalized before applying it to the neural network. The experimental weights are extracted from the conductance modulation measurement (Figure 6.4B) with 14 potentiation and depression cycles of 32 measured states. To introduce negative weight values, the weights are offset by $-5.02 \cdot 10^{-7}$ S ensuring an equal gradient value ΔG for potentiation and depression at $G=0$. The dataset is trained for 50 epochs with a ReLU activation function for the hidden layer and a piecewise linear activation function for the output layer. The piecewise linear function maps input values between 0 and 1 over a linear domain between the boundaries of -1 and 1. Between the layers the output is multiplied by $7.69 \cdot 10^5$ and $1 \cdot 10^6$, respectively, to correct for the low conductance value and scaled to the layer size, preventing the signals to vanish. To validate the efficacy of the EC-RAM based crossbar array the experimentally derived weights are compared to the ideal numeric weights. The numeric analyses simulate the perfect EC-RAM, i.e. no read/write noise and no non-linearity. The read/write noise and non-linearity that are used in the experimental analyses are directly derived from the measurements where potentiation and depression cycles are separated. The update value (conductance) consists of the average update step (ΔG_0) over multiple cycles plus the contribution of the write noise

which is characterized as the standard deviation (σ_{wr}) of the mean (ΔG_0) and then sampled from a Gaussian distribution $\mathcal{N}(0, \sigma^2)$. The non-linearity of the device is included as well since the average update step (ΔG_0) changes over the conductance domain. The read noise is also implemented as a standard deviation (σ_{rd}) with the assumption that state retention decays linearly. In this way, the measurement data accounts for both read/write noise and non-linearity (see Table 6.S2).

Table 6.S2: Read and write noise, and offset for both potentiation and depression used to simulate the EC-RAM based neural network

	Potentiation	Depression
Read noise (σ_{rd})	$4.60 \cdot 10^{-10}$	$4.27 \cdot 10^{-10}$
Write noise (σ_{wr})	$6.64 \cdot 10^{-10}$	$8.61 \cdot 10^{-10}$
Offset	$5.02 \cdot 10^{-7}$	$5.02 \cdot 10^{-7}$

Author Contributions

Eveline van Doremaele and YZ contributed equally to this work. YZ, GY, JS, and YvdB initiated the idea. YvdB supervised the project. GY, JS, and RCC designed the polymer. GY synthesized and characterized the polymer. **Eveline van Doremaele**, YZ, and YvdB designed the experiments. **Eveline van Doremaele** and YZ, performed device fabrications and the measurements. **Eveline van Doremaele** and TS performed the simulations. **Eveline van Doremaele**, YZ, and GY prepared the manuscript. **Eveline van Doremaele**, YZ, and YvdB wrote the manuscript. All the authors contributed to the comments and suggestions on the final manuscript.

Bibliography

1. Khodagholy, D. *et al.* [In vivo recordings of brain activity using organic transistors](#). en. *Nature Communications* **4**. Number: 1 Publisher: Nature Publishing Group, 1575. ISSN: 2041-1723 (Mar. 2013).
2. Khodagholy, D. *et al.* [High transconductance organic electrochemical transistors](#). en. *Nature Communications* **4**. Number: 1 Publisher: Nature Publishing Group, 2133. ISSN: 2041-1723 (July 2013).
3. Romele, P. *et al.* [Multiscale real time and high sensitivity ion detection with complementary organic electrochemical transistors amplifier](#). en. *Nature Communications* **11**. ISSN: 2041-1723 (Dec. 2020).
4. Pappa, A.-M. *et al.* [Organic Electronics for Point-of-Care Metabolite Monitoring](#). *Trends in Biotechnology* **36**, 45–59. ISSN: 0167-7799 (Jan. 2018).
5. He, R.-X. *et al.* [Detection of bacteria with organic electrochemical transistors](#). en. *Journal of Materials Chemistry* **22**. Publisher: The Royal Society of Chemistry, 22072–22076. ISSN: 1364-5501 (Oct. 2012).
6. Guo, K. *et al.* [Rapid single-molecule detection of COVID-19 and MERS antigens via nanobody-functionalized organic electrochemical transistors](#). en. *Nature Biomedical Engineering* **5**, 666–677. ISSN: 2157-846X (May 2021).
7. Van de Burgt, Y. *et al.* [A non-volatile organic electrochemical device as a low-voltage artificial synapse for neuromorphic computing](#). en. *Nature Materials* **16**, 414–418. ISSN: 1476-1122, 1476-4660 (Apr. 2017).
8. Gkoupidenis, P., Schaefer, N., Garlan, B. & Malliaras, G. G. [Neuromorphic Functions in PEDOT:PSS Organic Electrochemical Transistors](#). *Advanced Materials* **27**, 7176–7180. ISSN: 1521-4095 (2015).
9. Keene, S. T., Melianas, A., van de Burgt, Y. & Salleo, A. [Mechanisms for Enhanced State Retention and Stability in Redox-Gated Organic Neuromorphic Devices](#). *Advanced Electronic Materials* **5**, 1800686. ISSN: 2199-160X (Feb. 2019).
10. Fuller, E. J. *et al.* [Parallel programming of an ionic floating-gate memory array for scalable neuromorphic computing](#). en. *Science*, eaaw5581. ISSN: 0036-8075, 1095-9203 (Apr. 2019).

11. Gkoupidenis, P., Koutsouras, D. A. & Malliaras, G. G. **Neuromorphic device architectures with global connectivity through electrolyte gating.** en. *Nature Communications* **8**, 15448 (May 2017).
12. Keene, S. T. *et al.* **A biohybrid synapse with neurotransmitter-mediated plasticity.** en. *Nature Materials*. ISSN: 1476-1122, 1476-4660 (June 2020).
13. Nielsen, C. B. *et al.* **Molecular Design of Semiconducting Polymers for High-Performance Organic Electrochemical Transistors.** en. *Journal of the American Chemical Society* **138**, 10252–10259. ISSN: 0002-7863, 1520-5126 (Aug. 2016).
14. Keene, S. T. *et al.* **Enhancement-Mode PEDOT:PSS Organic Electrochemical Transistors Using Molecular De-Doping.** en. *Advanced Materials* **32**. _eprint: <https://onlinelibrary.wiley.com/doi/pdf/10.1002/adma.202000270>, 2000270. ISSN: 1521-4095 (2020).
15. Sun, H. *et al.* **Complementary Logic Circuits Based on High-Performance n-Type Organic Electrochemical Transistors.** en. *Advanced Materials* **30**. _eprint: <https://onlinelibrary.wiley.com/doi/pdf/10.1002/adma.201704916>, 1704916. ISSN: 1521-4095 (2018).
16. Sun, H., Gerasimov, J., Berggren, M. & Fabiano, S. **n-Type organic electrochemical transistors: materials and challenges.** en. *Journal of Materials Chemistry C* **6**. Publisher: The Royal Society of Chemistry, 11778–11784. ISSN: 2050-7534 (Nov. 2018).
17. Wang, Z. *et al.* **Resistive switching materials for information processing.** en. *Nature Reviews Materials* **5**. Number: 3 Publisher: Nature Publishing Group, 173–195. ISSN: 2058-8437 (Mar. 2020).
18. Doremaele, E. R. W. v., Gkoupidenis, P. & Burgt, Y. v. d. **Towards organic neuromorphic devices for adaptive sensing and novel computing paradigms in bioelectronics.** en. *Journal of Materials Chemistry C* **7**. Publisher: The Royal Society of Chemistry, 12754–12760. ISSN: 2050-7534 (Oct. 2019).
19. Moin, A. *et al.* **A wearable biosensing system with in-sensor adaptive machine learning for hand gesture recognition.** en. *Nature Electronics* **4**, 54–63. ISSN: 2520-1131 (Jan. 2021).
20. Ohayon, D. *et al.* **Influence of Side Chains on the n-Type Organic Electrochemical Transistor Performance.** en. *ACS Applied Materials & Interfaces* **13**, 4253–4266. ISSN: 1944-8244, 1944-8252 (Jan. 2021).

21. Samuel, J. J. *et al.* Single-Component CMOS-Like Logic using Diketopyrrolopyrrole-Based Ambipolar Organic Electrochemical Transistors. en. *Advanced Functional Materials* **31**. _eprint: <https://onlinelibrary.wiley.com/doi/pdf/10.1002/adfm.202102903>, 2102903. ISSN: 1616-3028 (2021).
22. Rashid, R. B. *et al.* Ambipolar inverters based on cofacial vertical organic electrochemical transistor pairs for biosignal amplification -supp. en. *Science Advances* **7**, eabh1055. ISSN: 2375-2548 (Sept. 2021).
23. Griggs, S., Marks, A., Bristow, H. & McCulloch, I. n-Type organic semiconducting polymers: stability limitations, design considerations and applications. en. *Journal of Materials Chemistry C* **9**. Publisher: The Royal Society of Chemistry, 8099–8128. ISSN: 2050-7534 (July 2021).
24. Surgailis, J. *et al.* Mixed Conduction in an N-Type Organic Semiconductor in the Absence of Hydrophilic Side-Chains. en. *Advanced Functional Materials* **31**. _eprint: <https://onlinelibrary.wiley.com/doi/pdf/10.1002/adfm.202010165>, 2010165. ISSN: 1616-3028 (2021).
25. Wang, S. *et al.* A Chemically Doped Naphthalenediimide-Bithiazole Polymer for n-Type Organic Thermoelectrics. en. *Advanced Materials* **30**. _eprint: <https://onlinelibrary.wiley.com/doi/pdf/10.1002/adma.201801898>, 1801898. ISSN: 1521-4095 (2018).
26. Liu, J. *et al.* N-Type Organic Thermoelectrics of Donor–Acceptor Copolymers: Improved Power Factor by Molecular Tailoring of the Density of States. en. *Advanced Materials* **30**. _eprint: <https://onlinelibrary.wiley.com/doi/pdf/10.1002/adma.201804290>, 1804290. ISSN: 1521-4095 (2018).
27. Zhong, Y., Saleh, A. & Inal, S. Decoding Electrophysiological Signals with Organic Electrochemical Transistors. en. *Macromolecular Bioscience* **21**. _eprint: <https://onlinelibrary.wiley.com/doi/pdf/10.1002/mabi.202100187>, 2100187. ISSN: 1616-5195 (2021).
28. Liu, Q. *et al.* Fully Printed All-Solid-State Organic Flexible Artificial Synapse for Neuromorphic Computing. en. *ACS Applied Materials & Interfaces* **11**, 16749–16757. ISSN: 1944-8244, 1944-8252 (May 2019).
29. Lee, K. H. *et al.* “Cut and Stick” Rubbery Ion Gels as High Capacitance Gate Dielectrics. *Advanced Materials* **24**. _eprint: <https://onlinelibrary.wiley.com/doi/pdf/10.1002/adma.201200950>, 4457–4462. ISSN: 1521-4095 (2012).

30. Cho, J. H. *et al.* High-Capacitance Ion Gel Gate Dielectrics with Faster Polarization Response Times for Organic Thin Film Transistors. *Advanced Materials* **20**. _eprint: <https://onlinelibrary.wiley.com/doi/pdf/10.1002/adma.200701069>, 686–690. ISSN: 1521-4095 (2008).
31. Sekitani, T. *et al.* Ultraflexible organic amplifier with biocompatible gel electrodes. en. *Nature Communications* **7**. Number: 1 Publisher: Nature Publishing Group, 11425. ISSN: 2041-1723 (Apr. 2016).
32. Jiang, C. *et al.* Printed subthreshold organic transistors operating at high gain and ultralow power. *Science* **363**. Publisher: American Association for the Advancement of Science, 719–723 (Feb. 2019).
33. Cea, C. *et al.* Enhancement-mode ion-based transistor as a comprehensive interface and real-time processing unit for in vivo electrophysiology. en. *Nature Materials* **19**, 679–686. ISSN: 1476-1122, 1476-4660 (June 2020).
34. Krauhausen, I. *et al.* Organic neuromorphic electronics for sensorimotor integration and learning in robotics. EN. *Science Advances*. Publisher: American Association for the Advancement of Science (Dec. 2021).
35. Melianas, A. *et al.* Temperature-resilient solid-state organic artificial synapses for neuromorphic computing. en. *Science Advances* **6**, eabb2958. ISSN: 2375-2548 (July 2020).
36. Choi, Y., Oh, S., Qian, C., Park, J.-H. & Cho, J. H. Vertical organic synapse expandable to 3D crossbar array. en. *Nature Communications* **11**. Number: 1 Publisher: Nature Publishing Group, 4595. ISSN: 2041-1723 (Sept. 2020).
37. Oh, S. *et al.* Flexible artificial Si-In-Zn-O/ion gel synapse and its application to sensory-neuromorphic system for sign language translation. *Science Advances* **7**. Publisher: American Association for the Advancement of Science, eabg9450 (Oct. 2021).
38. Quill, T. J. *et al.* Ion Pair Uptake in Ion Gel Devices Based on Organic Mixed Ionic–Electronic Conductors. en. *Advanced Functional Materials* **31**. _eprint: <https://onlinelibrary.wiley.com/doi/pdf/10.1002/adfm.202104301>, 2104301. ISSN: 1616-3028 (2021).
39. Moser, M. *et al.* Polaron Delocalization in Donor–Acceptor Polymers and its Impact on Organic Electrochemical Transistor Performance. en. *Angewandte Chemie International Edition* **60**. _eprint: <https://onlinelibrary.wiley.com/doi/pdf/10.1002/anie.202014078>, 7777–7785. ISSN: 1521-3773 (2021).

40. Ham, S. *et al.* One-dimensional organic artificial multi-synapses enabling electronic textile neural network for wearable neuromorphic applications. *Science Advances* **6**. Publisher: American Association for the Advancement of Science, eaba1178 (July 2020).
41. Zhang, Y. *et al.* Adaptive Biosensing and Neuromorphic Classification Based on an Ambipolar Organic Mixed Ionic–Electronic Conductor. en. *Advanced Materials* **34**. _eprint: <https://onlinelibrary.wiley.com/doi/pdf/10.1002/adma.202200393>, 2200393. ISSN: 1521-4095 (2022).
42. Dua, D. & Graff, C. *UCI Machine Learning Repository* 2019.
43. Plawiak, P. ECG signals (1000 fragments). *Mendeley Data*, V3 (2017).

Chapter 7

High-performance organic electrochemical transistors and neuromorphic devices comprising naphthalenediimide-dialkoxybithiazole copolymers bearing glycol ether pendant groups

Organic electrochemical transistors (OECTs) have emerged as building blocks for low power circuits, biosensors, and neuromorphic computing. While p-type polymer materials for OECTs are well developed, the choice of high-performance n-type polymers is limited, despite being essential for cation and metabolite biosensors, and crucial for constructing complementary circuits. N-type conjugated polymers that have efficient ion-to-electron transduction are highly desired for electrochemical applications. In this contribution, three non-fused, planar naphthalenediimide (NDI)-dialkoxybithiazole (2Tz) copolymers, which systematically increase the amount of polar tri(ethylene glycol) (TEG) side chains: PNDI2OD-2Tz (0 TEG), PNDIODTEG-2Tz (1 TEG), PNDI2TEG-2Tz (2 TEG), are reported. It is demonstrated that the OECT performance increases with the number of TEG side chains resulting from the progressively higher hydrophilicity and larger electron affinities. Benefiting from the high electron mobility, excellent ion conduction capability, efficient ion-to-electron transduction, and low-lying lowest unoccupied molecular orbital energy level, the 2 TEG polymer achieves close to 10^5 on-off ratio, fast switching, 1000 stable operation cycles in aqueous electrolyte, and has a long shelf life. Moreover, the higher number TEG chain substituted polymer exhibits good conductance state retention over two orders of magnitudes in electrochemical resistive random-access memory devices, highlighting its potential for neuromorphic computing.

This chapter is based on *High-Performance Organic Electrochemical Transistors and Neuromorphic Devices Comprising Naphthalenediimide-Dialkoxybithiazole Copolymers Bearing Glycol Ether Pendant Groups*, Y. Zhang, ..., Eveline R.W. van Doremale, et al., *Advanced Functional Materials*, **32**, (27), 2022. Main contribution to this work is in device fabrication and characterization.

7.1 Introduction

Organic electrochemical transistors (OECTs) are ion-gated devices operated by modulating the bulk conductivity of organic (semi)conductors. [1] This electrochemical doping process allows OECTs to operate at low voltage (<1 V) and achieve high transconductance,[2] key features and advantages of OECTs compared with field-effect transistors. OECTs are ideal devices for a wide variety of applications, including printed logic circuitry,[3] bioelectronics,[4] neural signal recording,[5] and neuromorphic computing.[6, 7] The active OECT channel material is an organic mixed ionic-electronic conductor (OMIEC), which effectively transports and couples ionic and electronic charges.[8] To develop high-performance OMIECs, it is crucial to understand the structure-properties relationship of the polymers in all aspects of molecular engineering, such as backbone, side chains, and substituents on the molecular structures.[9] Biological applications require stable OECT operation in aqueous environments, which means that water and oxygen should not deteriorate the organic semiconductors/conductors under electrical stress. During device operation, ions migrate from the aqueous electrolyte into the polymer thin films driven by a gate voltage, followed by electrochemically doping/de-doping of the polymers resulting in the modulation of the bulk conductivity. Organic p-type semiconducting/conducting polymers, which conduct holes, have been studied intensively,[10] including the widely used commercial conducting polymer poly(3,4-ethylenedioxythiophene):poly(styrenesulfonate) (PEDOT:PSS). The development of n-type semiconducting polymers has been driven by the expansion of organic electronic applications as they are indispensable components combined with p-type materials for complementary logical circuits and energy storage.[11] Moreover, n-type semiconductors are essential for enhancement-mode biosensors for anions and metabolites.[12]

The molecular design strategy for OECT channel materials revolves around improving the ion-to-electron transduction between semiconductor and electrolyte, which is usually referred to as the OECT transconductance g_m ($g_m = \partial I_d / \partial V_G = \frac{Wd}{L} \mu C^* (V_g - V_{Th})$), which is proportional to μC^* . Here, μ is the charge carrier mobility and C^* is the volumetric capacitance. Ordinary n-type conjugated polymers cannot be directly applied to aqueous electrolyte-gated OECTs due to the low ion transport into and throughout the film. This incompatibility is ostensibly due to the hydrophobic (alkyl) side chains that are commonly used to impart solubility in organic solvents and are not an intrinsic property of n-type polymer backbones. To test this hypothesis, we replaced the hydrophobic side chains with hydrophilic polar tri(ethylene glycol) (TEG). TEG substituted naphthalenediimide (NDI)-bithiophene (2T) conjugated polymers have previously been shown to function in n-type OECTs.[13] On the other hand, a follow-up study revealed that the electron mobility of that NDI-2T based polymer drops significantly from 0.132 to 0.00184 $\text{cm}^2 \text{V}^{-1} \text{s}^{-1}$ as the fraction of glycol chains (to alkyl chains) increases.[14] Moreover, the localization of charge carriers leads to the low electron mobility of NDI-2T donor-acceptor type conjugated polymer.[15, 16] Flexible polymer backbones exacerbate this problem by distorting in response to the intercalation of ions.[17] It is thus challenging to design a polymer that exhibits both high ionic and electronic mobility across a useful range of ionic doping levels. At the same time, the retention of a highly ordered crystalline structure during ionic doping is ideal for high-performance OECTs by retaining a high mobility μ as well as high volumetric capacitance C^* . For example, the

OECT performance of the NDI-2T based polymer P-90 has been further improved via solvent engineering to increase crystallinity.[18] It has been demonstrated that the fused, electron-deficient ladder-type polymer, poly(benzimidazobenzophenanthroline) (BBL), not only has a highly planar and rigid backbone but also has highly delocalized charge carriers,[19] performs well in n-type OECTs.[20] Based on this concept, polymers with highly planar and rigid backbones, such as the fully-fused, electron-deficient lactam-based PgNaN[21] and fused bithiophene imide dimer-based f-BTI2TEG-FT,[22] have been developed to enhance charge mobility.

Although fused conjugated polymers have achieved significant progress, they have a synthetically-limited library that makes it increasingly difficult to develop better materials for n-type OECT to match the high performance of their p-type counterparts. There are more choices for building blocks to construct non-fused conjugated polymers, but they must be designed carefully to avoid localizing carriers and attenuating mobility. It is possible to approach the coplanar and rigid polymer backbones by manipulating intramolecular interactions (such as S–O interaction and F–H bonding).[23] Moreover, TEG side chains favor dense molecular packing with decreased π – π stacking distances in diketopyrrolopyrrole (DPP) based polymers.[24] Hence, we propose that non-fused n-type planar and rigid conjugated polymers accompanying TEG side chains can simultaneously realize high ion transport capability as well as electron mobility for electrochemical applications.

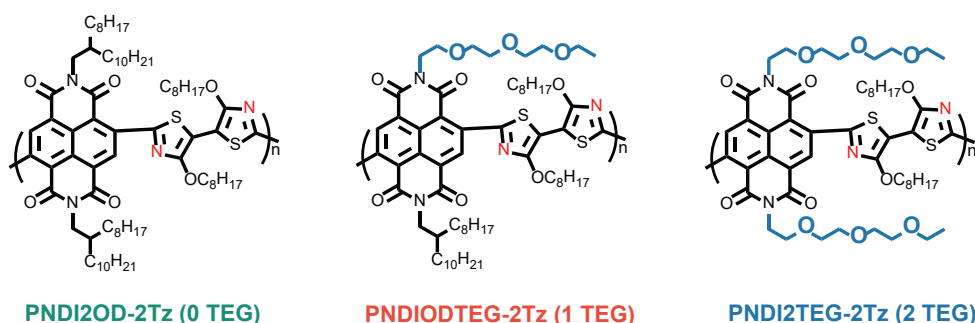


Figure 7.1: Chemical structures of NDI-2Tz based D–A copolymers with different substituted EG side chains: PNDI2OD-2Tz (0 TEG), PNDIODTEG-2Tz (1 TEG) and PNDI2TEG-2Tz (2 TEG).

In this contribution, we investigate non-fused planar naphthalenediimide (NDI)-dialkoxybithiazole (2Tz) based copolymers for electrochemical applications (shown in Figure 7.1). We opt to control the density of the polar tri(ethylene glycol) (TEG) side chains to achieve high electron mobility and ion penetration capability simultaneously. Owing to the high planarity and rigidity of the backbone and higher density of TEG chains, conjugated polymer PNDI2TEG-2Tz (2 TEG) led to n-type OECTs achieving a high μ_e of $3.16 \times 10^{-3} \text{ cm}^2 \text{V}^{-1} \text{s}^{-1}$, a good C^* of 367 Fcm^{-3} , and high μC^* $1.16 \text{ Fcm}^{-1} \text{V}^{-1} \text{s}^{-1}$, close to 10^5 on-off ratio, fast switching (within 0.1s), 1000 stable operation cycles in aqueous electrolyte, and long shelf life. Moreover, PNDI2TEG-2Tz (2 TEG) and PNDIODTEG-2Tz (1 TEG) also exhibit p-type performance due to their matched energy

levels. We also developed OECT based complementary inverters with a maximum gain of 23.4. Notably, PNDI2TEG-2Tz (2 TEG) exhibits good conductance state retention over 2 orders of magnitudes in electrochemical resistive random-access memory devices (EC-RAMs), highlighting its potential for neuromorphic computing. This work demonstrates that non-fused donor-acceptor conjugated polymer can achieve high electron mobility and ion penetration capability simultaneously for OECT. And it contributes to a deep understanding of the relationship between the polymer structures and the n-type OECT performance, which opens a window to design high-performance n-type OECT materials.

7.2 Results and discussion

7.2.1 Molecular Design and Characterization

N-type conjugated polymers that simultaneously have high electron mobility and efficient ion transport properties are highly desired and are ideal candidates for channel materials in OECTs. Generally, the mobility of conjugated polymers is governed by the backbone that controls the electronic structure.[25–28] Previous research has demonstrated that incorporation of hydrophilic TEG side chains onto the conjugated backbone can enhance the aqueous ions uptake and transport.[8, 29–32] A rational combination of a proper conjugated backbone and TEG side chain could achieve both high electron mobility and efficient ion transport properties. NDI-2T based conjugated polymers have been demonstrated to have a planar and rigid backbone due to the reduced steric repulsions between bithiazole and the adjacent NDI core. In addition, the electron-deficient nature of bithiazole enhances the polymer electron affinity which would be beneficial for electrochemical doping and charge carrier mobility.[15, 33]

Figure 7.1 shows the chemical structures of non-fused NDI-2Tz copolymers: PNDI2OD-2Tz (abbreviated as 0 TEG), PNDIODTEG-2Tz (abbreviated as 1 TEG), and PNDI2TEG-2Tz (abbreviated as 2 TEG). The NDI-2Tz based polymers were synthesized by a palladium-catalyzed typical Stille cross-coupling polymerization of dibromo-NDI based monomers with distannyl-alkoxybithiazole based monomer after refluxing the polymerization mixture for three days. After polymerization, the resulting polymers were purified and low-molecular-weight fractions were removed by successive Soxhlet extraction with methanol and hexane. The purified high-molecular-weight polymers were extracted with chloroform, precipitated in methanol, and further dried under vacuum. The relative molecular weights M_n , M_w and polydispersity (PDI) of these three NDI-2Tz based polymers were determined by high-temperature gel permeation chromatography (GPC) analysis against polystyrene standards using trichlorobenzene as the eluent at 150 °C.

The thermal properties of these three NDI-2Tz based conjugated polymers were evaluated by thermogravimetric analysis (TGA) and differential scanning calorimetry (DSC). The temperature of 5% weight loss was selected as the onset point of decomposition. All the polymers exhibited excellent stability with decomposition temperatures beyond 330 °C. We did not observe any thermal transition for these polymers from the differential scanning calorimetry analysis in the range of –20 to 300 °C.

Optical properties of all NDI-2Tz based polymers were measured by UV–vis–near-infrared absorption in dilute chloroform solution and thin film state, and the spectra are shown in Figure 7.S2 (Supporting Information) with the corresponding parameters summarized in Table 7.1. All NDI-2Tz polymers exhibit a strong absorption in the range of 600–1000 nm in solution due to intramolecular charge transfer between the acceptor NDI unit and the donor dialkoxybithiazole unit. The less pronounced π – π^* transition absorption (300–500 nm) in the NDI-2Tz based polymers indicate the highly planar backbone. When going from solution to film, we observed no obvious redshifts for the λ_{max} peaks, indicating high backbone rigidity for these three copolymers. The band-tail absorption increases as the density of the EG side chain in thin films increases. Because of the higher density of the tri(ethylene glycol) side chains, the polarizability around the polymer backbone increases. This phenomenon can be regarded as the solid-state equivalent of solvatochromism, which affects the charge-transfer band.[34] Based on the thin film absorption onsets, the optical band gaps are calculated to be 1.05, 1.00, and 0.97 eV for 0 TEG, 1 TEG, and 2 TEG, respectively.

Table 7.1: Optical properties, electrochemical properties, energy levels, and water contact angle (θ) of the TEG series polymers

Polymer	$\lambda_{onset\ film}$ (nm)	E_g^{opt} (eV)*	HOMO (eV) [†]	LUMO (eV) [‡]	E_{onset}^{ox} (V)	E_{onset}^{red} (V)	θ
0 TEG	1177	1.05	-5.81	-4.05	0.711	-1.049	104.2 ± 5.5
1 TEG	1238	1.00	-5.68	-4.24	0.581	-0.855	97.6 ± 1.0
2 TEG	1280	0.97	-5.63	-4.35	0.533	-0.746	83.3 ± 1.4

* Optical bandgap calculated using the onset of the thin film absorption spectra ($E_g^{opt} = 1240/\lambda_{onset}$)

[†] Onset of CV oxidation recorded in a CHCN3 solution containing Bu4NPF6 electrolyte. HOMO = $-(5.10 + E_{onset}^{ox})$ eV.

[‡] Onset of CV reduction recorded in a CHCN3 solution containing Bu4NPF6 electrolyte. LUMO = $-(5.10 + E_{onset}^{red})$ eV.

The cyclic voltammetry (CV) characterization of all NDI-2Tz based polymers was carried out to investigate the effects of TEG side-chain density on the energy level. As shown in Figure 7.S3 (Supporting Information), all polymers exhibit distinctive reduction and oxidation peaks in a CHCN3 solution containing 0.1 M Bu4NPF6 electrolyte. The highest occupied molecular orbital (HOMO) and the lowest unoccupied molecular orbital (LUMO) energy levels of these three polymers are calculated from the onset of oxidation and reduction potentials using the equation $E_{HOMO} = -(5.10 + E_{onset}^{ox})$ eV and $E_{LUMO} = -(5.10 + E_{onset}^{red})$ eV, respectively. The onset reduction potentials of 0 TEG, 1 TEG, and 2 TEG relative to the half-wave potential of ferrocene/ferrocenium (Fc/Fc⁺) were -1.05, -0.86, and -0.75 V, respectively, which correspond to estimated LUMO energies of -4.05, -4.24, and -4.35 eV. The relatively deep LUMO levels are the result of the strong electron affinity of the acceptor monomer naphthalenediimide (NDI) and the electron-deficient nature of bithiazole (2Tz). The LUMO levels decrease with the density of the TEG side chain which indicates the glycol ethers have inductive effects on the electronic structure.[35, 36] The onset oxidation potentials of 0 TEG, 1 TEG and 2 TEG relative to Fc/Fc⁺ redox were 0.71, 0.58, and 0.53 V, respectively, which correspond to estimated HOMO energies of -5.81, -5.68, and -5.63 eV. The increased HOMO energy level also benefits the hole transport, which results in ambipolar OECT operation.

7.2.2 Aqueous Electrolyte Gated OECTs

Following polymer synthesis and characterization, we fabricated OECTs by employing interdigitated electrodes as source and drain (channel length of 5 μm , MicruX technologies) and using these polymers as the channel material and evaluated their OECT performance, as illustrated in Figure 7.2. The conjugated polymers were deposited by spin coating using chloroform as a solvent without additives or further annealing steps. The device fabrication details are provided in the supporting information. We subsequently investigated the device performance employing an aqueous 100 mM NaCl solution electrolyte and an Ag/AgCl gate electrode. The transfer characteristics of these polymers are shown in Figure 7.2b and the corresponding OECT parameters are summarized in Table 7.2. Both 1 TEG and 2 TEG exhibit ambipolar OECT character with n-type dominated performance and increasing current with increasing VG indicating that the devices operate in accumulation mode. The solely alkyl chain substituted polymer 0 TEG is unable to be gated (i.e., no turn-on current when applying gate voltage). 2 TEG, which has the highest density of TEG side chains, exhibits the highest on-current among these three polymers. A detailed comparison between 1 TEG and 2 TEG in OECT performance is presented in Figure 7.2c–h. 2 TEG exhibits a large on-off ratio close to 10^5 (9.2×10^4 , Figure 7.2f) while 1 TEG displays $\approx 10^4$ ratio (Figure 7.2c) in semi-log transfer curves, compared with NDI-bithiophene based polymers that have a reported on-off ratio of $\approx 10^3$, [37] and BBL which has an on-off ratio of 6×10^3 . [20] The maximum transconductance of 2 TEG based OECTs is attained at a VG of 0.8 V with an average value of 51.8 mS, which is four times higher than that of 1 TEG (average value of 12.3 mS, at VG = 0.8 V). 1 TEG shows a much larger hysteresis in both transfer and output curves (Figure 7.2c,d) than 2 TEG (Figure 7.2f,g), indicating that ion motion in 1 TEG is much slower than in 2 TEG. To evaluate the response speed of 1 TEG and 2 TEG OECTs, the transient response time of 1 TEG is extracted by an exponent fit to the source-drain current under pulsed gate voltage in Figure 7.2e. 1 TEG is slow with time constants $\tau_{on/off} = 5.7/0.56$ s for ON and OFF. 2 TEG switches on and off in <100 ms (Figure 7.2h, the measurement is out of instrument resolution and therefore cannot be fitted).

Table 7.2: Aqueous electrolyte-gated OECT characteristics of the polymers.

Polymer	d (nm)	g_m (mS)	On/Off	V_{Th} (V)	μ_e^{OECT} ($\text{cm}^2\text{V}^{-1}\text{s}^{-1}$) [§]	C^* (Fcm^{-3})	μC^* ($\text{Fcm}^{-1}\text{V}^{-1}\text{s}^{-1}$)
PNDI2OD-2Tz	61.7 ± 13.0	N/A	N/A	N/A	N/A	N/A	N/A
PNDIODTEG-2Tz	56.0 ± 3.8	12.3 ± 3.7	$\approx 10^4$	0.75	N/A	N/A	N/A
PNDI2TEG-2Tz	49.4 ± 9.8	51.8 ± 2.5	$\approx 10^5$	0.54	3.16×10^{-3}	≈ 367	1.16 ± 0.28

To gain insight into the differences in performance of the polymers in OECTs, we investigated the influence of the side chains on the non-fused NDI-2Tz polymers' wettability, electrochemical properties, and molecular packing. Being able to interact with electrolytes is essential for OECTs and thus the wettability of the polymer film is critical for ion penetration and transport. The hydrophilicity of the polymers is studied by water contact angle (Figure 7.S1, Supporting Information), indicating that the contact angle decreases as the amount of TEG side chains increases. The 2 TEG polymer has the highest amount of TEG side chains, featuring the best wettability that enables efficient ion diffusion and electrochemical doping, while 0 TEG has

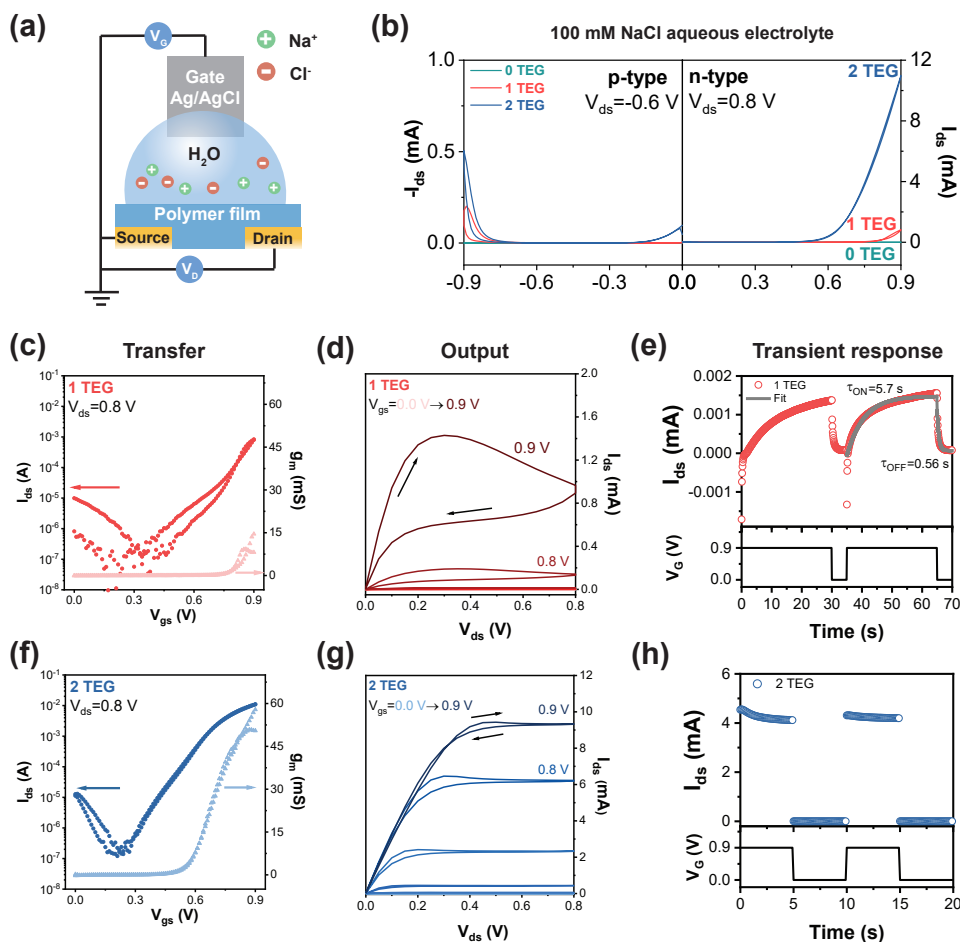


Figure 7.2: a) Cross-sectional schematic of OECT device. b) Comparison of OECT performance of the polymers with various number of TEG sidechains in 100 mM NaCl aqueous solution. Ambipolar linear transfer curves of 0 TEG, 1 TEG and 2 TEG. The on-current of OECTs increases with the hydrophilicity of the semiconducting polymers. Semi-log transfer curve of c) 1 TEG and f) 2 TEG. Output curve of d) 1 TEG and g) 2 TEG. Transient response of e) 1 TEG and h) 2 TEG.

only hydrophobic alkyl side chains, which prevents ions to approach the conjugated polymer backbones for electrochemical doping and therefore cannot be gated.

We carried out Cyclic Voltammetry (CV) measurements of the polymers on indium tin oxide (ITO) in a 100 mM NaCl aqueous solution to investigate the effect of side-chain substitution on the reduction potential in film. As shown in Figure 7.3a, we clearly observed that the reduction onset potentials gradually shift from -0.30 V for 0 TEG to -0.29 V for 1 TEG to -0.17 V for

2 TEG, indicating that the most hydrophilic 2 TEG is easiest to be reduced electrochemically in aqueous electrolyte (doped by cations).

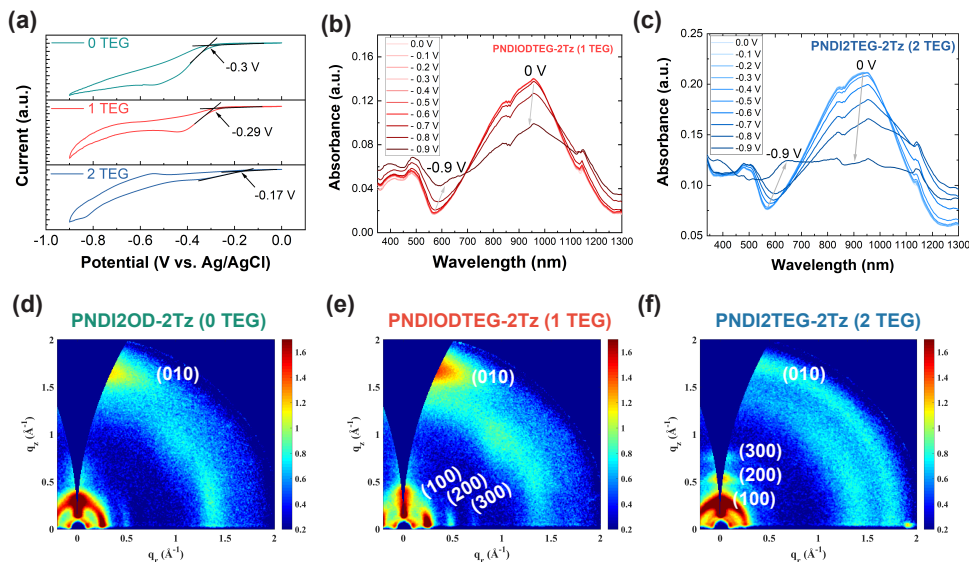


Figure 7.3: a) Cyclic voltammetry of polymer thin films (0 TEG, 1 TEG, and 2 TEG) on ITO substrates in 100 mM NaCl aqueous solution with the negative potential (reduction, n-type doping, scan rate 20 mVs^{-1}). Electrochemical spectroscopy of b) 1 TEG and c) 2 TEG with the negative potential versus Ag/AgCl in 100 mM NaCl aqueous solution (reduction, n-type doping). 2D GIWAXS patterns of d) 0 TEG, e) 1 TEG, and f) 2 TEG thin films.

The shift in reduction onset likely stems from the difference in electron affinity and ease of ion diffusion into the bulk film during electrochemical redox doping. The ion doping process of the polymer was monitored by spectroelectrochemistry measurements that were also carried out in the 100 mM NaCl aqueous solution. Here the films were electrochemically reduced and oxidized using an Ag/AgCl electrode (Figure 7.3, Figures 7.S4 and 7.S5, Supporting Information). Figure 7.3b,c show the absorbance spectra of 1 TEG and 2 TEG films in the reduced states at various bias potentials (from 0 to -0.9 V) displaying the reduced states. Upon increasing the reducing potential, the main neutral intramolecular charge transfer (ICT) absorption (around 950 nm) gradually diminishes while new absorbing species emerge at around 550 and $1200\text{--}1300 \text{ nm}$ due to a polaronic (and/or bipolaronic) absorption. 2 TEG exhibits a higher ratio (polaronic/ICT absorption) than that of 1 TEG at a given bias, indicating a higher electrochemical doping efficiency due to the higher number of TEG side chains, improving the ion-penetration capability. No polaron generation was observed in the 0 TEG spectra (Figure 7.S8, Supporting Information). These results confirm the importance of introducing TEG side chains to the polymer backbone to enhance ion transport. The volumetric capacitance C^* is extracted from electrochemical impedance spectroscopy (EIS) in 100 mM NaCl aqueous solution (Figure 7.S10, Supporting Information). The capacitance values are obtained from fits of EIS data to an equivalent circuit of $R_s(R_{\text{p}}||C)$ at each potential.

Only 2 TEG shows an increased capacitance with applying potential, while 0 TEG and 1 TEG do not increase (resembling the bare gold electrode) (Figure 7.S11, Supporting Information). The estimated C^* of 2 TEG is 367 Fcm^{-3} , which is similar to the reported NDI-2T based polymers. The OECT electron mobility was calculated using $\mu C^* = 1.16 \text{ Fcm}^{-1} \text{V}^{-1} \text{s}^{-1}$ (extracted from the slope of the linear fitting in the plot of g_m versus OECT channel geometry, Figure 7.S19, Supporting Information) and measured C^* . The OECT mixed ionic and electronic charge carrier mobility of 2 TEG is calculated to be $3.16 \times 10^{-3} \text{ cm}^2 \text{V}^{-1} \text{s}^{-1}$, which is on par with the well-performing n-type OECT polymers, like the NDI-thiophene based P-90[14] and BBL.[20] We next explore how the TEG side chains impact the charge mobility in non-fused NDI-2Tz backbone polymers. As previously shown in the literature,[14] introducing TEG side chains might result in a significant drop in electron mobility. We investigated the charge transport properties of pristine 0 TEG, 1 TEG, and 2 TEG using bottom contact/top gate field-effect transistors (Figure 7.S6, Supporting Information). The field-effect electron mobility for 0 TEG, 1 TEG, and 2 TEG, was determined to be $\approx 10^{-2} \text{ cm}^2 \text{V}^{-1} \text{s}^{-1}$ at room temperature. The reported 2 TEG field-effect mobility is $3.5 \times 10^{-2} \text{ cm}^2 \text{V}^{-1} \text{s}^{-1}$. [34] Unfortunately, due to relatively high gate leakage currents, we are unable to determine the field-effect mobility accurately, though the order of magnitude remains the same, see Figure 7.S6 (Supporting Information). The polymers exhibit the ambipolar properties both in OFETs and in OECTs (Figure 7.S6, Supporting Information). These results indicate that non-fused NDI-2Tz backbone-based 2 TEG are able to achieve both high electron mobility and efficient ion transport properties at the same time, which is essential for effective OECT performance. The aqueous electrolyte-gated OECT is summarized in Table 7.2.

To understand how the TEG side chains influence the polymer film crystallinity and molecular packing and how this correlate to the device performance, grazing incidence wide-angle X-ray scattering measurements on polymer films were carried out. The results are shown in Figure 7.3d–f and Figure 7.S12 (Supporting Information) includes the corresponding line cuts. Though all these polymers have the same NDI-2Tz backbone, replacing alkyl chains with TEG side chains results in significant differences in the microstructure and molecular packing. The 0 TEG chain shows a bimodal orientation with both face-on and edge-on fractions: a (100) peak at $q_{xy} = 0.25 \text{ \AA}^{-1}$ and (010) peaks at $q_z = 1.65 \text{ \AA}^{-1}$ and was observed together with a (100) peak at $q_z = 0.28 \text{ \AA}^{-1}$. On the contrary, both 1 TEG and 2 TEG chains tend to adopt monoidal orientation. 1 TEG shows a predominant face-on orientation with an improved crystallinity (compared with 0 TEG), exhibiting lamellar diffractions up to the third-order (300) at $q_{xy} = 0.71 \text{ \AA}^{-1}$ in the in plane (IP) direction together with the (010) peak at $q_z = 1.67 \text{ \AA}^{-1}$ in the out of plane (OOP) direction. 2 TEG appears to pack mostly with an edge-on orientation relative to the substrate, exhibiting lamellar diffractions progressing to the third order (300) at $q_z = 0.75 \text{ \AA}^{-1}$ in the IP direction together with an (010) peak at $q_z = 1.71 \text{ \AA}^{-1}$ in the OOP direction. This polymer further exhibits a preferential edge-on oriented molecular packing, which is known to be favorable for charge carrier transport in OFET devices. Based on the (010) diffraction, the π – π stacking was calculated to be 3.81 \AA for 0 TEG, 3.76 \AA for 1 TEG, and 3.67 \AA for 2 TEG, respectively, showing gradual reduced distance with increased amounts of TEG side chains. We also calculated the crystal coherence lengths (CCLs) to be 24.74 \AA for 0 TEG, 28.82 \AA for 1 TEG, and 33.60 \AA for 2 TEG, respectively, implying the crystallinity is enhanced. The increased crystallinity and preferential edge-on orientation of 2

TEG are the main contributing factors to the improved charge carrier transport in OEET and OFET devices.

To assess device operation performance, stability is a key factor that needs to be taken into account for successful applications. Figure 7.4a shows the stability of n-type drain current ($V_{ds} = 0.6$ V) upon consecutive gate voltage pulsing (5s with $V_G = 0.9$ V and 5s of delay). The device was stable, and no degradation was observed until 1000 cycles. The on current decreases to $\approx 25\%$ after 4000 cycles, but still displays the same on-off ratio (Figure 7.S23a, Supporting Information). The device eventually broke down at the 4887th cycle (Figure 7.S23, Supporting Information). Reproducibility of individual device performance is essential for integrated circuits and arrays. We repeated the OEET characterization measurements on different devices (as well as with different dimensions of interdigitated microelectrodes), and we find almost no variation among devices (Figure 7.S20, Supporting Information). The 2

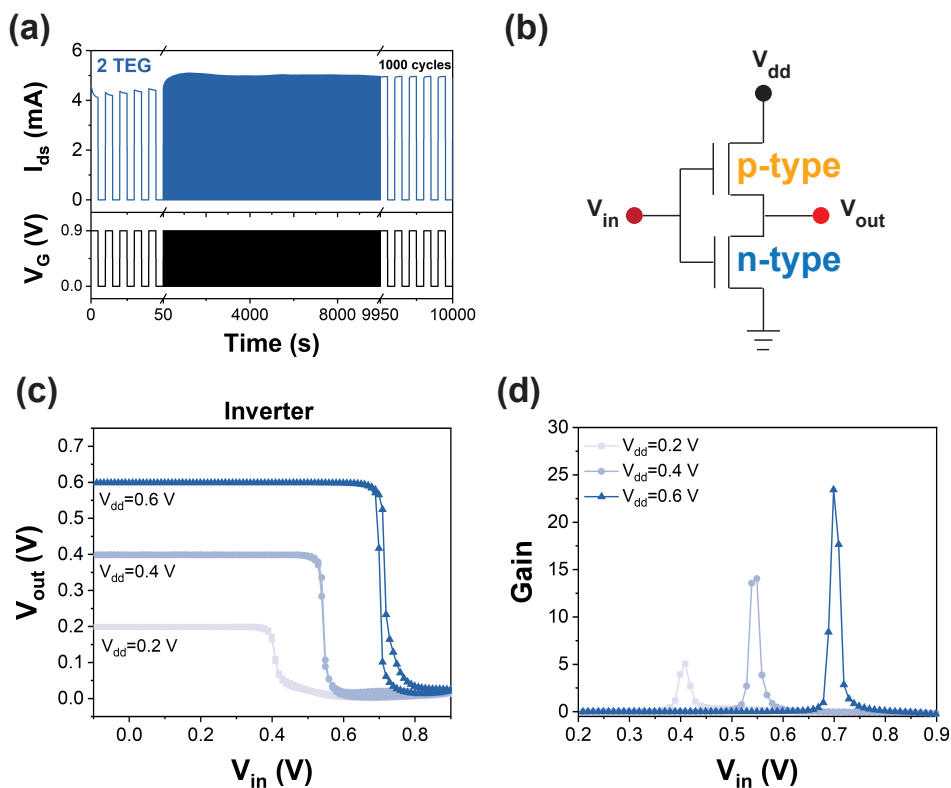


Figure 7.4: a) Operation stability measurement of 2 TEG OEET. 1000 pulse cycles of Drain current (I_{ds}) were monitored when a gate voltage pulse $V_G = 0.9$ V was applied for 5s with an interval time of 5s ($V_{ds} = 0.6$ V). b) The schematic of the inverter c) The complementary inverter input-output characteristics using Pg2T-TT as p-type channel and 2 TEG as n-type channel, 100 mM NaCl as electrolyte. d) The corresponding inverter gain ($\partial V_{out} / \partial V_{in}$).

TEG based OECTs can also operate in phosphate buffered saline (PBS) (Figure 7.S20d, Supporting Information), which has the potential for bio-applications like metabolite sensing.[12] Additionally, we performed a shelf-life stability test where the devices were stored in ambient condition. Even though the current degraded by over 40% after 1 month, the current remains at a \approx mA magnitude (Figure 7.S21, Supporting Information). In fact, only a very minor decrease in the on-off ratio is observed, which is still over 10^4 for all four devices (Figure 7.S22, Supporting Information). We combined our n-type 2 TEG based OECT with a p-type Pg2T-TT based OECT to form an inverter for logic circuits often used as an amplifier for biosignals[38] (see Figure 7.4b). The inverter shows small hysteresis and a maximum gain ($\partial V_{out}/\partial V_{in}$) of 23.4 at $V_{dd} = 0.6$ V (see Figure 7.4c,d). We also show the aqueous OECT operation of 2 TEG using devices made with lithography and parylene liftoff [39] (Figure 7.S26, Supporting Information). In general, we find that TEG side chains improve the OECTs performance with respect to the on-off ratio, transconductance, and operation speed by facilitating ion transport and ion coupling while introducing the nitrogen to the polymer backbone improves electron mobility. Together these two factors make for the high operating performance of the 2 TEG in aqueous electrolyte-gated OECTs.

7.2.3 Ion Gel Gated Electrochemical Transistors and Resistive Random-Access Memory Devices (EC-RAMs)

To demonstrate the versatility of the material, we also investigated ionic liquid-gated electrochemical devices. Ionic liquids are used in electrolyte-gated transistors because they have a larger electrochemical window compared to water,[40] a high capacitance, and can be printed.[41] Moreover, it has been previously reported that water can introduce traps in organic semiconductors and hinder OFETs performance during operation.[42–44] The ionic liquid - 1-ethyl-3-methylimidazolium bis(trifluorosulfonyl)imide (EMIM:TFSI) - is blended with poly(vinylidene fluoride-co-hexafluoropropylene) to prepare the ion gel solid electrolyte, as described in previous reports.[45] For ion gel gating we adopted a side gate architecture, which simplifies fabrication using lithography. Figure 7.5a shows the schematic of the organic electrochemical resistive random-access memory devices (EC-RAMs), which are also able to operate as conventional side-gated OECTs. The device microscope image is shown in Figure 7.S28 (Supporting Information). We first characterized the ion gel gated OECTs performance of 0 TEG, 1 TEG, and 2 TEG in ambient conditions. The n-type OECT transfer characteristic of these three polymers is shown in Figure 7.5b. 1 TEG shows the highest on-current among the three polymers, while no source-drain current is measured in 0 TEG devices (similar to aqueous electrolyte gating). The on-off ratio of 1 TEG is about two orders of magnitudes higher than 2 TEG in both p- and n-type transfer curves shown in Figure 7.S30 (Supporting Information). 1 TEG polymer film shows larger porous structures in the AFM image (Figure 7.S7, Supporting Information), which we speculate is to allow the large ionic liquid ions (larger than Na^+ and Cl^-) to penetrate the polymer film easier, resulting in enhanced doping efficiency. Both 1 TEG and 2 TEG exhibit ambipolar properties, like in the aqueous electrolyte case (shown in Figure 7.S16, Supporting Information). EC-RAMs typically operate at a low voltage and display numerous accessible non-volatile conductance states.[7] These conductance states could be implemented as synaptic weights in hardware-based artificial neural networks (ANNs). For these networks state retention is important.[46]

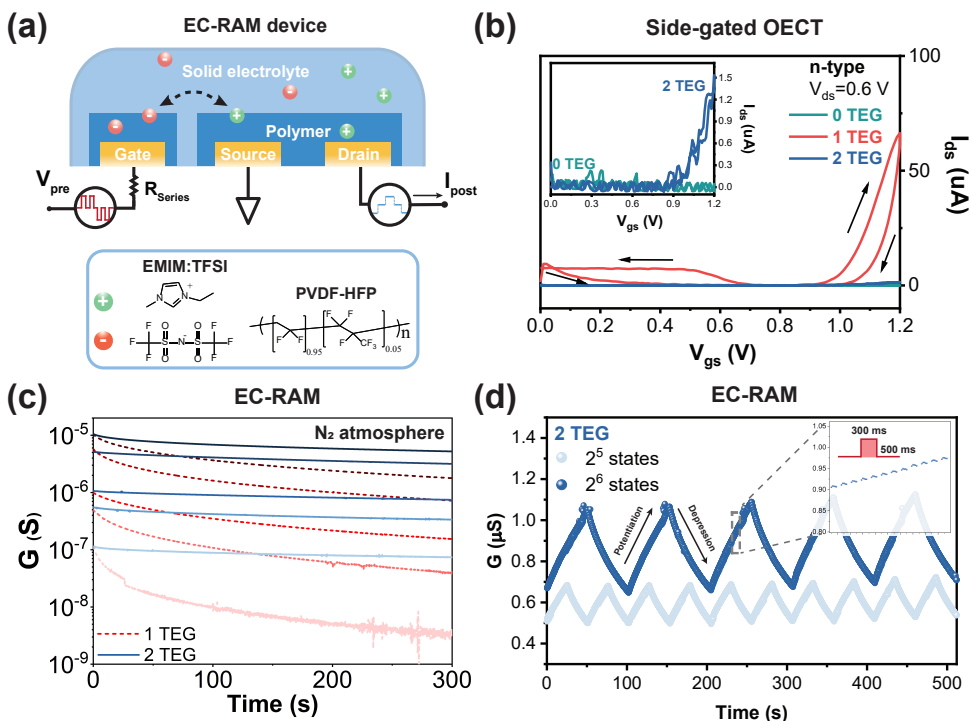


Figure 7.5: a) Schematic of the ion gel side-gated EC-RAMs including chemical structures of the ionic liquid (EMIM:TFSI) and PVDF-HFP. b) Linear transfer curves of 0 TEG, 1 TEG, and 2 TEG measured in ambient conditions (scan rate 10 mVs^{-1}). c) The state retention of 1 TEG and 2 TEG over 5 min while the gate is in open circuit. Measured in a nitrogen atmosphere. d) 2 TEG EC-RAM linear potentiation and depression programming individually with 32 or 64 conductance states (pulse width 300 ms and delay time 500 ms with a 1 GOhm series resistor. +10 V for potentiation and -3 V for depression). Measured in a nitrogen atmosphere.

We compared 1 TEG and 2 TEG based EC-RAM state retention over time in n-type mode (positive drain and gate voltage) when the gate is in an open circuit (shown in Figure 7.5c). The conductance states of 2 TEG show good state retention in all conductance ranges in the nitrogen atmosphere. 2 TEG exhibits 50% decrease in the conductance at a level of 10^{-5} S while that of 1 TEG decays over 80% in 5 min. At a low conductance level of 10^{-7} S, 1 TEG decays over an order of magnitude in 5 min, and 2 TEG decays <30% while remaining in the same order of magnitude. The state retention indicates that 2 TEG is better equipped to hold the cations and prevent the cation diffusion back to the electrolyte than 1 TEG. We hypothesize that TEG chains coordinate (or crown) cations such that the rate of their exfiltration from the film is inversely proportional to the density of TEG chains. Hardware-based ANNs (like parallel arrays) require that the accessible conductance states of each EC-RAM is linearly programmable by external write voltages.[47] Meanwhile, each state should be distinguishable. The linear programming cycles of 2 TEG based EC-RAM with 32 and 64 potentiation and

depression steps are shown in Figure 7.5d. As illustrated in Figure 7.5a, a series resistor is used to control the gate current and prevent the loss of the conductance state.[48] A voltage pulse (amplitude +10 V for potentiation and -3 V for depression, width of 300 ms) is applied at the gate. The inset is a zoom-in image clearly showing the individual conductance states during 500 ms. Although the number of required conductance states is hard to predict a priori, being strongly dependent on application, devices with 10-100 clearly distinct states often lead to sufficiently high ANN accuracy.[46] More importantly, the 2TEG EC-RAM allows for linear and symmetric programming, demonstrating its potential for neuromorphic computing applications. In summary, in ion gel gating, 1 TEG exhibits a higher on-off ratio than 2 TEG in transistor operation, while 2 TEG is a better candidate for EC-RAM applications based on the enhanced state retention. It is important to consider the application when designing a material and, for that, to understand the structure-property relationship. Currently, the mechanisms underlying the observed state retention of 1 TEG and 2 TEG remain unclear, requiring further investigation.

7.3 Conclusion

We have developed a series of non-fused, planar NDI-2Tz copolymers decorated with and without hydrophilic TEG side chains, and investigated their OECT performance in aqueous electrolyte and ionic liquid, as well as their EC-RAM performance. Compared to the non-TEG side-chain substituted or mono-TEG side-chain substituted polymers, the polymer with two TEG side chains (PNDI2TEG-2Tz, 2 TEG) exhibits the highest OECT performance in the merits of transconductance, μC^* , on-off ratio and operation speed in aqueous electrolyte, owing to improved ion conductivity and volumetric capacitance. In addition, benefiting from the highly planar and rigid backbone, favorable backbone orientation and low-lying LUMO energy level, PNDI2TEG-2Tz (2 TEG) achieved electron mobility up to $3.16 \times 10^{-2} \text{ cm}^2 \text{ V}^{-1} \text{ s}^{-1}$ in OECT and $\approx 10^{-2} \text{ cm}^2 \text{ V}^{-1} \text{ s}^{-1}$ in OFET operation. Moreover, the double TEG chain substituted polymer exhibits good conductance state retention over 2 orders of magnitudes in electrochemical resistive random-access memory devices (EC-RAMs), highlighting its potential for neuromorphic computing. This work demonstrates that non-fused donor-acceptor conjugated polymers can achieve high electron mobility and ion penetration capability simultaneously, an essential characteristic for OECTs. The work contributes to a deeper understanding of the relationship between the polymer structure and the performance of n-type OECTs, opening a window toward designing even higher performance n-type OECT materials.

7.4 Experimental Section

7.4.1 Materials

The synthesis details of the NDI-2Tz based D-A copolymers are described in the Supporting Information. Chloroform, 1-ethyl-3-methylimidazolium bis(trifluorosulfonyl)imide, poly(vinylidene fluoride-co-hexafluoropropylene) are purchased from Sigma-Aldrich and used as received. The interdigitated microelectrodes IDA-Au-1, IDA-Au-5, IDA-Au-6 are

purchased from MicruX technologies. The parameters of interdigitated microelectrodes are summarized in Table 7.S2 (Supporting Information).

7.4.2 Device Fabrication and Characterizations

The polymer solutions were prepared in chloroform (5 mg mL^{-1}). The interdigitated microelectrodes were treated with UV ozone for more than 15 min, following spin-coating the polymer solutions at 1000 rpm for 30 s. For ion gel side gated devices, the Au gate electrode is placed next to the interdigitated electrodes. The polymers were spun cast on top, followed by laser ablation to separate the gate and the active channel. The ion gel electrolyte spans over the gap. The electrical characterization of OECTs is recorded by a Keithley sourcemeter 2602B, which is controlled by the software Arkeo developed by Cici research. The fabrication of patterned N-type polymer OECTs is described in the Supporting Information. The thickness of spun polymer thin films was characterized by a Veeco Dektak 150 profilometer.

7.4.3 Cyclic Voltammetry (CV) and Electrochemical Impedance Spectroscopy (EIS)

Cyclic voltammetry measurements were performed using a Biologic SP-150 potentiostat with a standard three electrodes configuration in 100 mM NaCl aqueous solution. Polymer thin films were spun on an ITO glass used as a working electrode, together with a platinum wire as the counter electrode and an Ag/AgCl electrode as the reference electrode. Electrochemical Impedance Spectroscopy was also performed with the three electrodes system in a 100 mM NaCl aqueous solution. The polymers were spun on SU-8 patterned $2.5 \times 2.5 \text{ mm}$ Au electrodes used as working electrode, together with a platinum wire as the counter electrode and an Ag/AgCl electrode as the reference electrode.

7.4.4 UV-vis-NIR Electrochemical Spectroscopy

The measurements were carried out following a previously reported method.[49] The polymer thin films were deposited on ITO glass, and then immersed into a cuvette which is filled with 100 mM NaCl aqueous electrolyte, together with Ag/AgCl electrode. The UV-vis-NIR transmission of polymer films was monitored in situ at different voltages (vs Ag/AgCl) to probe the neutral and charged states during electrochemical doping.

7.4.5 GIWAXS

Grazing incidence wide-angle X-ray scattering (GIWAXS) measurements were performed using a MINA X-ray scattering instrument built on a Cu rotating anode source ($= 1.5413 \text{ \AA}$). 2D patterns were collected using a Vantec500 detector (1024×1024 pixel array with pixel size $136 \times 136 \mu\text{m}$) located 122 mm away from the sample. The films were placed in reflection geometry at certain incident angles with respect to the direct beam using a Huber goniometer. GIWAXS patterns were acquired using incident angles from 0.2° in order to probe the thin film structure. The direct beam center position on the detector and the sample-to-detector

distance were calibrated using the diffraction rings from standard silver behenate and Al₂O₃ powders.

7.5 Supporting Information

7.5.1 Water contact angle



Figure 7.S1: Water contact angle of PNDI2OD-2Tz (0 TEG), PNDIODTEG-2Tz (1 TEG) and PNDI2TEG-2Tz (2 TEG).

7.5.2 UV-vis-NIR Absorption Spectroscopy

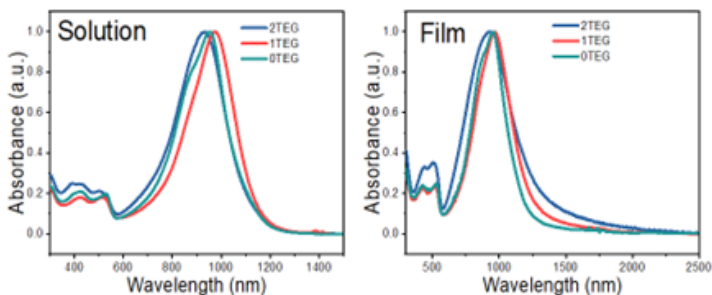


Figure 7.S2: The UV-vis-NIR absorption of PNDI2OD-2Tz (0 TEG), PNDIODTEG-2Tz (1 TEG) and PNDI2TEG-2Tz (2 TEG) in dilute CHCl₃ (10⁻⁵ M) and thin film state.

7.5.3 Cyclic voltammetry

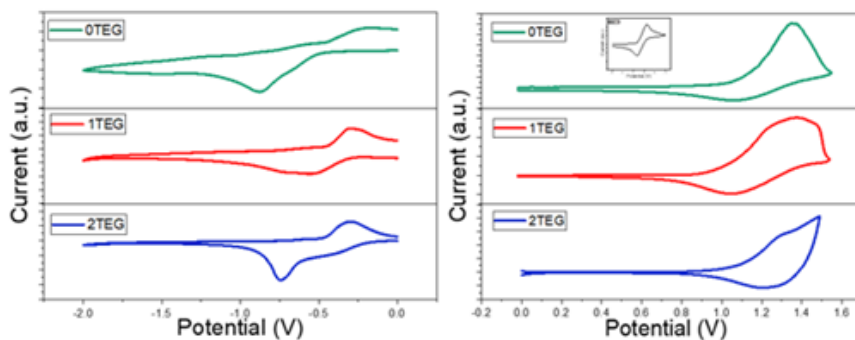


Figure 7.S3: Cyclic voltammograms of the conjugated polymer PNDI2OD-2Tz (0 TEG), PNDIODTEG-2Tz (1 TEG) and PNDI2TEG-2Tz (2 TEG) thin films deposited on the glassy carbon working electrode in CHCN3 solution containing Bu4NPF6 electrolyte.

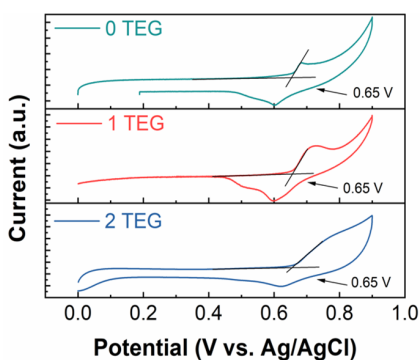


Figure 7.S4: Cyclic voltammetry of polymer films (0 TEG, 1 TEG, 2 TEG) on ITO substrates in 100 mM NaCl aqueous solution with positive potential (oxidation, p-type doping).

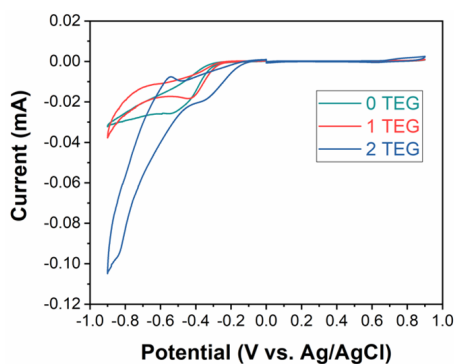


Figure 7.S5: Cyclic voltammetry of polymer thin films (0 TEG, 1 TEG, 2 TEG) on ITO substrates in 100 mM NaCl aqueous solution with both positive potential (p-type doping) and negative potential (n-type doping). The positive potential and negative potential were scanned individually with a scan rate of 20 mV/s.

7.5.4 Organic Field-Effect Transistor (OFET) Fabrication and Performance of Polymers. OFET fabrication and characterization

The top-gate/bottom-contact organic field-effect transistors (OFETs) were fabricated to investigate the charge transport properties of all polymers. Source/drain electrodes (3 nm Cr and 30 nm Au) were patterned on borosilicate glass by photolithography. The substrates were cleaned by sonication in acetone and isopropanol followed by UV-ozone and oxygen plasma treatment. The semiconductor layers (PNDI2OD-2Tz (0 TEG), PNDIODTEG-2Tz (1 TEG) and PNDI2TEG-2Tz (2 TEG)) were dissolved in chloroform and were spin-coated from 5 mg/mL solutions at 1500 rpm, and then they were thermally annealed at 120 °C temperatures for 10 min. The CYTOP-M material was purchased from Asahi Glass Co. Ltd., Japan. It was diluted in CT-SOLV180 solvent (volume ratio 2:1, CYTOP-M:CT-SOLV180) prior to use for dielectric coating. After spin-coating on the substrate, the dielectric layers were annealed at 100 °C for 10 min. The thickness of the dielectric layer is around 400 nm measured by profilometer and the area capacitance is calculated to be ca. 4.4 nF cm⁻². Finally, 50 nm Al was evaporated on top as the gate electrode to complete the devices. The channel length is 10 μm and the width is 5 mm. The devices were characterized with a Keithley 4200 semiconductor characterization system. All device fabrication and characterization were carried out in N₂-filled glove box.

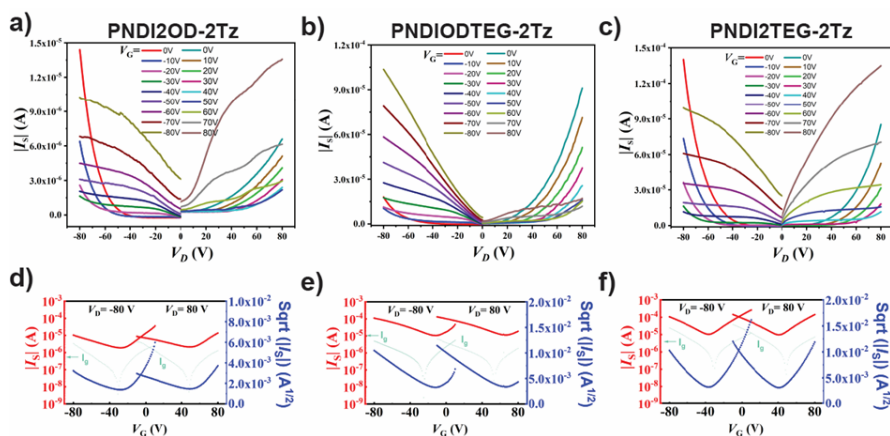


Figure 7.S6: Output and transfer characteristics of top-gate/bottom-contact OFET of (a, d) PNDI2OD-2Tz (0 TEG) and (b, e) PNDIODTEG-2Tz (1 TEG), and (c, f) PNDI2TEG-2Tz (2 TEG). L = 10 μm and W = 5 mm for all devices.

7.5.5 Atomic force microscopy

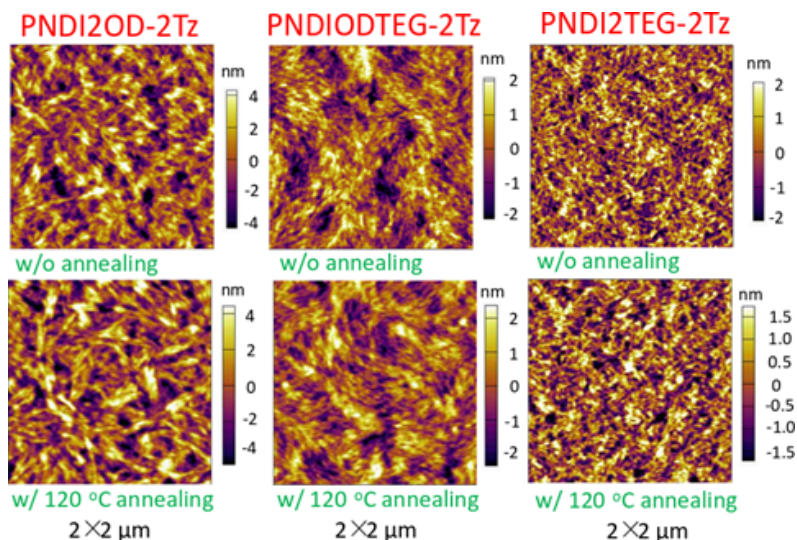


Figure 7.S7: AFM images of polymer films PNDI2OD-2Tz (0 TEG), PNDIODTEG-2Tz (1 TEG) and PNDI2TEG-2Tz (2 TEG) with or without annealing.

7.5.6 UV-vis-NIR Electrochemical Spectroscopy

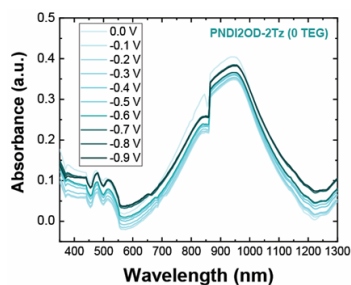


Figure 7.S8: Electrochemical spectroscopy measurement of PNDI2OD-2Tz (0 TEG) under negative potential versus Ag/AgCl in 100 mM NaCl aqueous solution (n-type doping).

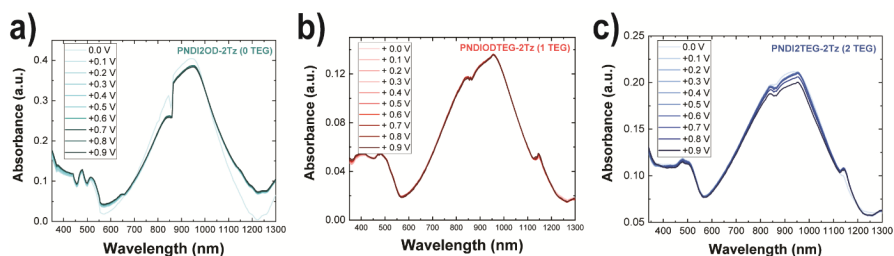


Figure 7.S9: Electrochemical spectroscopy measurement of PNDI2OD-2Tz (0 TEG), PNDI2ODTEG-2Tz (1 TEG), and PNDI2TEG-2Tz (2 TEG) under positive potential versus Ag/AgCl in 100 mM NaCl aqueous solution (p-type doping).

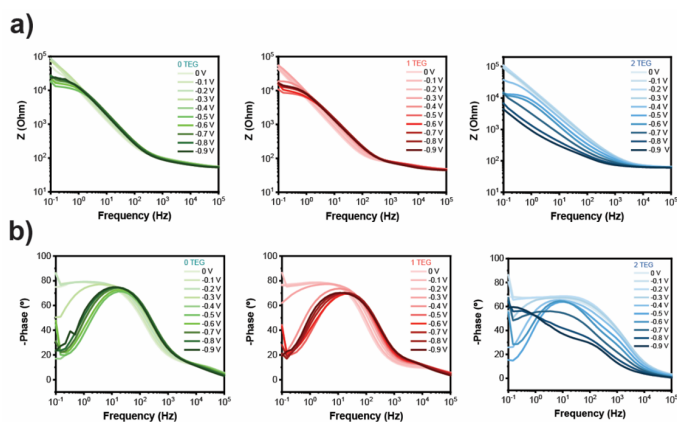


Figure 7.S10: Bode plot a) and phase angle b) of PNDI2OD-2Tz (0 TEG, thickness 181.8 nm), PNDI2ODTEG-2Tz (1 TEG, thickness 125.3 nm), PNDI2TEG-2Tz (2 TEG, thickness 79.0 nm) deposited on SU-8 patterned with Au as working electrodes (area 2.5 mm×2.5 mm, a layer of 5nm Cr followed by 50 nm Au was deposited on glass) in 100 mM NaCl aqueous solution. Potentials from 0 V to -0.9 V were applied at the working electrode.

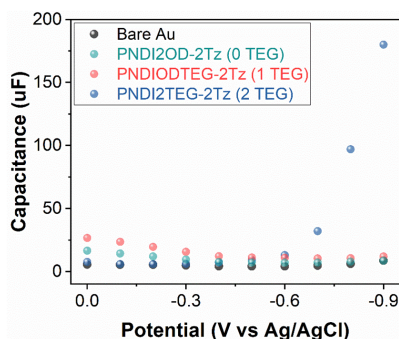


Figure 7.S11: The plot of the capacitance versus the potential. The capacitance values are obtained from fits of EIS data to an equivalent circuit of $R_s(R_p||C)$ at each potential in the Biologic EC-lab software. The volumetric capacitance C^* of 2 TEG is calculated from the maximum capacitance at -0.9 V divided by the polymer thin film volume.

7.5.7 Grazing Incidence Wide Angle X-Ray Scattering (GIWAXS)

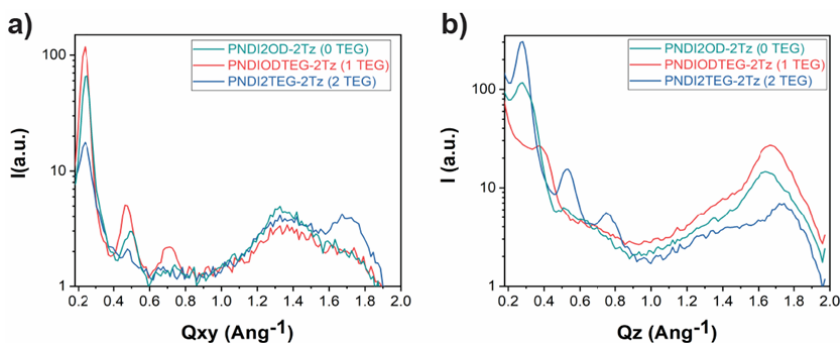


Figure 7.S12: The GIWAXS horizontal (in-plane) a) and vertical (out-of-plane) b) linecuts for 0 TEG, 1 TEG, and 2 TEG thin films.

Table 7.S1: Peak positions, estimated spacing and orientation for PNDI2OD-2Tz (0 TEG), PNDIODTEG-2Tz (1 TEG), and PNDI2TEG-2Tz (2 TEG) thin films from GIWAXS linecuts.

Polymer	PNDI2OD-2Tz (0TEG)	PNDIODTEG-2Tz (1TEG)	PNDI2TEG-2Tz (2TEG)
100 in plane	0.25	0.24	0.24
010 in plane			1.71
100 out of plane	0.28		0.27
010 out of plane	1.65	1.67	1.74
Orientation	Mixed face-on and edge-on	Relative face-on	Relative edge-on
$\pi - \pi$ distance (Å)	3.83	3.76	3.61
Crystal coherence length (Å)	24.74	28.82	33.60

7.5.8 Organic Electrochemical Transistors (OECTs)

Aqueous electrolyte

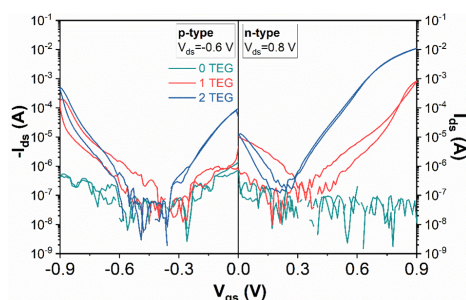


Figure 7.S13: The semi-log plot of OECT transfer curves of PNDI2OD-2Tz (0 TEG), PNDIODTEG-2Tz (1 TEG) and PNDI2TEG-2Tz (2 TEG) fabricated on IDA-Au-6 electrodes. Using 100 mM NaCl aqueous solution as the electrolyte.

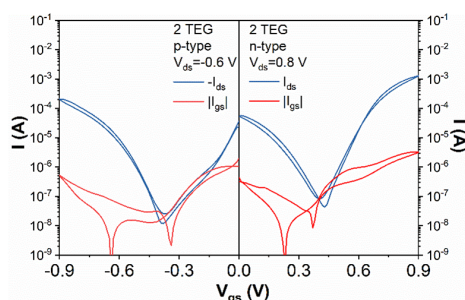


Figure 7.S14: The semi-log plot of OECT transfer curves of PNDI2TEG-2Tz (2 TEG) including the gate current fabricated on IDA-Au-6 electrodes. Using 100 mM NaCl aqueous solution as the electrolyte.

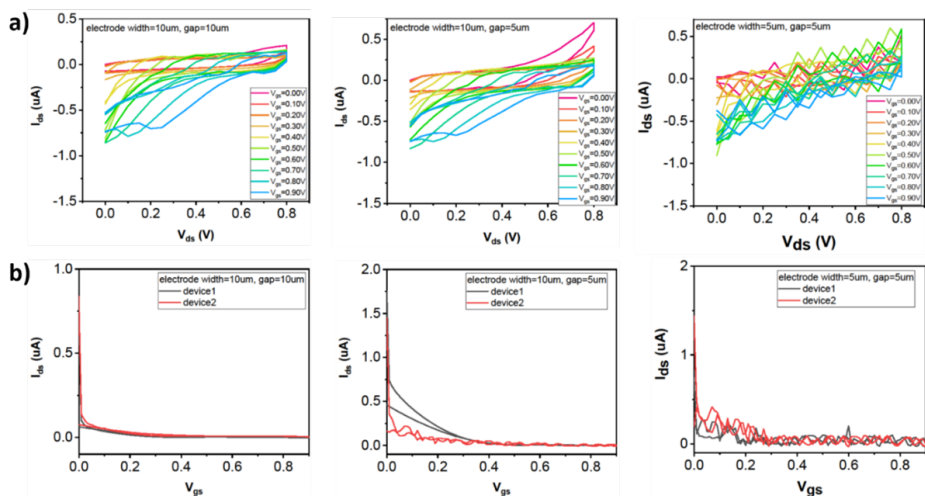


Figure 7.S15: The OECT characteristic (100 mM NaCl aqueous solution as the electrolyte) of PNDI2OD-2Tz (0 TEG) fabricated on interdigitated electrodes with different dimensions: IDA-Au-1 (electrode width=10 μm , gap=10 μm), IDA-Au-5 (electrode width=10 μm , gap=5 μm), and IDA-Au-6 (electrode width=5 μm , gap=5 μm). a) Output curves. b) Transfer curves.

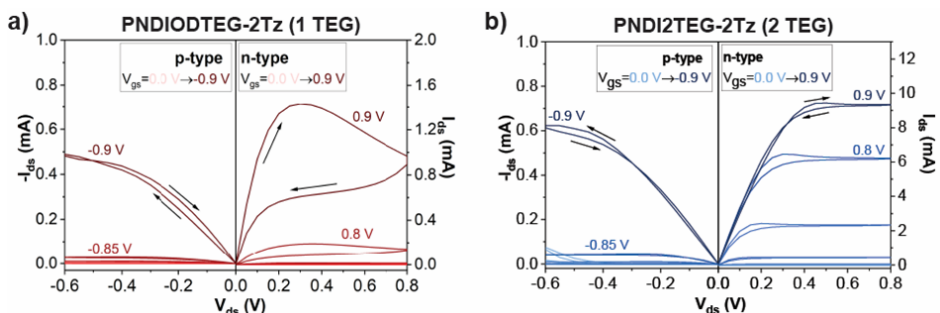


Figure 7.S16: OECT (100 mM NaCl aqueous solution as the electrolyte) ambipolar output curve of a) PNDIODTEG-2Tz (1 TEG) and b) PNDI2TEG-2Tz (2 TEG) fabricated using IDA-Au-6 electrode.

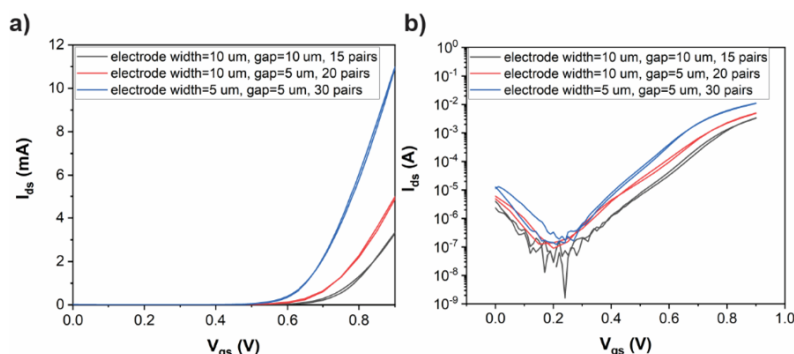


Figure 7.S17: OECT (100 mM NaCl aqueous solution as the electrolyte) transfer curves of PNDI2TEG-2Tz (2 TEG) fabricated on interdigitated electrodes with different dimensions a) linear plot; b) semi-log plot.

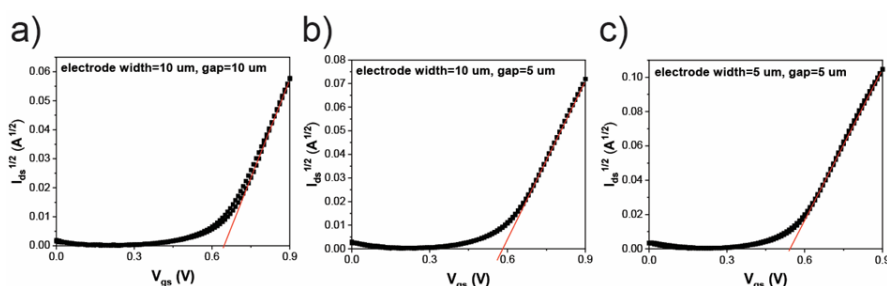


Figure 7.S18: $I_{ds}^{1/2}$ vs V_{gs} plots of PNDI2TEG-2Tz (2 TEG). The threshold voltages are extracted from the x-intercept: $V_{Th}=0.63\pm0.02$ V (IDA-Au-1, electrode width=10 μm , gap=10 μm); $V_{Th}=0.58\pm0.02$ V (IDA-Au-5, electrode width=10 μm , gap=5 μm); $V_{Th}=0.54\pm0.01$ V (IDA-Au-6, electrode width=5 μm , gap=5 μm), respectively. Using 100 mM NaCl aqueous solution as the electrolyte. The extracted values of V_{Th} are used to calculate μC^* in Figure 7.S19.

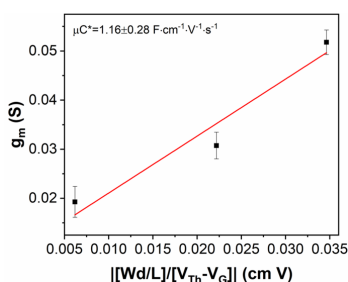


Figure 7.S19: Plot of maximum transconductance versus OECT channel geometry and operation parameters of PNDI2TEG-2Tz (2 TEG). The μC^* is extracted from the slope with the linear fitting. Using 100 mM NaCl aqueous solution as the electrolyte.

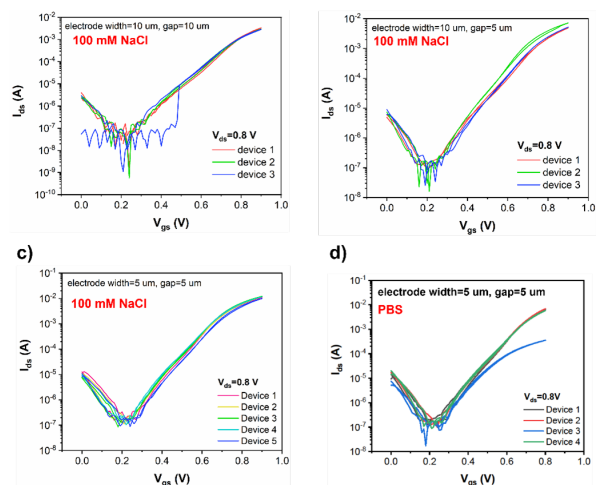


Figure 7.S20: The semi-log transfer plots of multiple OECT devices of PNDI2TEG-2Tz (2 TEG) on different dimensional electrodes showing the reproducibility. a) IDA-Au-1 gating with 100 mM NaCl aqueous solution. b) IDA-Au-5 gating with 100 mM NaCl aqueous solution. c) IDA-Au-6 gating with 100 mM NaCl aqueous solution. d) IDA-Au-6 gating with phosphate buffered saline (PBS).

Shelf-life stability

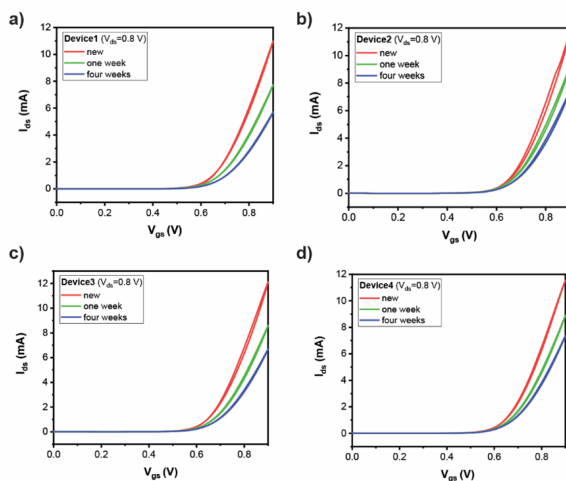


Figure 7.S21: The OECT transfer curves of PNDI2TEG-2Tz (2 TEG) (on IDA-Au-6 electrodes) over time describing the self-life stability. The devices were stored in ambient environment. The devices were characterized immediately after fabrication, one week later, and four weeks later, respectively. 100 mM NaCl aqueous solution was used as gating electrolyte.

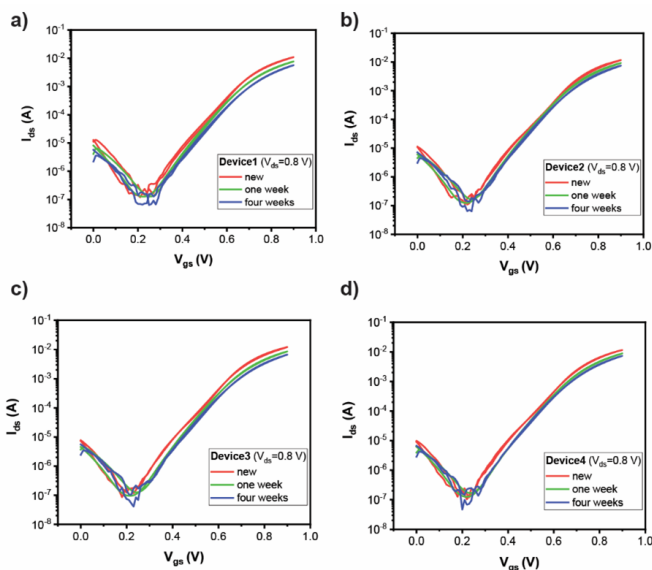


Figure 7.S22: The semi-log OECT transfer curves of PNDI2TEG-2Tz (2 TEG) (on IDA-Au-6 electrodes) with time showing the shelf-life stability. The devices were stored in ambient environment. The devices were characterized immediately after fabrication, one week later, and four weeks later, respectively. 100 mM NaCl aqueous solution was used as gating electrolyte.

Operational stability

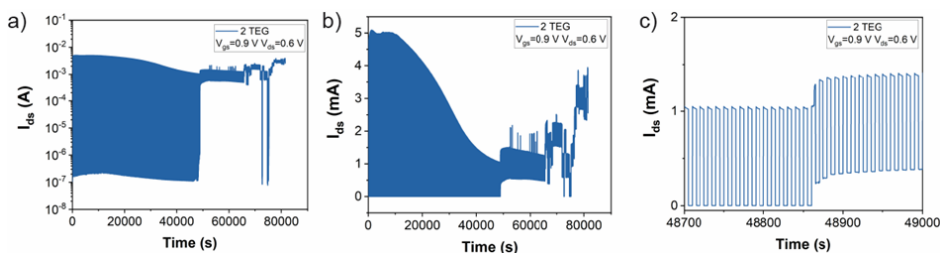


Figure 7.S23: N-type operation stability measurement of the OECT in 100 mM NaCl aqueous solution. Drain current (I_{ds} , $V_{ds}=0.6$ V) was monitored when a gate voltage pulse $V_G=0.9$ V was applied for 5 s with an interval time of 5 s. a) Semi-log plot of drain current versus time. b) linear plot of drain current versus time. c) The breakdown of the device at the 4887th cycle.

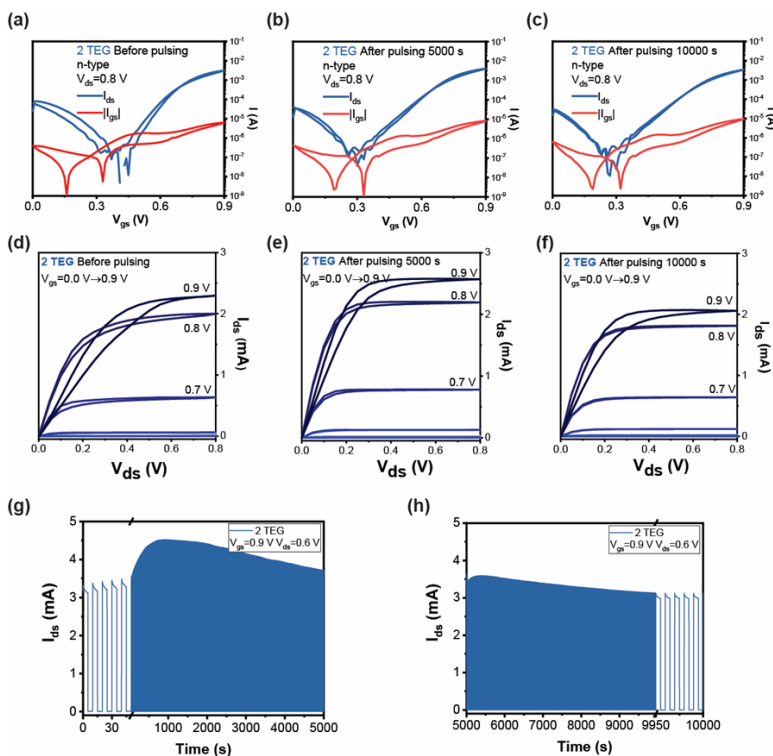


Figure 7.S24: N-type operation stability measurement of the OECT in 100 mM NaCl aqueous solution. Drain current (I_{ds} , $V_{ds}=0.6$ V) was monitored when a gate voltage pulse $V_G=0.9$ V was applied for 5 s with an interval time of 5 s. a) Transfer curve before pulsing. b) Transfer curve after 5000 s. c) Transfer curve after 10000 s. d) Output curve before pulsing. e) Output curve after 5000 s. f) Output curve after 10000 s. g) first 5000 s and h) second 5000 s drain current versus time when the gate voltage pulse was applied.

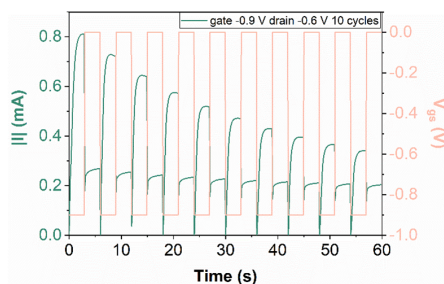


Figure 7.S25: P-type operation stability measurement of the OECT in 100 mM NaCl aqueous solution. 10 cycles of drain current (I_{ds} , $V_{ds}=-0.6$ V) were monitored while a gate voltage pulse $V_G=-0.9$ V was applied for 5 s with an interval time of 5 s.

Patterned N-type Polymer Devices Fabrication

Devices were fabricated following a protocol specified previously[39]. Standard microscope glass slides (75 mmx25 mm) were sonicated first in a soap bath (Micro-90) and then in a 1:1 (vol/vol) solvent mixture of acetone and isopropanol. The cleaned glass slides were patterned with source, drain and gate gold electrodes for two types of devices using photolithography. A positive photoresist (S1813) was used. A chromium layer was used to achieve better adhesion of the gold on glass. Two layers of parylene-C that were separated by a layer of soap (Micro-90 soap solution, 1% vol/vol in deionized water) were deposited. An adhesion promoter (silane A-174 (gamma-Methacryloxypropyltrimethoxysilane)) was added to the lower layer of parylene-C to prevent removal. This layer insulates the gold electrodes. In a second photolithography step (with positive photoresist AZ 9260), the channel and lateral gate dimensions are outlined. Reactive Ion Etching (RIE) with O₂/CF₄ plasma was used to open up the channel and corresponding gates. The channel dimensions for type 1 devices are: W x L = 80 μ m x 240 μ m with a lateral gate of the same size (80 μ m x 240 μ m) and 450 μ m distance between gate and channel. Type 2 devices have the following dimensions: W x L = 80 μ m x 480 μ m with a lateral gate of 2000 μ m x 2000 μ m and 450 μ m distance between gate and channel. The upper parylene-C layer was sacrificed in a peel-off process after spin-coating the 2 TEG polymer.

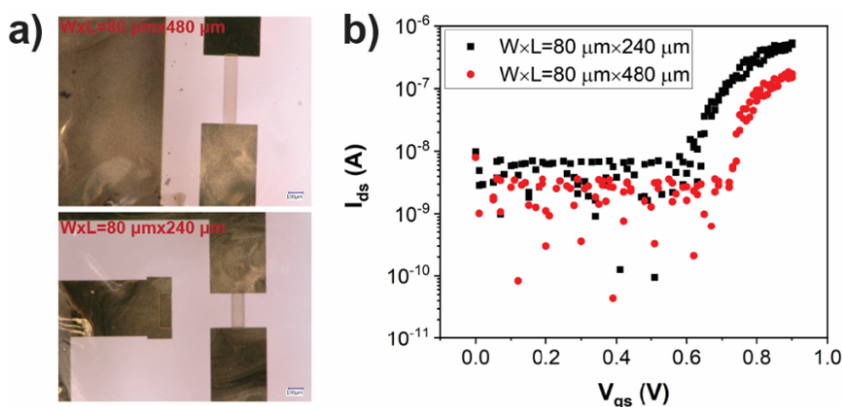


Figure 7.S26: a) Microscope images of patterned 2 TEG polymer film as OECTs active channel with size of W x L = 80 μ m x 480 μ m and 80 μ m x 240 μ m. b) Transfer curve of patterned 2 TEG OECTs using 100 mM NaCl aqueous electrolyte and Ag/AgCl gate electrode.

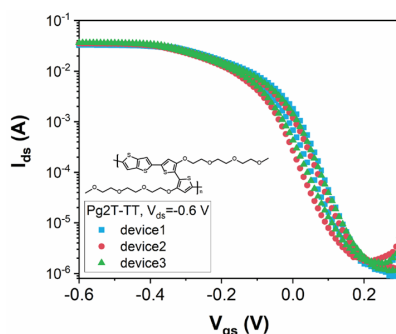


Figure 7.S27: The semi-log OECT transfer curves of p-type Pg2T-TT (IDA-Au-6 electrodes). 100 mM NaCl aqueous solution was used as gating electrolyte, and an Ag/AgCl electrode as gate.

7.5.9 Ion gel electrolyte side-gated OECTs

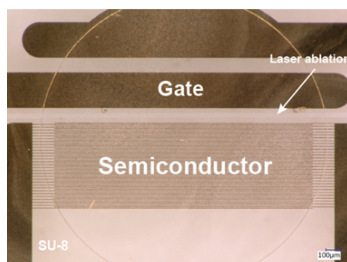


Figure 7.S28: A microscope image of a 2 TEG polymer film deposited on IDA-Au-6 interdigitated electrodes with ion gel on top. The gate and active channel are separated by excimer laser ablation.

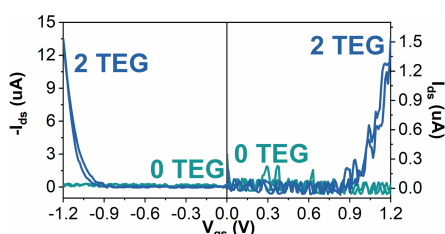


Figure 7.S29: Linear ambipolar transfer curves of 0 TEG, 2 TEG ion gel side-gated OECTs (interdigitated electrodes, IDA-Au-6) measured in ambient.

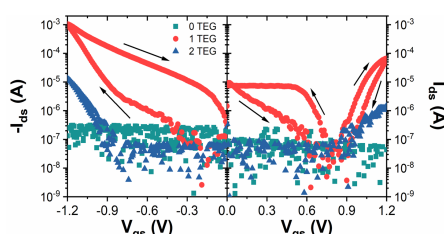


Figure 7.S30: Semi-log ambipolar transfer curves of 0 TEG, 1 TEG, and 2 TEG ion gel side-gated OECTs (interdigitated electrodes, IDA-6) measured in ambient.

Table 7.S2: Dimensions of the interdigitated electrodes.

	Length (um)	Individual channel width (mm)	Number of pairs	Number of channels n	Total width of channels W (W=n×w) (cm)	d(nm)	Wd/L(cm)	WdL (μm ³)
IDA-Au-1	10	1.8	15	29	5.22	49.4	2.58×10^{-2}	25786.8
IDA-Au-5	5	1.8	20	39	7.02	49.4	6.94×10^{-2}	17339.4
IDA-Au-6	5	1.8	30	59	10.62	49.4	1.05×10^{-1}	26231.4

Table 7.S3: Transconductance and threshold voltage of PNDI2TEG-2Tz (2 TEG).

	V_{Th} (V)	V_g (V)	$g_{m_{max}}$ (mS)	$\frac{g_{m_{max}} \cdot L}{W \cdot d}$ (S·cm ⁻¹)	Peak current (mA)	$\frac{Peakcurrent}{W \cdot d \cdot L}$ (μA·μm ⁻³)
IDA-Au-1	0.63±0.02	0.87	19.27±3.15	0.747	3.04±0.26	0.118
IDA-Au-5	0.58±0.02	0.90	30.73±2.72	0.443	5.79±1.22	0.334
IDA-Au-6	0.54±0.01	0.87	51.78±2.50	0.493	11.46±0.48	0.437

Author Contributions

YZ and GY, initiated the idea. YvdB supervised the project. GY, JS, and RCC designed the polymer. GY synthesized the polymer. YZ, GY and TvdP characterized the polymer. **Eveline van Doremaele** and YZ characterized the devices. **Eveline van Doremaele**, YZ, IK and PG fabricated devices. JD and GP performed the GIWAXS. YL performed the DFT calculation. YZ, GY and YvdB wrote the manuscript.

Bibliography

1. Rivnay, J. *et al.* **Organic electrochemical transistors**. en. *Nature Reviews Materials* **3**, 17086. ISSN: 2058-8437 (Feb. 2018).
2. Khodagholy, D. *et al.* **High transconductance organic electrochemical transistors**. en. *Nature Communications* **4**. Number: 1 Publisher: Nature Publishing Group, 2133. ISSN: 2041-1723 (July 2013).
3. Andersson Ersman, P. *et al.* **All-printed large-scale integrated circuits based on organic electrochemical transistors**. en. *Nature Communications* **10**. Number: 1 Publisher: Nature Publishing Group, 5053. ISSN: 2041-1723 (Nov. 2019).
4. Inal, S., Rivnay, J., Suiiu, A.-O., Malliaras, G. G. & McCulloch, I. **Conjugated Polymers in Bioelectronics**. *Accounts of Chemical Research* **51**, 1368–1376. ISSN: 0001-4842 (June 2018).
5. Cea, C. *et al.* **Enhancement-mode ion-based transistor as a comprehensive interface and real-time processing unit for in vivo electrophysiology**. en. *Nature Materials* **19**, 679–686. ISSN: 1476-1122, 1476-4660 (June 2020).
6. Van de Burgt, Y., Melianas, A., Keene, S. T., Malliaras, G. & Salleo, A. **Organic electronics for neuromorphic computing**. en. *Nature Electronics* **1**, 386–397. ISSN: 2520-1131 (July 2018).
7. Van de Burgt, Y. *et al.* **A non-volatile organic electrochemical device as a low-voltage artificial synapse for neuromorphic computing**. en. *Nature Materials* **16**, 414–418. ISSN: 1476-1122, 1476-4660 (Apr. 2017).
8. Paulsen, B. D., Tybrandt, K., Stavrinidou, E. & Rivnay, J. **Organic mixed ionic–electronic conductors**. en. *Nature Materials* **19**, 13–26. ISSN: 1476-4660 (2020).
9. Bronstein, H., Nielsen, C. B., Schroeder, B. C. & McCulloch, I. **The role of chemical design in the performance of organic semiconductors**. en. *Nature Reviews Chemistry* **4**. Number: 2 Publisher: Nature Publishing Group, 66–77. ISSN: 2397-3358 (Feb. 2020).
10. Zeglio, E. & Inganäs, O. **Active Materials for Organic Electrochemical Transistors**. en. *Advanced Materials* **30**. _eprint: <https://onlinelibrary.wiley.com/doi/pdf/10.1002/adma.201800941>, 1800941. ISSN: 1521-4095 (2018).

11. Sun, H., Guo, X. & Facchetti, A. High-Performance n-Type Polymer Semiconductors: Applications, Recent Development, and Challenges. en. *Chem* **6**, 1310–1326. ISSN: 2451-9294 (June 2020).
12. Pappa, A. M. *et al.* Direct metabolite detection with an n-type accumulation mode organic electrochemical transistor. *Science Advances* **4**. Publisher: American Association for the Advancement of Science, eaat0911 (June 2018).
13. Giovannitti, A. *et al.* N-type organic electrochemical transistors with stability in water. en. *Nature Communications* **7**. Number: 1 Publisher: Nature Publishing Group, 13066. ISSN: 2041-1723 (Oct. 2016).
14. Giovannitti, A. *et al.* The Role of the Side Chain on the Performance of N-type Conjugated Polymers in Aqueous Electrolytes. *Chemistry of Materials* **30**. Publisher: American Chemical Society, 2945–2953. ISSN: 0897-4756 (May 2018).
15. Wang, S. *et al.* A Chemically Doped Naphthalenediimide-Bithiazole Polymer for n-Type Organic Thermoelectrics. en. *Advanced Materials* **30**. _eprint: <https://onlinelibrary.wiley.com/doi/pdf/10.1002/adma.201801898>, 1801898. ISSN: 1521-4095 (2018).
16. Wang, S. *et al.* Effect of Backbone Regiochemistry on Conductivity, Charge Density, and Polaron Structure of n-Doped Donor–Acceptor Polymers. en. *Chemistry of Materials* **31**, 3395–3406. ISSN: 0897-4756, 1520-5002 (May 2019).
17. Surgailis, J. *et al.* Mixed Conduction in an N-Type Organic Semiconductor in the Absence of Hydrophilic Side-Chains. en. *Advanced Functional Materials* **31**. _eprint: <https://onlinelibrary.wiley.com/doi/pdf/10.1002/adfm.202010165>, 2010165. ISSN: 1616-3028 (2021).
18. Savva, A. *et al.* Solvent Engineering for High-Performance n-Type Organic Electrochemical Transistors. en. *Advanced Electronic Materials* **5**, 1900249. ISSN: 2199-160X, 2199-160X (Aug. 2019).
19. Wang, S. *et al.* Thermoelectric Properties of Solution-Processed n-Doped Ladder-Type Conducting Polymers. *Advanced Materials* **28**. _eprint: <https://onlinelibrary.wiley.com/doi/pdf/10.1002/adma.201603731>, 10764–10771. ISSN: 1521-4095 (2016).
20. Sun, H. *et al.* Complementary Logic Circuits Based on High-Performance n-Type Organic Electrochemical Transistors. en. *Advanced Materials* **30**. _eprint: <https://onlinelibrary.wiley.com/doi/pdf/10.1002/adma.201704916>, 1704916. ISSN: 1521-4095 (2018).

21. Chen, X. *et al.* n-Type Rigid Semiconducting Polymers Bearing Oligo(Ethylene Glycol) Side Chains for High-Performance Organic Electrochemical Transistors. en. *Angewandte Chemie International Edition* **60**. _eprint: <https://onlinelibrary.wiley.com/doi/pdf/10.1002/anie.202013998>, 9368–9373. ISSN: 1521-3773 (2021).
22. Feng, K. *et al.* Fused Bithiophene Imide Dimer-Based n-Type Polymers for High-Performance Organic Electrochemical Transistors. en. *Angewandte Chemie* **133**. _eprint: <https://onlinelibrary.wiley.com/doi/pdf/10.1002/ange.202109281>, 24400–24407. ISSN: 1521-3757 (2021).
23. Huang, H., Yang, L., Facchetti, A. & Marks, T. J. Organic and Polymeric Semiconductors Enhanced by Noncovalent Conformational Locks. en. *Chemical Reviews* **117**, 10291–10318. ISSN: 0009-2665, 1520-6890 (Aug. 2017).
24. Chen, X., Zhang, Z., Ding, Z., Liu, J. & Wang, L. Diketopyrrolopyrrole-based Conjugated Polymers Bearing Branched Oligo(Ethylene Glycol) Side Chains for Photovoltaic Devices. en. *Angewandte Chemie International Edition* **55**. _eprint: <https://onlinelibrary.wiley.com/doi/pdf/10.1002/anie.201602775>, 10376–10380. ISSN: 1521-3773 (2016).
25. Wu, W., Liu, Y. & Zhu, D. π -Conjugated molecules with fused rings for organic field-effect transistors: design, synthesis and applications. en. *Chemical Society Reviews* **39**. Publisher: The Royal Society of Chemistry, 1489–1502. ISSN: 1460-4744 (Apr. 2010).
26. Guo, X., Facchetti, A. & Marks, T. J. Imide- and Amide-Functionalized Polymer Semiconductors. en. *Chemical Reviews* **114**, 8943–9021. ISSN: 0009-2665, 1520-6890 (Sept. 2014).
27. Liu, C., Wang, K., Gong, X. & Heeger, A. J. Low bandgap semiconducting polymers for polymeric photovoltaics. en. *Chemical Society Reviews* **45**. Publisher: The Royal Society of Chemistry, 4825–4846. ISSN: 1460-4744 (Aug. 2016).
28. Shi, L., Guo, Y., Hu, W. & Liu, Y. Design and effective synthesis methods for high-performance polymer semiconductors in organic field-effect transistors. en. *Materials Chemistry Frontiers* **1**. Publisher: The Royal Society of Chemistry, 2423–2456. ISSN: 2052-1537 (Nov. 2017).
29. Nielsen, C. B. *et al.* Molecular Design of Semiconducting Polymers for High-Performance Organic Electrochemical Transistors. en. *Journal of the American Chemical Society* **138**, 10252–10259. ISSN: 0002-7863, 1520-5126 (Aug. 2016).

30. Giovannitti, A. *et al.* Controlling the mode of operation of organic transistors through side-chain engineering. *Proceedings of the National Academy of Sciences of the United States of America* **113**, 12017–12022. ISSN: 0027-8424 (Oct. 2016).
31. Wang, Y. *et al.* Hybrid Alkyl–Ethylene Glycol Side Chains Enhance Substrate Adhesion and Operational Stability in Accumulation Mode Organic Electrochemical Transistors. en. *Chemistry of Materials* **31**, 9797–9806. ISSN: 0897-4756, 1520-5002 (Dec. 2019).
32. Hallani, R. K. *et al.* Regiochemistry-Driven Organic Electrochemical Transistor Performance Enhancement in Ethylene Glycol-Functionalized Polythiophenes. en. *Journal of the American Chemical Society* **143**, 11007–11018. ISSN: 0002-7863, 1520-5126 (July 2021).
33. Liu, J. *et al.* N-Type Organic Thermoelectrics of Donor–Acceptor Copolymers: Improved Power Factor by Molecular Tailoring of the Density of States. en. *Advanced Materials* **30**. _eprint: <https://onlinelibrary.wiley.com/doi/pdf/10.1002/adma.201804290>, 1804290. ISSN: 1521-4095 (2018).
34. Liu, J. *et al.* Amphipathic Side Chain of a Conjugated Polymer Optimizes Dopant Location toward Efficient N-Type Organic Thermoelectrics. en. *Advanced Materials* **33**. _eprint: <https://onlinelibrary.wiley.com/doi/pdf/10.1002/adma.202006694>, 2006694. ISSN: 1521-4095 (2020).
35. Shin, Y.-h. *et al.* Synthesis and Aggregation Behavior of a Glycolated Naphthalene Diimide Bithiophene Copolymer for Application in Low-Level n-Doped Organic Thermoelectrics. en. *Macromolecules* **53**, 5158–5168. ISSN: 0024-9297, 1520-5835 (July 2020).
36. Ye, G. *et al.* Controlling n-Type Molecular Doping via Regiochemistry and Polarity of Pendant Groups on Low Band Gap Donor–Acceptor Copolymers. en. *Macromolecules* **54**, 3886–3896. ISSN: 0024-9297, 1520-5835 (Apr. 2021).
37. Paterson, A. F. *et al.* Water stable molecular n-doping produces organic electrochemical transistors with high transconductance and record stability. en. *Nature Communications* **11**. Number: 1 Publisher: Nature Publishing Group, 3004. ISSN: 2041-1723 (June 2020).
38. Rashid, R. B. *et al.* Ambipolar inverters based on cofacial vertical organic electrochemical transistor pairs for biosignal amplification -supp. en. *Science Advances* **7**, eabh1055. ISSN: 2375-2548 (Sept. 2021).

39. Koutsouras, D. A., Prodromakis, T., Malliaras, G. G., Blom, P. W. M. & Gkoupidenis, P. **Functional Connectivity of Organic Neuromorphic Devices by Global Voltage Oscillations**. en. *Advanced Intelligent Systems* **1**. _eprint: <https://onlinelibrary.wiley.com/doi/pdf/10.1002/aisy.201900013>, 1900013. ISSN: 2640-4567 (2019).
40. Galiński, M., Lewandowski, A. & Stępnia, I. **Ionic liquids as electrolytes**. en. *Electrochimica Acta* **51**, 5567–5580. ISSN: 0013-4686 (Aug. 2006).
41. Kim, S. H. *et al.* **Electrolyte-Gated Transistors for Organic and Printed Electronics**. en. *Advanced Materials* **25**. _eprint: <https://onlinelibrary.wiley.com/doi/pdf/10.1002/adma.201202790>, 1822–1846. ISSN: 1521-4095 (2013).
42. Zuo, G., Linares, M., Upreti, T. & Kemerink, M. **General rule for the energy of water-induced traps in organic semiconductors**. en. *Nature Materials* **18**. Number: 6 Publisher: Nature Publishing Group, 588–593. ISSN: 1476-4660 (June 2019).
43. Bobbert, P. A., Sharma, A., Mathijssen, S. G. J., Kemerink, M. & de Leeuw, D. M. **Operational Stability of Organic Field-Effect Transistors**. en. *Advanced Materials* **24**. _eprint: <https://onlinelibrary.wiley.com/doi/pdf/10.1002/adma.201104580>, 1146–1158. ISSN: 1521-4095 (2012).
44. Iqbal, H. F. *et al.* **Suppressing bias stress degradation in high performance solution processed organic transistors operating in air**. en. *Nature Communications* **12**. Number: 1 Publisher: Nature Publishing Group, 2352. ISSN: 2041-1723 (Apr. 2021).
45. Lee, K. H. *et al.* **“Cut and Stick” Rubbery Ion Gels as High Capacitance Gate Dielectrics**. *Advanced Materials* **24**. _eprint: <https://onlinelibrary.wiley.com/doi/pdf/10.1002/adma.201200950>, 4457–4462. ISSN: 1521-4095 (2012).
46. Gumyusenge, A., Melianas, A., Keene, S. T. & Salleo, A. **Materials Strategies for Organic Neuromorphic Devices**. *Annual Review of Materials Research* **51**. _eprint: <https://doi.org/10.1146/annurev-matsci-080619-111402>, 47–71 (2021).
47. Fuller, E. J. *et al.* **Parallel programming of an ionic floating-gate memory array for scalable neuromorphic computing**. en. *Science*, eaaw5581. ISSN: 0036-8075, 1095-9203 (Apr. 2019).
48. Li, Y. *et al.* **In situ Parallel Training of Analog Neural Network Using Electrochemical Random-Access Memory**. *Frontiers in Neuroscience* **15**. ISSN: 1662-453X (2021).

49. Paulsen, B. D. *et al.* Time-Resolved Structural Kinetics of an Organic Mixed Ionic–Electronic Conductor. en. *Advanced Materials* **32**. _eprint: <https://onlinelibrary.wiley.com/doi/pdf/10.1002/adma.202003404>, 2003404. ISSN: 1521-4095 (2020).

Chapter 8

Conclusion

Neuromorphic computing has emerged as a new type of computing to overcome limitations of traditional computing methods. Neuromorphic computing is based on the principles of the human brain and nervous system, which can perform complex computations extremely efficiently. By mimicking these biological processes, neuromorphic computing has the potential of creating more intelligent and energy-efficient computing systems. Especially in the field of bioelectronics, organic neuromorphic computing has the capability to make a significant impact and drive further advancement towards realizing intelligent healthcare systems interfacing with biology.

8.1 Conclusions

Bioelectronics has made enormous progress towards the development of concepts, materials and devices that are capable of sensing, monitoring and controlling a biological environment, enabling concepts such as local drug delivery and electrical, chemical or mechanical stimulation. However, to achieve fully autonomous bioelectronic applications, it is necessary not only to acquire biological signals but also to process and store data locally and with low power, and to extract particular relevant features. Organic neuromorphic devices can address these requirements to further advance the field of bioelectronics. In **chapter 2** of this thesis, we have presented an overview of trends in organic neuromorphic devices and organic bioelectronic sensing platforms. We discussed the potential of merging these two fields. Neuromorphic materials and devices that exhibit memory and have the potential to operate at the interface with biology can pave the way for novel data classification paradigms with bio-inspired features in information processing. These materials might offer promising solutions for the manipulation and the processing of biological signals, and enable applications spanning from novel brain–computer-interfaces and adaptive prosthetics to bioinformatics and the definition of novel computational paradigms at the interface with biology. For such applications, we envision a central role of smart multi-modal sensor platforms and local neuromorphic processing.

We presented a smart biosensing platform in **chapter 3** that could pave the way for such adaptive bioelectronic systems. Importantly, this biosensor can be trained locally to classify cystic fibrosis as an example disease, without the aid of software. The classification of cystic fibrosis from human sweat samples serves as proof-of-principle. The sensor module can, in principle, be replaced by another sensor to retrain the network for other applications in diagnostics or environmental monitoring. We have shown the versatility by varying the input signals and demonstrated the on-chip retraining. The training was done using an error signal feedback to modulate the conductance of organic neuromorphic devices that represent the weights in a software neural network. The training of the neural network is a direct translation of the software single layer perceptron algorithm executed in hardware. Expanding the neural network to multiple layers allows for more complex classification tasks beyond linearly separable problems but requires a new strategy for the backpropagation in hardware, as presented in **chapter 4**.

In **chapter 4** we discussed a novel approach of the backpropagation in hardware, that is executed layer-by-layer. The essence of this strategy is that the weights of only one layer are updated every training cycle, and every next cycle the layer before will be updated. The update is the product of the backflowing error and the feed forward input signal, an efficient vector multiplication at the gate of the neuromorphic devices representing the weights. Due to this method, no information regarding the state of the weights needs to be remembered to update the weights, which is the bottleneck of the traditional backpropagation algorithm limiting its speed and energy-efficiency. We have demonstrated using simulations that the novel backpropagation approach does not impact the accuracy when classifying the two layer

XOR problem. We have implemented this approach fully in hardware to demonstrate the principle of neuromorphic backpropagation using progressive gradient descent. We showed that this strategy allows to execute the training of neuromorphic circuits fully in hardware leveraging the efficient multiply-accumulate operations not only during inference but also during backpropagation allowing for updating the weights in parallel. These results pave the way for training large neural networks with higher speed and energy-efficiency than the software alternatives.

While the previous chapters focused on the brain-inspired hardware implementation of software neural network algorithms, **chapter 5** targets the information processing and communication of the nervous system. A fundamental difference with chapters 3 and 4 is that (sensor) inputs are encoded in a spiking frequency analogous to the sensory systems in the human body, rather than a voltage amplitude. We fabricated a neuromorphic spiking circuit that can facilitate the encoding of sensor inputs, such as pressure and light, into a frequency of spikes, and subsequently modulate the frequency using neurotransmitters (dopamine and serotonin) mimicking two essential biological functions of neurons and their synapses, sensory coding and neuromodulation. Computing in the brain requires a collective set of neurons and central to efficient computation are the connections. Neural pathways link neurons from different locations and enable the transmission of signals from one region of the nervous system to another. We demonstrated such pathway by connecting two artificial synapses through an electronic circuit and showed that the connected synapses are able to replicate the dependency of dopamine expression on the activity of serotonergic neurons. Moreover, we replicated a full neuronal pathway inspired by the retina that mimics the biological photic regulation mediated by dopamine. We demonstrated a fundamental building block for programmable neural pathways, which enables computing systems to interact with the biological environment and facilitates adaptive biohybrid connections between distinct biological processing units.

Advanced concepts enabling computing systems that can interact with the biological environment clearly need stable materials that can operate at biological interfaces. In **chapter 6** the material P-3O stood out due to the various high-performance functionalities. In this chapter, we demonstrated several properties in both aqueous and solid state environment, such as the high on/off ratios that can be achieved with excellent ambient p- and n-type stability in transistor performance. This allowed us to fabricate a tunable sensing circuit, based on a complementary logic inverter combined with a neuromorphic memory element constructed from the single polymer. We demonstrated the tuning of the gain of the sensing circuit and showed the local signal normalization of electromyograms (EMGs) of two different gestures. Furthermore, we showed that a small neuromorphic array based on this material results in a high accuracy in classifying heartbeat anomalies. While this material exhibits exceptional performance and allows for a monolithically integrated adaptive sensor, research in developing improved materials remains an ongoing effort.

In order to effectively design higher performance materials, **chapter 7** contributes to a deeper understanding of the relationship between the polymer structure and the performance of n-type OECTs. We developed a series of non-fused, planar NDI-2Tz copolymers decorated with and without hydrophilic TEG side chains, and investigated their OECT performance in aqueous electrolyte and ionic liquid, as well as their EC-RAM performance. We demonstrated that the

transistor performance in terms of transconductance, μC^* , on-off ratio and operation speed, in an aqueous environment, increases with the number of TEG chains, owing to an increase in the hydrophilicity and electron affinity improving the ion conductivity and volumetric capacitance. We showed that the polymer with two TEG side chains achieves an electron mobility up to $3.16 \times 10^{-3} \text{ cm}^2 \text{V}^{-1} \text{s}^{-1}$ in OEET and $\approx 10^{-2} \text{ m}^2 \text{V}^{-1} \text{s}^{-1}$ in OFET operation, which we attributed to the highly planar and rigid backbone, favorable backbone orientation and low-lying LUMO energy level.

8.2 Outlook

In this work, we have demonstrated novel neuromorphic algorithms, concepts and materials that can further advance the field of organic neuromorphic computing for bioelectronic applications. Part of the work presented serves as a proof-of-principle. In chapter 3 we showed a programmable biosensor which could be trained and retrained fully in hardware eliminating the need for software. As a result calculations supporting the training were done on the hardware itself improving the performance in speed, energy and accuracy. The neural network considered here is very small, replicating the software perceptron algorithm that consists of 1 layer with 2 inputs and a bias. Its output is binary, true or false. This directly limits the possible applications to classification problems that are linearly separable. In order to broaden the range of applications, the neural network structure has to scale up and the size of the individual components has to decrease accordingly. While in this work we have used relatively large components for demonstration purposes, many could be made smaller. However, the performance of the organic neuromorphic devices, the ECRAMs we use, is strongly related to their size. Shrinking the volume of the material reduces the range and thus reduces the available states that represent the values of the weights in the neural network. At the edges (maximum and minimum) of the conductance range the state retention typically worsens, which reduces the stability of the neural network. Therefore, ongoing research is needed on alternative materials and devices, such as 3D-architectures, to reduce the footprint and encapsulation methods to improve the stability. Scaling up the size of the neural network structure presents an additional challenge of adapting to different algorithms, particularly with regards to the updating mechanism, such as backpropagation. In chapter 4 we discussed a strategy that allows the neural network to increase in the number of layers and performing the backpropagation in hardware. Although all the computational expensive multiplications are executed in hardware, still some software was used to enact the training, particularly the data generation, controlling of the switches and, the sigmoid and error calculation. The sigmoid function used here is an approximation that can be executed in hardware. The controlling of the switches as well as the error calculation, which merely subtracts the output value from its target value, can be done without software, if full hardware neural networks are desired. These functionalities impact only the front-end (data input) and the back-end (output and error), and are independent of the amount of layers. Efficient labeling of the input data and assigning its output, will be a notable challenge for supervised learning entirely in hardware. While finding a suitable solution is feasible, it is closely tied to the application of interest.

In chapter 5 we successfully demonstrated neuromorphic circuits that exhibit functionalities similar to those found in biological neuronal pathways. While other researchers have shown partial integration with biology, sensing, actuation and tuning based on environmental cues, a hybrid artificial/biological neuronal pathway has not been established. A logical next step would be to integrate biological cells with the neuromorphic circuitry. In order to replace (damaged) biological parts, the whole neuromorphic system needs to be compatible with and roughly of the same size as the biological cells and synapses. Currently, the complete system is based on connected individual devices. However, down scaling of the components and fabrication on a single substrate is an improvement that can be easily achieved. Via encapsulation and patterning methods, device electrolytes that interfere with each other can be separated. Similarly, the devices in the adaptive circuit of chapter 6 could benefit from single substrate integration and encapsulation. Furthermore, the tuning of the adaptive circuit was now driven by manually tuning the neuromorphic element (ECRAM) to the desired conductance state to correctly normalize the different signals, while ideally this tuning is done automatically. Future adaptive circuits could realize automatic normalization by incorporating a feedback-loop where the normalized output controls the tuning of the ECRAM conductance value. However, dealing with these types of biosignals in real-time remains a challenge.

We hope that the work presented in this thesis helps to advance the field of organic neuromorphic computing and provides building blocks for future real-life intelligent bioapplications.

Publications

Organic neuromorphic spiking circuit for retina-inspired sensory coding and neurotransmitter-mediated neural pathways, G. Matrone*, **E. van Doremaele***, S. Griggs, G. Ye, I. McCulloch, F. Santoro, Y. van de Burgt. *In submission*.

*Equal contribution

Retrainable neuromorphic biosensor for on-chip learning and classification, **E. van Doremaele**, X. Ji, J. Rivnay, Y. van de Burgt. *Under review*.

Adaptive Biosensing and Neuromorphic Classification Based on an Ambipolar Organic Mixed Ionic–Electronic Conductor, Y. Zhang*, **E. van Doremaele***, G. Ye, T. Stevens, J. Song, R. Chiechi, Y. van de Burgt, *Advanced Materials*, **34**, (20), 2022.

*Equal contribution

High-performance organic electrochemical transistors and neuromorphic devices comprising naphthalenediimide-dialkoxybithiazole copolymers bearing glycol ether pendant groups, Y. Zhang, G. Ye, T. van der Pol, J. Dong, **E. van Doremaele**, I. Krauhausen, Y. Liu, P. Gkoupidenis, G. Portale, J. Song, R. Chiechi, Y. van de Burgt, *Advanced Functional Materials*, **32**, (27), 2022.

Towards organic neuromorphic devices for adaptive sensing and novel computing paradigms in bioelectronics, **E. van Doremaele**, P. Gkoupidenis, Y. van de Burgt, *Journal of Materials Chemistry C*, **7**, (41), 2019.

In preparation

Novel backpropagation approach for in situ training of multilayer hardware neural networks using progressive gradient descent, **E. van Doremaele**, T. Stevens, S. Ringeling, M. Fattori, Y. van de Burgt. *In preparation*.

The influence of the ethylene glycol sidechain length on Naphthalenediimide-Dialkoxybithiazole Copolymers based electrochemical transistors, inverters, and memory devices, Y. Zhang*, **E. van Doremaele***, G. Ye*, J. Li, T. van der Pol, R. Chiechi, Y. van de Burgt. *In preparation*.

*Equal contribution

Unrelated to this thesis

Effect of plasma on gas flow and air concentration in the effluent of a pulsed cold atmospheric pressure helium plasma jet, **E. van Doremaele**, V. Kondeti, P. Bruggeman, *Plasma Sources Science and Technology*, **27**, (9), 2018.

Conference contributions

Contributed talks

Adaptive neuromorphic biosensing and artificial neuronal pathways, **Oral presentation**.

Workshop on Neuromorphic Organic Devices, 2022. Crete, Greece.

On-site trainable biosensor and locally adaptive sensing based on organic neuromorphic circuits, **Oral presentation**.

MRS, 2022. Honolulu, USA.

Smart and adaptable biosensor based on an organic neuromorphic circuit, **Oral presentation**.

MRS, 2021. Boston, USA.

Contributed posters

Trainable organic neuromorphic biosensors, **Poster**.

E-MRS, 2019. Warsaw, Poland.

Neuromorphic engineering and hardware-based A.I. for adaptive sensing and point-of-care health monitoring, **Poster**.

EASIS symposium, 2019. Eindhoven, The Netherlands.

Trainable organic neuromorphic biosensors, **Poster**.

Asilomar, 2019. Pacific Grove, USA.

Curriculum Vitae

Eveline van Doremaele was born in Sittard, the Netherlands on the 20th of March in 1994. Her pre-university education involved both Science & Technology and Science & Health profiles and included the study of Latin and Greek. Thereafter she moved to Eindhoven to study Applied Physics at the Eindhoven University of Technology. After completing her Bachelor in 2015 on the topic of magnetization reversal in cobalt wires supervised by prof.dr. Bert Koopmans, she continued her physics Master interested in various topics. In particular drawn to the medical applications of physics she did a research internship at the Swinburne University of Technology in Melbourne, Australia, where she studied the cell uptake of ligand functionalized gold nanospheres using high-order image correlation spectroscopy supervised by prof. James Chon. For her graduation project she went to the University of Minnesota in Minneapolis, USA, to the group of prof.dr.ir.lic. Peter Bruggeman to investigate the morphology and the effect of plasma on the gas flow in cold atmospheric pressure plasma jets impinging on a substrate. In 2018 she obtained her MSc Applied Physics including both the Honors certificate and the Research certificate.



She got excited by the combination of research and the application of technology for medical purposes and joined the neuromorphic engineering group of dr.ir. Yoeri van de Burgt in January 2019 as a PhD candidate. Her PhD project is part of BIOMORPHIC with the goal to create a microfluidic chip with integrated sensors able to detect and classify biological cells using machine-learning. The results of her research are presented in this thesis.

Acknowledgements

Like many things in life, it is all about the people around you that help you to grow, achieve your goals and enjoy it. During my PhD I was lucky to be around so many great people that have supported me and to which I like to dedicate this section.

First of all, I want to thank my promotor **Yoeri van de Burgt**. You are always positive and excited about new ideas or results. Your enthusiasm is contagious. Every time after our meeting I was even more inspired to get new results. I really admire your optimistic view and skills to make from something that I - with my often too critical mindset - deem 'okay-ish' to something great and amazing. I truly appreciate all the freedom that you gave me to explore everything that I thought was interesting, to travel as much as possible and, to guide students my own way. You taught me how to be an independent researcher and that learning Illustrator for making figures is worth it! I am grateful for your connections and efforts that allowed me to visit Stanford. It is my honor to be your first PhD student to graduate.

Next, I want to thank my second promotor **Jaap den Toonder**. Thank you for welcoming me in the Microsystems section and for making my time in this group so nice by facilitating many group activities such as Glow and the annual Microsystems lunches. Even when the group started to grow exponentially you always found the time to have a regular meeting with me. I learned a lot during our meetings and I admire your ability to always ask the right questions whether the topic is in your field or not.

Thanks to all members of the committee for being part of my defense and for their time to read the thesis. **Bert Meijer**, thank you for your insight and the discussion we had about the dilemma for a job in academics or industry. **George Malliaras**, thank you for always being very kind when we talked at conferences. **Jonathan Rivnay**, thank you for your valuable input during our meetings. **Simone Fabiano**, thank you for trusting me in finding a nice restaurant in Honolulu. **Francesca Santoro**, thank you for sharing your name badge at MRS. **Leon Govaert**, thank you for chairing the defense.

I would like to thank the members of the Microsystems section that made my time here so enjoyable. First of all the other staff members. **Regina Luttge**, thank you for inviting me to the conference in Minneapolis and for actively promoting women

in science! **Hans Wyss**, thank you for being the dedicated photographer during all the group outings. **Ye Wang**, thank you for the interesting discussions in the lunch rooms about all kinds of topics, scientific and non-scientific, and of course for giving me **Sha**.

Sha-lalala, my first office mate! It was a pleasure to share the office with you (even though you really liked to work in the dark). Together we also shared the girls' office with **Yagmur** and **Bhavana**. Thanks **Yagmur** for working early in the mornings too! **Bhavana**, thank you for the nice talks and laughs in the office and sharing frustrations every once in a while. Thank you too, **Kalpiti**. Maybe you forgot, but we also shared the girls' office briefly before you became our neighbour. Although you left the office, you still made the coffee and lunch breaks enjoyable. **Emma**, thank you for filling the empty desk when **Sha** left. Besides being an amazing office mate, you are also a wonderful labmember. You are always looking to help out with various tasks in the lab! I enjoyed our many discussions and brainstorm sessions to improve our *Illustrator* and *Origin* skills to make the best figures as possible. While not all afternoons were as productive as it could be, it was always super *gezellig*. I am very thankful for you to be my paranymp.

Thanks to all the *NeuroGoats*! **Star, Setareh**, it was great to have you by my side at the conferences and in the lab. Especially in the beginning when we had to develop all protocols and try everything to fabricate our devices without the RIE. **Imke** and **Charles**, thank you for joining the group and the fresh energy you brought with you. It was nice to share the fabrication frustrations together and for the time in Boston. I will never forget *Wizard*! **Simone**, thank you for introducing me to fuzzy and for continuing with my projects. It's been great picking your brain. **Benn**, thank you for your enthusiasm on 3D printing and all of you for your great support during the presentation stress. Thank you **Gianmaria**, for your continuous effort on our manuscript, the delicious Limoncello that you surprised me with and the fun Mario Kart parties. And last, **professor Yanxi**. Thank you for the work we did together, the coca-cola celebrations and your amazing laugh. I enjoyed our many discussions and your efforts to explain me my chemistry questions.

When I started in the *Microsystems* there were many people who gave me a warm welcome that have already left. Thank you **Jelle**, for sharing the same humour. You and **Andreas** were my go-to persons if I needed inspiration for new fabrication approaches and always happy to help. Both of you were very active organizing activities and in helping managing the lab, thereby setting a great example for new members, including myself. **Alex**, your PhD defense was the first I ever attended. I was so nervous! Thank you for the many talks we had. **Shuai**, thank you for giving me the introductions to the spin and sputter coater and showing me how to be a superuser. **Marvelous, James**! With you it is always a mystery. You were the person I needed to avoid during group outings since you were the best in capturing the

funny pictures of someone. Thank you for your adventures on fighting crocodiles and providing perspective by sharing your culture. Thank you **Sophia**, for making me feel at home right from the start and for having me as your paranymp. I am grateful for the conversations we had both science related and not. It's great to see how successful you already are, and I am sure it is not done yet. Please continue to inspire people with your excitement and enthusiasm! **Tanveer (Tan-4)**, you also started before me but I am happy to have you still around! Thank you for being always available to help out and endure so many discussions I had with **Yanxi**. **Jiajing**, thank you for always smiling. **Sertan**, thank you for all your knowledge on impedance spectroscopy. During my time at Microsystems the section has been growing a lot which resulted in a diverse group with many nice personalities that each contributed to making my PhD unforgettable. Thanks to all (in no particular order): **Joey**, for accepting your new name for you warm hugs; **Rahman**, for always being kind and interested; **Gülden**, for organizing a beautiful calendar together with **Alex**, **Tanveer**, **Suzanne** and **Jia-Jun**; **Suzanne**, for the interesting conversations in the short time we met; **Jia-Jun**, for always smiling, being super kind and convincing me to go bouldering with the 'Monks': **Jia-Jun**, **Kalpiti**, **Imke**, **Charles**, **Mohammad** and **Sofia**. **Imke**, for being the coach; **Sofia**, for showing me how it's actually done; **Inês**, for sharing doubts about what to do next; **Sevda**, for discussing chloride and glucose sensors; **Zhiwei**, for making me instantly happy by waving from a far distance in the hallways; **Roel**, for sharing our passion for playing the saxophone; **Emiel**, for trying new stuff; **Jordy**, for helping the lab and being the milling expert. Thanks also to **Tongsheng**, **Pan**, **Yiqing**, **Wei**, **Hossein**, **Jing**, **Oscar**, **Yangu**, **Chris**, for always being kind.

Mamali, **Mohammad**! Oops, I almost forgot you. Good thing that you kept reminding me. (And not only because you asked, but) here is my special thanks for you. You were around for most of my PhD and you truly are one-of-a-kind. You introduced me to foosball and always loved to make a wager (which almost caused you to go bald). You shared books that you know I would like and initiated many discussions on various interesting and/or debatable topics. We shared many laughs. I am very grateful that you were around, just being you. Thank you!

I also like to thank my students which each contributed to my own development: **Carlos**, for being my first student; **Bob**, for taking on the challenge of an online project; **Karen**, for being very receptive; **Tom**, for being very independent; **Joris**, for being super enthusiastic; **Pranshu**, to keep on going even when things are difficult; **Gijs**, to explore all the possibilities with ordyl; **Ibrahim** and **Roy**, for your determination to really understand the project. Unfortunately, I cannot supervise the project until the end but I wish you all the best. You are in great hands. Last but not least, **Tim**, thank you for staying around after your graduation. I think we achieved very nice results. Who knows, maybe one day we will build those jetpacks.

Many thanks for the labmanagers of the Microfab/Lab! **Willie**, for showing me all the equipment; **Irene** and **Jaapie**, for your continuous effort on making the lab an enjoyable place for everyone and claiming the new space including Turing (which I often considered *my* lab). Thank you, for always willing to help out. **Sjoukje** and **Katherine**, for making sure that we work safely with chemicals. Also thanks to **Erik** for helping me with 'talking' to the Keithley, and teaching me the saying that it is very time-efficient if you start at the last minute.

I would also like to thank **Liesbeth** and **Joceline**, for ensuring the administration was in order, time sheets were filled in correctly and on time, and found time in Jaap's busy calendar. Thank you for organizing the social activities with the group. **Liesbeth**, I enjoyed the talks we had when I came looking for coffee and that you made sure I had a pen in every color.

I am thankful for the opportunity I had to work in other labs and facilities. Thank you, **Tjibbe**, for your help with the dirty RIE in the NanoLab. **Paul** at EPC, I appreciate that you were willing to help me with designing the neuromorphic circuit even though you really preferred the simple digital components over our organic devices. **Marco**, thank you for giving me access to the cage in the electrical engineering department. I enjoyed working together and I hope that even more results will follow. **Tom van der Pol**, thank you for introducing me to the equipment in the physics and chemistry lab. You are very kind, smart and always happy to help. Thank you, **Vahid**, for making the 4th floor interesting and challenging **Mohammad** with foosball. **Hamid**, you make the best cocktails!

I also like to thank the Salleo Lab, especially **Alberto Salleo** and **Scott**. Thank you for showing me around and really introducing me to research. It has been a wonderful time and a great experience.

These four years would not have been possible with the opportunity to relax and unwind supported by many different people. I like to start with thanking my other paronymph, **Tumi**, **Niki**. We have been friends since we were *Sjaarsen* studying Applied Physics. I deeply appreciate our friendship that has grown stronger throughout the years. Thank you for always being there, for your unconditional support when times were difficult and enthusiasm to celebrate the good times! Also thanks to all the other study friends, the **parallelepipedo's**. I enjoyed all the boardgame nights and pubquizes, our annual trips and the Christmas dinners that often took place somewhere in April. Thank you for still keeping in touch.

Big thanks to all my **teammates of BC Bumpers**! Basketball has always been an important part of my life and especially during the busy times it was great to be able to clear my mind. Nevertheless, the friendship among all of us is the best part. Some of you I know for more than 15 or even 20 years! Thanks for the **drive buddies** and

jonkies, and in particular **Maritti** and **Beks** who traveled all over the world to visit me! You were always there for me. I am very grateful for our friendship. **Joleintje**, I loved our snowboots trips and I am very happy with you and **lucky shadow** and *the best nights evahrr*. **Loesje**, **Marloes**, I am so glad that we found each other in high school. We are so different and yet so alike (exactly like a club sandwich). Thank you for all your support throughout the years. **Denise**, who I also met in high school, I am grateful that we are always there for each other, even when we don't see each other too often. Despite being in different phases of our life our friendship has never changed. Thank you!

Dankjewel **pap** en **mam**! Bedankt voor het stimuleren om niet op te geven en het vertrouwen in mezelf te hebben, me uit te dagen om zo het beste uit mezelf te halen, me te accepteren dat ik altijd *waarom* vraag, het mij lekker zelf laten proberen en mijn perfectionisme af en toe te temperen. Mam, jouw "*Maar wat héb je er nu aan?*" speelt nog altijd een belangrijke rol. Het is fijn om thuis te komen in Mtown, want het is daar eigenlijk altijd gezellig, zeker als we er allemaal zijn. **Joost** en **Koen**, dankjewel *kleine* broertjes. Het was af en toe zwaar met mij als zus maar ik waardeer de band die we hebben opgebouwd heel erg. Bedankt voor de koffiemomentjes, de telefoongesprekken, de autoritjes en er altijd voor me te zijn. Thanks bro's!

Tot slot **Gabje**, my love. Ik ben blij dat je er voor me was toen ik corona had, al wist je meteen dat het dat niet was. Dankjewel voor je onvoorwaardelijke liefde, steun, en vertrouwen in mij. Je hebt mij geholpen om het beste uit mezelf te halen en het soms iets rustiger aan te doen maar me altijd de ruimte gegeven om het op mijn manier te doen. Ik ben je dankbaar dat je dit avontuur met mij hebt willen delen.

